Commissioning and characterization of a plasma source for atomic hydrogen

Master's Thesis of

David Frese

At the KIT Department of Physics
Institute for Astroparticle Physics
Tritium Laboratory Karlsruhe

First examiner:	Prof. Dr. Kathrin Valerius
Second examiner:	Prof. Dr. Sebastian Böser
First advisor:	Dr. Caroline Rodenbeck
Second advisor:	Dr. Genrich Zeller

25. November 2024 – 21. November 2025

Karlsruher Institut für Technologie
Fakultät für Physik
Wolfgang-Gaede-Str. 1
76131 Karlsruhe

Commissioning and characterization of a plasma source for atomic hydrogen (Master's Thesis)

Ich versichere wahrheitsgemäß, die Arbeit selbstständig angefertigt, alle benutzten Hilfsmittel vollständig und genau angegeben und alles kenntlich gemacht zu haben, was aus Arbeiten anderer unverändert oder mit Abänderungen entnommen wurde.

Karlsruhe, 21. November 2025

. . . .
(David Frese)

Als Prüfungsexemplar genehmigt
Ort, Datum

. . . .
(Prof. Dr. Kathrin Valerius)

«Тяжело в учении —легко в бою.»

—По мотивам высказывания
А. В. Суворова

Contents

List of Figures

List of Tables

Introduction

The neutrino is an elementary particle that is described in the *Standard Model of particle physics (SM)*. There, it is considered massless. However, the observation of neutrino oscillations prove that neutrinos have a mass [1]. Neutrinos exist in three flavor states (electron muon, tau) and their masses are at least six orders of magnitude smaller than the mass of the second-lightest particle, the electron [2]. Because the mass is so small, no experiment at the time of writing this thesis was able to measure it yet. Different approaches exist to determine the neutrino mass.

The Karlsruhe Tritium Neutrino (KATRIN) experiment provides the most stringent upper limit on the neutrino mass of 0.45 eV (90 % C.L.) from direct measurements [3]. This limit is determined from the shape of the endpoint region of the β-electron spectrum measured from tritium β-decay. Tritium, ^3H, is a radioactive isotope of hydrogen with a lifetime of 12.3 years. In this work, it is denoted as T instead of ^3H. In KATRIN, molecular tritium T_2 is circulated in a windowless gaseous tritium source (WGTS).

The main measurement phase of KATRIN ended recently after 1000 days of neutrino mass measurements [4]. From 2026 on, the so-called TRISTAN phase will explore the full β-spectrum to search for sterile neutrinos and new physics at the keV scale [5, 6]. Meanwhile, efforts are made to improve the sensitivity of KATRIN for a neutrino mass experiment after TRISTAN.

Building an experiment based on β-decay of tritium beyond KATRIN, aiming for a sensitivity that resolves the inverted mass ordering, necessitates new technologies. Developments on improving the detector technology are currently ongoing, and once significant improvements are made here, the molecular tritium source will become a limiting factor. The β-spectrum of molecular tritium is highly complex due to electronic and ro-vibrational excitations of the daughter molecule, compared to that of atomic tritium. Even with the precise theoretical knowledge of the final states available [7, 8], the broadening due to the molecular final states will limit achievable statistics. Therefore, the switch to atomic tritium is necessary for a future tritium-based neutrino mass experiment.

The development of an atomic tritium source for neutrino mass measurements is highly complex, as it involves the dissociation of T_2, cooling the atoms to a few mK, and trapping them [9]. A joint effort is made by the Karlsruhe Mainz Atomic Tritium Experiment (KAMATE) to identify suitable dissociators, characterize them, and develop cooling mechanisms. The first milestone is to characterize three commercially available atomic sources with nonradioactive hydrogen isotopes. One of the sources is a plasma-based RF discharge source that produces an inductively coupled plasma (ICP). The task of this work was to commission and characterize this source with protium.

For the commissioning, the plasma source is operated in a dedicated vacuum setup that was assembled during this work. The plasma is ignited in a cavity consisting of pyrolytic boron nitride (PBN). In literature [10], boron contamination on SiGe samples was observed with a similar plasma source with a PBN cavity. Thus, boron or boron nitride contamination in the main vacuum system had to be investigated.

The cavity contains an orifice that emits a particle beam as a result of the pressure difference between the plasma cavity and the main vacuum. The characterization of the plasma source is demonstrated in a twofold way:

Characterization of the beam emitted from the plasma source Graphene is utilized as a beam sensor, and a novel method is developed to determine the beam profile. The exposure of graphene samples to the plasma source produces vacancies and sp^3-defects. The latter corresponds to the well-known atomic/ionic adsorption of hydrogen on graphene [11], allowing it to be used as an atomic hydrogen sensor. By performing two-dimensional scans of the graphene samples, the profile of the defect density can be mapped to the particle profile of the beam.

For advanced monitoring of the processes occurring on graphene, the combination of an in-situ and an ex-situ diagnostic tool is applied.

1. As an ex-situ tool, Raman spectroscopy has been demonstrated to be a powerful tool for the analysis of graphene [12]. The defect density can be determined as well as the distinction between vacancy-type and sp^3-type defects [13, 14, 15]. A confocal Raman microscope (CRM) was constructed at TLK [16] with which tritiated graphene samples have been measured [17]. The CRM was used for measurements of graphene samples in this work.
2. As an in-situ tool, the measurement of the sheet resistance is widely used [18]. One extension of the sheet resistance measurement that allows the distinction between vacancy-type and sp^3-type defects is thermal annealing [19]. The increase in sheet resistance due to hydrogenation is reversible when heating the graphene sample to 300 °C. Therefore, establishing an experimental setup that performs in-situ sheet resistance measurements and provides reproducible values after thermal

annealing of up to 300 °C is an important step towards the development of a novel atomic sensor.

Characterization of the plasma with optical emission spectroscopy Optical emission spectroscopy (OES) is a powerful noninvasive diagnostic tool that is widely used in plasma source development in nuclear fusion research [20]. Low temperature plasmas emit light in a visible wavelength range. The measured spectra can be compared to calculations from collisional radiative (CR) models describing complex plasma chemistry. The comparison allows the determination of plasma parameters like electron temperature, electron density, atomic density and molecular density. An absolute intensity calibration of the optical system for OES is required in order to perform such advanced analyses [20].

This thesis is structured as follows:

First, an introduction to neutrinos and the neutrino mass is given in Chapter 1. In particular, the KATRIN experiment and its limitations on the sensitivity are discussed. In this scope, the transition from molecular tritium to atomic tritium for future neutrino mass experiments is motivated, and the current status of the development of an atomic tritium source is outlined.

In Chapter 2, the theory of low temperature plasmas and the method that allows the determination of plasma parameters is explained.

In Chapter 3, the theory of Raman spectroscopy of graphene is presented. Furthermore, the Van der Pauw method [21] to measure the sheet resistance of graphene is explained.

In Chapter 4, the experimental setup for the operation of the plasma source is shown. Furthermore, a study on potential boron and boron nitride contamination in the vacuum system is presented. Finally, the experimental setup to load graphene with the plasma source is shown. There, the contacting setup for the in-situ sheet resistance measurements of the graphene is presented.

The results of the sheet resistance measurements and Raman microscopy measurements of graphene samples that were exposed to the plasma source are presented in Chapter 5.

In Chapter 6, results on the plasma stability and the plasma mode controls are presented. An absolute intensity calibration of the optical system for OES is shown. Furthermore, a graphical approach is demonstrated that is based on a method from U. Fantz et al. [20] that determines plasma parameters with OES.

Finally, a summary of the work and an outlook on future extensions of research efforts are given.

1. Atomic tritium for neutrino mass determination

In Section 1.1, the theory of neutrino oscillations and the resulting mass of the neutrino is explained. Furthermore, an overview on neutrino mass experiments is given.

In Section 1.2, the focus lies on the Karlsruhe Tritium Neutrino (KATRIN) experiment that is designed to measure the neutrino mass. Following, in Section 1.3, the limitations of KATRIN are highlighted and the efforts that have to be made to improve the sensitivity on the neutrino mass for future KATRIN-type experiments are outlined. One technology that needs to be developed is an atomic tritium source rather than a molecular one. An overview of the research on atomic tritium is given in Section 1.4.

1.1. Neutrinos and their mass

The neutrino is the most abundant particle in the universe. It is described in the *Standard Model of particle physics (SM)*. Neutrinos exist in three flavors that correspond to the three generations of electrically charged leptons: electron-, muon- and tau-neutrino. In the SM, neutrinos are considered to be massless. However, the observation of neutrino oscillations proves that neutrinos have a mass unequal to zero (see *e.g.* [22, 1]). Hence, the eigenstates of the neutrinos differ between weak force interactions and propagation through space-time. For the former, the weak eigenstates ν_e, ν_μ and ν_τ are responsible. For the latter, the mass eigenstates ν_1, ν_2 and ν_3 are responsible. The physical neutrino is defined by a non-trivial mixing of these states via the Pontecorvo-Maki-Nakagawa-Sakata (PMNS) matrix U [23]:

$$\begin{pmatrix} |\nu_\mathrm{e}\rangle \\ |\nu_\mu\rangle \\ |\nu_\tau\rangle \end{pmatrix} = \underbrace{\begin{pmatrix} U_{\mathrm{e}1} & U_{\mathrm{e}2} & U_{\mathrm{e}3} \\ U_{\mu 1} & U_{\mu 2} & U_{\mu 3} \\ U_{\tau 1} & U_{\tau 2} & U_{\tau 3} \end{pmatrix}}_{U} \cdot \begin{pmatrix} |\nu_1\rangle \\ |\nu_2\rangle \\ |\nu_3\rangle \end{pmatrix} . \tag{1.1}$$

The PMNS matrix U can be parametrized as in Reference [2], resulting in four free parameters; three mixing angles and one CP-violating phase.[1] For simplicity, the neutrino oscillation is shown in the case of two flavors α and β. The two-flavor transition probability is given by:

$$P(\nu_\alpha \to \nu_\beta) = \sin^2\theta \cdot \sin^2\left(\frac{\Delta m_{12}^2}{4E} L\right) . \tag{1.2}$$

Here, the first factor describes the oscillation amplitude, which includes the mixing angle θ. The second factor describes the oscillation frequency, which contains the neutrino energy E, the distance L that the neutrino has traveled from the source, and the difference of the squared masses of the mass eigenstates $\Delta m_{12}^2 = m_1^2 - m_2^2$ [23]. Hence, the oscillations provide information about the neutrino mass, but not on the absolute mass scale.

At the time of writing this thesis, the mass of the neutrino remains unknown. Furthermore, the ordering of the masses is an open question, except that $m_2 > m_1$ [23]. It can be either a normal hierarchy with $m_3 > m_2 > m_1$ or an inverted hierarchy with $m_2 > m_1 > m_3$. The JUNO experiment aims to determine the ordering [24].

Three different approaches are currently employed to investigate the neutrino mass [25]. If the neutrino is a Majorana particle, meaning it is it's own anti-particle, a neutrinoless double beta decay might be possible. Here, the effective mass $m_{\beta\beta}$ of the Majorana neutrino

$$m_{\beta\beta} = \left|\sum_i U_{ei}^2 m_i\right| . \tag{1.3}$$

is measured through the proportionality to the decay rate. The KamLAND-Zen collaboration reports an upper limit of 0.036 – 0.156 eV at 90 % C.L. [26].

The second approach to determine the neutrino mass is with cosmology. The sum of the neutrino masses

$$\Sigma m_\nu = m_1 + m_2 + m_3 , \tag{1.4}$$

is an input parameter for different cosmological models. Constraints can be derived for Equation (1.4) by measuring cosmological observables like the cosmic microwave background (CMB) or Baryon Acoustic Oscillations (BAO) [25]. DESI reported an upper limit on the sum of the neutrino masses of 0.072 eV with 95 % C.L. by combining CMB data and BAO data [27].

Both approaches named above to measure the neutrino mass are model dependent. Hence, a third type of experiments is exploited that is model independent. It is the direct measurement of the neutrino mass based on the kinematics of weak interactions.

---

[1] If the neutrino is a Majorana particle, two additional phases must be added.

The idea dates back to E. Fermi who discussed the shape of the continuous β-decay spectrum near its endpoint and how it depends on the mass of the neutrino [28]. This method determines the squared effective neutrino mass [25]:

$$m_\nu^2 = \sum_i |U_{\nu,i}|^2 m_i^2 \tag{1.5}$$

Two main approaches are being followed, that is β-decay and electron capture (EC). The isotopes utilized for this measurement require properties like a low Q value and a high decay rate. For EC, ^{163}Ho is used with a very low Q value of 2.833 keV and a lifetime of 4570 years [29]. The isotope is placed inside cryogenic microcalorimeters, that measure the total energy released from the reaction:

$$^{163}\mathrm{Ho} + \mathrm{e}^-_{\text{inner shell}} \longrightarrow {}^{163}\mathrm{Dy}^* + \nu_e \ . \tag{1.6}$$

The ECHo experiment aims to achieve a sensitivity on the neutrino mass in the sub-eV range [30, 31].

For the β-decay experiments, the super-heavy variant of hydrogen, tritium, is exploited. A detailed explanation on this type of experiments is given in the next section.

1.2. Tritium-based neutrino mass determination

Tritium is a radioactive isotope of hydrogen. The decay reaction is:

$$\mathrm{T}_2 \longrightarrow {}^3\mathrm{HeT}^+ + e^- + \bar{\nu}_\mathrm{e} \ . \tag{1.7}$$

The effective mass of the electron anti-neutrino $\bar{\nu}_\mathrm{e}$ is determined by measuring the energy of the electrons that are produced in the decay in Equation (1.7). More precisely, the shape of the endpoint region depends on the mass of $\bar{\nu}_\mathrm{e}$. This is illustrated in Figure 1.1.
The choice for tritium yields from its properties: Tritium has a simple structure because it is an isotope of hydrogen. Moreover, it has a fairly low Q value of 18.6 keV with a lifetime of 12.3 years.[2] Therefore, tritium naturally provides high statistics at the endpoint region of the β-spectrum including a simple structure [25].

There are several established methods for the measurement of the β-spectrum. The Karlsruhe Tritium Neutrino (KATRIN) experiment provides the most stringent upper limit on the neutrino mass of 0.45 eV (90 % C.L) and aims to achieve a sensitivity better

---

[2] Only ^{187}Re has an even lower endpoint of 2.6 keV but a very large lifetime of 4.3×10^{10} years which makes it unsuitable for an experiment where high statistics is required.

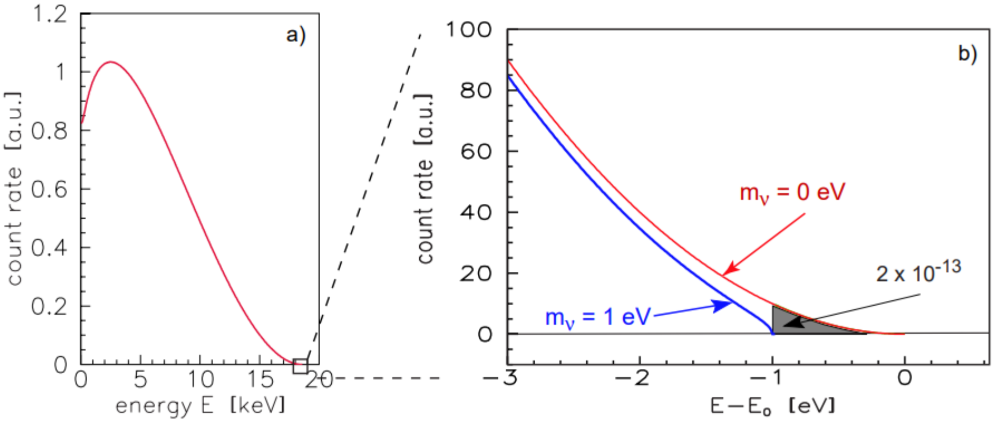

Figure 1.1.: The electron energy spectrum of tritium β-decay. **(a)** The full spectrum. **(b)** Zoom-in into the endpoint region. It is shifted by the endpoint energy E_0. The shape of the endpoint region is compared for a hypothetical effective anti-electron neutrino mass of 1 eV and 0 eV. Reprinted from [32].

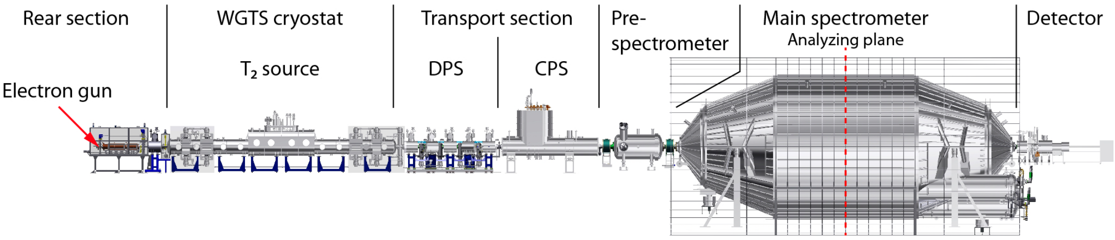

Figure 1.2.: Experimental setup of the KATRIN experiment. A detailed explanation is given in the main text. Reprinted from [34].

than 0.3 eV [3]. The technology exploited in KATRIN to measure the endpoint of the β spectrum is Magnetic Adiabatic Collimation combined with an Electrostatic filter (MAC-E). Only electrons, with a surplus energy above a threshold, can overcome this high-pass filter and are counted with a 148-pixel silicon-PIN-diode focal plane detector [33]. In Figure 1.2, the experimental setup of KATRIN is presented. In a Windowless Gaseous Tritium Source (WGTS), 40 g of tritium are circulated per day [33]. The β-electrons produced there, are guided through the transport system with superconducting magnets to the MAC-E filter. On the way, the amount of tritium is reduced by 14 orders of magnitude [33]. This is achieved with a Differential Pumping Section (DPS) followed by a Cryogenic Pumping Section (CPS), which freezes T_2 by applying a cold argon frost layer on the transport-pipe walls. The backside of the experiment is the rear system. It consists of a gold-plated disc which absorbs β-electrons such that they are not reflected. Furthermore, an electron gun allows calibration and monitoring of the WGTS [34].

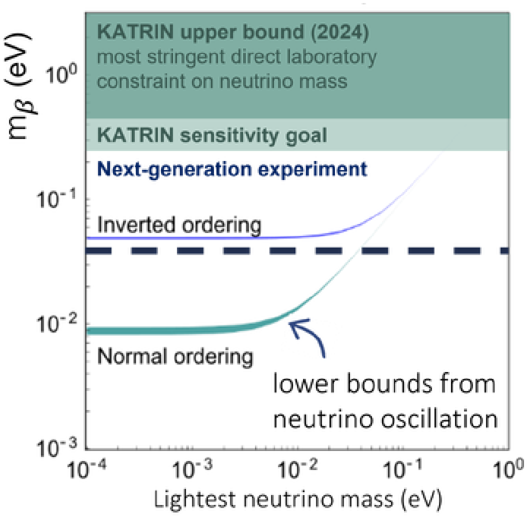

Figure 1.3.: Sensitivity limits of the effective neutrino mass depending on the mass of the lightest neutrino. The light shaded area is the sensitivity that KATRIN will reach. The lower bounds on the effective neutrino mass for inverted and normal ordering are determined from neutrino oscillation experiments [2]. To cover inverted mass ordering, a sensitivity of below 50 meV is aimed for. The figure was kindly provided by S. Heyns. [35].

1.3. Future neutrino mass experiments

At the time of writing this thesis, no neutrino mass experiment has been able to resolve the actual neutrino mass, only upper limits have been determined so far. The world leading value was reported by KATRIN (see Section 1.2). To resolve inverted mass ordering, the sensitivity on the neutrino mass m_β has to be $< 50\,\text{meV}$ [2].[3] This corresponds to an improvement of one order of magnitude compared to KATRIN's sensitivity (see Figure 1.3). Therefore, new technologies needed for this sensitivity improvement are identified in the following.

1.3.1. Detector technology

The MAC-E filter in combination with the silicon-PIN-diode detector is an integral measurement technology, in the sense that it counts the electrons that pass the filter. A differential method with comparable energy resolution, that would measure the energy of each single electron, would outperform the integral method. In combination with an atomic tritium source, a sensitivity below the inverted mass ordering could be achieved

---

[3] In this case: $m^2_{\beta,min} \sim |U_{\beta 1}|^2 m_1^2 + |U_{\beta 2}|^2 m_2^2$.

with a detector resolution of $\Delta E_{\mathrm{FWHM}} < 0.7\,\mathrm{eV}$. Furthermore, a differential detector would decrease the systematic uncertainty, due the distinction between spectrometer background and signal electrons [36].

Arrays of calorimeter-based quantum sensors One approach to a differential measurement is an array of micro-calorimeters. Currently preferred are metallic magnetic calorimeters (MMC) because they have the world's leading resolution of $\sim 1\,\mathrm{eV}$ [37, 38]. Additional advantage of this detector-type is a near linear detector response over a wide energy range [39] and the absence of a dead layer. Recently, it was shown that MMCs can be used for measurements of an external electron source [40], which is a requirement for a future neutrino mass experiment with tritium.
With the current detector geometry of $200\,\mu\mathrm{m}\times 200\,\mu\mathrm{m}$ [41] one would need to construct an array consisting of $1-10$ million of such detectors to cover the full KATRIN flux tube. This endeavor is extremely challenging from the fabrication point of view, as producing such a large number of pixels has not been done before. As a result, there are on-going efforts to design MMCs with a larger area, decreasing the number of required pixels to $\sim 10\,000$. Furthermore, investigations are ongoing to operate MMCs in low magnetic fields and improve the resolution to sub-eV.

Single electron tagging with time-of-flight measurement An alternative approach to the differential detector is the time-of-flight (ToF) measurement using an electron tagger [42]. Developments on possible techniques to tag electrons are ongoing. Such an electron tagger would generate a start-signal at the entrance of the main spectrometer. Inside the main spectrometer, the electrons flight-time depends on its surplus energy relative to the retarding potential. A fast detector after the main spectrometer provides a stop-signal [36].

Cyclotron radiation emission spectroscopy Another approach for single-channel electron detection is a technique called cyclotron radiation emission spectroscopy (CRES). If the β-electrons are placed in a magnetic field, they perform a cyclotron motion. By measuring the emitted cyclotron frequency, the kinetic energy of the electron can be determined [43]. The approach is currently pursued by Project 8 [44] as well as QTNM [45].

1.3.2. Atomic tritium

For the source part, T_2 is currently utilized in KATRIN. However, this will become a limiting factor in sensitivity improvements at the point where detector resolutions below 1 eV are feasible. The sensitivity study in Figure 1.4 shows a leveling out of the sensitivity above the inverted mass ordering when using molecular tritium. Improvements in

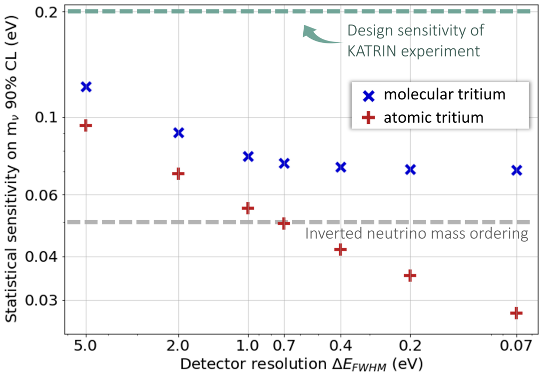

Figure 1.4.: Sensitivity study for a future neutrino mass experiment. Scaling of statistical sensitivity on the neutrino mass with the detector resolution. The column density in the simulation is 3.78×10^{21} molecules/m^2. Background rates are not considered here. At a detector resolution $\Delta E_{\mathrm{FWHM}} < 500\,\mathrm{meV}$, the inverted mass ordering could be reached if atomic tritium is utilized. The figure was kindly provided by S. Heyns. [35].

detector resolution would only have a positive effect on the sensitivity if atomic tritium is used. This limitation yields from a broadening of the energy spectrum due to molecular final states of the daughter molecule $^3\mathrm{HeT}^+$ of the T_2-decay (see Equation (1.7)). The final state distribution (FSD) of this molecule consists of electronic and ro-vibrational excitations. Around the endpoint of the β-spectrum only the molecules in the electronic ground state are relevant. They cause a broadening of a full width half maximum of $FWHM = 1\,\mathrm{eV}$. Even with a precise theoretical knowledge of the FSDs [8, 7], the broadening limits the statistical sensitivity. As the ro-vibrational excitations are a purely molecular effect, the broadening vanishes for T [46]. This is shown in Figure 1.5. Furthermore, the statistics increase for T because 70 % of the $^3\mathrm{He}^+$ daughter atoms are in the electronic ground state, whereas only 57 % of $^3\mathrm{HeT}^+$ daughter molecules end up in the ground state [8].

1.4. Atomic tritium source development

One approach for the construction of an atomic tritium source for neutrino mass experiments is four staged:

1. A *dissociation section* that dissociates T_2 and provides a beam of atomic tritium with as few remaining molecules as possible [9].
2. A *cooling section* that cools the atoms down to mK range. Such low temperatures are essential for the trapping section [9].

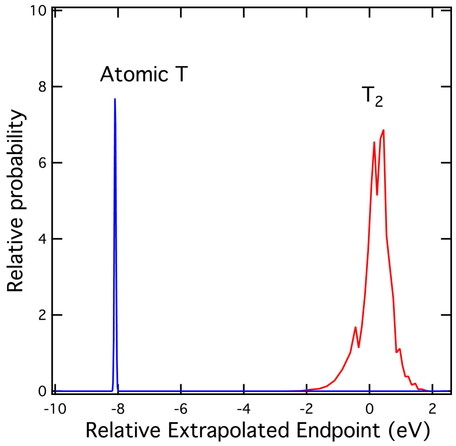

Figure 1.5.: Comparison of the ground state FSDs for atomic (blue) and molecular (red) tritium. The endpoint energies E_0 differ by ~ 8 eV due to the combination of recoil effects, and the rovibrational broadening of the molecular states. Reprinted with permission from [9]. Copyright from © 2021 Elsevier B.V.

3. A *velocity selector section* Only atoms which reach the desired temperature should enter the trap. Hence, a time-of-flight (TOF) setup should filter the atoms that are too hot [9].
4. The *trapping section* provides the final stage for the atomic tritium source. Tritium atoms can be trapped with magnetic fields [9]. In particular, the so-called „low field seekers“ that are atoms where the magnetic moment μ aligns parallel with the magnetic field can be trapped for example in a Ioffe-Pritchard-type trap [47].

Multiple working groups are investigating all four sections in parallel (see *e.g.* Reference [47]). The demonstration of a dissociation section and first cooling stage is the goal of the Karlsruhe Mainz Atomic Tritium Experiment (KAMATE) collaboration. It is formed by scientists from the KATRIN experiment at the Karlsruhe Institute of Technology (KIT) and Project 8 at Johannes Gutenberg-University (JGU) Mainz. The goal is split into milestones that are described in Reference [48]. Currently, KAMATE is approaching its first milestone: Three different commercially available dissociators are being commissioned and characterized with hydrogen and deuterium. The sources tectra H-flux[4] and HABS[5] are based on thermal dissociation. The third source is a RF discharge plasma source[6]. The Mainz Atomic Tritium Source (MATS) test stand is used for the characterization. The setup of MATS is described in detail in Reference [49].

---

[4] tectra GmbH, Reuterweg 51-53, 60323 Frankfurt/M, Germany.

[5] © 2024 Dr. Eberl MBE-Komponenten GmbH, Josef-Beyerle-Str. 18/1, 71263 Weil der Stadt, Germany

[6] © 2025 SVT Associates, Inc. 7620 Executive Drive, Eden Prairie, Minnesota 55344 USA

An idea that differs from the four-stage approach was recently proposed by Semakin et al. [50]. The concept is to perform the dissociation already at a temperature below 1 K. Within a cryostat, T_2 is frozen on the walls of the vacuum chamber. Then, a ^{3}He-^{4}He-mixture is placed on top of that to prevent the tritium from vaporizing. A RF discharge in a helical configuration is located inside this chamber and dissociates T_2. All of this is accompanied by magnetic fields with a maximal strength of $4 - 5$ T that push low-field seeking atoms into a transfer line. The transfer line is intended to further cool the atoms down to 0.1 K. The proposal of this project increases the relevance for research on plasma based dissociators.

In the past, some efforts have been made to produce atomic tritium. E.B. Nelson and J.E. Nafe used a DC discharge source [51], whereas A.G. Prodell and P. Kusch [52] and B.S. Mathur et al. [53] used RF discharges. All groups reported that tritium was lost from circulation in a matter of hours. The losses were observed from reaction with hydrocarbons like pump oils [52] and the adsorption on the discharge tubes [53]. Mathur et al. reported that the transition from Pyrex to quartz as a tube material reduced the adsorption sufficiently, but the signal for atomic tritium was still too short to perform measurements with it [53]. Furthermore, the stability of the dissociation fraction for plasma discharge sources is inconclusive. The research on atomic tritium in the Los Alamos National Laboratory [54] observed a decrease in dissociation fraction with protium and deuterium operation over time periods of hours to days. They used an RF discharge device, with driving frequency of 50 MHz and a borosilicate or silica glass tube. J.A. Formaggio et al. assume reduction of the glass tube to silicon monoxide causing discoloration of the tube, and conversion of the hydrogen atoms to water with the free oxygen radical [9]. The water was observed in cold traps after the operation of the discharge. However, J. Slevin and W. Stirling constructed a similar RF discharge source with a Pyrex tube that produced a „(hydrogen) beam of density constant to within a few percent over periods of several thousand hours“ [55].[7] Hence, not all relevant factors have been identified to conclude whether a plasma discharge is suitable for the production and long-term operation of atomic tritium.

The objective of this thesis is to commission and characterize the RF discharge plasma source. This is done in a dedicated vacuum setup, before the insertion into more delicate setups like MATS. As explained above, different observations were made concerning the stability of the dissociation fraction. In this scope, the stability of the plasma during long-term operation must be tested.

Due to the issues of past atomic tritium experiments concerning the plasma cavity material, this source is equipped with a cavity consisting of pyrolytic boron nitride (PBN). However, in a study by Lambert et al. [10] boron contamination was observed

---

[7] Neither R. G .H. Robertson et al. [54], nor J. A. Formaggio et al. [9], nor J. Slevin and W. Sterling [55] explained how they measured the dissociation fraction in these publications.

on SiGe samples when exposed to a plasma source with a PBN cavity. Before inserting the plasma source into a complex system like MATS and placing delicate diagnostic tools like a quadrupole mass spectrometer (QMS) in front of it, the amount of boron and boron nitride that is emitted from the source has to be investigated.

2. Low temperature hydrogen plasma

To characterize a tritium plasma it is essential to understand what a plasma is and what the parameters are that explain the behavior of the plasma. Section 2.1 gives an introduction into the understanding of low temperature plasma. Following that, in Section a toolbox of plasma properties is introduced that enables an understanding of processes in an inductively coupled plasmas (ICP) which is the type of plasma investigated in this work. Because a low temperature plasma is a multi species gas, plasma chemistry is relevant. This is explained in Section 2.3 and followed by the introduction into a method that determines plasma parameters with optical emission spectroscopy (OES) and collisional-radiative (CR) modeling.

2.1. Overview on plasma

Plasma is often called „the fourth state of matter“, along with solid, liquid, and gas. It is widely used in human-made products such as neon street lights, the semiconductor industry, or in nuclear fusion experiments. Also, nature has some phenomena that are plasma. For instance, lightning is a plasma discharge. Moreover, the occurrence of plasma is very significant in our universe. 99% of baryonic matter is a plasma [56]. The stars, nebulae, and most of the gas in the universe is in a plasma state. From this point onward, the question arises as to what essentially defines a plasma and what makes it so special. Hence, the following two sections explain the basics of plasma physics.

2.1.1. Plasma physics and low temperature plasmas

The justification for considering plasma as a different state of matter is the *collective behavior* of the species inside the plasma that arises from the existence of a significant amount of charged particles. In addition, a plasma is *quasi-neutral* because the following requirement has to be met:

$$N_{+} = N_{-} \tag{2.1}$$

There are an equal number of positive and negative charges in steady-state.

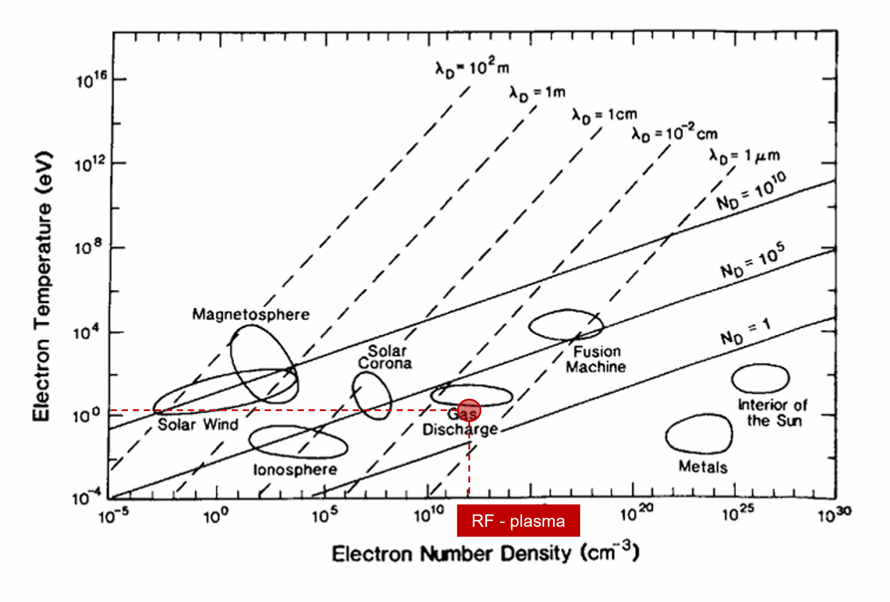

Figure 2.1.: Different types of plasmas categorized by T_e and n_e. The red selection marks the location of the plasma source on this map used in this work.

In a neutral gas, collisions between all gas particles redistribute their kinetic energy to give a *single energy distribution* and therefore a *single temperature.* This is called *thermal equilibrium.* In a plasma, external power sources can input energy in specific plasma species, In particular electrons (e) are much more strongly accelerated by external electric and magnetic fields than ions (i) because $m_e \ll m_i$. Therefore, electrons get a lot of energy so $T_e \gg T_i$ which implies:

$$v_e \gg v_i \; . , \tag{2.2}$$

with $v_{e,i} = \sqrt{\frac{3\,k_B\,T_{e,i}}{.}m_{e,i}}$. Hence, the dynamics inside a plasma is strongly governed by the electrons. The two parameters that allow for a classification of the wide variety of plasmas are the electron temperature T_e and the electron density n_e. Figure 2.1 shows a map of the different plasmas depending on those quantities.

For many plasmas, the energy gets redistributed via collisions, leading to thermal equilibrium. This is the case for a tokamak plasma or welding arcs. However, under certain circumstances, this equilibration mechanism is incomplete, so the system remains in a *non-equilibrium* and is then called *low temperature plasma* . A significant advantage of these plasmas is the production of reactive gas chemistry, driven by hot electrons, at relatively low temperatures of $10^2 - 10^3$ K [57]. Typical electron temperatures are $T_e \approx 10^1$ eV and electron densities of $n_e = 10^{14} - 10^{19}\,\mathrm{m}^{-1}$.

2.1.2. Maxwell's Equations

As in the previous Section described, the majority of species inside a low temperature plasma is non-neutral. Therefore, the *Maxwell's Equations* become relevant to explain plasma dynamics. This section follows the explanations from Reference [58].
The usual macroscopic form of Maxwell's equations are

$$\nabla \times \mathbf{E} = -\mu_0 \frac{\partial \mathbf{H}}{\partial t} \tag{2.3}$$

$$\nabla \times \mathbf{H} = \epsilon_0 \frac{\partial \mathbf{E}}{\partial t} + \mathbf{J} \tag{2.4}$$

$$\epsilon_0 \, \nabla \cdot \mathbf{E} = \rho \tag{2.5}$$

$$\mu_0 \, \nabla \cdot \mathbf{H} = 0 \, . \tag{2.6}$$

Here, $\mathbf{E}(\mathbf{r}, t)$ and $\mathbf{H}(\mathbf{r}, t)$ are the electric and magnetic field vectors and $\mu_0 = 4\pi \times 10^{-7}\,\mathrm{H/m}$ and $\epsilon_0 = 1/(\mu_0\, c^2)$ are the permeability and permittivity of free space, respectively [58]. The sources of the fields, the charge density $\rho(\mathbf{r}, t)$ and the current density $\mathbf{J}(\mathbf{r}, t)$, are related by the charge continuity equation:

$$\frac{\partial \rho}{\partial t} + \nabla \cdot \mathbf{J} = 0 \tag{2.7}$$

If Equation (2.5) is integrated over a volume $\mathcal{V}$, enclosed by a surface $\mathcal{S}$, then *Gauss' Law* is obtained:

$$\epsilon_0 \oint_{\mathcal{S}} \mathbf{E} \cdot d\mathbf{A} = q \, , \tag{2.8}$$

where q is the total charge inside a volume. Similarly, integrating Equation (2.7):

$$\frac{dq}{dt} + \oint_{\mathcal{S}} \mathbf{J} \cdot d\mathbf{A} = 0 \tag{2.9}$$

which states that the rate of increase of charge inside $\mathcal{V}$ is supplied by the total current flowing across $\mathcal{S}$ into $\mathcal{V}$, that is, that charge is conserved.
In Equation (2.4), the first term on the right-hand side is the displacement current density flowing in the vacuum, and the second term is the conduction current density due to the free charges. Thus, a total current density is defined as:

$$\mathbf{J} = \epsilon_0 \frac{\partial \mathbf{E}}{\partial t} + \mathbf{J} \, . \tag{2.10}$$

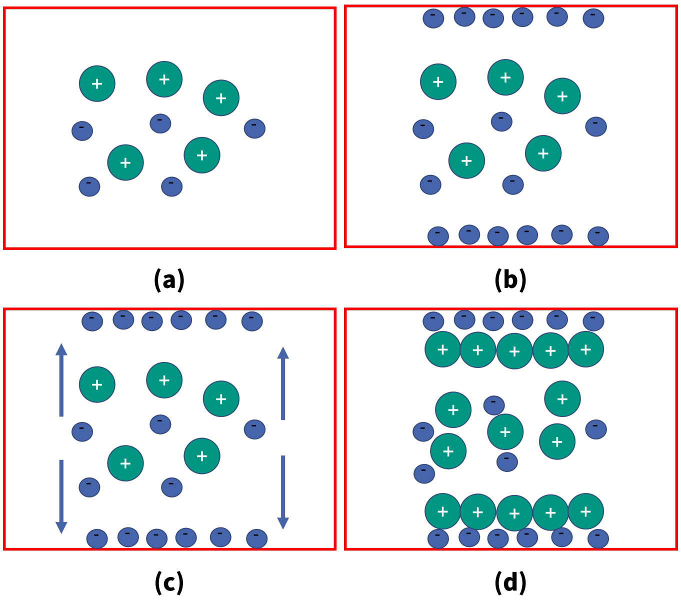

Figure 2.2.: Creation of the plasma sheath. The red box indicates the edge of a plasma cavity which is insulating. For simplicity, only charged particles are illustrated. **(a)** At t=0 a plasma is ignited. **(b)** Because the electrons move much faster than the ions, they move towards the cavity walls and an electron layer is built-up. **(c)** The electron layer attracts the positively charged ions. **(d)** A positively charged ion layer is formed on top of the electron layer. The combination of both layers is called plasma sheath.

2.1.3. Plasma dynamics

Ionization degree A very basic parameter to characterize a plasma is the *ionization degree* [57]:

$$I = \frac{n_e}{n_e + n_0} \ . \tag{2.11}$$

where n_e is the electron density and n_0 the neutrals density. If, for instance, $I = 1$ the plasma is fully ionized. This is the case for fusion reactors or the sun. For low temperature plasma $I \ll 1$, that is, it is weakly ionized. The majority species are neutral atoms.

Plasma sheath As a reminder, electrons move much faster than ions in a low temperature plasma. Assuming a low temperature plasma in an insulating cavity[1] (see Figure 2.2). The electrons cannot drain away at the cavity walls, resulting in a negative charge build-up. This layer blocks further electrons and attracts ions until the ions form another layer on top of the electron layer. The combination of these layers is called

---

[1] even if it is not an insulator, a plasma sheath still forms but Figure 2.2 would look differently.

plasma sheath. The rest of the plasma is called plasma bulk. The shielding is essentially the plasma's way to conserve quasi-neutrality of the plasma bulk [58].

Debye length In general, in a gaseous environment where charged particles predominate, there is always a screening effect present. In a plasma, a positive ion is surrounded by the fast-moving electrons, resulting in an „electron cloud“ around the ion. The charge of the ion appears to be smaller to particles that are located outside of this cloud. The *Debye length* λ_D represents the size of this cloud. Mathematically, it is the distance from the center of the ion to the point where the electric potential decreases by one order of magnitude of e. Physically, it is the distance scale over which significant charge densities can spontaneously exist. For example, low-voltage sheaths are typically a few Debye lengths wide [58]. The cloud, illustrated in Figure 2.3, is called *Debye sphere*.

The Debye length for a plasma consisting of particles with electron density n_e, charge e and temperature T_e is given by [57]:

$$\lambda_D^2 = \frac{\epsilon_0 \, k_B \, T_\mathrm{e}}{n_\mathrm{e} \, e^2} \tag{2.12}$$

Plasma oscillations Considering an undriven motion of a plasma slab of finite width l containing a density $n_e = n_i = n_0$ of cold ($T_e = 0$) electrons and infinite mass (stationary) ions, the electric field is zero. If the electrons get displaced to the right by a small

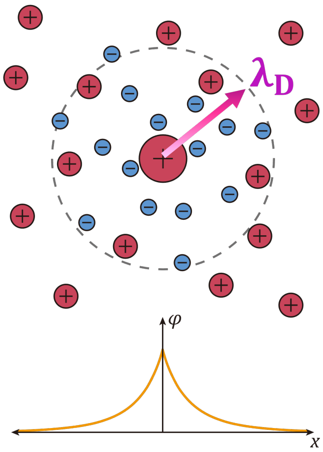

Figure 2.3.: Upper Figure: Illustration of the formation of the Debye sphere. A screening effect on a positive ion is produced by surrounding electrons. The radius of the Debye sphere is the Debye length λ_D. **Lower Figure:** Electrical potential depending on the distance from the central positive ion. More details are explained in the main text. The Figure is adapted from [59].

distance $\zeta_\mathrm{e}(t)$ (see Figure 2.4), this results in a harmonic oscillator [58]. The force equation is:

$$m\frac{d^2\zeta_\mathrm{e}}{dt^2} = -e\,E_x \tag{2.13}$$

with the electric field generated by the charge separation and derived from Equation (2.8)

$$E_x = \frac{e\,n_\mathrm{e}\,\zeta_\mathrm{e}}{\epsilon_0}\ . \tag{2.14}$$

Substituting Equation (2.13) into Equation (2.14) yields

$$\frac{d^2\zeta_\mathrm{e}}{dt^2} = -\omega_\mathrm{pe}^2\zeta_\mathrm{e} \tag{2.15}$$

where

$$\omega_\mathrm{pe} = \sqrt{\frac{n_\mathrm{e}\,e^2}{m_\mathrm{e}\epsilon_0}} \tag{2.16}$$

is the *electron plasma frequency*. It is the reciprocal of the time-scale on which the electron population as a whole can react to a change in the potential. Typical frequencies for discharges are in the microwave region (1-10 GHz) [58].
The Debye length and the plasma frequency are connected through the thermal velocity v_th:

$$\lambda_\mathrm{D} = \frac{v_\mathrm{th}}{\omega_\mathrm{pe}}\ . \tag{2.17}$$

In reality, plasma oscillations are significantly damped in time by collisions or collisionless mechanisms known as Landau damping, although the former is usually the

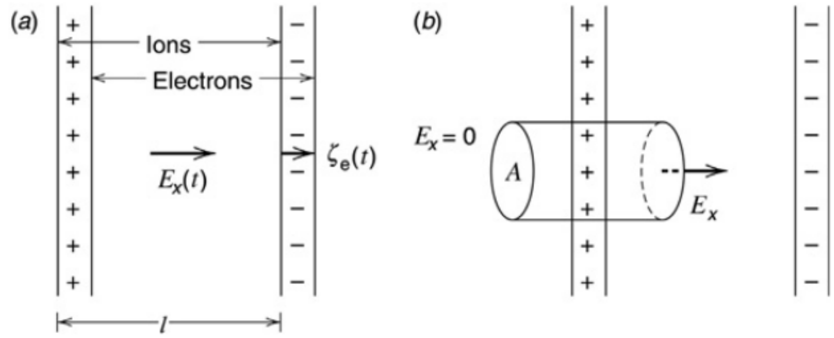

Figure 2.4.: Plasma oscillations in a slab geometry of finite width l. **(a)** Displacement $\zeta_\mathrm{e}(t)$ of the electron cloud with respect to the ion cloud. **(b)** Illustration of the resulting electric field. Reprinted with permission from [58]. Copyright © 2005 John Wiley & Sons, Inc.

dominant process [58].

Considering damping by collisions with an electron-neutral collision frequency v_m in a uniform plasma in the presence of a background gas that is driven by a small-amplitude time-varying electric field

$$E_x(t) = \mathrm{Re}\left(\tilde{E}_x\, e^{i\omega\, t}\right) \tag{2.18}$$

with the amplitude $\tilde{E}_x$, the resulting differential equation yields:

$$m\,\frac{du_x}{dt} = -e\,E_x - m\,v_m u_x\ . \tag{2.19}$$

A solution for Equation (2.19) is the complex velocity amplitude

$$\tilde{u}_x = -\frac{e}{m}\frac{1}{i\omega + v_m}\tilde{E}_x\ . \tag{2.20}$$

Using Equation (2.10), this results in a current *through the plasma*:

$$J_{\mathrm{T}}x = \epsilon_0\frac{\partial E_x}{\partial t} + J_x\ . \tag{2.21}$$

Here, J_x is the conduction current that results from the electron motion and can be approximated as

$$\tilde{J}_x = -e\,n_0\,\tilde{u}_x\ . \tag{2.22}$$

Inserting Equations (2.18), (2.22) and (2.20) into Equation (2.21) results in

$$\tilde{J}_{\mathrm{T}}x = i\omega\epsilon_{\mathrm{p}}\tilde{E}_x\ . \tag{2.23}$$

Here, the effective *plasma dielectric constant* ϵ_{p} is introduced:

$$\epsilon_{\mathrm{p}} = \epsilon_0\,\kappa_{\mathrm{p}} = \epsilon_0\left[1 - \frac{\omega_{\mathrm{pe}}^2}{\omega\,(\omega - i\,v_m)}\right] \tag{2.24}$$

where κ_{p} is the relative dielectric constant.

On the other hand, a *plasma conductivity* can be defined by writing Equation (2.23) in the form $\tilde{J}_{\mathrm{T}}x = (\sigma_p + i\omega\epsilon_0)\,\tilde{E}_x$, with

$$\sigma_{\mathrm{p}} = \frac{\epsilon_0\omega_{\mathrm{pe}}^2}{i\omega + v_m} \tag{2.25}$$

Eventually, a plasma has the property of transporting currents including a dielectric response. Depending on the regime, it is more useful to consider σ_{p} or ϵ_{p}.

2.2. Overview on inductively coupled plasmas (ICP)

A complete description of a plasma discharge requires a choice of heating mechanism to sustain it. These mechanisms in turn play essential roles in determining the plasma density, the voltages between the plasma and the surfaces, and the bombarding ion energies [58]. In Figure 2.5 the types of plasmas depending on n_e and the gas density N_0 are shown. The types relevant for low temperature plasma are electron cyclotron resonance discharges (ECR), helicon discharges, electron beam discharges, capacitively coupled plasmas (CCP) and inductively coupled plasmas (ICP). For the sake of relevance, only the latter is explained. In particular, the coupling between RF power and plasma is outlined.

2.2.1. Electric and magnetic fields in an ICP

Figure 2.6a shows one geometry for an ICP from D. Sydorenko et al. [61]. An alternating radio frequency current is applied to the coil. Due to the Ampère-Maxwell law (Equation

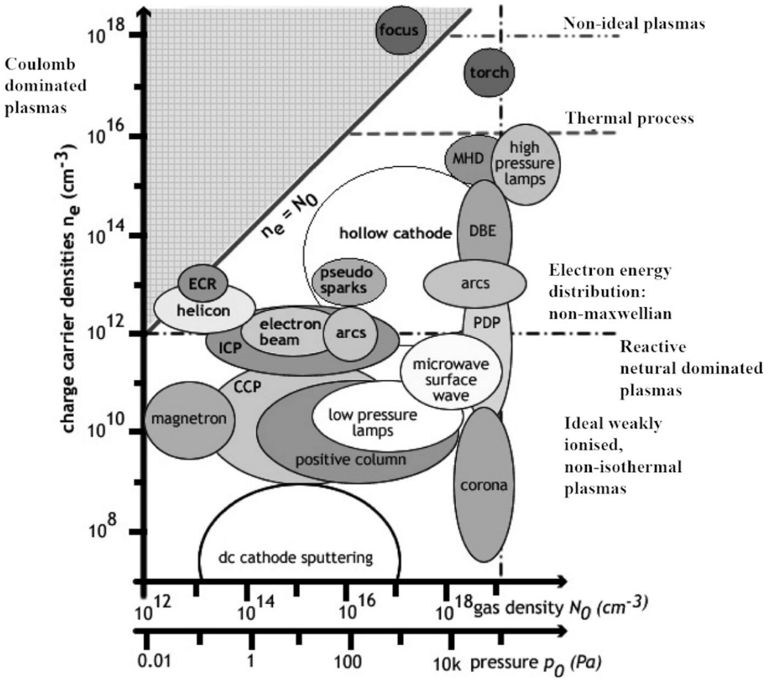

Figure 2.5.: Different types of low-temperature plasma categorized by the driving mechanism. They are sorted on the gas density/pressure-electron density plane. The type of plasma relevant for this work is the inductively coupled plasma (ICP). Reprinted from [60]. Reproduced with permission from Springer Nature.

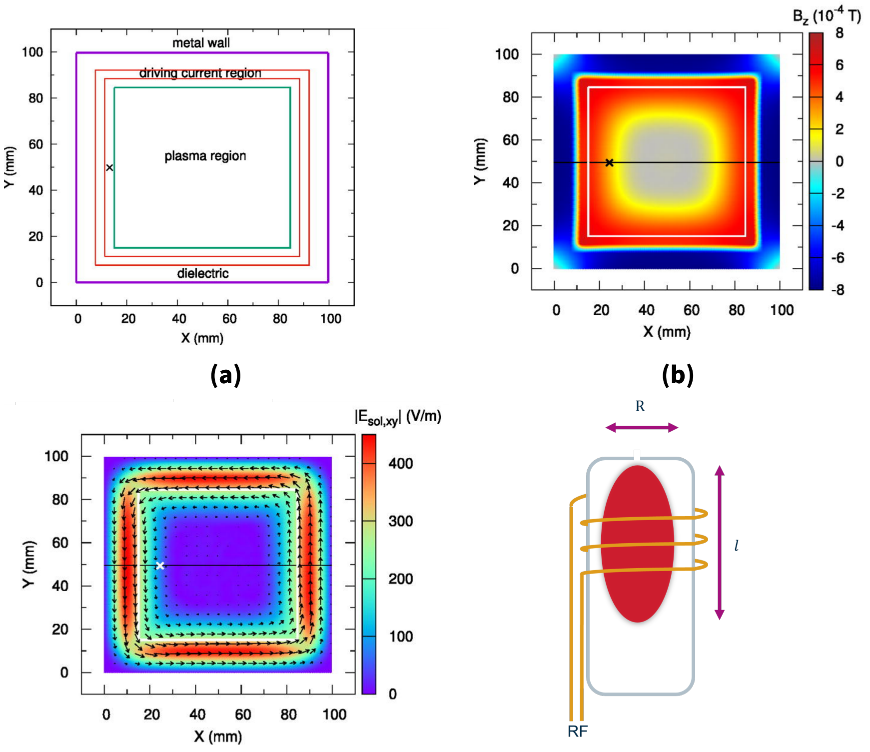

(a) **(b)**

(c) **(d)**

Figure 2.6.: **(a)**-**(c)** Simulation of an ICP by D. Sydorenko et al. The cross indicate a point that is investigated more in detail in Reference [61]. **(a)** two dimensional geometry of the simulation domain. The driving current region is usually a RF coil. **(b)** Produced magnetic field in a late stage of the simulation ($t = 28\,024.8$ ns). Because the driving current circulates in the x-y plane, the magnetic field lines point in z-direction. The white square marks the boundaries of the plasma region. **(c)** Solenoidal electrical field at a late stage of the simulation ($t = 28\,049.6$ ns). Reprinted from [61]. **(d)** Sketch of the geometry of the ICP device that is characterized in this work. The plasma (red) is ignited via an RF coil (gold) inside a cavity (grey). The plasma length l and the plasma radius R are indicated with the purple arrows. A detailed explanation of the source is given in Chapter 4. Reprinted **(a)**-**(c)** from [61].

(2.4)) an alternating current produces a magnetic field (see Figure 2.6b). In contrast, this time-varying magnetic field induces an azimuthal electric field inside the plasma due to Faraday's law (Equation (2.3)). The electric field forms a closed loop similar to eddy currents. In Figure 2.18, the electric field is the largest near the plasma surface and decreases exponentially with greater depth in the plasma bulk. This is the so-called *skin effect* that describes the tendency of an AC-current to become distributed within a conductor such that the current density is largest near the surface of the conductor and decreases exponentially towards the bulk. This underlines the conducting properties of plasma explained in Section 2.1.3. The electric current flowing along the electric field lines is located mainly at the skin layer (the most outer layer of the plasma bulk) with a skin depth δ.

2.2.2. Equivalent transformer coupled circuit of an ICP

Due to the conductive/resistant behavior of the plasma, an equivalent transformer coupled circuit can be derived that simplifies plasma processes with basic electronic components. In Figure 2.7, the equivalent transformer coupled circuit of an ICP is illustrated. The operation of the plasma source requires a matching network with which the impedance of the equivalent circuit is minimized. In this work, the plasma is stabilized with a network that automatically regulates the capacitors of the matching network. Therefore, the reader is asked to refer to [62, 58] for a detailed explanation of the equivalent circuit.

The integrated power flow into an ICP depends on the density regime of the plasma. In this work, the high density regime that is defined by plasma length l and plasma radius R being much larger than the skin depth δ_p is the most relevant. In this case δ_p is called *collisionless skin depth*. Typical plasma dimensions are $R, l \approx 10\,\mathrm{cm}$ with a driving frequency of $\omega = 13.56\,\mathrm{MHz}$ [58]. The integrated power flow into an ICP with the geometry shown in Figure 2.6d is defined as:

$$P_{\mathrm{abs}} = \frac{1}{2}\frac{J_\theta^2}{\sigma_{\mathrm{eff}}}\pi\, R\, l\, \delta_{\mathrm{p}}\ . \tag{2.26}$$

The amplitude of the induced RF azimuthal current density at the plasma edge near $r = R$ is J_θ. It flows in the opposite direction of the applied azimuthal current in the coil. Furthermore, $\sigma_{\mathrm{eff}} = \frac{e^2\, n_S}{m\, v_{\mathrm{eff}}}$ is the effective DC conductivity. The effective velocity $v_{\mathrm{eff}} = v_{\mathrm{m}} + v_{\mathrm{stoc}}$ is the sum of collisional and stochastic heating. The former describes the heat deposition inside the plasma through electron-neutral collisions. However, for low pressures, a stochastic heating can occur [58]. The accelerated electrons do not collide with neutrals but rather with the oscillating inductive electric fields within the skin layer.

2.2.3. Capacitive (E) and Inductive (H) coupling in an ICP

Figure 2.7 shows different voltages for the RF circuit (V_{rf}) and the plasma circuit (V_{p}). From this a capacitance naturally arises to which the particles inside the plasma can couple. The contribution of this coupling to the RF voltage depends on the plasma density. For the high density regime, the contribution is small [58]. However, for low

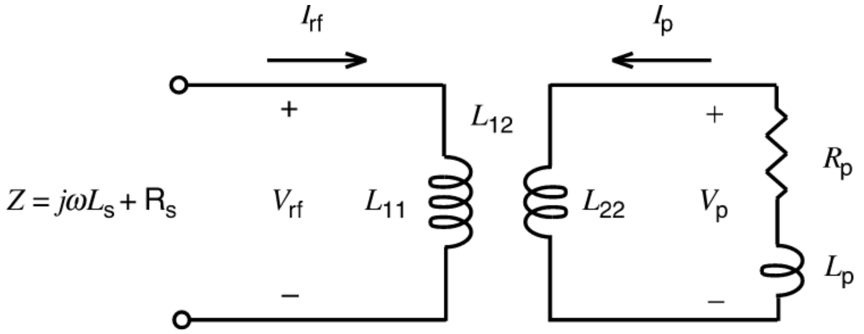

Figure 2.7.: Equivalent transformer coupled circuit of an ICP. The left circuit correspond to the driving circuit from the RF coil. It contains a RF voltage V_{rf}, an AC current I_{rf} and an inductance L_{11}. The plasma circuit is contains a resistance R_{p}, an inductance L_{p} and the magnetic storage inductance L_{22} that couples to L_{11}. A detailed explanation is given in Reference [58]. Reprinted with permission from [58]. Copyright © 2005 John Wiley & Sons, Inc.

densities this is the major source of power deposition. Hence, it is very convenient to realize this regime for start-up of an inductive discharge, as the ignition relies on a high potential difference in the discharge chamber, before the high-density inductive plasma is formed. A plasma that is driven by a capacitive coupling is known to be in *E-mode* [63]. A plasma that is driven by the inductive process is known to be in *H-mode* [63].

The capacity is created across the sheath with voltage $\tilde{V}_{\mathrm{sh}}$. Assuming that the plasma is at ground potential, the sheath voltage follows from the capacitive voltage divider formula:

$$\tilde{V}_{sh} = V_{\mathrm{rf}} \frac{s_{\mathrm{m}}}{b - R + s_{\mathrm{m}}} \tag{2.27}$$

where s_{m} is the sheath thickness, the coil radius b and the plasma radius R.

The sheath thickness can be calculated from Child law (see [58]). It shows that s_{m} is in the magnitude of 10^{-2} cm in the high density regime and it would exceed the distance $b - R$ in the low density regime so that eventually the voltage drops mostly across the sheath. An increase in s_m corresponds to a decreasing density n_0. Therefore, the capacitive power absorbed increases with decreasing n_0.

To drive the plasma in a capacitive or inductive mode, the crucial parameters are the absorbed power P_{abs}, the density n_0 and the RF current I_{rf}. In Figure 2.8 the qualitative relation between these parameters is shown. By increasing I_{rf} to a threshold current I_{min} a transition from capacitive-to-inductive is possible. The inductive-to-capacitive transition goes vice versa [58].

Various additional plasma and circuit effects can produce a hysteresis between the capacitive-to-inductive transition and the inductive-to-capacitive transition. Reference [58] gives an argument for this: Considering a nonlinear P_{loss} curve in Figure

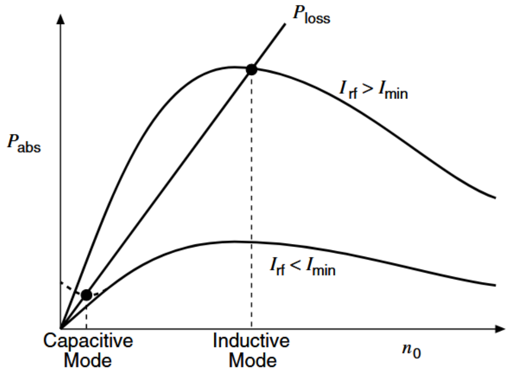

Figure 2.8.: Absorbed power versus density in an ICP. Exemplary are two curves shown for different driving currents I_{rf}. Furthermore, the power lost versus density is displayed (straight line). The dotted curve includes the additional capacitive power at low density for $I_{\mathrm{rf}} < I_{\mathrm{min}}$. Reprinted with permission from [58]. Copyright © 2005 John Wiley & Sons, Inc.

2.8, then there is a range of currents where there are three intersections, such that the discharge characteristic has hysteresis. The low-density intersection is in a stable capacitive equilibrium, the high-density intersection is a stable inductive equilibrium, and the intermediate density intersection is an unstable equilibrium.

There can be several reasons for a nonlinear P_{loss}-curve [58]. One is the presence of negative ions in the discharge. This can result in instabilities, in which there is no stable discharge equilibrium. This issue can be worth it to be investigated in the scope of an atomic tritium source. The cavity of the plasma source used in this work consists of pyrolytic boron nitride (PBN). A tritium-plasma could form impurities such as tritiated ammonia NT_3, which eventually could result in instabilities. Hence, this could be visible in hysteresis studies.

2.3. Determine plasma parameters by optical emission spectroscopy (OES)

Focusing the characterization of a plasma source on the scientific goal of producing atomic tritium, the question arises how to evaluate a dissociation fraction or, even better, an *absolute number of atoms* $N(\mathrm{H})$ inside the plasma. In this work, an iterative method is chosen in which intensity measurements from the optical light emitted from the plasma is compared to CR-model calculations. This method investigates the electron temperature T_{e}, electron density n_{e} and the gas temperature T_{gas} in addition to $N(\mathrm{H})$.

To understand this method, some fundamentals of plasma chemistry are explained, including an introduction to Corona- and CR-models.

2.3.1. Plasma chemistry in low-temperature plasmas

Like in a gas, there are many collisions in a plasma. In a room-temperature gas, these are almost all *elastic collisions*. Hence, the velocity distribution function is Maxwellian. In a plasma there are many *inelastic collisions* as well, so kinetic energy converts to internal energy of the particles. In a low temperature plasma where the ionization degree is $I \ll 1$ (Equation (2.11)), this energy conversion results in an excitation of the species. Essentially, the plasma consists of a „species-zoo". For example, a hydrogen plasma consists of H, H_2, H^-, H^+, H_2^+, H_3^+, H^*, H_2^*, etc., resulting in a very complex system. It is not trivial to model this because the species have electronic excited states and the molecules additional ro-vibrational states [57]. Therefore, every species has a different temperature and a different distribution function.

2.3.1.1. Electron energy distribution function (EEDF)

As noted in Section 2.1.1, the electrons govern the dynamics of a plasma. Hence, knowledge of the *electron energy distribution function (EEDF)* is crucial to model a low temperature plasma . For elastic collisions the EEDF is a Maxwellian energy distribution:

$$f(E)dE = \frac{2}{\sqrt{\pi}} \frac{\sqrt{E}}{(k_B\, T_e)^{3/2}}\, e^{\frac{-E}{k_B\, T_e}}\, dE\ . \tag{2.28}$$

Deviations from it arise from inelastic collisions of the electrons. A Plasma with an ionization degree of $I \leq 10^{-4}$ is considered as non-Maxwellian [64]. However, a Maxwellian distribution is assumed in the following as it is sufficient for a first-order description of electron dynamics in an RF discharge with small electron energies.

2.3.1.2. Corona model

A low temperature plasma is in an equilibrium state if the electron density is low ($n_e \lesssim 10^{19}\,\mathrm{m}^{-3}$), the ionization degree is low ($I \ll 1$), each particle species has its own temperature, electronic excitations are dominated by electrons and electronic de-excitation is dominated by radiative decay [65]. Then, the following equations describe the plasma fully:

1. The *Planck blackbody function* determines the radiation energy

2. The *Saha equation* relates the number densities of atoms, ions and electrons.
3. The *Boltzmann distribution* describes the population among excited states
4. The *Maxwell distribution* describes particle velocities for all types of particles.

With the so-called *Corona model* these equations can be solved to determine populations densities for any excited state a^* [65]. The processes that are taken into account are

$\mathrm{a} + \mathrm{e_f} \longrightarrow \mathrm{a}^* + \mathrm{e_s}$	electron impact ionization
$\mathrm{a} + h\nu \longleftarrow \mathrm{a}^*$	spontaneous emission
$\mathrm{a} + \mathrm{e_f} \longrightarrow \mathrm{i} + \mathrm{e} + \mathrm{e_s}$	electron impact ionization
$\mathrm{a} + h\nu \longleftarrow \mathrm{i} + \mathrm{e}$	radiative recombination

Here, a and i are an atom and ion, respectively. $h\nu$ corresponds to a photon, and e_f, e_s denote a fast and slow electron. Building upon that, the corona equation for excitation is [65]:

$$n_1\, n_\mathrm{e}\, X_{1,p}^{exc}(T_\mathrm{e}) = n_p \sum_k A_{p,k}\,, \tag{2.29}$$

where n_p is the population density, n_1 the particle density in the ground state, and n_e the electron density. $X_{1,p}^\mathrm{exc}$ is the *rate coefficient* for electron impact excitation. It is defined by the integral of the EEDF weighted with the cross section $\sigma_{1,p}$ of this process [65]:

$$X_{1,p}^\mathrm{exc}(T_\mathrm{e}) = \int_{E_\mathrm{thr}}^{\infty} \sigma_{1,p}(E) \sqrt{\frac{2\,E}{m_\mathrm{e}}}\, f(E)\, dE\,, \tag{2.30}$$

where E_thr is the threshold energy that the electron must have to contribute to this process. Equation (2.29) balances electron impact excitation on the left-hand side with spontaneous emission on the right-hand side. Electron impact ionization and radiative recombination are balanced by [65]:

$$n_Z\, n_\mathrm{e}\, S_{Z,Z+1}(T_\mathrm{e}) = n_{Z+1}\, n_\mathrm{e}\, \alpha(T_\mathrm{e})\ . \tag{2.31}$$

Here, n_Z and n_{Z+1} denote the particle density in the ionization stage Z and $Z+1$, respectively. $S_{Z,Z+1}$ is the rate coefficient for electron impact ionization which is given by Equation (2.30). $\alpha(T_\mathrm{e})$ is the radiative recombination coefficient [65].

2.3.1.3. Collisional-radiative model

For electron densities $n_e \gtrsim 10^{19}\,\mathrm{m}^{-3}$ the corona model no longer holds, and thus, has to be extended to the so-called *collisional-radiative (CR) model* [65]. It takes into account population and depopulation processes among a set of relevant levels. The time development of the population density is then the following [65]:

$$\begin{aligned}
\frac{dn_p}{dt} = & \sum_{k<p} n(k) n_\mathrm{e} X^\mathrm{exc}_{k,p} + \sum_{k>p} n(k) n_\mathrm{e} X^\text{de-exc}_{k,p} \\
& - \sum_{k<p} n(p) n_\mathrm{e} X^\text{de-exc}_{p,k} - \sum_{k>p} n(p) n_\mathrm{e} X^\mathrm{exc}_{p,k} \\
& - \sum_{k<p} n(p)\, A_{p,k} + \sum_{k>p} n(k)\, A_{k,p} \\
& - n(p) n_\mathrm{e}\, S_p + n_\mathrm{e}\, n_\mathrm{e}\, n_i\, \beta_i + n_\mathrm{e}\, n_i\, \alpha_p \ .
\end{aligned} \tag{2.32}$$

The population processes by electron impact from all levels are represented by the first two terms. The inverse depopulating process corresponds to terms 3 and 4. Terms 5 and 6 in Equation (2.32) describe the spontaneous emission from and into state p. The last three terms take into account ionization and recombination.

In most cases, the system in state p is considered to be quasi-stationary, so that:

$$\frac{dn_p}{dt} = 0 \ . \tag{2.33}$$

The set of coupled differential equations (2.32) is transformed into a set of coupled linear equations. The quasi-steady-state solution has the form:

$$n_p = R_{0,p} n_i\, n_\mathrm{e} + R_{1,p} n_1\, n_\mathrm{e} \ . \tag{2.34}$$

R_0 and R_1 denote the so-called population coefficients. They describe ionic and ground state population and depopulation processes, respectively [65]. The second term in Equation (2.34) can be neglected in most cases because recombination is a negligible process in low pressure plasmas.

The construction of a CR model for atoms requires precise knowledge of several thousand reactions from cross sections, rate coefficients or transition probabilities. The complexity increases dramatically if vibrationally and rotationally excited states of molecules have to be considered. Providing a full data base of cross sections or rate coefficients is a common issue for CR models [65]. They can be calculated, for example, by the Coulomb-Born or Born-Bethe approximation. Cross sections can also be measured, mostly with electron beam experiments. When the probability of a certain reaction is not known, the value has to be extrapolated from the known probability of a similar reaction [66]. More details are given in Reference [65].

There are several CR models existing mainly for hydrogen and helium. The CR model used in this work is the **Yacora** model.

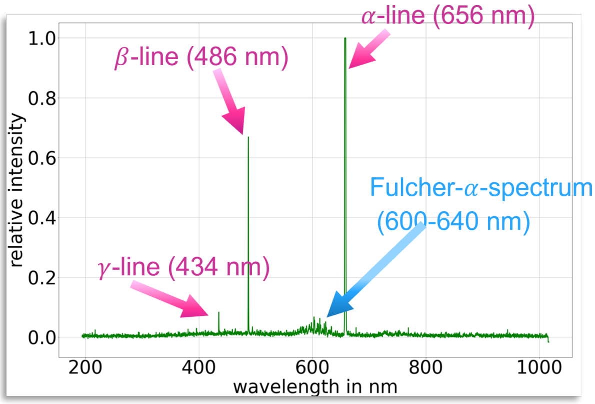

Figure 2.9.: Hydrogen plasma spectrum measured with a CCD spectrometer. Important spectral features are annotated.

2.3.2. OES on hydrogen plasmas

The plasma source used in this work, has an optical port to which various diagnostics can be applied. Here, a simple CCD spectrometer was attached with a fiber and a lens to perform **optical emission spectroscopy (OES)**. It measures the emitted light from the plasma source through the port in a wavelength range of 200 – 1000 nm. This technique has the advantage of being noninvasive.

In Figure 2.9 a typical hydrogen plasma spectrum measured with this optical system is shown. The most prominent emission is the Balmer α-line at ~656 nm which results from an electronic transition of $n = 3 \longrightarrow n = 2$. Other detectable atomic lines are the Balmer β- and γ-line at ~486 nm and ~434 nm, respectively. They show the transitions of $n = 4$ and $n = 5$ to $n = 2$, respectively. Furthermore, the molecular Fulcher-α band is partially detectable. In Figure 2.10b, the full Fulcher-α band is shown. There are different branches defined for transitions in the rotational quantum number $\Delta J = J_{d^3} - J_{a^2}$:

P-branch $\Delta J = -1$

Q-branch $\Delta J = 0$

R-branch $\Delta J = +1$.

For OES in low temperature plasma, usually the part of the Fulcher-α band that lies within ~600-640 nm (Figure 2.9) is used because it is easily distinguishable and hardly overlaps with other emission band lines [67]. It corresponds to the following transitions:

$$d^3\Pi_\mathrm{u} \longrightarrow a^3\Sigma_\mathrm{g}^+ \qquad \text{for } \nabla v = 0 \,. \tag{2.35}$$

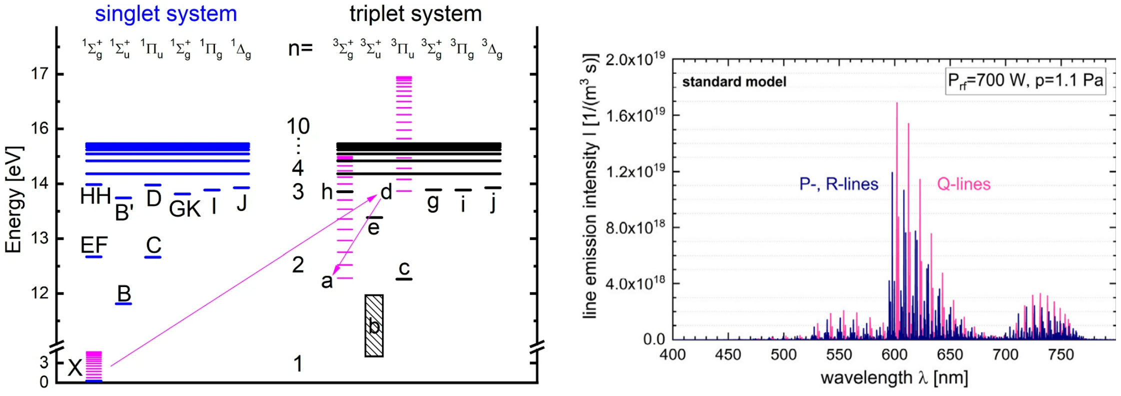

(a) **(b)**

Figure 2.10.: **(a)** Electronic energy level diagram of the hydrogen molecule. The ground state is denoted as $X^1\Sigma_g^+$. The Fulcher-α band is marked in magenta. In the interest of clarity, the figure depicts for these states solely the vibrational. but not the rotational levels. **(b)** Simulated line emission intensities for the entire Fulcher-α spectrum with a corona model. **(a)** Reprinted from [67]. **(b)** Reprinted from [69].

It is a relaxation from the triplet state with the principal quantum number $n = 4$ to $n = 2$ as depicted in Figure 2.10a. The Σ and Π are the molecular orbitals, respectively. The subscripts g and u characterize even or odd parity of the electronic ground state (symmetry under electron coordinate inversion through the center of the molecule). For Σ the superscripts + and - refer to the reflection symmetry of the electronic wavefunction through a plane containing the internuclear axis. v is the vibrational quantum number. A detailed explanation on molecular bands and the notation is given in Reference [68].

If the rate coefficients for the full Fulcher-α band are required, an extrapolation has to performed via a fully ro-vibrationally resolved corona model. A detailed explanation is given in [69]. In this work, an extrapolation factor of 2 is applied to the Fulcher-α band measurement.

The measured line intensities can be linked to the population coefficients calculated with CR models [20]. The measured intensity for a specific transition from p to k is:

$$I_{\text{measured}} = n_0 \, n_\text{e} \, X_{pk,\text{eff}}(T_\text{e}, n_\text{e}, \dots) \, , \tag{2.36}$$

where $X_{pk,\text{eff}}(T_\text{e}, n_\text{e}, \dots) = R_{0,p} \, A_{pk}$.
$R_{0,p}$ is the population coefficient from the Ansatz in Equation (2.34). It is the output of the CR model and has to be multiplied with the Einstein coefficients A_{pk} which can be extracted from Reference [68]. $X_{pk,\text{eff}}(T_\text{e}, n_\text{e}, \dots)$ is the *effective emission rate coefficient*. Thus, line radiation essentially depends on n_e, T_e and particle density n_0. If T_e and n_e

are not known from other diagnostics, such as Langmuir probes, an iterative approach must be used to determine them.

2.3.3. Collisional-radiative (CR) model calculations with Yacora on the web

The CR model used in this work can be accessed via a web application developed by D. Wünderlich, U. Fantz et al.[2] It is called **Yacora on the Web** [70] and is based on the flexible solver **Yacora** [71]. The main application range is plasma diagnostics for low-pressure plasma. The output from Yacora are population coefficients of the desired electronic states in m^{-3}. Furthermore, this can be an array for different input parameters.

Yacora provides CR models for atomic hydrogen, molecular hydrogen and helium. In this work, only the former two are used.

2.3.3.1. Atomic hydrogen model

This model includes six possible excitation channels which are depicted in Figure 2.11a. Essentially, Yacora solves Equation (2.32), but splits the excitation channels, depending on the regime. The full corresponding Ansatz for the particle density n_p in state p is:

$$n_p = n_\mathrm{e}\left(R_{\mathrm{H}p}\, n_\mathrm{H} + R_{\mathrm{H}^+p}\, n_{\mathrm{H}^+} + R_{\mathrm{H}_2p}\, n_{\mathrm{H}_2} + R_{\mathrm{H}_2^+}\, n_{\mathrm{H}_2^+} + R_{\mathrm{H}_3^+p}\, n_{\mathrm{H}_3^+} + R_{\mathrm{H}^-p}\, n_{\mathrm{H}^-}\right) \tag{2.37}$$

The terms in parentheses denote effective excitation of H, recombination of H^+, dissociative excitation of H_2, dissociative recombination of H_2^+, dissociative recombination of H_3^+ and mutual neutralization of H^- and H_X^+, respectively. If the plasma is in an ionizing mode (Figure 2.11b), which means that $T_\mathrm{e} \approx 10\,\mathrm{eV}$ and $n_\mathrm{e} \approx 10^{15}\,\mathrm{m}^{-3}$, the contributions from recombination, dissociative recombination from H_2^+ and H_3^+ and mutual neutralization can be neglected. On the other hand, if the plasma is recombining, which means $T_\mathrm{e} < 1\,\mathrm{eV}$ and $n_\mathrm{e} \approx 10^{22}\,\mathrm{m}^{-3}$, the channels direct excitation and dissociative excitation can be neglected. Yacora solves Equation (2.32) with an integration technique. Because of stiffness of the equation system, ordinary integration techniques are too slow. Therefore, the solver *CVODE* [72] was chosen instead.

Yacora includes the 40 energetically lowest lying electronic states [70]. For this work, the states up to the γ-line are of relevance. The density of the ground state H(1) is a fixed parameter because it is quasi-constant. Thus, reactions which only change the

---

[2] Max-Planck-Insitut für Plasmaphysik, 85748 Garching, Germany

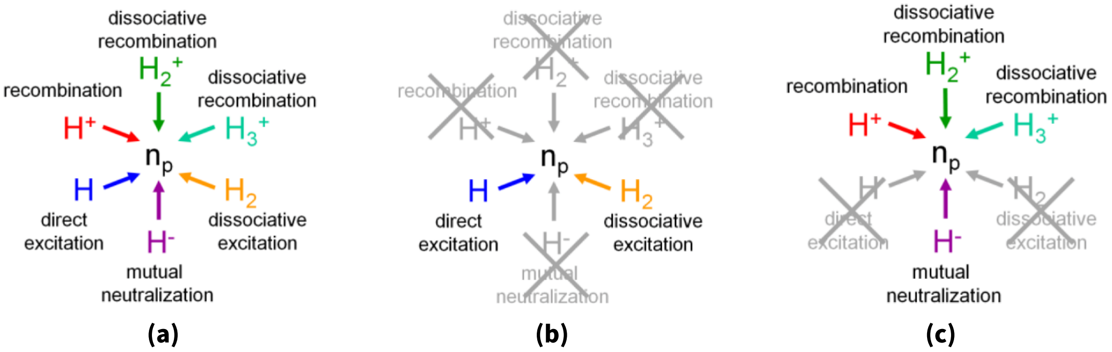

Figure 2.11.: Excitation channels for atomic hydrogen included in the Yacora CR model. **(a)** All channels. **(b)** Channels relevant for ionizing plasmas. **(c)** Channels relevant for recombining plasma. Reprinted from [73].

ground state density and not the population densities of excited states do not need to be considered by the model. For example, stripping of negative ions by electrons:

$$H + e^- \longrightarrow H(1) + 2e^- \tag{2.38}$$

In Reference [71], the sources for the cross sections are listed. The cross sections that are unknown are estimated as done in Reference [74]. In Figure 2.12 the cross sections for the excitation channels $H(1) \longrightarrow H(p)$ with the principal quantum number $p = (2, 7)$ are shown.

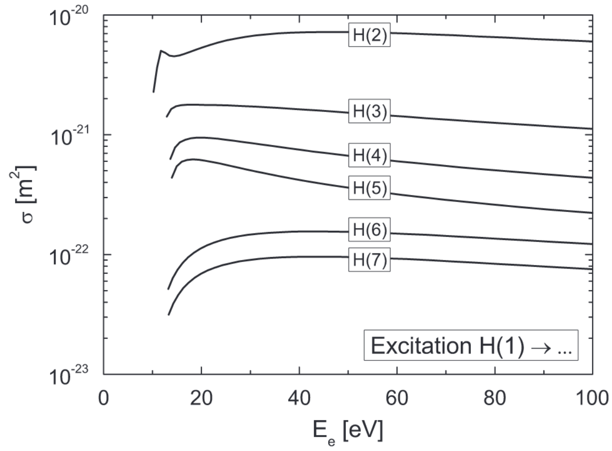

Figure 2.12.: Excitation cross sections for electron collisions with hydrogen atoms in the ground state. The relevant cross sections for this work are H(2), H(3) and H(4) corresponding to the Balmer H_α-, H_β- and H_γ-line, respectively. Reprinted from [75]

Table 2.1.: Einstein coefficients A_i for atomic Balmer lines i from NIST: `https://physics.nist.gov/PhysRefData/ASD/lines_form.html`

atomic line i	A_i in s^{-1}
α	$4.410\,78 \times 10^{7}$
β	$8.420\,76 \times 10^{6}$
γ	$2.531\,15 \times 10^{6}$

The validity of Yacora has been tested extensively. For instance, it was compared to measurements from OES, langmuir probes, double probes and microwave interferometry. A study can be found in [71, 73].

2.3.3.2. Population coefficients for atomic lines

The calculation for the atomic hydrogen model requires the excitation channel as an input. In the case of an ionizing plasma (see Figure 2.11b), the main excitation channels are direct excitation:

$$H(1) + e^{-} \longrightarrow H(p) + e^{-} \,, \tag{2.39}$$

and dissociative excitation:

$$H_2 + e \longrightarrow H(p) + H(1) + e^{-} \,. \tag{2.40}$$

Here, $H(p)$ is a hydrogen atom in an electronically excited state p and $H(1)$ is an hydrogen atom in the ground state.
In this work only the contributions from direct excitation are considered. However, for a complete picture of excitation processes, the dissociative excitation can be of importance (see Section 6.4.5).

The Einstein coefficients $A_{p,k}$ in Equation (2.36) for the atomic lines are listed in Table 2.1:

2.3.3.3. Molecular hydrogen model

The CR model for H_2 solves a system of equations similar to Equation (2.32) [73, 70]:

$$\frac{dn_p}{dt} = \sum_{q \neq p} \left(X_{q\to p} n_q - X_{p \to q} n_p \right) \,. \tag{2.41}$$

$X_{q\to p}$ is the total rate coefficient which includes all processes from the state q to the state p and $X_{p\to q}$ is the total rate coefficient which includes all the processes from the state p to the state q. The reactions considered by Yacora for the H_2 model are listed on the web page[3]. Furthermore, there are reactions which are optional:

- **Quenching** is the de-excitation from the state a^3 and metastable state c^3 to the ground state by heavy particle collisions. A detailed description is given in Reference [73].
- **Dissociative attachment** is the collision between an electron and a hydrogen molecule which leads to H_2^- that is not a stable ion, thus it dissociates in H and H^-:
$$\mathrm{H} + \mathrm{e}^- \rightarrow \mathrm{H}_2^- \rightarrow \mathrm{H} + \mathrm{H}^- \tag{2.42}$$
- **Charge exchange** of the excited states of H_2 with a positive ion of H
$$\mathrm{H}_2 + \mathrm{H}^+ \rightarrow \mathrm{H}_2^+ + \mathrm{H} \tag{2.43}$$

Sensitivity studies can be performed to investigate whether these processes have a relevant contribution to the measured intensities.

The web application of Yacora provides two possible datasets for the cross sections, namely *Janev* [75] and *Miles* [76]. However, they are in significant disagreement, in some cases differing by an order of magnitude (see Reference [73]). Thus, a new dataset has been published by Scarlett et al. [77] in which cross sections are calculated with the so-called *molecular convergent close-coupling (MCCC)* approach. A benchmarking of Yacora calculations with old and new datasets can be found in Reference [73]. During the writing of this thesis, the MCCC cross sections are not available in Yacora on the Web. Thus, the calculations for the molecular population coefficients including the MCCC cross-sections are performed directly by D. Wünderlich and R. C. Bergmayr.

2.3.3.4. Population coefficients for molecular bands

The Einstein coefficient for the Fulcherα-spectrum is taken from Reference [68] (Table 4, page 955). It is the effective transition probability for the $\mathrm{d}^3\Pi_u - \mathrm{a}^3\Sigma_g^+$ transition:

$$A_{\mathrm{Fulcher}} = 2.4551 \times 10^7\ \mathrm{s}^{-1}\ . \tag{2.44}$$

As discussed in Reference [68], it is not possible to estimate uncertainties in percent on the Einstein coefficients because they strongly depend on the underlying potential curve that is used for the calculations. However, since the Fulcher-α-band and the atomic Balmer lines are the most prominent parts in the hydrogen plasma spectrum,

---

[3] https://www.yacora.de/help/help-page-for-h2-model (visited on 11/21/2025).

it would have been recognized in literature if significant errors were present in the calculations. Furthermore, the analysis in this work includes an uncertainty of 20 % (see Section 6.4.2) that most probably covers all uncertainties from theory.

2.3.4. Comparison of OES measurements with CR model calculations

Depending on the calibration of the optical system, there are different possibilities to monitor and determine plasma parameters. Three types of calibration are presented below.

2.3.4.1. Plasma species identification

A wavelength calibration is the minimum calibration required to identify the correct plasma species (see *e.g.* Figure 2.9). It enables the monitoring of the plasma and plasma stability. The measurements that are shown in Sections 6.2 and 6.3 in principle only require a wavelength calibration. The wavelength was already calibrated when the spectrometer was purchased.

2.3.4.2. Line ratio method

For the determination of the Balmer line ratios and the ratio of the molecular Fulcher-α-band and the Balmer lines, a relative intensity calibration is needed. The calibration is provided by Thorlabs[4] The direct dependence on particle density and electron density of the line radiation cancels out in Equation (2.36). The measured line ratio is then directly given by the ratio of the corresponding effective emission rate coefficients. The resulting Equation yields:

$$\frac{I_i}{I_j} = \frac{R_{0,i}\,A_{ik}}{R_{0,j}\,A_{jk}} \tag{2.45}$$

with emission line/band i and j for $i \neq j$. When calculating the population coefficients for different T_e and n_e, this gives a n_e-intensity ratio and a T_e-intensity ratio plot. In this work, the ratios of the atomic α-, β-, γ-lines are evaluated. An atomic fraction $\alpha_{\mathrm{H,H_2}}$ can also be evaluated if the electron temperature is known T_e. The starting point is to calculate a theoretical ratio of atomic line to molecular band emission assuming

$$n(\mathrm{H}) = n(\mathrm{H_2})\ . \tag{2.46}$$

---

[4] Calibration service: `https://www.thorlabs.de/thorproduct.cfm?partnumber=CAL-CCS2` Calibration date: 23/05/2025.

This is, again, compared to the measured ratio. By taking n_e and T_e into account which are derived before hand, a deviation can be obtained between theory and experiment. The deviation can be transferred to a deviation from Equation (2.46). The result is eventually the atomic fraction:

$$\alpha_{H,H_2} = \frac{n(H)}{n(H_2)} \, . \tag{2.47}$$

The relative calibration enables the investigations for different plasma parameters. However, it is limited, because the ratio depends only weakly on T_e, which must be known for the atomic fraction. This is discussed in Reference [20] and also shown in the analysis from this work in Figure 6.8d.

2.3.4.3. Absolute emission of atomic lines and molecular bands

If the optical system includes an absolute intensity calibration, the information about the system increases. The absolute line intensities are much more sensitive to T_e than the ratios. Furthermore,n_H and n_{H_2} can be evaluated without the detour via Equations (2.46) (2.47), because they serve as a direct input in the CR-model calculations (see Equation 2.36).

If T_e, n_e, n_H and n_{H_2} is evaluated from the absolute intensities and the intensity ratios, the pressure inside the plasma cavity must be known. For N particles inside the plasma volume V follows from the ideal gas law:

$$N = N_H + N_{H_2} = \frac{p\,V}{k_B\,T_{gas}} \, . \tag{2.48}$$

The particle density is then $n = N/V$. Because the plasma is quasi-neutral (see Equation (2.1)), and the electron density is in the region of $10^{18}\,m^{-3}$, and the particle number is in the region of $10^{20}\,m^{-3}$ (see Section 6.4.4), the number of ions is neglected.

At this point it becomes clear, that an absolute intensity calibration is essential when utilizing OES as a quantitative diagnostics tool for the determination of plasma parameters. Hence, a graphical method is demonstrated to determine plasma parameters like T_e, n_e, n_H and n_{H_2} in Chapter 6 including the absolute intensity calibration of the optical system. Furthermore, the theoretical toolbox is now provided to understand the processes inside the plasma source. In Chapter 4, the experimental setup is presented that is required to operate the plasma source.

The theoretical description of the E- and H- modes is supported by measurements of this transition in Chapter 6. However, the characterization of the plasma source in this work includes investigations of the beam that is emitted from the source. Therefore, graphene is exposed to the plasma source and structural changes are measured (see Chapter 5). Therefore, the succeeding chapter provides a theoretical introduction to graphene and measurements of defects on graphene.

3. Graphene as an atomic hydrogen sensor

The interaction between condensed matter and an electromagnetic field opens intriguing possibilities for characterization of solid state samples. Although most of the photons traveling through a medium are transmitted or absorbed, a very small fraction is scattered in all directions by inhomogeneities inside the medium. These inhomogeneities can be static or dynamic. For instance, an impurity or a vacancy is considered as static, whereas a phonon mode or something more exotic like charge density waves or spin waves are dynamic scatterers. There are different instruments to investigate inhomogeneities with electromagnetic waves, for example the Fourier transform infrared (FTIR) spectrometer, which uses light in the infrared range, or the Raman spectroscopy, which uses light from the visible wavelength spectrum.

The working principle of the latter is explained in Section 3.1. In Section 3.2 the two-dimensional material *graphene* is introduced. In this work, graphene is exposed to the plasma source. Two diagnostic tools are utilized to investigate structural changes on the graphene. One is Raman spectroscopy. The theory of Raman spectroscopy on graphene is elaborated on in Section 3.3. A confocal Raman microscope (CRM) is used to scan the graphene samples *ex-situ* after exposure to the plasma source. The experimental setup of the CRM is introduced in Section 3.4. The second diagnostics tool to observe structural changes on the graphene is the measurement of the sheet resistance of the graphene samples. In contrast to the CRM, this approach aims to be monitored *in-situ* to observe time resolved changes. In Section 3.5 the theoretical basis for sheet resistance measurements is given and the Van der Pauw method [21] is explained.

3.1. Raman spectroscopy of solids

The inelastic scattering of light by molecular vibrations was first reported by C.V. Raman [78]. In 1930 Raman was awarded the Nobel prize for his discovery of Raman scattering. Today, Raman scattering is a fundamental spectroscopic tool in solid-state physics. This section describes the basics of Raman scattering in condensed matter and

primarily guides towards Raman spectroscopy of graphene. The theory explained here is a classical and empirical description that is sufficient for the interpretation of the measurements in this thesis. This qualitative analysis mainly follows Reference [79]. A complete quantum mechanical derivation is to find in *e.g.* Reference [80].
Assuming a sinusoidal electromagnetic wave

$$\mathbf{F}(\mathbf{r},t) = \mathbf{F}_i(\mathbf{k}_i,\omega_i)\ \cos(\mathbf{k}_i\cdot\mathbf{r}-\omega_i\,t)\ , \tag{3.1}$$

entering a crystal, a sinusoidal polarization $\mathbf{P}(\mathbf{r},t)$ will be induced. Its amplitude is given by

$$\mathbf{P}(\mathbf{k}_i,\omega_i) = \chi\mathbf{F}_i(\mathbf{k}_i,\omega_i)\ . \tag{3.2}$$

Here, χ is the electric susceptibility that describes the electrical response to the incoming wave. χ is influenced by phonons. Mathematically, phonons can be described by an atomic displacement function $\mathbf{Q}(\mathbf{r},t)$. In an adiabatic approximation, in which the characteristic electronic frequencies are much larger than ω_0, χ can be expanded as a Taylor series in $\mathbf{Q}(\mathbf{r},t)$:

$$\chi(\mathbf{k}_i,\omega_i,\mathbf{Q}) = \chi(\mathbf{k}_i,\omega_i) + \left(\frac{\partial\chi}{\partial\mathbf{Q}}\right)_0 \mathbf{Q}(\mathbf{r},t) + \dots\ , \tag{3.3}$$

where χ_0 denotes the electric susceptibility in the crystal without any distortion. The second term in Equation (3.3) corresponds to an oscillating susceptibility induced by phonons or other similar fluctuations in the atomic displacement. Inserting Equation (3.3) into Equation (3.2) the polarization can be split into two contributions:

$$\mathbf{P}(\mathbf{r},t,\mathbf{Q}) = \mathbf{P}_0(\mathbf{r},t) + \mathbf{P}_{\text{ind}}(\mathbf{r},t,\mathbf{Q})\ , \tag{3.4}$$

where

$$\mathbf{P}_0(\mathbf{r},t) = \chi_0(\mathbf{k}_i,\omega_i)\mathbf{F}_i(\mathbf{k}_i\omega_i)\cos(\mathbf{k}_i\cdot\mathbf{r}-\omega_i\,t) \tag{3.5}$$

is a polarization vibrating in-phase with the incident radiation. $\mathbf{P}_{\text{ind}}(\mathbf{r},t,\mathbf{Q})$ is the polarization induced by phonons:

$$\mathbf{P}_{\text{ind}}(\mathbf{r},t,\mathbf{Q}) = \frac{1}{2}\left(\frac{\partial\chi}{\partial\mathbf{Q}}\right)_0 \mathbf{Q}(\mathbf{q},\omega_0)\mathbf{F}_i(\mathbf{k}_i,\omega_i\,t) \tag{3.6}$$

$$\times\{\cos[(\mathbf{k}_i+\mathbf{q})\cdot\mathbf{r}-(\omega_i+\omega_0)\,t] \tag{3.7}$$

$$+\ \cos[(\mathbf{k}_i-\mathbf{q})\cdot\mathbf{r}-(\omega_i-\omega_0)\,t]\}\ . \tag{3.8}$$

Here, $\mathbf{q}$ is the wavevector of the phonon which oscillates with frequency ω_0. The induced polarization consists of two sinusoidal waves: a Stokes shifted wave with wavevector $\mathbf{k}_S = (\mathbf{k}_i - \mathbf{q})$ and frequency $\omega_S = (\omega_i - \omega_0)$ and an anti-Stokes shifted wave with wavevector $k_{\text{AS}} = (\mathbf{k}_i + \mathbf{q})$ and frequency $\omega_{\text{AS}} = (\omega_i + \omega_0)$. The former corresponds to the incident photon that transfers energy to the crystal, whereas the latter corresponds to the incident photon that gains energy from a phonon. The phonon frequency is equal to the difference between the incident photon frequency ω_i and the scattered photon frequency ω_S. This is referred to as the **Raman frequency** or **Raman shift**.

For Raman spectroscopy of graphene, only the Stokes-shifted part is relevant because all scans are performed at room temperature and therefore the energy transfer from excited phonons is suppressed. In general, not only one phonon eigenmode can interact with the incident photon. Hence, assuming n phonons with wavevectors $\mathbf{q}_1, \ldots, \mathbf{q}_n$ to participate in the Raman process. The energy and momentum conservation laws are

$$\omega_i = \omega_S + \sum_{i=1}^{n} \omega_{\mathbf{q}_i} \tag{3.9}$$

$$\mathbf{k}_i = \mathbf{k}_S + \sum_{i=1}^{n} \mathbf{q}_i \,. \tag{3.10}$$

The theoretical basics given in this section allow the understanding of the qualitative Raman spectra of defect-free and defective graphene which are explained in detail in Section 3.3 (see also [81]).

3.2. Properties of graphene

To understand the qualitative Raman spectra in graphene (see also [81]) electronic and phononic properties of graphene are introduced in this section.

Graphite is a stack of atomic carbon layers that form a hexagonal honeycomb lattice. A monoatomic layer of this three-dimensional material is called graphene (see Figure 3.2a). This planar graphene layer itself has been presumed not to exist in the free state, being unstable with respect to the formation of curved structures such as soot or nanotubes [82]. However, K.S. Novoselov and A.K. Geim achieved the production of few-layer graphene (FLG) in 2004 which was sufficient to investigate the peculiar properties of this material [82]. In 2010, they received the Nobel price *'for groundbreaking experiments regarding the two-dimensional material graphene'*[1].

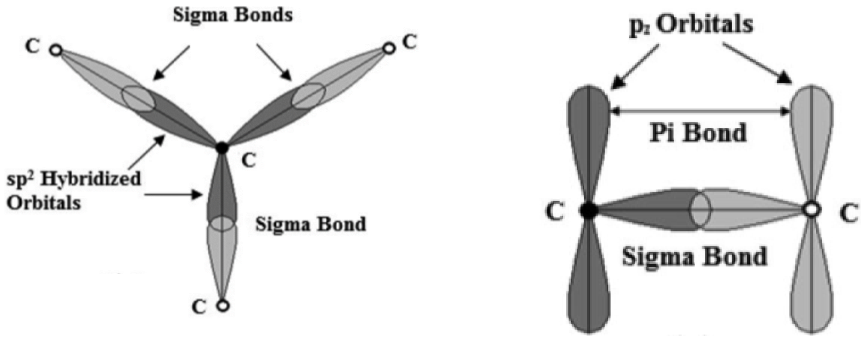

(a) **(b)**

Figure 3.1.: Illustration of covalent bonds in graphene. **(a)** Illustration of the sp^2 hybridization of a carbon atom between its nearest neighbors. **(b)** Illustration of the remaining electrons forming π bonds in vertical orientation to the sp^2-plane. Reprinted from [83].

3.2.1. Electronic properties of graphene

In pristine graphene the electronic configuration of the carbon atoms is $1\mathrm{s}^2$, $2\mathrm{s}^2$ and $2\mathrm{p}^2$ which corresponds to a carbon atom having 4 valence electrons. Those form sp^2 hybrid orbitals which form σ-bonds in in-plane orientation (see Figure 3.1a). The lattice structure results in a honeycomb pattern that is illustrated in Figure 3.2a. The remaining electron in the vertical component of the $2\mathrm{p}^2$ orbital forms weaker π-bonds (see Figure 3.1b).

The electronic band structure of graphene can be derived starting from the two basis vectors in reciprocal space which span the unit cell [84]. The wavefunction of the electrons is approximated with the tight binding model in which electrons are considered to be strongly bonded to the atomic nuclei [85]. This reduces the computational cost of solving the Schrödinger equation compared to density functional theory but preserves the quantum mechanical nature of the wavefunctions. The solution is performed with the Linear Combination of Atomic Orbitals (LCAO) method [85]. More intuitively, all atomic orbitals $1\mathrm{s}^2$, $2\mathrm{s}^2$ and $2\mathrm{p}^2$ overlap and thus form electronic bands that are named as $1\mathrm{s}^2$, $2\mathrm{s}^2$ and $2\mathrm{p}^2$ bands. Hereby, the s- and p-bands perform an analogous mixing which results in a sp^2-band. The dispersion relation yields:

$$E = E_0 \pm \gamma_0 \left(1 + 4\cos\left(\frac{\sqrt{3}k_x\, a}{2}\right)\cos\left(\frac{k_y\, a}{2}\right) + 4\,\cos^2\left(\frac{k_y\, a}{2}\right)\right)^{\frac{1}{2}} . \tag{3.11}$$

Here, k_x and k_y are the represent the in-plane components of the wave vector $\mathbf{k}$ and $a = 1.42\,\text{Å}$ the lattice constant. The tight-binding integral or the transfer integral

---

[1] The Nobel Prize in Physics 2010. NobelPrize.org. Nobel Prize Outreach 2025. Fri. 29 Aug 2025. `https://www.nobelprize.org/prizes/physics/2010/summary/` (visited on 11/21/2025).

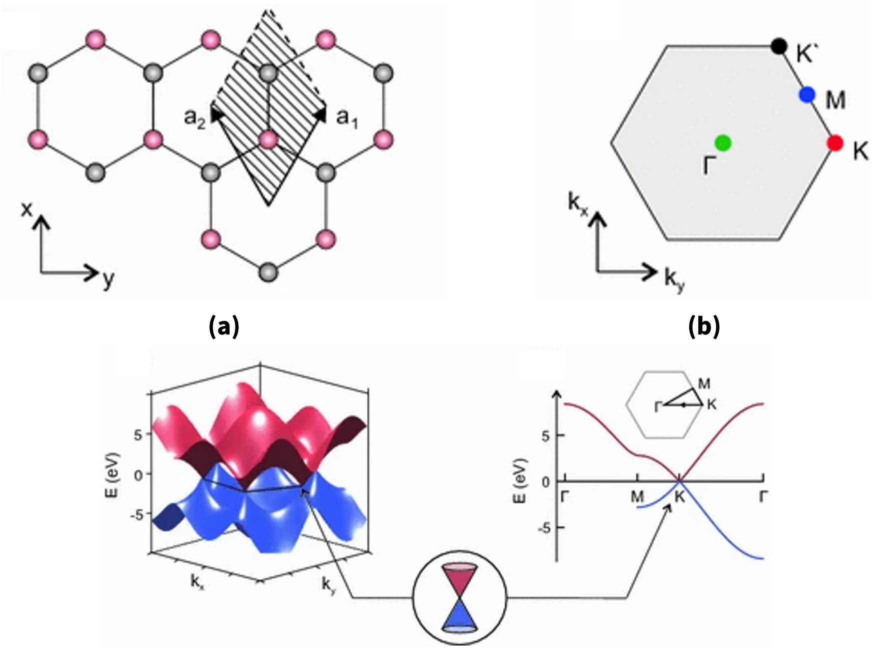

(a) **(b)**

(c)

Figure 3.2.: Electronic band structure of graphene. **(a)** Illustration of the graphene lattice that consists of two sublattices that are marked in red and black, respectively. The vectors $\mathbf{a}_1$ and $\mathbf{a}_2$ span the unit cell. **(b)** Illustration of the first Brillouin zone corresponding to the unit cell including the high symmetry points Γ, K, K' and M. **(c)** Plot of the electronic band structure. Three-dimensional representation on the left side and cut along the high symmetry points on the right side. The valence band is blue and the conduction band is red. The linear dispersion relation at the Dirac points (K,K') is shown in the inset. Reprinted with permission from [88]. Reproduced with permission from Springer Nature.

$\gamma_0 \approx 2.8\,\mathrm{eV}$ measures the strength of exchange interaction between nearest neighbor atoms. The density of states (DOS) in graphene can be derived from Equation (3.11) and it is found to be zero at the Fermi level. Along with the zero band gap, this is why graphene is a zero band gap semiconductor (see Figure 3.2c). The symmetry points K-and K' are also called Dirac points because the dispersion relation for graphene is linear there and therefore the charge carriers behave like massless Dirac fermions [86, 87].

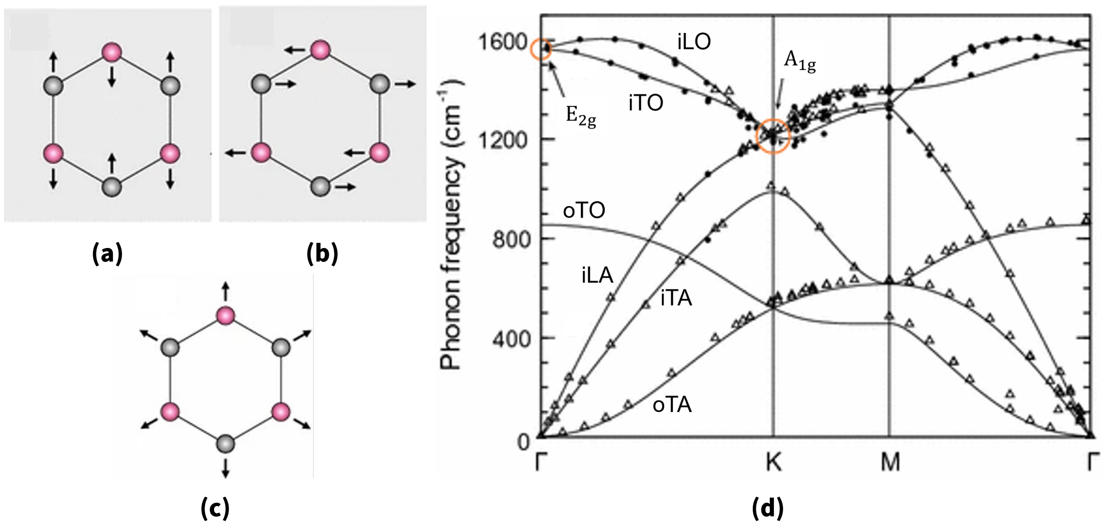

Figure 3.3.: Phonons of graphene. **(a)**,**(b)** illustration of Raman active phonon modes. **(c)** illustration of breathing motion of the lattice. **(d)** Phonon dispersion relation obtained from DFT-GW (density functional theory supplemented by GW) calculations from Venezuela et al. [89]. Reprinted with permission from [88]. Copyright 2018 Springer International Publishing AG.

3.2.2. Phonon modes in graphene

A three-dimensional crystal with r atoms in the unit cell exhibits 3 acoustic modes and $3r - r$ optical modes [87]. Graphene has two atoms in the unit cell. Therefore, there are one longitudinal acoustic mode (iLA), two transverse acoustic modes (iTA, oTA) and three optical modes (iLO, iTO, oTO) (see Figure 3.3d). Here, **i** and **o** denote **i**n-plane and **o**ut-of-plane phonons. From the symmetries of the phonon modes and the Raman tensor, Raman selection rules determine the Raman-active phonons [80]. For graphene, only the iLO mode in Figure 3.3a and iTO mode in Figure 3.3b at the Γ-point are Raman-active [12]. The phonon mode at the K-point in Figure 3.3c corresponds to a radial breathing motion of the lattice. This branch is not directly Raman active, but is very important for understanding the D and 2D Raman peaks of graphene.

3.3. Raman spectroscopy of graphene

In this work, Raman spectroscopy is used to investigate structural changes to the graphene. Hence, an explanation for Raman spectra of graphene is given. The difference between the spectra of pristine and defective graphene is explained. Furthermore, the

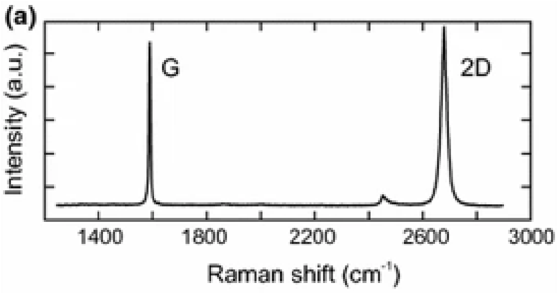

(a)

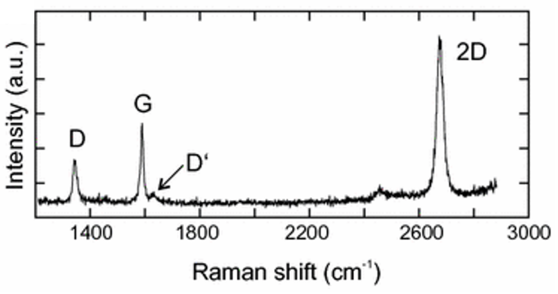

(b)

Figure 3.4.: Raman spectra of **(a)** pristine and **(b)** defective graphene. Important spectral features are annotated. Reprinted from [88]. Reproduced with permission from Springer Nature.

current state of knowledge about the connection between the defect density L_D, different defect-types and corresponding changes in the Raman spectra is given in this Section.

3.3.1. Raman spectrum of pristine graphene

With Raman spectroscopy, the structure of graphene can be investigated. As described in Section 3.1, incident light scatters with phonons and shifts the wavelength of the reflected light. Depending on the structure of the graphene different phonons interact with the light. For pristine graphene, the conservation of momentum determines the possible interactions. The sum of the wavevectors q_i of the phonons must be zero:

$$\sum_{i=1}^{n} \mathbf{q}_i = 0 \ . \tag{3.12}$$

A Raman spectrum of pristine graphene is displayed in Figure 3.4a. The process that cause the peaks are illustrated in Figure 3.5**(a)**-**(d)**. A green arrow in Figure corresponds to an incident photon which produces an electron-hole-pair in the π^*- and π-band, respectively. A red arrow corresponds to a scattered photon which results from

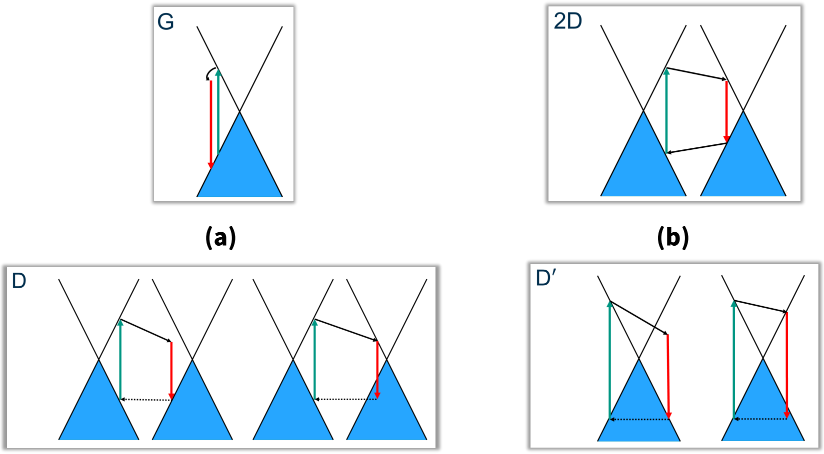

(a) (b)

(c) (d)

Figure 3.5.: Representation of the origins of the four peaks in Figure 3.4. **(a)** The origin of the G-peak. The electron loses energy to a zero momentum phonon and transits into the π^*-band. **(b)** The origin of the 2D-peak. Two phonons with $\mathbf{q}_1 = -\mathbf{q}_2$ scatter electron to the π^*-band and hole to the π-band. **(c)** and **(d)** The origin of the D- and D'-peak. Due to the presence of defects the electron scatters with a none zero momentum phonon and the hole scatters with the defect. The difference between D and D' is the scattering process which is intervalley and intravalley.

recombination of electron and hole. The black arrows represent phonons which change energy and band of the electron and hole.

The **G-peak** is a one-phonon scattering process. Due to Equation 3.12, the phonon must have zero momentum. This is illustrated in Figure 3.5a. Hence, iTO and iLO modes contribute to this process because they are Raman-active modes at the Γ-point. The G-peak is a degenerate Raman-peak located around $1580\,\mathrm{cm}^{-1}$.

The **2D-peak** in Figure 3.4a originates from a two-phonon scattering process in which Equation (3.12) requires the two phonon momenta to be $\mathbf{q}_1 = -\mathbf{q}_2$. This peak is broader because it results from a continuum of phonons. This is due to the fact that there are no further restrictions on the modulus of $\mathbf{q}_i$. The phonon can be anywhere within the Brillouin zone. The dominant contributions yield from the TO-branch, with $\mathbf{q}$ near the K-point. A representation of the process is shown in Figure 3.5b.

3.3.2. Raman spectrum of defective graphene

Defects in the graphene structure change the Raman spectrum (see Figure 3.4b). The most prominent defect types in graphene that are relevant for this work are edges, vacancies and sp^3-defects:

Edges	The graphene samples used in this work consist not of a perfect monolithic graphene layer but rather of many graphene ’flakes’ with a maximum size of about 20 μm [90]. Hence, every scan with the Confocal Raman Microscope (CRM) includes edges.
Vacancies	If a carbon atom is missing in the honey comb structure of graphene it is called a vacancy.
sp^3-defects	In Section 3.2.1 the band structure of pristine graphene is explained. In in-plane direction the carbon atoms form sp^2 hybridized orbitals. In out-of-plane direction every C atom has an electron in a p$_z$ orbital, If a radical bonds to covalently to this point the electro-chemical configuration changes from sp^2 to sp^3. In this work atomic hydrogen as a radical is most relevant.

If defects are present in graphene, the structural symmetry breaks and Equation (3.12) does not hold anymore because electron-defect scattering contributes to the conservation of momentum. This gives rise to further peaks in the Raman spectrum (see Figure 3.4b). The degeneracy of the G-peak (see Section 3.3.1) is abolished, and phonons away from the Γ-point contribute to the one-phonon scattering processes. A defect can activate the breathing motion in Figure 3.3c which enables intervalley electron-phonon scattering as shown in Figure 3.5c. This results in the **D-peak** that is located around 1350 cm^{-1}[12]. Furthermore, intravalley processes as double resonance also occur which give rise to the **D’-peak** located around 1600 cm^{-1}[12].

3.3.3. Models for the defect density L_D

The ratio of the D-and G-peak enables the extraction of information about the defect density L_D which describes the average distance between two lattice defects. At the time of writing this thesis, there is not a singular model available that is valid for all defect types (from *e.g.* Reference [91]). In Reference [92] an analytic relation between I_D/I_G and L_D is obtained from Raman scans with different excitation laser lines of Ar-ion-bombarded samples (see Figure 3.7b):

$$\frac{I_D}{I_G} = C_A \frac{(r_A^2 - r_S^2)}{(r_A^2 - 2r_S^2)} [e^{-\pi r_S^2/L_D^2} - e^{-\pi (r_A^2 - r_S^2)/L_D^2}] \ . \tag{3.13}$$

The length scales r_A and r_S determine the region where the D band scattering takes place. The quantity r_S is the radius of the structurally disordered area caused by the impact of an ion. r_A is the radius of the area surrounding the point defect in which the D band scattering takes place. The parameter C_A is a scaling factor for the activated region. In Equation (3.13) C_A represents the maximum possible I_D/I_G. This maximum would be reached in an ideal case where the D-peak is activated throughout the sample, with no disruption of the hexagonal carbon rings. Equation (3.13) was originally proposed by *Lucchese et al.* [14]. Because this model was intended for ion-induced point-defects rather than chemical functionalization, it is an incomplete description of sp^3-type defects. Therefore, *Fournier et al.* developed a model that includes, in addition to the radii r_A and r_S, a third radius r_{sp^3} which corresponds to the radius of the sp^3-hybridized region of the carbon atom. It is visualized in Figure 3.6a. This is not Raman active and, if taken into account, an overestimation of L_D is prevented. The contribution from the sp^3-C surface fraction is proportional to the intensity of the G-band, whereas in literature, that uses the Lucchese model, the G-peak is set to be constant [92]. The resulting formula is:

$$\frac{I_D}{I_G} = \frac{C_S\, f_S + C_A\, f_a}{1 - f_{sp^3}}\ , \tag{3.14}$$

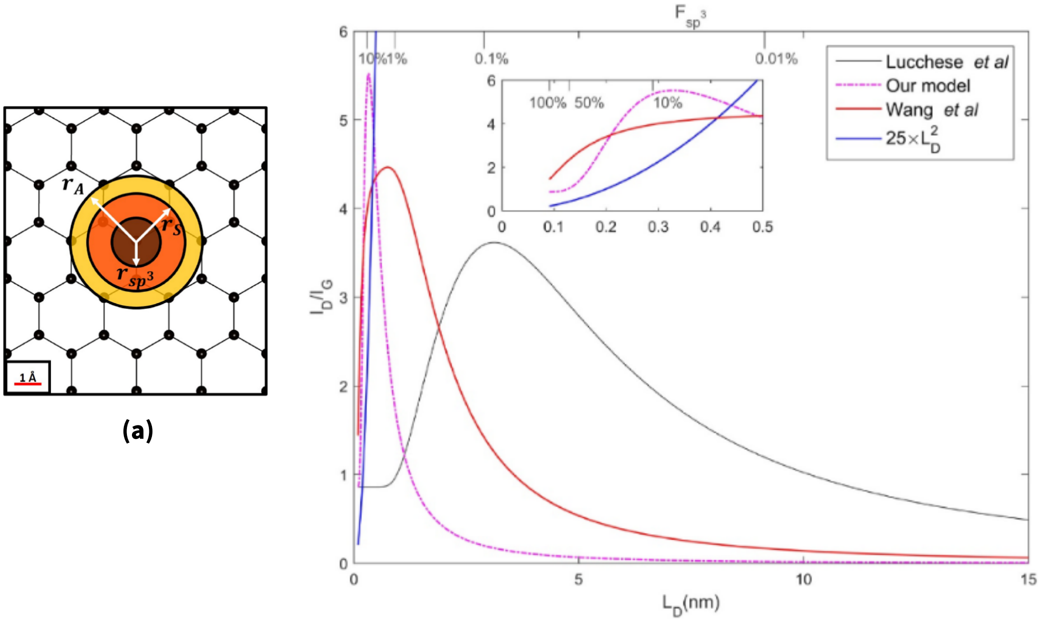

(a)

(b)

Figure 3.6.: Defect density L_D models. **(a)** Visualization of the Fournier et al. model. **(b)** Comparison of different models relating defect density and I_D/I_G. The *Wang et al.* model is not explained in this work. Reprinted from [13].

with the surface fractions:

$$f_S = e^{-\pi\, r_{sp3}^2 \sigma} - e^{-\pi r_S^2 \sigma}\,,$$
$$f_A = e^{-\pi\, r_s^2 \sigma} - e^{-\pi r_A^2 \sigma}\,,$$
$$f_{sp3} = 1 - e^{-\pi\, r_{sp3}^2 \sigma}\,.$$

Here, $\sigma = \frac{N}{S_T}$ is the defect concentration, N the number of molecules, and S_T the total surface of graphene. This model is non-empirical and incorporates input parameters from quantum chemistry calculations.
In Figure 3.6b the different models are compared. Taking the sp^3-radius into account, leads to significant differences in L_D and sp^3 coverage depending on the model.

3.3.4. Defect density regimes

In Figures 3.6b and 3.7b the relation between I_D/I_G and L_D can be divided into two regions:
Stage 1 is defined as defect densities $L_D \geq 3\,\mathrm{nm}$ where the relation $I_D/I_G \propto (1/L_D)^2$ holds. With decreasing L_D, I_D increases because the distance between two defects decreases, so the e-h pairs have a higher probability of scattering with those defects.
Stage 2 is defined as $L_D \leq 3\,\mathrm{nm}$. The distance between two defects is smaller than the

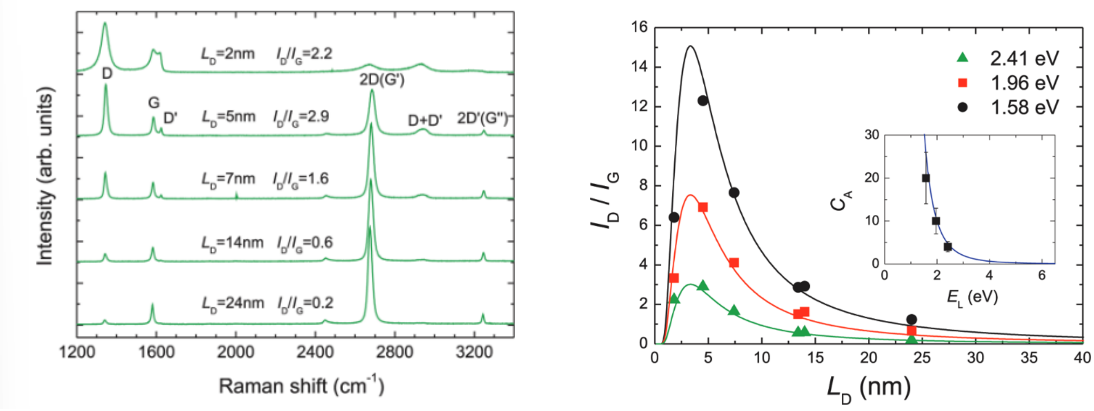

(a) **(b)**

Figure 3.7.: Defect density in graphene in relation to the D/G ratio. **(a)** Raman spectra for different L_D. **(b)** I_D/I_G for different SLGs and laser energies. The solid lines are fits according to Equation (3.13) with $r_S = 1\,\mathrm{nm}$ and $r_A = 3.1\,\mathrm{nm}$. The inset plots C_A as a function of the laser energy E_L. The solid curve is given by $C_A = 160\,\mathrm{E}_\mathrm{L}^{-4}$. Reprinted with permission from [92]. Copyright © 2011, American Chemical Society.

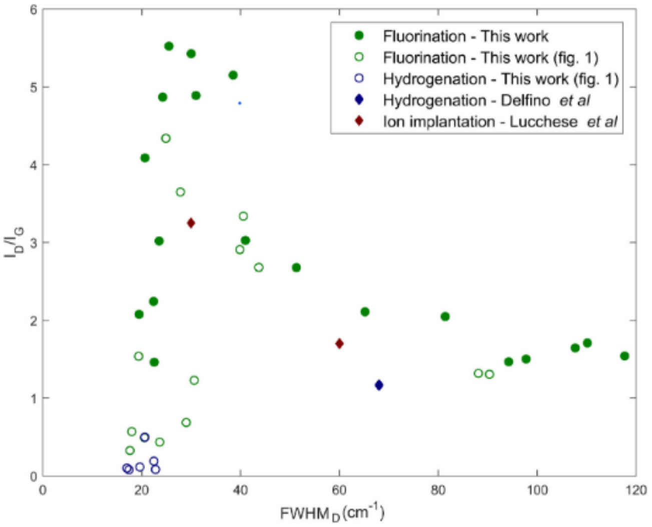

Figure 3.8.: I_D/I_G over the full width half maximum (FWHM$_D$) of the D-peak. For different measurements of functionalized graphene. To distinct areas visible with FWHM$_D$ $\approx 40\,\mathrm{cm}^{-1}$ as a threshold. Reprinted from [13].

average distance an e-h pair travels before scattering with a phonon. Therefore, the contributions of defects and phonons will not sum independently [92]. Furthermore, the relation $I_D/I_G \propto 1/L_D^2$ does not hold anymore because I_G can be assumed roughly as constant because the G-peak is related to the relative motion of sp^2-carbons. In this regime a different relation is proposed $I_D/I_G \propto L_D^2$ because the development of the D-peak indicates ordering of the honeycomb lattice [92].

The assignment of different I_D/I_G measurements to the defect density region enables comparability between them. In literature (see Ref. [92]) the Raman spectrum evolves in the high defect density as follows: The G-peak position decreases from $\sim 1600\,\mathrm{cm}^{-1}$ towards $\sim 1510\,\mathrm{cm}^{-1}$. The width Γ of the D'-and G-peak is so big that they overlap and a Lorentzian fit with a shoulder cannot separate them anymore. Furthermore, there are no more well-defined second-order peaks (see Figure 3.7a).[2] Hence, combining the width Γ_G of the G-peak and I_D/I_G allows discrimination between the two regimes [92]. In addition, in Reference [13], the width of the D-peak is used instead. Figure 3.8 shows two distinct behaviors between the width of the D-peak and the measured I_D/I_G. At low coverage rates, $FWHM_D$ remains nearly constant. At large coverage rates, a significant overlap of the sp^3-disks (see Figure 3.6a) occurs, and so $FWHM_D$ increases as I_D/I_G decreases [13].

---

[2] Here, second order means scattering processes with two phonons. For example the 2D-peak.

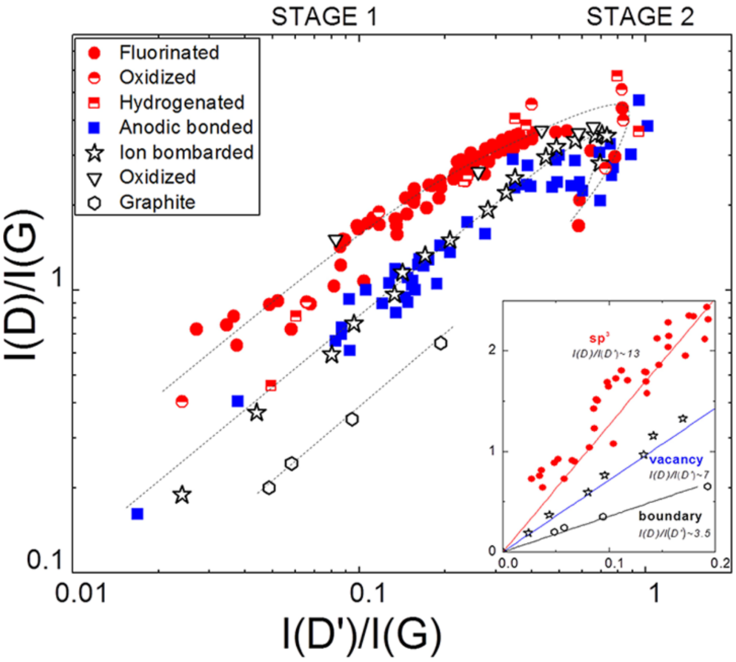

Figure 3.9.: Collection of data from literature for $I_\mathrm{D}/I_\mathrm{G}$ ratio over $I_{\mathrm{D}'}/I_\mathrm{G}$ ratio. The dotted lines are only a guide for the eyes. The linear dependence of the ratios in a low defect density regime is shown on the inset. This allows to distinguish between defect types from the $I_\mathrm{D}/I_{\mathrm{D}'}$ ratio. Reprinted from [15]. Copyright © 2012, American Chemical Society.

3.3.5. Raman spectroscopy of hydrogenated graphene

Hydrogenation is the adsorption of atomic hydrogen on a 2D material. Graphene, which is fully hydrogenated, is also known as *graphane*.

Hydrogenation of graphene assumes no breakage of carbon-carbon bonds and therefore only one hydrogen atom can bond covalently to each lattice-carbon [11]. This process changes the sp^2- to a sp^3-configuration, resulting in a defective behavior of the graphene because it breaks the rotational symmetry, and one-phonon scattering processes with a wavevector $\mathbf{q} \neq 0$ become more likely.

To quantify the hydrogen coverage on the graphene the defect density L_D is required. However, the ratio $I_\mathrm{D}/I_\mathrm{G}$ is not sensitive to the defect type (see Figure 3.6b). Therefore, the D'-peak and its ratio $I_\mathrm{D}/I_{\mathrm{D}'}$ are used in the literature (see *e.g.* [15]). Figure 3.9 shows a difference in $I_D/I_{D'}$ assuming I_G constant. *Eckmann et al.* plot their own data and data from literature on this. To see is that sp^3-type defects formed with F, O and H[3] follow a different $I_D/I_{\mathrm{D}'}$ ratio than vacancy-type defects. Hence, *Eckmann et al.* give values

---

[3] A Raman scan cannot distinguish between the three atoms because they all form sp^3-bonds.

on the intensity ratio if it ensured that the data is assigned to the low defect density regime *Stage 1*:

$$\frac{I_D}{I_{D'\,\mathrm{max}}} \approx 13 \tag{3.15}$$

for sp^3-type defects and

$$\frac{I_D}{I_{D'\,\mathrm{max}}} \approx 7 \tag{3.16}$$

for vacancy-type defects. Values in between 7 and 13 indicate a mixture of sp^3-type and vacancy-type defects. In this case, it is not possible to extract a defect density with neither the Lucchese et al. nor the Fournier et al. model (see Figure 3.6b).

3.4. Confocal Raman Microscope (CRM)

In this work, Graphene samples are exposed to the plasma source. The experimental setup is presented in Section 4.4. To observe structural changes on the graphene Raman microscopy is utilized. In this section, a Confocal Raman Microscope (CRM) is presented that is used to scan the graphene samples after they have been exposed to the plasma source.

The Raman microscope used in this work was constructed by Diaz Barrero et al. [16]. The CRM is tailored to be compatible with tritium contaminated samples and enable a large operational flexibility. It is constructed nearly from off-the-shelf optomechanical and optical components. The device is a combination of confocal (laser scanning) microscopy and Raman spectroscopy. A detailed discussion on hardware and software is given in References [16] and [81]. The scanning and imaging of all samples is performed by G. Zeller, as it is a specialized device that requires experience in confocal Raman microscopy.

The setup of the CRM is illustrated in Figure 3.10. It is divided into three functional groups:

Segment A Monochromatic light with a wavelength of 532 nm is generated by a laser. In contrast to the initial design with a diode-pumped solid-state (DPSS) laser [16] a LaserBoxx LCX-532L unit is utilized, at 100 mW output power equating to a power density on the graphene surface of $\sim 2.4 \times 105\,\mathrm{W/cm^2}$. The light is coupled into the system using a single-mode optical fiber. A dichroic beam splitter combined with a microscope objective is used to focus the laser. Furthermore, it filters Raman light from Rayleigh light which is reflected from the sample. However, a sub-percent of the 532 nm light can pass the filter.

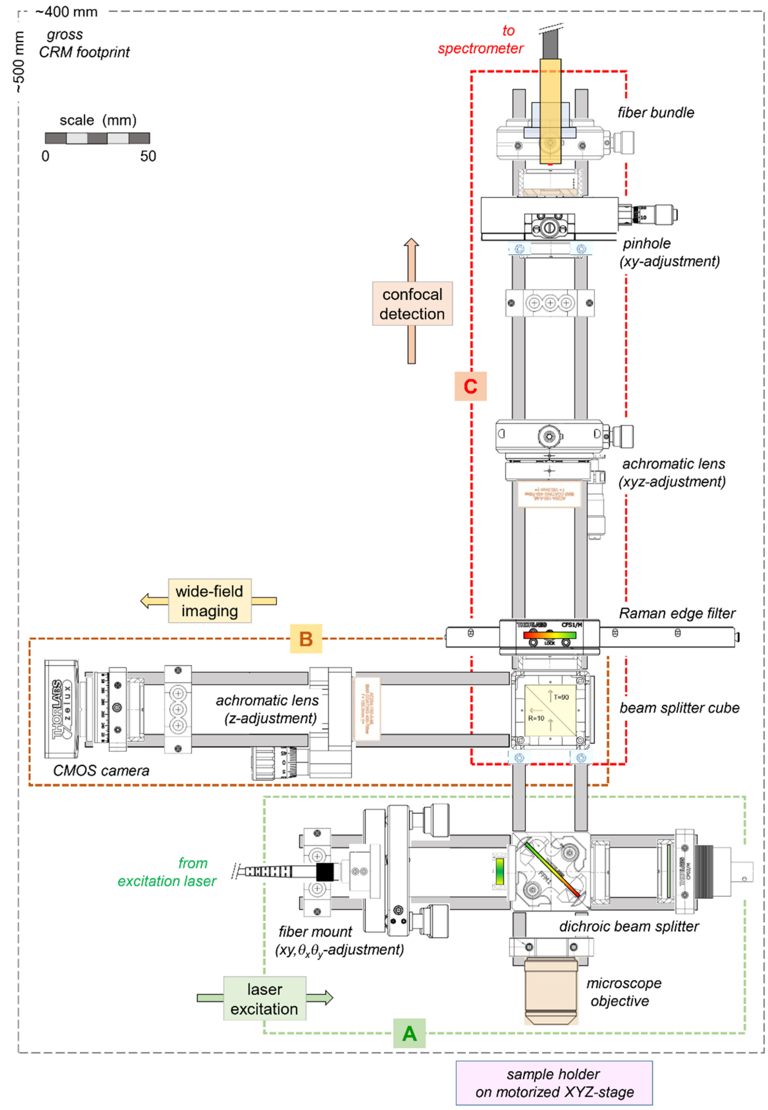

Figure 3.10.: Technical drawing of the confocal Raman microscope. Details on the different segments can be found in the main text. Reprinted from [16].

Segment B The reflected light, that passed the dichroic beam splitter enters a beam splitter cube. The Rayleigh light is redirected to a CMOS camera which is used to position the samples. The Raman light is transmitted into segment C.

Segment C The light from the beam splitter cube still contains Rayleigh light and laser light reflections. They are filtered with a long-pass filter. The remaining Raman light is focused and coupled into an optical fiber which is guided to a spectrometer with a CCD detector. The initial grating with 300 grooves/mm was updated in May 2024 to a high-resolution grating of 1200 grooves/mm resulting in a spectral resolution of $(9.6 \pm 0.7)\,\mathrm{cm}^{-1}$.

For alignment and two dimensional scanning, the sample is mounted on a motorized XYZ-stage. Data acquisition and automated scanning modes are performed with the LabView™ - based analysis software LARAsoft2 [81].

The CRM is utilized as an ex-situ diagnostics tool for the plasma exposed graphene samples (see Chapter 5). In Section 3.3 Raman theory for graphene is described. The 2D/G intensity ratio is used in general to determine the quality of the graphene layer. In this work, the presence of the 2D-peak is in addition used to visualize if the graphene layer was fully removed by the plasma source exposure. Furthermore, the D/G intensity ratio is used as an indicator for the defect density L_D, and the D/D’ intensity ratio is used to distinguish between vacancy-type defects and sp^3-type defects.

3.5. Sheet resistance of graphene

In this work, graphene samples are exposed to the plasma source. To analyze structural changes on the samples, a CRM is utilized (see previous section). The graphene samples are scanned *ex-situ* after the exposure to the plasma.
Structural changes on the graphene are caused by defects. All types of defects change the sheet resistance of graphene. For sp^3 type defects like hydrogenation, the radical (hydrogen atom) bonds covalently to each lattice-carbon [11]. The conduction electron from the π-band is then included in this bond and does not contribute to the electrical conductance anymore. Hence, the sheet resistance of the graphene sample increases. In this work, a second analysis tool (in addition to Raman microscopy) is implemented that enables *in-situ* monitoring of structural changes to the samples. This is the measurement of the sheet resistance of the sample. However, the sheet resistance is not sensitive to the type of defect on its own. Therefore, the sheet resistance measurement is combined with a thermal annealing method that enables the reversibility of the hydrogenation process.

3.5.1. Definition of the sheet resistance

The resistivity of the graphene sample is measured with a four-point technique which is more robust compared to two-point techniques. This is because it uses one channel for the current and a different channel for the voltage measurement, so that contact and lead resistance errors are minimized [93]. A general contacting setup is illustrated

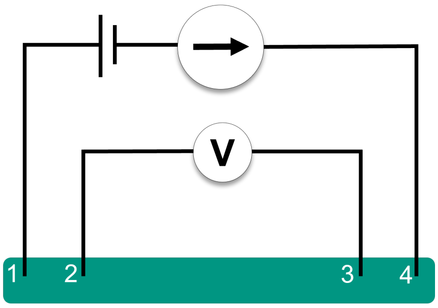

Figure 3.11.: Four-point measurement method of a quadratic material sample. This is an exemplary vertical configuration. A current I is applied from contact 2 to contact 1 and the voltage is measured between contact 3 and 4.

in Figure 3.11. The material dependent resistivity of a three-dimensional conductor ρ is defined as:

$$\rho \equiv R\frac{w \cdot h}{l} \tag{3.17}$$

where, R is the ohmic resistance $R = \frac{V}{I}$, with the measured voltage V and the applied current I. The factors w,h and l are the width, height and length of the material, respectively. In the case of a square film, the width is equal to the length and the sheet resistance becomes equal to the resistance:

$$R = R_{\square} \equiv \frac{\rho}{h} . \tag{3.18}$$

The unit for the sheet resistance is $\Omega/\square$. Thus, it corresponds to the resistance of a square piece of the material.

3.5.2. The Van der Pauw method

To measure the sheet resistance of a graphene sample the *Van der Pauw* method is used [21]. It employs a four-point probe placed in the corners of a sample (see Figure 3.12), in contrast to a standard linear four point probe (see Figure 3.11). Thus, the Van der Pauw method provides an average resistance of the sample, whereas a linear configuration measures the resistance in the sensing direction.

The following conditions must be met, in order to use the measurement as a quantitative method [21]:

1. The four contacts (1,2,3,4) are placed on the circumferences of the sample.
2. The area of contacts of any individual contact is at least an order of magnitude smaller than the area of the sample.

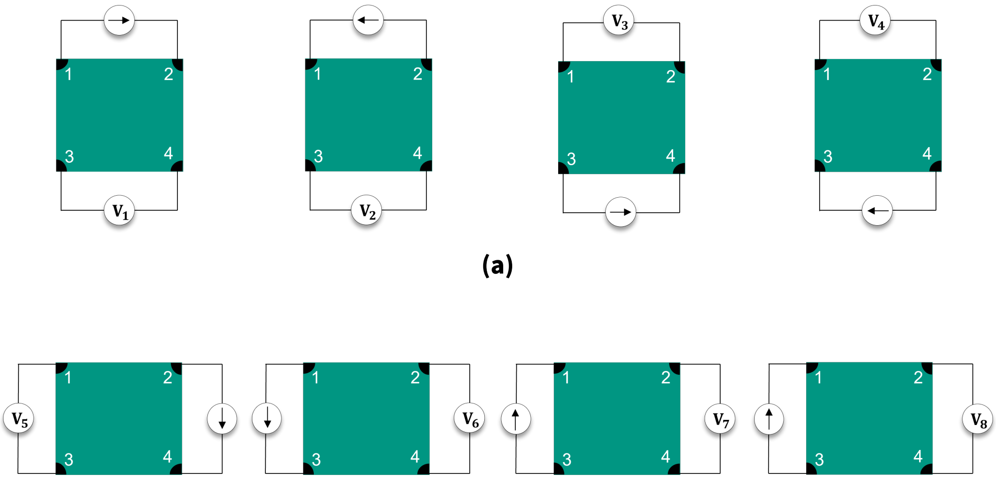

(a)

(b)

Figure 3.12.: Different four point contact configurations for sheet resistance measurements with the Van der Pauw method. **(a)** Configurations for R_{H}. **(b)** Configurations for R_{V}. Image adapted from [94].

3. The sample is homogeneous.
4. The sample does not contain any isolated holes.

If these conditions are not fulfilled perfectly, the measurement method can still be used as a qualitative monitoring tool.
A sheet resistance is determined by combining the different permutations of the four point contacts. The permutations are illustrated in Figure 3.12. The sheet resistance is defined as:

$$R_{\square} = \frac{\pi}{\ln 2} \cdot \frac{R_H + R_V}{2} \cdot f \, . \tag{3.19}$$

where R_{H} is a linear combination of the horizontal four-point measurements (Figure 3.12a)

$$R_{\mathrm{H}} = \frac{R_{12,34} + R_{21,43} + R_{34,12} + R_{43,21}}{2} \, , \tag{3.20}$$

and R_{V} is a linear combination of the vertical four-point measurements (Figure 3.12b)

$$R_{\mathrm{V}} = \frac{R_{13,24} + R_{31,42} + R_{24,13} + R_{31,42}}{2} \, . \tag{3.21}$$

The asymmetry factor f depends on the ratio of R_{H} and R_{V}.

3.5.3. Reversibility of sp^3 defects on graphene

In addition to a sheet resistance measurement of graphene, a thermal annealing setup is required to distinguish between vacancy-type and sp^3-type defects. If a hydrogenated graphene sample is heated, the adsorbed hydrogen atoms desorb but the vacancy-defects remain. Cha et al.[19] demonstrated the reversibility of hydrogen adsorption on graphene samples. They measured the resistivity of a graphene monolayer on a 300 nm SiO_2/Si substrate in-situ with a two-point contacting method. The graphene sample was placed in a distance of 15 cm away from a microwave driven hydrogen plasma source. This study was focused on hydrogenation with the ions H^+, H_2^+ and H_3^+. To filter for them, a quadrupole magnet from a quadrupole mass spectrometer (QMS) was utilized. The resistivity of the graphene sample on the left side of Figure 3.13 increases from 4 kΩ up to 1 MΩ after 600 s of exposure. Subsequently, an electrical current was applied to the graphene sample, which induced Joule heating. The resistivity decreased to 9 kΩ. The hydrogenated graphene was annealed at 300 °C for 3 h.

In this work, one aim is to characterize the beam emitted from a plasma source. The approach is to place graphene samples in front of the source and investigate structural changes via in-situ sheet resistance measurements and ex-situ CRM. Therefore, the

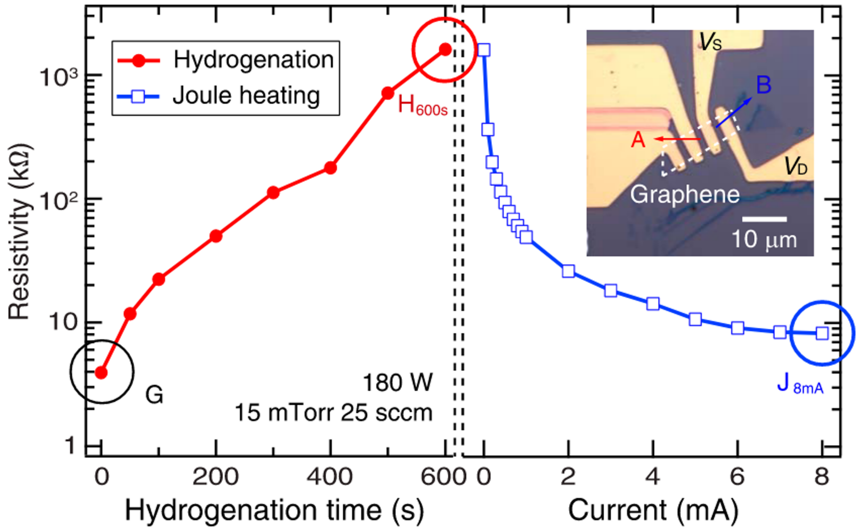

Figure 3.13.: Reversibility of hydrogenation via thermal annealing. *Left*: Relative change in electrical resistivity of graphene measured in-situ after the exposure to hydrogen plasma. *Right*: Subsequent Joule heating. *Inset*: Optical image of the graphene sample. Reprinted from [19]. Copyright © 2021 the Japan Society of Applied Physics.

experimental exposure setup and the contacting setup for the Van-der-Pauw measurements is presented in Chapter 4.

In Chapter 5, results of sheet resistance measurements and CRM scans are presented. The theoretical toolbox given here is necessary to understand these measurements. Furthermore, the discussion in Chapter 5 on hydrogenation results includes the literature that was described here.

4. Commissioning of the experimental setup

Developing and characterizing a source which dissociates molecular tritium is an extensive project. As a first step, different atomic dissociators must be tested with hydrogen. The sources, which are commercially available, are listed in Section 1.4. In this work, a plasma-based dissociator from the company SVT Associates, Inc. (SVTA)[1] is characterized. In Section 4.1 the vacuum system which is needed to operate the plasma source is introduced. In Section 4.2 the components and the operation of the plasma source are explained. In Section 4.3 a study on potential boron contamination of the vacuum system caused by the plasma source is presented.

Samples of monolayer graphene on a SiO_2/Si substrate are placed in front of the orifice of the plasma source. The samples are exposed to the emission from the source. A Confocal Raman microscope (CRM) is used ex-situ to observe structural changes in the graphene. In Section 4.4 a hardware setup to expose the graphene samples to the plasma source is presented. The realization of an electrical contacting method for Van der Pauw measurements is presented. This enables monitoring the sheet resistance of graphene samples in-situ while loading them with the plasma source.

4.1. Vacuum system

To operate a low temperature plasma source, a dedicated vacuum system was built and is described in the following. In Figure 4.1 a photograph and in Figure 4.2 a flow chart of the system is shown. It consists of a CF100 vacuum cross (left part) and a CF100 vacuum double cross (right part). The plasma source is mounted into the left cross and can be supplied with H_2, D_2 and Ar gas from the left. In this work, only H_2 is used. Two flow controllers are connected in series: The flow controller *FIRC RF102* [2] allows coarse

---

[1] © 2025 SVT Associates, Inc. 7620 Executive Drive, Eden Prairie, Minnesota 55344 USA

[2] Brooks Instrument GmbH, Zur Wetterwarte 50, Gebäude 337/B, 01109 Dresden, Germany. `https://cdn.brooksinstrument.com/-/media/brooks/documentation/products/mass-flow-controllers/metal-sealed/gf80/data-sheet-gf80-gf81.pdf?rev=-1&sc_lang=en&hash=bc74d83f25695c0a1bc0c112fc9953d4` (visited on 11/21/2025).

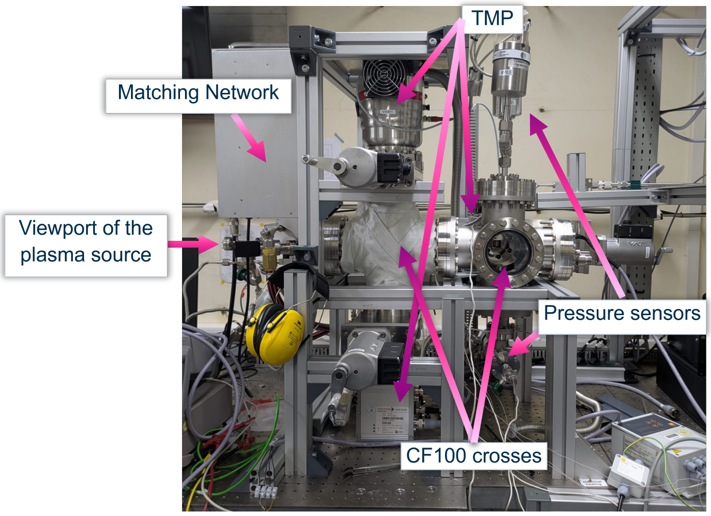

Figure 4.1.: Photo of the dedicated UHV system for the plasma source. The plasma source is mounted from the left in to the left CF100 vacuum cross. The gas comes from the back of the system. There, *RP10* is installed. Furthermore, *RP20* is the lower of the marked pressure sensors. It is mounted on the back side as well.

setting between 20 sccm and 2000 sccm and *FIRC RF100* [3] sets the final flow between 0.01 sccm and 20 sccm. The gas supply line includes a bypass with a scroll pump *VA202* that circumvents the flow controller. Therefore, the supply line can be flushed before starting experiments.

SVTA requires for the operation of the plasma source a vacuum-side pressure of around 10^{-6} to 10^{-5} mbar. To ensure this, three turbo molecular pumps (TMP) *VA100*, *VA300* and *VA301* are attached to the main vacuum system, namely the HiPace 350 from Pfeiffer Vacuum[4]. They are connected in parallel to another TMP that connects to a scroll pump. To ensure safety, any exhaust gas is safely transported to the laboratory exhaust air system.

Various pressure sensors are attached to the system. The sensors that are installed for safety are connected to interlocks such that all gas valves close automatically if a a pressure of > 1 mbar is measured inside the UHV system. In the following only the sensors that are relevant for science measurements are described. For monitoring of the inlet pressure, *RP10* [5] is utilized. It has a measurement range of $10^{-8} - 10^{3}$ mbar. In this

---

[3] © 2025 Alicat Scientific, Inc. `https://documents.alicat.com/specifications/DOC-SPECS-MC-MID.pdf` (visited on 11/21/2025).

[4] Pfeiffer Vacuum GmbH, Berliner Straße 43, 35614 Aßlar, Germany. `https://www.pfeiffer-vacuum.com/global/de/product/hipace-350-450.html`

[5] © 2003 - 2025 Ideal Vacuum. `https://www.idealvac.com/files/manuals/Pfeiffer-PKR-360-Gauge_Manual.pdf` (visited on 11/21/2025).

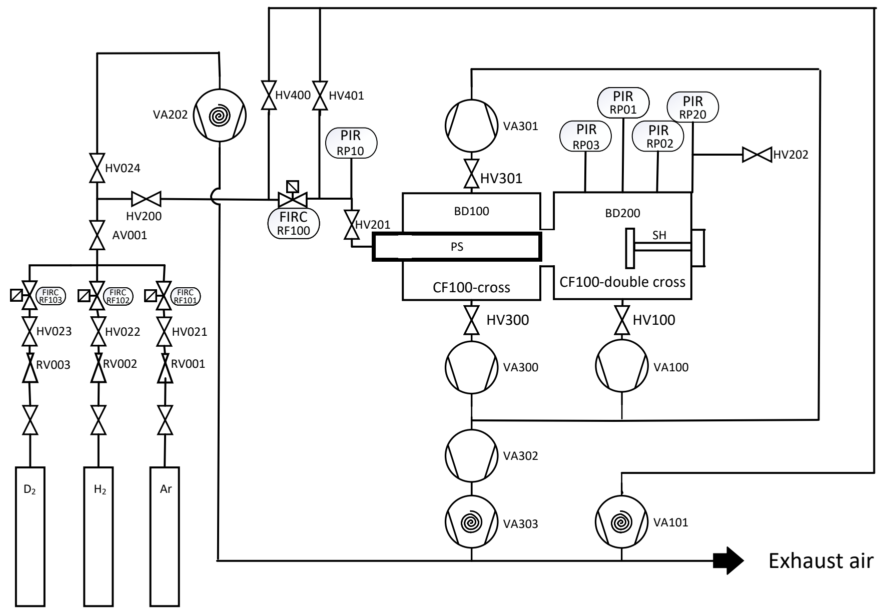

Figure 4.2.: Flow chart of the process design, including gas supply and vacuum system. PS stands for plasma source and SH for sample holder. Two different sample holders are used in this work. One for boron and boron nitride investigations (see Section 4.3) and one for exposing graphene to the plasma source (see Section 4.4).

work, it is assumed that the inlet pressure is equal to the pressure inside the plasma cavity. To monitor UHV conditions, *RP20* [6] is utilized with a measurement range of $10^{-9} - 10^{3}$ mbar. All pressure sensors are monitored and recorded with an autarkic data acquisition system[7]. The background pressure was successfully reduced to 10^{-9} mbar with the pumping setup combined with a bake-out system that allows heating up to 210 °C.

---

[6] `https://www.idealvac.com/files/manuals/PKR-251_Operating_Instructions.pdf` (visited on 11/21/2025).

[7] © 2025 gbm - Gesellschaft für Bildanalyse und Messwerterfassung mbH. `https://www.dydaqlog.de/messtechnik-produkte/dydaqlog` (visited on 11/21/2025).

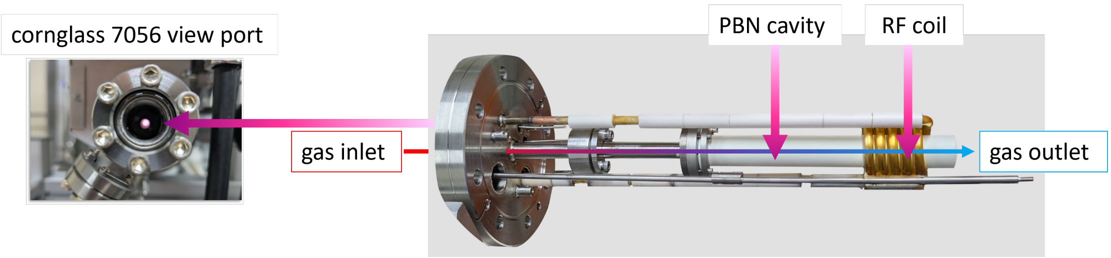

Figure 4.3.: Photo of the ICP plasma source. H_2 gas is transported from the left into a PBN cavity. An AC current with 13.56 MHz is driven in the RF coil to ignite the gas inside the cavity. On the right end of the cavity is an orifice that leads to a beam emitted into the UHV system due to the difference between inlet pressure and UHV pressure. At the back of the plasma source direct line of sight is given through a view port. To this, the optical system for OES is attached.

4.2. Design of the plasma source

SVTA states that the plasma source 'is designed to dissociate diatomic nitrogen, oxygen and hydrogen without producing high energy ions' [8]. Its purpose is to be used in semiconductor industry, more precisely, for cleaning of substrates for thin film deposition.

4.2.1. Components for operation

The plasma source is an ICP-source (see Section 2.2) with RF powers of a maximum of 600 W. The RF-frequency is a widely used standard value of 13.56 MHz [95, 96]. The cavity in which the plasma is ignited consists of pyrolytic boron nitride (PBN). It has a length of 25.4 cm (10.0 ″) and a width of 5.969 cm (2.35 ″). The orifice size of the cavity is 0.46 mm (0.018 ″) which was custom made to optimize for an operation flow of 0.1 sccm. This is important when comparing the different atomic hydrogen sources for KAMATE (see Section 1.4).

In Figure 4.4 the components needed to operate the plasma source are illustrated. A RF generator produces an AC current that is transferred into the RF coil at the plasma source (see Figure 4.3). The plasma transports electromagnetic waves via its high amount of charged particles [58]. A transformer circuit in Figure 2.7 is used to react on and control the plasma response. The *forward power (FP)* can be set at the generator panel. This is the power with which the AC current is driven through the RF coil. The power absorbed by the plasma is the *load power (LP)*. Optimally, the plasma can absorb

---

[8] `https://www.svta.com/uploads/documents/RF_4.5.pdf` (visited on 11/21/2025).

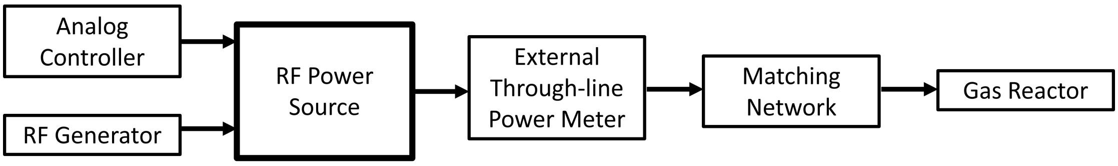

Figure 4.4.: Schematic of components for plasma source operation. The gas reactor is the area where the plasma is running. The RF coil is directly connected the matching network which is connected to the RF power source via RF power cables. The power source is controller with an RF generator and an analog controller. Figure adapted from SVTA manual [97].

all the power. However, this is usually not the case. Especially after igniting the plasma, it needs time to stabilize and thermalize with the cavity walls. Hence, the power which is not absorbed is reflected back into the coil and strains the power supply. This is called *reflected power (RP).*

The following analogy is used in order to illustrate the system: Assume a resonant circuit, consisting of a capacitor and a wire connecting both plates of the capacitor. The circuit is operated with an AC current. If the capacitor can follow the frequency of the AC current by charging and discharging with the same frequency, the impedance is 0. If the oscillation is too fast, the capacitor can not follow, which results in an impedance of $\neq 0$. The capacitor induces a current which points in the opposite direction of the AC current. The same happens with the plasma source, where the capacitor represents the coil with the plasma. The strength of the wave induced by the plasma is the RP.
FP, LP, and RP are related as follows

$$\mathrm{LP} = \mathrm{FP} - \mathrm{RP}\,. \tag{4.1}$$

To avoid serious damage to the electronics, a matching network is implemented between the power source and the RF coil (Figure 4.4). This network adjusts internal impedances to minimize RP and maximize LP.
SVTA includes an analog controller that enables customized control options. In this work, the controller has a vacuum interlock, a water cooling interlock, a shutter, and a connection to the computer including a labview software which allows to control all source parameters through the PC. Furthermore, the software includes plasma monitoring if an optical spectrometer is connected.

4.2.2. Optical system for OES

The plasma source is designed so that there is a direct line of sight to the plasma in the direction of the gas inlet (see Figure 4.3). SVTA provides an optical system to monitor the plasma. It includes a lens with a holder to attach to the view port, an optical

SMA-SMA fiber [9] from Thorlabs and a CCD spectrometer [10] from Thorlabs covering a wavelength range of 200 − 1000 nm with a 2 nm uncertainty (see Figure 6.1).

The SVTA software displays the spectra measured with the CCD spectrometer. Furthermore, integration limits can be set, so that two integral values are plotted and saved over time. In Section 2.3.2 a detailed explanation of the hydrogen plasma spectrum is given.

4.3. Boron and Boron Nitride deposition on glass

The purpose of this research is to investigate potential boron (B) or boron nitride (BN) emission from the plasma source. Figure 4.3 shows an image of the source. The white cylinder of the source, which is surrounded by the water-cooled radio frequency (RF) coil, is the cavity in which the plasma is ignited. More precisely, only in the range of the coil is plasma burning. The cavity material was chosen to be tritium-plasma compatible: First of all, it needs to be nonmagnetic to let magnetic fields, induced by the RF coil, pass through freely. The cavity encapsulates the plasma and is in direct communication with it. Therefore, the material needs to be chemically inert. Physical robustness is also important because the plasma can consist of species with high dynamics, which means that a low sputter rate is required. Furthermore, the material should preferably have high purity in order to have predictable plasma properties. The manufacturer provides three different materials for the cavity: pyrolytic boron nitride (PBN), aluminia (Al_2O_3) and quartz (SiO_2). Materials containing oxygen were avoided because the plasma could release oxygen leading to the formation of tritiated water, i.e., T_2O or HTO. This substance is highly reactive and has much higher permeation through various materials which is extensively described in Reference [98]. Furthermore, as described in Section 1.4, past efforts in atomic tritium research observed losses in the dissociation fraction within hours when using cavity materials like quartz or Pyrex. Thus, PBN is chosen for the cavity material.

4.3.1. Motivation for the study

There are two main reasons for the possibility of contamination. Firstly, according to the source manufacturer, the cavity is built in layers so that it flakes off from time to

---

[9] © 1999-2025 Thorlabs, Inc. `https://www.thorlabs.de/thorproduct.cfm?partnumber=M14L01` (visited on 11/20/2025).

[10] `https://www.thorlabs.de/newgrouppage9.cfm?objectgroup_id=3482&pn=CAL-CCS2` (visited on 11/20/2025).

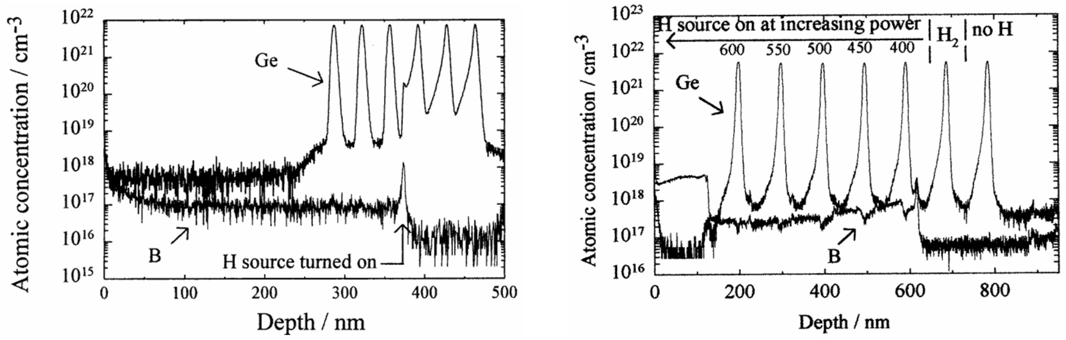

(a) **(b)**

Figure 4.5.: SIMS depth profile of SiGe sample with an H plasma as a surfactant. **(a)** Running H plasma for 30 minutes inbetween layer three and four and letting plasma run for layer four to six with a constant driving power of 600 W. **(b)** First layer without hydrogen. Second layer with molecular hydrogen. Hydrogen plasma was ignited in a ten minute growth interrupt kept running for the remaining layers with driving powers from 400 to 600 W in 50 W steps. Reprinted from [10] with permission from © IOP Publishing Limited 2024.

time to produce a self-cleaning effect. The BN-flakes should remain inside the cavity. This needs to be verified before it is used in a more delicate setup.
Second, A.D. Lambert et al. observed B-contamination in their samples ([10]). Therein, silicon germanium molecular beam epitaxy (SiGe MBE) is performed. From a solid source MBE system, Ge is grown on a silicon substrate in a thin layer-wise manner. According to the paper, with this setup, the surface roughness appears to be high as a result of a mismatch of the isostructural lattices of Si and SiGe. Therefore, a surfactant species, here atomic hydrogen, is used during growth to reduce the roughness between the growth processes. This paper specifically focuses on the electrical quality and contamination of epilayers deposited by this technique.

For hydrogen cleaning, a commercial plasma source was used, with the exact type and model number unknown, to produce atomic hydrogen.[11] This source was also an ICP source with a driving radio frequency of 13.56 MHz and, most importantly, a PBN cavity. It is not specifically mentioned whether the plasma is in E- or in H-mode (see Section 2.2.3.
To analyze their samples, Lambert et al. used secondary ion mass spectrometry (SIMS) to resolve different mass species for different depths and electrochemical capacitance-

---

[11] While explaining the difference between thermal cracking sources and inductively coupled plasma (ICP) sources, the paper states: „Both types of source have been widely reported in the literature ... In this study we choose the latter [plasma source] because of its smaller thermal loading on the growth system and less risk of **metallic impurity contamination**“. Knowing this, it would be reasonable to investigate thermal source used in the atomic tritium research as well in the scope of metallic contamination.

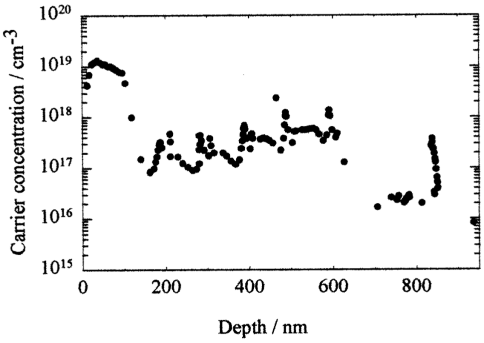

Figure 4.6.: Electrochemical capacitance-voltage (eCV) depth profiles showing carrier distribution of SiGe sample. It is the same sample as in Figure 4.5b. Reprinted from [10] with permission from © IOP Publishing Limited 2024.

voltage (eCV) depth profiling to investigate charge carrier concentrations. Figure 4.5a shows a SIMS depth profile. There, the growth was interrupted after three layers and the H plasma was ignited for 30 minutes. After that, the remaining Ge structures were grown with plasma burning. The maximum driving power of 600 W has been applied. This plot shows clear evidence for B-contamination. Interestingly, there is a B-peak at the position where the H source was turned on, which could lead one to assume that the ignition process has some special effect on the B-emission.

In Figure 4.5b a SIMS depth profile with different source powers is shown to investigate whether an increase in H flux leads to increases in B-contamination. Again, a clear B-contamination is observable. However, an increase in power shows a decrease in B-contamination. To explain this, the paper supposes a self-cleaning effect, which is achieved at higher RF powers, so that the hydrogen atoms clean the B-contaminated surface. In Figure 4.6 an eCV measurement of the same sample as in Figure 4.5b is presented. Therefore, the same structure is visible. The carrier concentration is in the range of 10^{16} to 10^{19} cm^{-3}. Such an amount of B could influence the resistivity of hydrogenated graphene.

Lambert et al. assumed that B-contamination could be caused by diborane, B_2H_6, created inside the cavity, as the discharge reacts with the walls of the cavity.

Due to the fact that the long-term goal is to measure dissociation fractions with a quadrupole mass spectrometer (QMS) it is inevitable to investigate B or BN emission from the plasma source because the most QMS require pressures in the range of 10^{-6} to 10^{-5} mbar. Moreover, B could be a background for the hydrogenation of graphene (see Section 4.4). If a significant amount of B is deposited on the graphene sample, the resistivity is expected to decrease, because B is a metal.

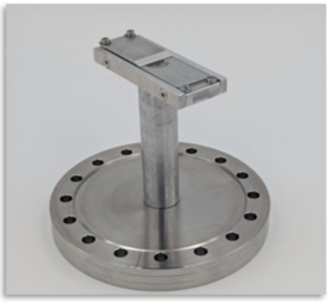

Figure 4.7.: Component that holds a glass slide. It includes a piece of aluminum that covers half of the glass slide. In principle other materials than glass can be mounted in this holder. The construction was made such that the holder can be mounted in any orientation without the possibility of dropping the glass slide. The holder is attached to a CF100 flange.

4.3.2. Experimental setup

To test B-/BN-emission, a microscopy glass plate is mounted in front of the orifice of the plasma source. In Figure 4.7 a tailored holder for this purpose is shown.[12] It consists of aluminum and holds the glass slide. Holder and glass slide are placed at the position of *SH* facing the outlet of the plasma source (see Figure 4.2). The distance between the glass sample and the plasma source orifice is approximately 15 cm. This distance is sufficient for the beam to hit the glass plate because a beam profile is observed on graphene samples that were placed in a similar distance (see Chapter 5).

Table 4.1.: Overview of the investigation process. Three glass slides have been loaded with different loading parameters, which are: loading cycle, loading time per cycle t, hydrogen gas flow Φ, plasma driving power P_{RF}, microscopy tool (MT) before and after exposing the glass slide to the plasma source, and if the optical system (OS) (see Section 4.2.2) was moved between the loading cycles. The star behind DLM indicates that a cross-polarized configuration was used (see main text).

slide	cycle	t in h	Φ in sccm	P_{RF} in W	MT before	MT after	OS moved?
1	1	23	0.5	350	none	DLM*	yes
2	1	21	0.5	350	SEM	SEM	yes
	2	67	1	450	SEM	SEM	no
	3	16	0.5	350	SEM	SEM	yes
3	1	21	0.5	350	WLI	WLI	yes

---

[12] Many thanks to T. Weber who designed, constructed and built this holder.

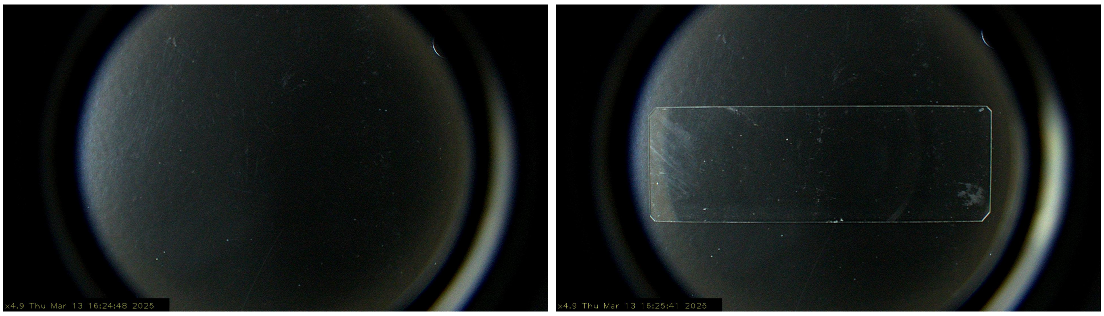

(a) **(b)**

Figure 4.8.: Images taken with the DLM with a black background and no cross polarization. **(a)** no glass slide, just the black background and **(b)** black background with glass slide.

4.3.3. Measurements and results

Because glass is transparent, a digital light microscope (DLM)[13] is used as a first level ex-situ measurement method. For higher resolution scans, a scanning electron microscope (SEM)[14] and a white light interferometer (WLI [99]) are utilized.
In addition, half of the glass slide is covered with a metal piece during loading to produce distinction with respect to the loading area. In principle, only one side is exposed and the other not. Hence, a clear difference between left and right is expected if a significant amount of B is deposited. However, the metal piece does not have a very fine and sharp edge and, therefore, the strict edge could be smeared out. To reduce uncertainties, the glass slide is scanned before and after the loading cycle.
Table 4.1 contains an overview of the different glass slides loaded, the loading time, the plasma source parameters and the microscope used for ex-situ scans.

4.3.3.1. Digital light microscope (DLM)

The DLM used in this work is the OMNI 3 from Ashvision. Because the plasma source is in a horizontal orientation, it is not expected that BN flakes will emit from it, but the scenario with B-emission similar to the Lambert case [10] is plausible. The typical resolution of such microscopes is in the 10 μm range. If nothing is visible, one can artificially increase the resolution by implementing a cross-polarized configuration

---

[13] ASH United Kingdom, Covert Farm, Long Lane, East Haddon, Northamptonshire, NN6 8DU, United Kingdom. `https://www.ashvision.com/omni-3/` (visited on 11/20/2025).

[14] © 2025 S3 Alliance. `https://s3-alliance.com/de/products/cube-2-desktop-rem/` (visited on 11/20/2025.)

using two Thorlabs linear polarizers[15]. Figure 4.9a shows a schematic of the setup. With this, a light polarization difference (birefringence imaging-like) effect could be observed if the deposited layers have a thickness of visible light (nm) or thicker. This birefringence-like effect would depend on the difference between the refractive index of the glass slide (SiO_2) and what else is deposited on it. There are literature values available for refractive indices, which can be used as an orientation:

- $n_{\mathrm{SiO_2}} = 1.46$ from [100]
- $n_{\mathrm{BN}} = 1.65 - 1.67$ from [101]
- $n_{\mathrm{B}} = 3.00 - 3.35$ from [102]

The refractive indices of BN and glass do not differ too much, therefore, it is expected that thin BN layers are observed barely or not at all. However, the refractive index of B is more than twice that of glass. This is the more interesting case for the specific geometry of the system. If there is nothing visible with the DLM one can eventually conclude that there are only few monolayers of B or not even complete layers but possibly rather small islands or single atoms.

In Figure 4.8 the first images taken with the DLM are shown. Due to technical problems, the glass slide was placed on a black plate instead of shining through the glass with a light source. There are a few marks and dots visible on the glass (Figure 4.8b), especially in the bottom right and top left corner. At first glance, it appears to be more like traces resulting from the cleaning procedure that was performed before inserting the glass slide into the vacuum system. Another evidence that these marks are background is that there is no difference between left and right on the slide, which should be the case because one side was covered during the loading process. Figure 4.9b shows an image taken with the DLM in a cross-polarized configuration. All structures in Figure 4.8b disappear, which means that they must be in the nm-range, or their refractive index does not differ much from $n_{\mathrm{SiO_2}}$, which could be the case for BN.
With the observations from Figure 4.8b, an upper bound of about 10 μm can be set for the thickness of the deposited layers of B and BN. Using a cross-polarization setup (see Figure 4.9b), this can be further constrained to layer thicknesses below 200 nm (visible light) for B. Because the difference between the refractive indices of glass and BN is rather small, the exclusion does not apply to BN.

---

[15] `https://www.thorlabs.com/thorproduct.cfm?partnumber=FMP1/M#ad-image-0` (visited on 11/20/2025).

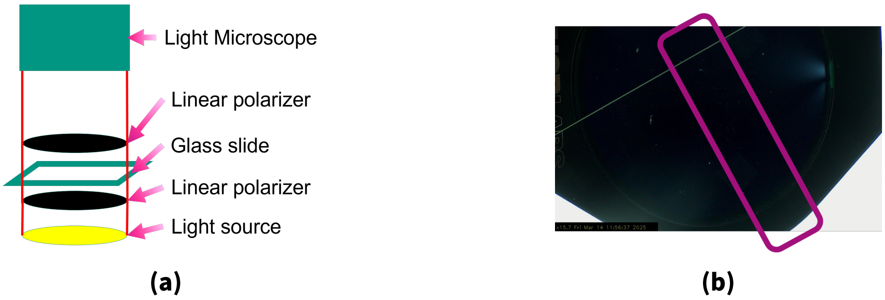

Figure 4.9.: **(a)** A schematic of the cross-polarized measurement setup with the DLM. To achieve cross polarization, the linear polarizers have a 90 deg orientation difference. **(b)** Image from DLM of glass silde. The violet box marks the area where an edge should be visible, meaning the left side was covered and the right was loaded. The slightly bright spot in the top right is due to the screw from the linear polarizer applying mechanical stress to it.

4.3.3.2. Scanning electron microscopy (SEM)

For resolving potential deposits of B with finer detail and higher magnification than optical microscopy, Scanning Electron Microscopy (SEM) is employed.[16] SEM is a powerful surface characterization technique that provides high-resolution topographical and compositional information about a sample by irradiating it with a focused beam of electrons. If carefully applied, this method is non-destructive. Because the amount of detail is more fine, it is possible to identify types of impurities and contamination (though, expecting primarily B impurities). It is also valuable to have general images of all depositions on the glass surface, since this would give contaminant data on the sample. It is also feasible, with fine-detail images, to identify and minimize sources during handling and transport.

The fundamental operational principle involves generating an electron beam, typically from a pre-aligned Tungsten filament via thermionic emission within an electron gun (as with the EmCrafts CUBE 2 that is used in this work). These electrons are then accelerated by a high voltage, adjustable in the CUBE 2 from 1 kV to 30 kV, through an evacuated electron column. Within this column, a series of electromagnetic lenses (condenser and objective lenses) and apertures focus and demagnify the electrons into a fine probe beam. This probe is then (point-by-point) raster-scanned across the sample surface by scan coils, for topographically scanned signal acquisition. When the primary electron beam interacts with the atoms of the sample, various signals are emitted. The key among these are secondary electrons (SEs), which are low-energy electrons (typically < 50 eV) ejected from the very near-surface region (top few nanometers) of

---

[16] Many thanks to P. Winney for performing all the SEM-scans.

the sample due to inelastic scattering. The yield of SEs is highly sensitive to surface topography, making them ideal for generating detailed morphological images. Another important signal comes from back scattered electrons (BSEs), which are primary beam electrons that are elastically scattered from deeper within the sample.

The EmCrafts CUBE 2 is a high-vacuum SEM featuring a motorized stage, capable of achieving a resolution down to 5.0 nm (at 30 kV, SE Image) and magnifications ranging from $\times 10$ to $\times 200,000$. The EmCrafts CUBE 2 utilizes an ET (Everhart-Thornley)-style detector for collecting these SEs, producing secondary electron images (SEI). It can also be equipped with a BSE detector, which is particularly useful in its optional low-vacuum mode for imaging non-conductive samples. The intensity of the BSE signal is strongly correlated with the atomic number (Z) of the elements in the scanned region, with higher Z elements appearing brighter; this Z-contrast is invaluable for differentiating between phases or identifying heavier elemental contaminants.
Critically for elemental analysis, the EmCrafts CUBE 2 also supports Energy Dispersive X-ray Spectroscopy (EDS or EDX). This mode relies on the detection of characteristic X-rays, which are emitted when the incident electron beam causes inner-shell electron ejections in the sample atoms and higher-energy electrons subsequently fill these vacancies. By measuring the energy and intensity of these emitted X-rays, EDS allows for both qualitative identification and, with appropriate calibration, quantitative determination of the elemental composition of the scanned area. Thus, it is possible to investigate different species in two ways.

The Figures in A.1.1 show the line scans performed with the SEM on glass slide 2 (table 4.1) in x-ray mode. This sample is loaded for about 104 h in total with two interrupts during loading. This is done to increase potential B-emission because this was observed in the studies by Lambert et al. (see Figure 4.5a) where the B-concentration peaks around a depth of 380 nm where the plasma source was turned on.
For the electron energies $E_\mathrm{e} = 1\,\mathrm{keV}$ and 5 keV there is a scan before and after the loading, respectively. Each scan shows an image of the scanned area, a line scan of oxygen (O) (as a sanity check), and a line scan of B, which is then fitted with a linear regression to investigate any B deposition differences along the line. The uncertainty $\sigma_{a,b}$ of the linear fit parameters a and b yields from the inversion of the approximated hessian matrix (see Equation (5.19)). In addition, there are scans of the loaded slide for $E_\mathrm{e} = 300\,\mathrm{eV}$ and 30 keV.

After loading the slide, a scratch is added along the edge of the covering plate to have a spatial orientation where the difference in B-contamination would be expected between the left and right sides of the scratch. Furthermore, the scratching should in principle remove all deposition layers, meaning that a dip in the signal is expected at the scratch. The two scans of the unloaded slide are performed in a nonmarked center area of the

slide. Because the loaded slide has a scratch on it, it is possible to compare the loaded scan slides in a spatial manner. However, it is not directly possible to compare the loaded and unloaded scans in a very detailed way, because the scans are performed at slightly different positions. Hence, they rather give an estimate for the magnitudes and, again, narrow down the upper bound for any boron deposition.
Before discussing the results, it is important to mention some interesting observations for the plots in Appendix A.1.1: The O-scan in the line scan for 1 keV shows a dip at the position of the scratch (Figure A.2b). Therefore, the O-signal from the scratch is used to determine the optimal electron energy. When the energies are further increased, the electrons may travel deeper into the material and this may not be the region of interest anymore where B could be deposited. Subsequently, an increase in energy means an increase in noise, as is observed in the scans from 1 keV to 5 keV. However, when looking at the 30 keV scan, the counts decrease by a factor of 10 compared to the 5 keV scan. This is perhaps due to the energy that is so high that all electrons pass through the glass slide completely. Because behind the glass slide there is nothing but a thin holding structure, the noise could be reduced and the noise level of low electron energies could approach. This would suit the data when comparing the 300 eV and the 30 keV scan.

Table 4.2 shows no tendency for the linear regression to have an increase in slope after the loading procedure. The narrow 1 σ-band show the high statistics of the data. Because the slope is for all scans below $3 \times 10^{-3}\,\mu\text{m}^{-1}$, the fitting constant b can be assumed roughly to be a reference point for an average value of boron counts. With this precondition, the 1 keV scans can be compared and an increase from 1 count to 9.9 counts is visible. However, this lies within the possible fluctuations since the min-max intervals of both scans overlap, and again, the scans are performed on different positions of the glass slide. The 5 keV scan even shows a decrease in b after loading.

Another indication that the boron signal is just noise is the constant fluctuation compared to some oxygen scans: Figures A.2b, A.3b and A.4 show a clear spatial dependence of the amount of oxygen that represents the inhomogeneity of the glass slide. The boron does not show any spatial dependence for any scan, which is notable because the scan distances are between 250 μm and 12 mm.

From these results, it is reasonable to conclude that no significant increase in boron deposition is visible after loading with the plasma source for 104 h on it. The upper limit can be set to 10 nm as this is double the resolution of the SEM due to the manual.

Table 4.2.: Overview of SEM line scan results. E_e is the electron energy, a and b are the parameters of the linear regression of the form $y = a\,x + b$ which was performed on the boron data.

E_e (keV)	a $\times 10^{-3}$	σ_a $\times 10^{-3}$	b	σ_b	max cts	min cts	loaded? (y/n)
0.3	−0.004	0.0036	0.103	0.026	2	0	y
1.0	−0.16	0.12	1.06	0.088	6	0	n
1.0	−0.24	0.16	9.88	0.27	20	4	y
5.0	−2.6	3	18.1	0.003	28	8	n
5.0	0.6	0.2	11.4	0.29	20	3	y
30.0	0.1	0.07	1.77	0.14	8	0	y

4.3.3.3. White light interferometry (WLI)

Interferometry is another method that can be used to obtain detail on the nanoscale order.[17] WLI differs slightly from normal (laser) interferometry using a source made of a broad spectrum of visible-wavelength light. The basic operational principle is identical to a traditional interferometry setup, using a source, beam splitter (to divide the light into reference and measurement paths), mirror, and read-out sensor to capture the resulting interference pattern. This approach inherently avoids the phase ambiguity issues common in monochromatic interferometry, which typically limits unambiguous step height measurements to within $\pm\lambda/4$. Consequently, WLI allows for the measurement of significantly larger step heights and rougher surfaces over a wider wavelength range. As the objective lens (containing the interferometric components) is scanned vertically (along the z-axis) relative to the sample surface, interference fringes are generated for each point on the surface when the optical path difference (OPD) between the light reflected from the sample and the light from the reference mirror is within the coherence length of the broadband source. The position of maximum fringe contrast is often referred to as the zero-order fringe, or coherence peak. After processing the OPD broadband interferogram, allowing for a larger measurement range (compared to single-wavelength interferometry which is limited to half-wavelength ranges), which in-turn allows rough surface measurements and topographical step heights.

The measurements are conducted using a Keyence VK-X3000 Series 3D Surface Profiler, specifically configured with the WLI module (VK-H3I) and a corresponding specialized interference objective lens, as stipulated by the manufacturer for WLI operation [99]. The VK-X3000 system identifies the coherence peak for each pixel in the field of view to construct a 3D topographical map of the surface. The Keyence system further offers settings such as averaged measurements, which can enhance the ability to measure steep slopes and lower height uncertainty, particularly in environments with some

---

[17] Many thanks to A. Schwenk, M. Sagawe and J. Schneider for performing all the WLI-scans.

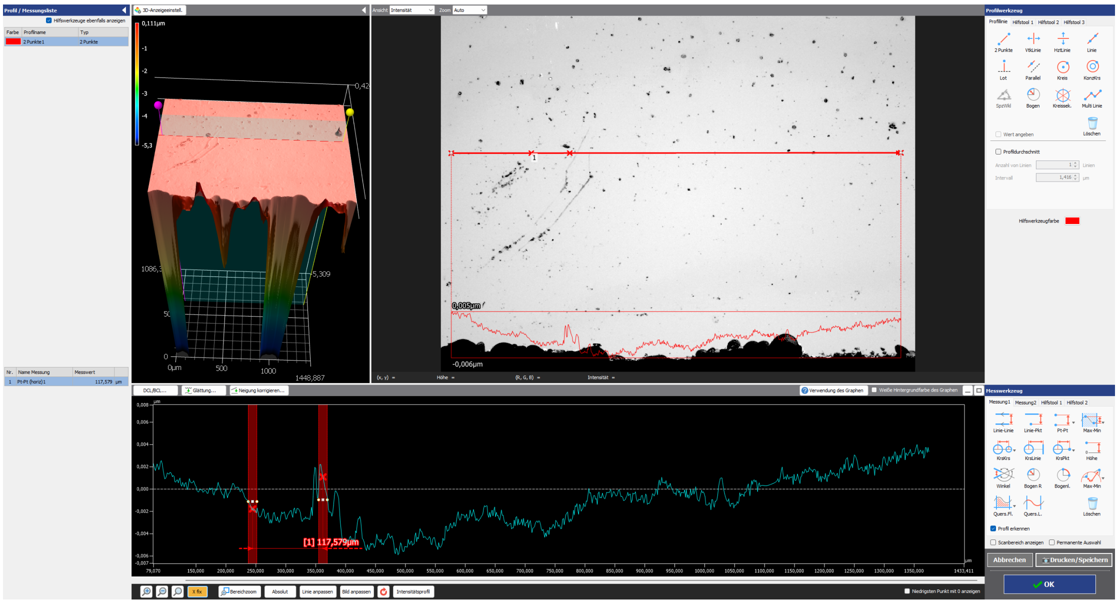

Figure 4.10.: Height profile of the edge of the glass slide after loading with minimal height-cutting-limit and maximal x-axis zoom.

ambient vibrations [99]. The achievable vertical resolution can extend to the nanometer or even sub-nanometer scale, contingent on the system's noise floor and the algorithm's precision in peak detection, while the lateral resolution is primarily diffraction-limited by the objective's numerical aperture and the mean wavelength of the light used.

Appendix A.1.2 shows the profile scans performed with the WLI on glass slide 3 (Table 4.1). The coordinate system is defined in the left image in Figure 4.10. The horizontal axis corresponds to x, the vertical axis to y and the remaining to z.
This sample was loaded for 21 h, but this time the slide was scratched even before loading. However, this time the scratch was very subtle, so it is barely seen on the scans. Nevertheless, it is still visible with the eye as the red boxes indicate in Figure A.7. The scratch was again placed at the position where the glass slide was covered on the right side of the scratch, and the left side was exposed to the plasma source.
Table 4.3 summarizes the maximal peak heights of the different scans. They are in the range of 10^3 nm, which means that looking for a step at 10 nm level or below required some data processing, more precisely, a height-cutting filter. In principle, the maximum resolution of the device used is 0.01 nm due to the manufacturer [99]. Figure 4.10 shows an optical image of the lower edge of the glass slide. The black structures on the bottom correspond to damage at the edge. That is why they appear on the left 3D profile image as large holes. The profile height image was filtered with the smallest possible height-cutting limit to eliminate the large peaks that are noise, as one can see in the unloaded scans as well. Furthermore, a quantified profile scan is displayed along the

Table 4.3.: Overview of the results of the WLI scans (Appendix A.1.2). The maximum peak of the scans is noted.

position	maximum for loaded (μm)	maximum for not loaded (μm)
edge	0.68	2.45
uncovered side	0.73	0.83
covered side	1.05	1.04

blue line. The profile can be seen in the lower plot. The blue line does not show any fluctuations in the profile within at least 10 nm, not to mention any expected steps between the covered and exposed side of the glass slide. This step is expected in the marked interval.

In conclusion, the WLI scans confirm the measurements with the SEM and set a similar conservative upper limit for the boron deposition of approximately (10 ± 0.01)nm.[18] When comparing the scans of the edge region before and after the loading process (Figures A.10 and A.11), there is a slight decrease in height and number of large peaks, which could mean that the plasma source cleans primarily cleans the surfaces rather than depositing something on them.

4.3.4. Summary and Outlook

Three glass samples where loaded for different time periods and where analyzed with different devices. The analysis of all three devices show the same result: *No significant boron deposition is detectable on the glass slide.* Table 4.4 provides a summary of the upper limits obtained for the deposition of the thickness of boron layers on the glass. The results show an upper limit of about 10 nm. The reason for this could be either that no boron (or only undetectable traces) are emitted from the plasma source or that the boron does not stick on the glass slide. A combination of both seems reasonable, meaning that not enough boron is emitted from the source for it to form big structures on the glass.

It is concluded that boron contamination is not a show stopper for using beam analysis devices such as the hydrogenation of graphene and quadrupole mass spectrometers within the specific setup. In this context, it is important to mention the specific geometry. In this work, the plasma source is operated in a horizontal orientation. If there is a setup in which the source would be in a vertical position, it is advised to repeat some of the measurements to exclude any geometric dependencies on the operation of the

---

[18] this, being the resolution of the WLI due to the manufacturer.

Table 4.4.: Overview of the upper limits of B-/BN-layer thickness deposited on glass slides that were exposed to the plasma source, measured with the different analysis tools.

analysis tool	upper limit in nm
DLM	200
SEM	10
WLI	(10 ± 0.01)

source, although the manufacturer of the source claims that it can be operated in both orientations.

BN flakes have been found on the gas inlet part of the experimental setup. If the source is operated in a vertical orientation these flakes could fall through the orifice into the main vacuum. In this case, it would already be sufficient to have a look with the DLM on a glass slide.
For the hydrogenation of graphene, the background of boron contamination is expected to be rather small. To ensure what the effect would be on this, one needs to do literature research on the debonding temperature of boron on graphene. Nevertheless, the upper limit on the boron deposition can be added as a constantly increasing impurity background. Although this may be too conservative, because the hydrogen beam has a cleaning effect on the boron deposition, as Lambert et al. showed in Figure 4.5b.
With the specific QMS[19] that will be installed, it is possible to observe masses up to 50 u, which means that boron (mass 5) and N_2 (mass 14) can be investigated. Furthermore, Lambert et al. speculated that diborane, B_2H_6 (mass 16), is created inside the cavity or even B_2O_3 (mass 34) if oxygen remains somewhere. This could also be observed with the QMS.

4.4. Experimental setup to expose graphene samples to the plasma source

The study about B and BN emission from the plasma source does not show any significant contamination in the vacuum setup. As a next step, the beam emitted from the plasma source is investigated by placing graphene samples in front of its orifice. In this section, the experimental setup is presented. Furthermore, two diagnostic tools are utilized to observe structural changes on the graphene.

---

[19] © 2016 Extrel CMS, LLC. `https://extrel.com/wp-content/uploads/2020/12/High-Resolution-App-Note-RAH103A.pdf` (visited on 11/20/2025).

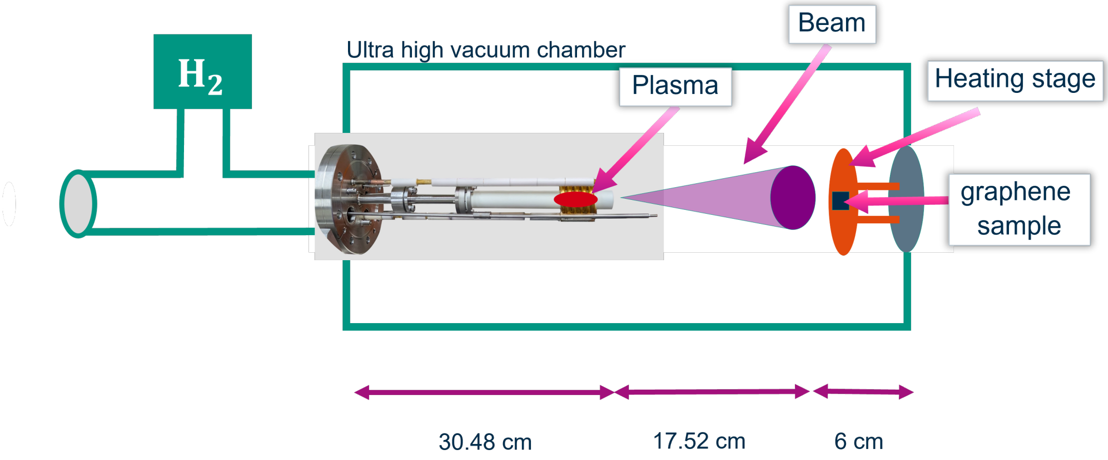

Figure 4.11.: Illustration of the experimental setup to load graphene samples with the plasma source. The gray circle on the left side of the illustration indicates the optical viewport.

Ex-situ: After the graphene samples have been exposed to the plasma source, they are placed in a CRM. Details about the CRM are given in Section 3.4. The D-, D'-, 2D- and G-peak from the Raman spectra give information about the defect density L_D and the type of defects. A detailed explanation is given in Section 3.3. Results are shown in Chapter 5.

In-situ: The sheet resistance of the graphene samples is measured in-situ during exposure to the plasma source. In this section, a contacting setup for this measurement is presented. The increase in sheet resistance can be caused by different types of defects. To distinguish between the type of defects, thermal annealing can be used. A detailed explanation is given in Section 3.5. Therefore, the graphene samples are mounted on a heating stage. The new contacting method has to be tested for robustness and reproducibility when heating the stage up to 300 °C. The results are shown in Chapter 5.

4.4.1. Exposure setup

The geometrical setup for exposing graphene samples to the plasma source in a UHV system is illustrated in Figure 4.11. The samples are placed inside the UHV system in a distance of 17.52 cm to the orifice of the plasma source.
In this work, 1 cm × 1 cm graphene chips from *Graphenea*[20] are used. The chips consist

---

[20] Graphenea, Inc. 1 Broadway Cambridge, MA 02142 USA. `https://www.graphenea.com/collections/buy-graphene-films/products/monolayer-graphene-on-sio-si-90-nm` (visited on 11/20/2025).

of a monolayer graphene on a 90 nm SiO_2/Si substrate. The graphene chips are glued with a PBN-paste[21] to a custom holder. The holder is attached to a sample heater[22] (see Figure 4.12a). The material of the holder is copper because it has a larger thermal conductivity ($\kappa = 413\,\frac{\mathrm{W}}{\mathrm{m\,K}}$) than aluminum ($237\,\frac{\mathrm{W}}{\mathrm{m\,K}}$) or steel ($\leq 66\,\frac{\mathrm{W}}{\mathrm{m\,K}}$) [103].

4.4.2. Setup for in-situ sheet resistance measurements

In the following a novel contacting setup is presented that enables in-situ sheet resistance measurements with the Van-der-Pauw method. Because the whole setup is heated to 300 °C, all components have to be high temperature compatible.

Contacting setup The four-point contacting is performed with four stainless steel M3 washers that are placed at the corners of the graphene chip. To isolate the washers from the copper holder, PBN slides are placed and glued with PBN-paste in-between. The washers are tightened with PBN screws. The contacting has to be performed with utmost caution because the graphene monolayer is very sensitive to forces in in-plane direction. When the washers are pinned down, a slight turn can already destroy the graphene. To reduce this risk, multiple crinkled washers made of beryllium copper are placed between the head of the screw and the contacting washers. Thus, the spring-like design decouples the turning of the screw from the washer. The setup in Figure 4.12c is the result of multiple iterations.[23] A Kapton-coated wire[24] that is suited for temperatures of up to 350 °C is placed in between the stack of washers.

Data acquisition All wires are guided via an electrical vacuum feed-through to a *Keithley DAQ6510* multimeter[25]. It is equipped with a programmable *7709-matrix switching card*. The data acquisition system is reused from the work of G. Zeller [81]. Figure 4.13 shows the internal wiring of the DAQ6510 system and the connections to the graphene sample via the matrix switching card. The DAQ6510 system performs four wire measurements by setting a test current from INPUT HI to INPUT LO and measuring the voltage between SENSE HI and SENSE LO. The device automatically returns the resistance values. The matrix card is controlled with a custom LabVIEW[26] software

---

[21] © 2006-2025 Thermo Fisher Scientific Inc. `https://www.thermofisher.com/order/catalog/product/043773.14?SID=srch-srp-043773.14` (visited on 11/20/2025).

[22] tectra GmbH, Reuterweg 51-53, 60323 Frankfurt/M, Germany. `https://tectra.de/wp-content/uploads/2017/03/Heater-Stage.pdf` (visited on 11/20/2025).

[23] Many thanks to M. Lai that helped to develop this contacting method.

[24] © VACOM 2024. `https://www.vacom.net/de/kap-lack-d-040.html` (visited on 11/20/2025).

[25] © 2025 TEKTRONIX, INC. `https://download.tek.com/manual/DAQ6510-900-01B_Aug_2019_User.pdf` (visited on 11/20/2025).

[26] National Instruments, Austin, Texas, USA.

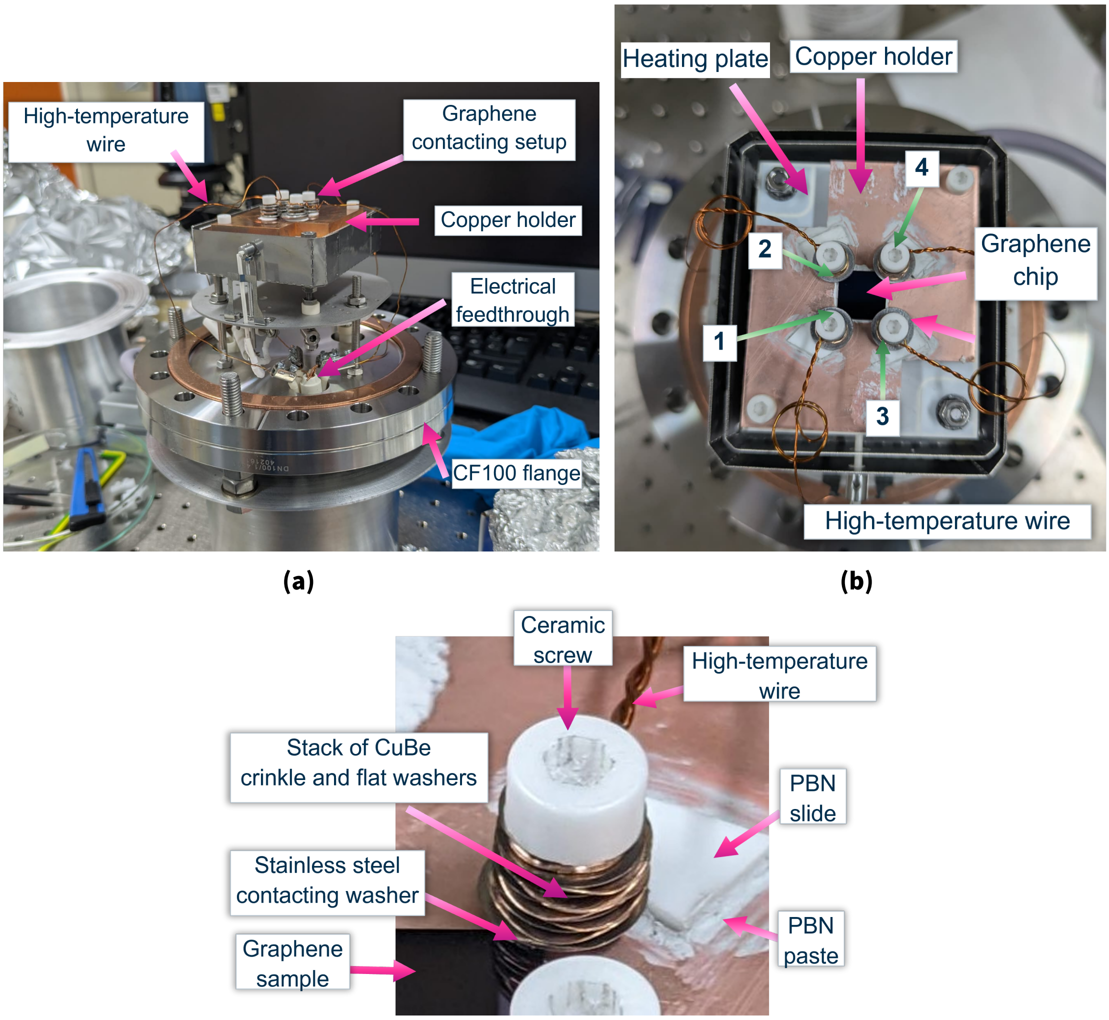

(a)

(b)

(c)

Figure 4.12.: Photos of graphene sample setup of generation 2 for exposure to the plasma source. Photos of generation 3 and 4 are shown in Figure 4.14. **(a)** Side view showing the heater and sample holder. **(b)** Top view showing the contacting setup of the graphene chip.**(c)** Zoomed-in view of the electrical contact of the graphene sample.

written by G. Zeller. Thus, one measurement point consists of eight four-wire resistance permutations and six two-wire resistances. The software additionally computes and displays R_H, R_V and $R_\square$ and $R_\square$ with $f = 1$ (see Section 3.5). The monitoring of the two-wire resistances gives more information about contacting issues. For instance, if one contact is damaged, it can be explicitly identified with the two wire resistances. This is further explained and demonstrated in Section 5.2.2.

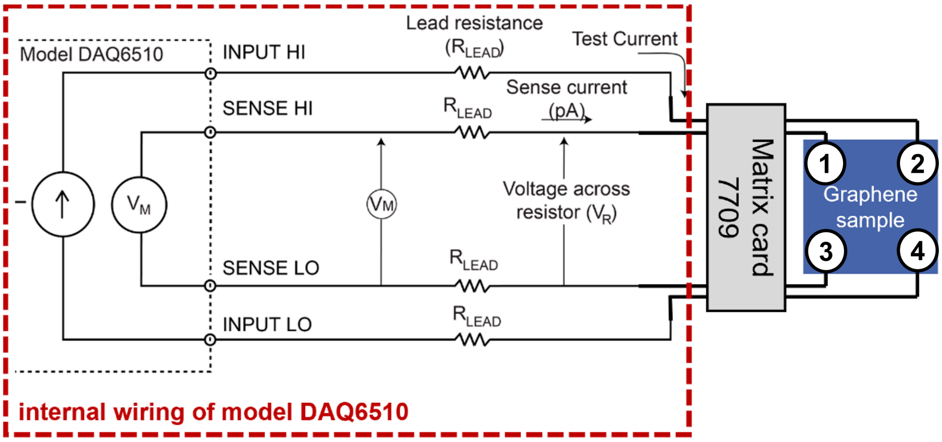

Figure 4.13.: Schematic of internal wiring of the DAQ6120 system and the connections to the graphene sample via the matrix card 7709. Reprinted from [81].

Fulfillment of Van der Pauw conditions In order to use the sheet resistance measurements quantitatively the four conditions must be met that are listed in Section 3.5.2. In the following, it is discussed whether the conditions are fulfilled with the contacting setup in this work.

1. The first condition is met because the four contacts are placed on the circumferences of the sample. However, improvements can be made by reducing the size of the contacting washers so that the contacting area is refined towards the edges of the sample.
2. It is not conclusive if the second condition is met. The area of the graphene sample covered by the washers is only about half an order of magnitude smaller than the area of the sample (see *e.g.* Raman scans in Figure 5.4). However, since stainless steel washers most likely have an uneven microscopic structure, smaller parts of the washers actually contact the graphene monolayer.
3. Condition three is fulfilled because the graphene layer is homogeneous as the 2D-G ratio in Figure 5.5b indicates.
4. The fourth condition is met for the same reason as condition three.

In summary, it is not clear yet whether all conditions are met for a quantitative measurement of the sheet resistance of the graphene sample. Therefore, improvements should be made to reduce the size of the contact area between graphene and washers by at least 1 mm.

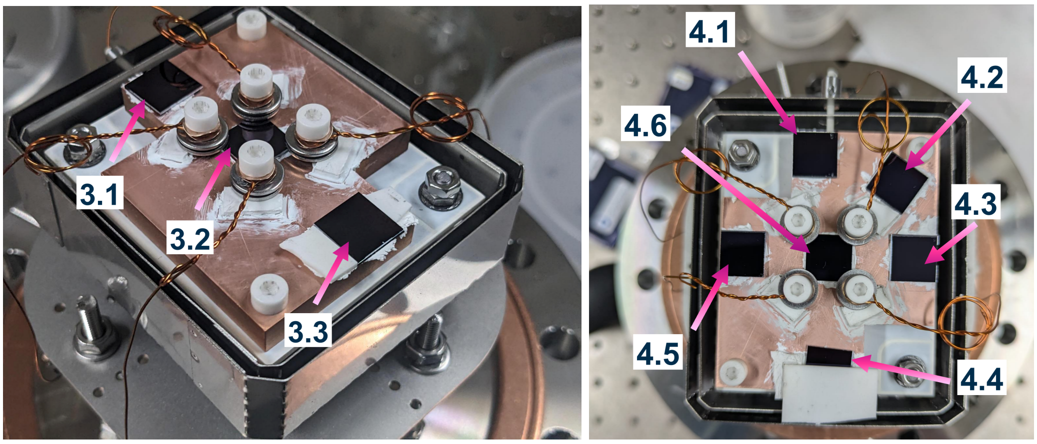

(a) **(b)**

Figure 4.14.: Measurement setup for loading experiments after loading of graphene sample in Figure 5.4a. The measurement campaign in **(a)** is entitled as *generation 3*. Sample 3.2 is contacted for resistance measurements. The measurement campaign in **(b)** is entitled as *generation 4*. Sample 4.6 is contacted for resistance measurements. The samples 3.3 and 4.4 are partly covered (see in **(b)**) to observe differences between graphene which is exposed to the beam and graphene which is not.

4.4.3. Setup for graphene as a beam profile sensor

The Raman scans of the plasma source exposed graphene samples show a beam profile structure in the D/G intensity ratios (see Figure 5.6). To increase the statistics for a beam profile analysis in Section 5.4 a larger area of the beam profile is covered. Placing a large graphene wafer (*e.g.* [90]) would be preferable to map a beam profile without interruptions on it. However, the CRM used in this work to perform the Raman scans, limits the size to the samples to about 1 cm^2. Therefore, multiple 1 cm × 1 cm graphene chips are attached to the copper holder with the PBN-paste (Figure 4.14). The setup in Figure 4.14a is the first configuration that maps the beam profiles. It is destined for a proof of concept for graphene as a beam profile sensor. The setup in Figure 4.14b shows an improved configuration of graphene samples to be able to perform a beam profile analysis that determines characteristics of the beam profile like the beam profile position and the beam profile size. The analysis includes a comparison of different beam profile models and an estimation of systematic errors that are Monte Carlo propagated. The full analysis is presented in Section 5.4.

The central sample is always contacted at the corners for the in-situ sheet resistance measurements (see in Figure 4.14 sample 3.2 and 4.6). Furthermore, one sample is partially covered (sample 3.3 and 4.4) to investigate the effect of heating to the graphene.

Thus, one part is exposed to the plasma and can be heated and the other part is only heated.

With the experimental setup described in this chapter, measurements of graphene samples that are exposed to the plasma source are presented in the succeeding chapter. Furthermore, OES measurements of the plasma with OES and the comparison to theoretical CR model calculations are shown in Chapter 6.

5. Graphene exposure to the plasma source

In this Chapter, the graphene is exposed to the plasma source with the setup that is described in the previous chapter. After an overview of the measurement campaigns in Section 5.1, the sheet resistance measurements during the heating of the graphene samples are shown. Hereafter, the results of in-situ sheet resistance measurements and ex-situ CRM scans of loaded graphene samples are presented, discussed and compared in Section 5.3. In Section 5.4 a novel method is presented that determines the beam profile of the plasma source by analyzing the two dimensional D-G ratio Raman scans of the graphene samples that were exposed to the source.
Finally, the findings are summarized in Section 5.5.

5.1. Overview of measurement campaigns

Multiple experiments of graphene samples loading with the plasma source were performed. In Table 5.1 an overview is given on the different runs including the corresponding settings, loading time t, plasma driving power P_{RF} and gas flow Φ. The latter two parameters were derived from previously performed plasma stability measurements (see Section 6.2). In this work, the different loading experiments are called *generations*. Each generation iteratively improves on the previous one and incooperates the lessons learned, aiming to improve the setup for loading graphene samples with atomic/ionic hydrogen. In generation 2 a single sample is exposed to the plasma source. The loading time t was chosen such that a saturation in the sheet resistance could be observed. The beam profile structure observed in the $I_{\mathrm{D}}/I_{\mathrm{G}}$ intensity ratio of the scanned graphene samples in the CRM, enables a characterization of beam profile parameters (see Figure 4.11). Therefore, in generation 3 are three samples exposed to the plasma source to cover large area of the beam profile and therefore increase statistics. Generation 3 is intended as a proof principle measurement for a beam profile analysis. Generation 4 is an improved variant of generation 3 with six samples exposed to the plasma source. A detailed explanation of the experimental setup is given in Section 4.4.3.

Table 5.1.: Overview of measurement campaign for graphene loading with the plasma source. The relevant parameters are loading time t, plasma driving power P_{RF}, gas flow Φ.

Generation	t in minutes	P_{RF} in W	Φ in sccm
2	237	250	0.5
	1058	350	1.0
3	56	350	0.5
4	30	50	0.5
	13	250	0.5

5.2. Sheet resistance characterization

In the scope of developing a setup to use graphene as an atomic/ionic hydrogen sensor, a setup is built to measure the sheet resistance of the graphene during exposure to the plasma source (see Section 4.4). The exposure to the plasma source produces defects on the graphene. The defects increase the sheet resistance of graphene as described in detail in Section 3.5. To distinguish between vacancy-type and sp^3-type defects thermal annealing is used. By heating their samples to 300 °C, Cha et al. [19] demonstrated the reversibility of hydrogenation while the vacancy defects remained. Building on that, the newly developed contacting method for the in-situ sheet resistance measurement of the graphene samples (see Section 4.4) is characterized and tested. Thermal annealing can only be utilized if the contacting quality is independent of the heating procedures. In this work, the contacting quality is defined as the reproducibility of the sheet resistance in the order of ±10 % after heating the setup to 300 °C. If this quality requirement is not fulfilled, it is important to identify the parts of the setup that cause the quality loss.

5.2.1. Sample Heating

The robustness of the contacting setup to temperature gradients is crucial when heating the graphene sample after loading with the plasma source to monitor in-situ changes of the sheet resistance. The contacting setup must be robust against heating procedures up to 300 °C [19] to be able to observe thermal annealing of adsorbed hydrogen atoms. Therefore, the different loading generations that are summarized in Table 5.1 are heated to 300 °C. To do this in a controlled way, the temperature is increased stepwise and the proportional-integral-derivative (PID) controller of the sample heater [104] is adjusted to ensure that the temperature does not overshoot. In Figure 5.1 a heating curve for generation 3 is shown as an example. The sample is heated stepwise up to 300 °C (Figure 5.1c). The sheet resistance $R_{\square}$ increases with increasing temperature up to

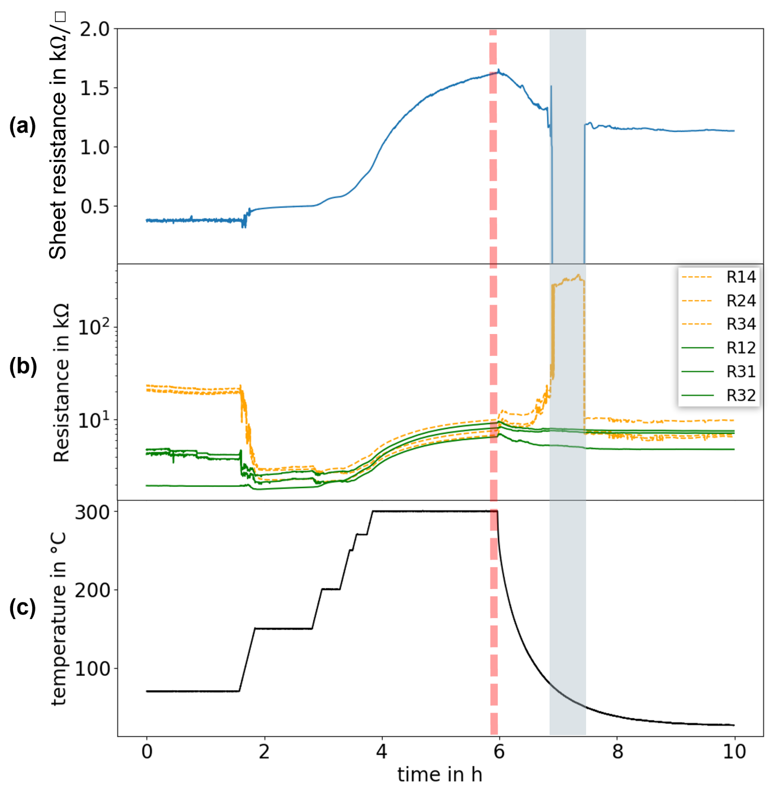

Figure 5.1.: Sheet resistance measurements during heating procedure. **(a)** Sheet resistance of the graphene sample. **(b)** two wire resistances of the graphene sample. The two wire resistances including contact four show connection problems. **(c)** temperature of the heating stage. The dashed red line indicates when the heating power is turned off. The gray area indicates where the contact is lost.

1.652 kΩ/□ at 300 °C. After 6 h the heater is turned off. Thereafter, the temperature decreases within two hours to nearly room temperature. The measurement for $R_\square$ becomes nonphysical[1] at around 7 h. After 1 h the connection to contact 4 „recovers“ so that the sheet resistance again shows values of 1.13 kΩ/□. This is an increase in sheet resistance of 0.7 kΩ/□ from the heating process only. The contacting quality requirement from above is therefore not satisfied.
Furthermore, the temperature gradient seems to have an influence on the contact quality. In Figure 5.1a the contact is lost during an absolute of the temperature gradient of about 4 °C/min (see Figure 5.1c) and recovered as the absolute of the gradient decreases to approximately 0.3 °C/min.

---

[1] This means around −80 kΩ/□.

5.2.2. Contact damage identification via two-wire resistances

The two-wire resistances can provide a qualitative monitoring of the resistance. They are also influenced by defects, e.g. Cha et al. [19] measured the hydrogenation with a two-wire contacting method.

Because only two contacts are involved in the measurement, contacting issues are simpler to locate. The loss of contact in Figure 5.1a is analyzed with the two-wire resistances in Figure 5.1b. The two-wire resistances that include contact 4 (see contact labeling in Figure 4.12c) are around 300 kΩ. This is two orders of magnitude higher than a two-wire resistance from graphene. This indicates that contact 4 is not properly connected to the graphene sample. In conclusion, the observation of the two-wire resistances helps to diagnose contacting damages in-situ.

5.2.3. Discussion of the quality of the contacting setup

Intermittent loss of contact is observed similarly for heating procedures of the other graphene generations. Contact number 4 is consistently responsible for the loss of contact during periods of large temperature gradients. However, in stable temperature regimes, the contact is typically re-established.

One possible reason for the loss in the electrical contact during heating and cooling of the graphene samples can stem from thermal expansion of the contacting setup caused by drastic changes in temperature. The graphene sample is contacted via M3 washers as shown in Figure 4.12c. They are placed directly on top of the monolayer of graphene, so any movement of the washers could result in damages to the graphene. For small damages, this should not be a problem because the covering surface of the washer is fairly large with about $2\,\mathrm{mm} \times 2\,\mathrm{mm}$, and the washer being made of stainless steel, has probably an uneven microscopic structure which would result in multiple contacting points between washer and graphene. However, macroscopic motion of the washer could destroy the graphene layer to an extent that the electrical contact is lost. This could be the case during the drastic cool-down process after 6 hours in Figure 5.1. On the other hand, the loss of contact during large temperature gradients could stem from a continuous movement of the washers in a way that no sheet resistance can be measured.

In conclusion, the contacting setup in Figure 4.12 is sensitive to temperature changes. For an absolute temperature gradient of $4\,^\circ\mathrm{C/min}$ the contact was lost. The damage could be located with the two-wire resistances.

When no contact is damaged, the sheet resistance can be used as a qualitative monitoring parameter. For future experiments, heating and cooling might be performed as slow as possible ($\Delta T < 0.3\,^\circ\mathrm{C}$) to minimize temperature gradients and thermal expansion of the contacting setup. To increase the robustness of the contacting setup, a metallic contacting layer, like gold, could be applied to the corners of the graphene sample. If heating procedures are performed and $R_\Box$ returns to the original value, the sheet resistance can also be used quantitatively.

5.3. Loading experiments

In this section, results of loading experiments are shown. In-situ measurements of the sheet resistance and ex-situ Raman scans of the graphene samples are discussed individually, and then compared in order to combine the observations from both diagnostic tools and improve the characterization of the beam emitted from plasma source.

5.3.1. Determination of loading parameters

Figure 5.2 shows the first successful operation of the full experimental system, including the plasma source, OES and sheet resistance measurements. The graphene sample used in this experiment is generation 2 (see Table 5.1). The gray area indicates a running plasma. After 5 h the plasma was restarted due to technical problems with the water cooling of the plasma source. Figure 5.2b shows an increase in sheet resistance $R_\Box$ over 15 h. In Figure 5.2a the first 1.5 h of the measurement are displayed. The start value of the resistance is around 447 $\Omega/\Box$. This value lies within the range specified by the manufacturer of $(450 \pm 40)\Omega/\Box$ [90]. The sheet resistance increases at the same time as the plasma ignites, given the time resolution of the sheet resistance measurement of 6 s. After 0.5 h $R_\Box$ reaches a local maximum at 9053 $\Omega/\Box$. However, the horizontal resistance R_H starts to decrease after 14 h. The different R_H and R_V indicate an asymmetric sheet resistance which could yield from damages on the graphene or from problems at the contact. Moreover, the plateau is very noisy. Furthermore, a jagged structure is visible between 7 and 10 h in $R_\Box$. The plasma monitor in Figure 5.2c and the sample temperature in 5.2d are stable and therefore do not cause the jagged structure.
G. Zeller et al. have exposed a similar graphene chip to tritium gas [17]. The shape of the resistance curve is similar to Figure 5.2a and 5.2b . The local maximum is lower, around $R_\Box \approx 5900\,\Omega/\Box$, and a similar jagged structure appears after 16 h. The contacting setup is different from the setup in this work, but the measurement device and the type of graphene samples are the same. Thus, it is possible that the local maximum and the jagged structure, are properties of the loaded chips.

After the exposure, the sample is heated to study the thermal annealing of possible sp^3-type defects. Therefore, various heating procedures are performed. Furthermore, the sample is also scanned with the CRM after all heating and exposure procedures.

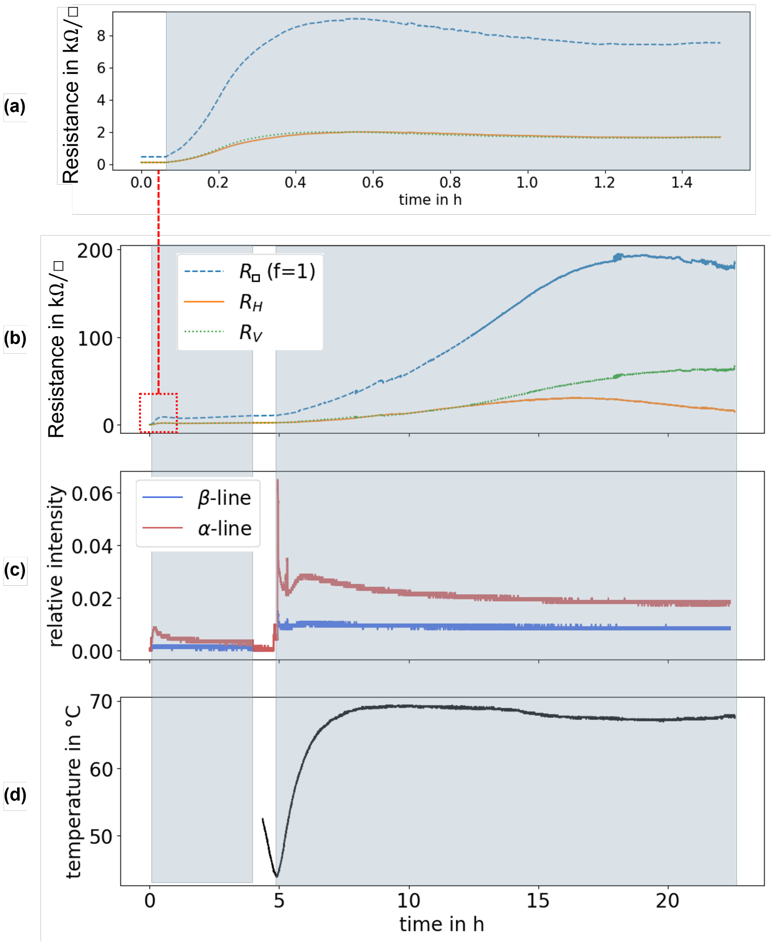

Figure 5.2.: Van der Pauw measurement of graphene sample generation 2 while exposure to the plasma source. The gray area corresponds to a turned on plasma source. **(a)** Initial increase in sheet resistance during ignition of the plasma. **(b)** Sheet resistance measurement until a plateau is reached. The dashed line is the sheet resistance $R_\square$ in kΩ/□. The solid line is the horizontal sheet resistance R_H. The dotted line is the vertical sheet resistance R_V. (c) Plasma monitoring through integration of the atomic Balmer α- and β- line with integrations limits $654.5 - 663$ nm and $485 - 491$ nm, respectively. **(d)** Temperature of the graphene sample monitored with the temperature read out of the heating stage. The measurement started after ~ 4.5 h.

A temperature of up to 300 °C is set for 1.5 h after stepwise increase. In Figure 5.3 the resistances are compared before loading, after exposure and after heating. Before loading, a sheet resistance of ~ 0.448 ± 0.0015 kΩ/□ is measured which is compatible with pristine graphene values of 0.45 ± 40 kΩ/□ [90]. After exposure, the sheet resistance is around ~ 192.49 ± 0.82 kΩ/□. The heating procedures did not reduce the sheet resistance (see Figure 5.3c).

If the increase in resistance is caused by hydrogenation, $R_\square$ would decrease after heating [19, 105]. However, $R_\square$ does not change significantly and the Raman scan made with the CRM (see Section 3.4) shows that there is no graphene left (Figure 5.4a).[2] After exposure (see Figure 5.3a), the sheet resistance of Si/SiO$_2$ was measured to be in the order of 192 k$\Omega/\square$ which is close to values reported in literature of $(200 - 300)$k$\Omega/\square$ (see *e.g.* Figure 3 in Reference [106]). In Figure 5.4a graphene is only left in the corners of the chip. This is, where the chip was covered with the washers for the Van der Pauw measurement.
To avoid complete removal of the graphene layer during exposure to the plasma source, the exposure time is drastically reduced (see Table 5.1). Generation 3 is for 56 minutes and generation 4 for 43 minutes exposed to the plasma source. The Raman scans show an improvement. The graphene layers are not removed in generation 3 and 4. The map averaged I_{2D}/I_G value is 0.78 for generation 3 and 1.07 for generation 4. In comparison, the graphene sample manufacturer claims $I_{2D}/I_G > 1$ for pristine graphene [90]. Utilizing the 2D/G-ratio as an indicator whether graphene is present, the exposure parameters for generation 4 are identified as a first set of parameters to safely expose graphene samples without removing the graphene layer.

In conclusion, the operation of the full experimental system including the plasma source, OES and sheet resistance measurements was successful. The structural changes of

---

[2] The 2D peak and the G peak are introduced in Section 3.3. The intensity ratio in general is used to determine the quality of the graphene layer. In this work, the presence of the 2D-peak is in addition used to visualize if the graphene layer was fully removed by the plasma exposure.

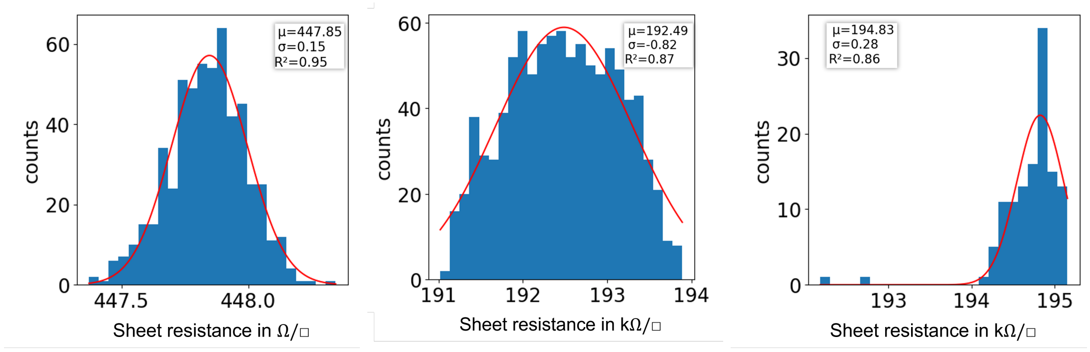

(a) **(b)** **(c)**

Figure 5.3.: Histograms of sheet resistance $R_\square$ from 1 hour of measurement time. In red is a gaussian fit to determine the mean μ and standard deviation σ. The goodness of the fit is defined via $R^2 = 1 - \sum(c_{\text{data}} - c_{\text{fit}})/\sum((c - \bar{c})^2)$ with c being the counts and $\bar{c}$ the average of the counts. Comparison of sheet resistance **(a)** before loading the graphene chip with the plasma source versus **(b)** after loading, and versus **(c)** after loading and heating. In **(a)** the sheet resistance, μ and σ are given in $\Omega/\square$, whereas in **(b)** and **(c)** its given in k$\Omega/\square$.

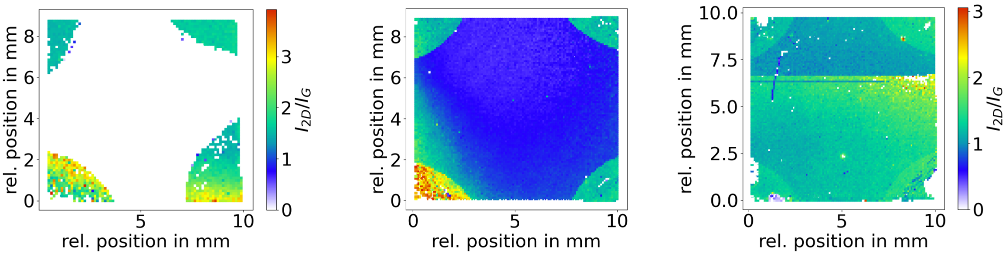

(a) **(b)** **(c)**

Figure 5.4.: Ex-situ measured Raman map of the center graphene samples from **(a)** generation 2 with a spatial resolution of $\sigma_{\text{res}} = 125\,\mu\text{m}$, **(b)** generation 3 with $\sigma_{\text{res}} = 91.25\,\mu\text{m}$, **(c)** generation 4 with $\sigma_{\text{res}} = 87.5\,\mu\text{m}$. The 2D-G ratio indicates whether graphene is present. White pixels correspond to data points where the fit did not converge and is therefore interpreted as removed graphene. **(b)** and **(c)** share the same color axis. In **(c)** the upper third of the map is slightly different from the rest. The measurement for this part had to be restarted due to technical problems. The measurement settings of the CRM were slightly different for this run.

the graphene could be monitored in-situ during exposure to the plasma. However, a decrease in sheet resistance after heating could not be observed for generation 2, neither for generation 3 and 4. Therefore, thermal annealing of sp^3-type defects could not be detected with this sample. Furthermore, exposure parameters are found to avoid removing the graphene layer. They are $P_{\text{RF}} \leq 250\,\text{W}$, $\Phi \leq 0.5\,\text{sccm}$ and loading times of $t \leq 43$ minutes.

5.3.2. Correlation of sheet resistance $R_\square$ and defect peak ratio I_D/I_G

To test whether damages and defects on the graphene layer are caused only by exposure to the plasma source or also by heating, the samples 3.3 and 4.4 are installed in generation 3 and 4, respectively (see Figure 4.14b). Experimental details for the setup in generation 3 and 4 are given in Section 4.4.3.
The samples 3.3 and 4.4 are partly covered during the exposure to the plasma source. Hence, a difference in Raman scans for a plasma exposed+heated sample and a just heated sample is investigated. The sample 4.4 was damaged during disassembly. Therefore, only sample 3.3 is scanned in the CRM. The I_D/I_G map[3] in Figure 5.5b shows that the covered part is damaged and the uncovered part is undamaged. Furthermore, the 2D-G ratio in Figure 5.5a is homogeneous through out the whole graphene sample. The average value is > 1 which matches the specifications of the graphene chip

---

[3] The D peak and the G peak are explained in Section 3.3. The ratio is correlated to the defect density L_D. However, the proportionality factor between L_D and $\text{I}_\text{D}/\text{I}_\text{G}$ depends on the regime (Figure 3.7b) and on the defect type (Figure 3.6b).

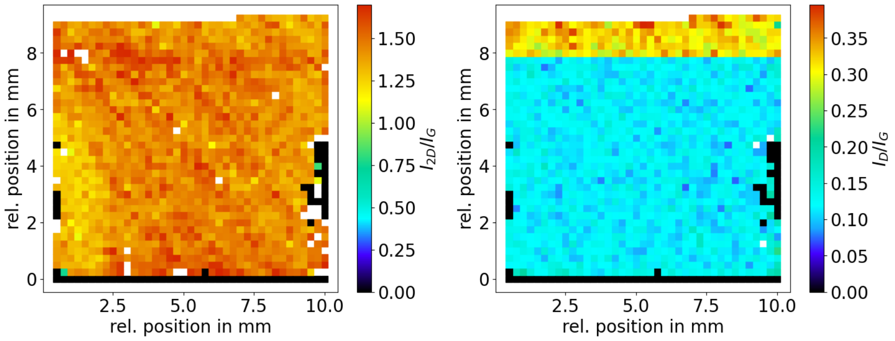

(a) **(b)**

Figure 5.5.: Ramans scan of sample 3.3 with a spatial resolution of 250 μm. **(a)** is I_{2D}/I_G and indicates the existence of graphene. **(b)** is I_D/I_G which is proportional to the defect density. The upper part of the sample which is yellow and red was exposed to the plasma. The rest was covered with a PBN plate.

manufacturer [90]. Hence, heating does not damage the graphene or produces any defects.

As shown in Section 5.2.1, large temperature gradients applied to the graphene samples influence the contact-quality significantly. Therefore, the sheet resistance monitoring is mostly unreliable during heating procedures. When the temperature is constant however, the electrical contact is stable and the sheet resistance values can be analyzed. The sheet resistance $R_\square$ is compared for pristine graphene with the graphene sample after all plasma loading and heating processes. In Figure 5.7 the initial $R_\square$ value is compared with the final $R_\square$ value for generation 3 and generation 4, respectively. The values for the pristine graphene are $< 0.5\,\mathrm{k\Omega/\square}$. The values for the processed graphene are $11.4\,\mathrm{k\Omega/\square}$ and $6.8\,\mathrm{k\Omega/\square}$ averaged over 3 hours for generation 3 and 4, respectively.

To compare $R_\square$ to the D-G ratio maps, the defect density regime must be identified [92]. This is explained in detail in Section 3.3.4. The width of the D-peak is utilized as a filter. All data points with

$\mathrm{FWHM_D} < 40\,\mathrm{cm^{-1}}$ are assigned to the low defect density regime (see Figure 3.6). The data points above a width of $\mathrm{FWHM_D} = 40\,\mathrm{cm^{-1}}$ are filtered [13]. For the samples 3.2 and 4.6 almost all data points are in the low defect density regime. Hence, the D-G ratios can be compared with each other. Furthermore, a qualitative comparison with the sheet resistances is possible as well. In Figure 5.7 the correlation between the sheet resistance and the average values of I_D/I_G are shown. Sample 3.2 had a total loading time of $t = 56$ minutes and sample 4.6 $t = 43$ minutes. Furthermore, the plasma driving power P_{RF} was lower for sample 4.6. The details are to find in Table 5.1. Figure 5.7

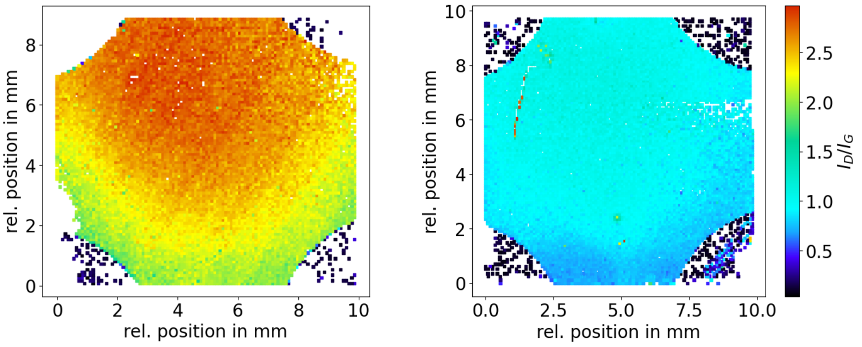

(a) **(b)**

Figure 5.6.: $I_\mathrm{D}/I_\mathrm{G}$ scans of **(a)** sample 3.2 and **(b)** sample 4.6 with a spatial resolution of 91.25 μm and 87.5 μm, respectively.

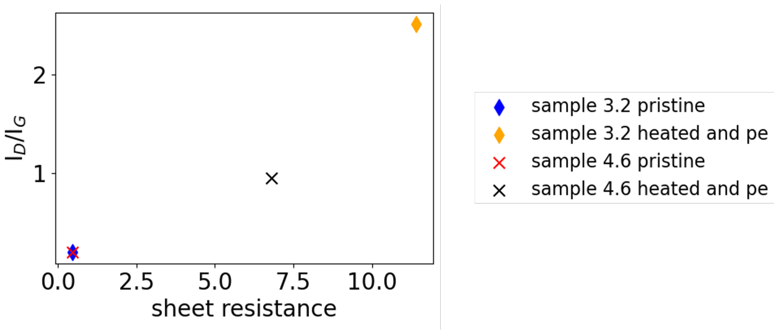

Figure 5.7.: Qualitative comparison of map-averaged $I_\mathrm{D}/I_\mathrm{G}$ values with sheet resistance measurements of sample 3.2 and sample 4.6. Compared are the values for the samples in a pristine form with after heating and plasma exposure (pe).

shows an increase of $R_\square$ for an increase of $I_\mathrm{D}/I_\mathrm{G}$. This is a positive result as it is expected that the sheet resistance increases for an increased defect density.

Furthermore, $R_\square$ and $I_\mathrm{D}/I_\mathrm{G}$ correlate with t and P_RF positively. This observation could be explained with the velocity distribution of the gas emitted from the plasma source (see *e.g.* Reference [107]).[4] The particles that are contained in the high energy tail of the distribution probably cause the damages on the graphene. Therefore, it was expected that shorter exposure times would decrease the defect density. Also it was assumed that a larger driving power of the plasma causes more particles to be within the high energy tail, also increasing the defect density for the same exposure time.

---

[4] In this work, the dynamics of a plasma are ass

5.3.3. Hydrogenation of graphene

The observation of hydrogenation was not possible with the sheet resistance measurements due to contact instabilities during heating procedures. The challenges are outlined in Section 5.2. However, the measurements with the CRM allow to distinguish between vacancy-type defects and sp^3-type (adsorption) defects. The peak ratio $I_\mathrm{D}/I_\mathrm{D'}$ is a measurement parameter for hydrogen adsorption on graphene based on the empirical model by Eckmann et al. [15] (see Section 3.3.5). Data points with $I_\mathrm{D}/I_\mathrm{D'} = 13$ are assigned to sp^3-type defects and data points with $I_\mathrm{D}/I_\mathrm{D'} = 7$ are assigned to vacancy defects [15].[5] Everything in between is a mixture of both defect types. At the time of writing, there is no established model for the de-mixing of the defect type, which is not linear.

The results of the $I_\mathrm{D}/I_\mathrm{D'}$ maps of sample 3.2 and sample 4.6 are shown in Figure 5.8. In sample 3.2 almost no sp^3-type defects are observed. The expectation value is $\mu_{3.2} = 6.9 \pm 0.69$ (Figure 5.8c) which corresponds to vacancy defects [15]. Sample 4.6 has more sp^3-type defects as visible by the large number of red pixels in Figure 5.8b. The histogram in Figure 5.8d has a Gaussian shape with a peak around 10. Performing a Gaussian fit, gives an expectation value of $\mu_{4.6} = 10.04 \pm 2.69$. Hence, the main defect type is a mixture of vacancies and sp^3-type defects.

By assigning a majority defect type on the graphene samples, a defect density L_D can be assigned. For sample 3.2 the model of Lucchese et al. [14] is valid. With this an average defect density of $L_\mathrm{D} = 5.5\,\mathrm{nm}$ for $I_\mathrm{D}/I_\mathrm{G} = 2.51$ can be estimated (see Figure 3.6b). A defect density is not assigned to sample 4.6 because neither the model of Lucchese et al. nor the model of Fournier et al. apply for a mixture of vacancy defects and hydrogenation (see Section 3.3.3.
When combining the D-G ratio, D-D' ratio and the Van der Pauw measurements under consideration of the loading parameters of sample 3.2 and sample 4.6 the following conclusion can be made:

1. The longer the graphene sample is exposed to the plasma source, the more defects are produced.
2. A decrease in sp^3-type defects and a decrease in sheet resistance is observed between sample 3.2 and sample 4.6. Therefore, the assumption can be made that adsorbed hydrogen atoms are removed during exposure to the plasma source. The bonding energy for C-C bonds in graphene are $\approx 7.5\,\mathrm{eV}$ [108] and for H-C bonds ≈ 0.8 to $1.9\,\mathrm{eV}$ [109]. Hence, particles in the high energy tail of the kinetic distribution of the gas emitted from the plasma source could be the reason for this observation.

---

[5] Data points with $I_\mathrm{D}/I_\mathrm{D'} = 7$ are assigned to edges

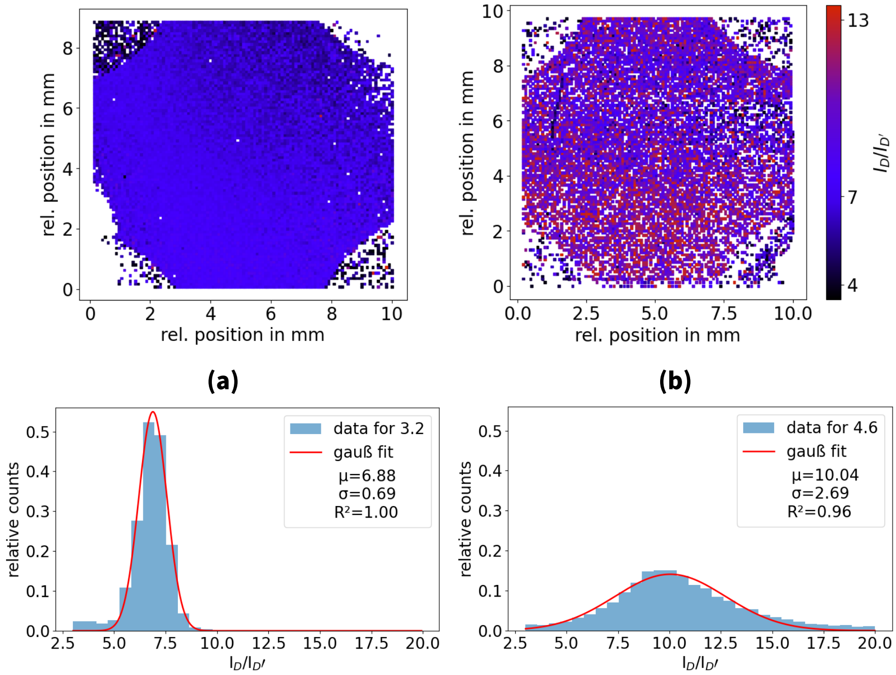

(a) (b)

(c) (d)

Figure 5.8.: Ex-situ measured Raman $I_\text{D}/I_{\text{D}'}$ map of **(a)** sample 3.2 and **(b)** sample 4.6 with a spatial resolution of $\sigma_\text{res} = 100\,\mu$m. White pixels are data points where the fit did not converge. Data points from **(a)** are shown in the histogram in **(c)** and data points from **(b)** are shown in the histogram in **(d)**. The histograms have the same binning. The goodness of the fit of the histogram is $R^2 = 1 - \frac{\sum(y_i - f_i)^2}{\sum(y_i - \bar{y})^2}$ with the heights of the $I_\text{D}/I_{\text{D}'}$ bins y_i, the fitted data f_i and the counts average $\bar{y}$.

5.4. Determination of beam profiles (BP) of the plasma source

The experimental setup for the measurements with the graphene samples from generation 3 and generation 4 are described in Section 4.4.3. Generation 3 is designed to map the beam profile (BP) on three samples. Therefore, the statistics and coverage of the beam area should be increased compared to one single graphene sample as in generation 2. Every sample is scanned one after the other in the CRM after the exposure to the plasma source (see Section 3.4). The Generation 3 data set is used for the proof of principle of an analysis framework for the determination of BP characteristics. Generation 4 was intended to improve statistics and coverage of the beam area even further by exposing six graphene samples to the plasma source. However, sample 4.1 and 4.4 (see Figure 4.14b) were damaged during the disassembly of the vacuum system.

The BP analysis for generation 4 is presented in this section: The mapping of the I_D/I_G Raman scans to a photograph of the setup is presented in Section 5.4.1. Furthermore, three different models are fitted to the combined I_D/I_G Raman maps in Section 5.4.2. The models are compared in terms of goodness of the fits. A Monte Carlo (MC) error propagation is performed on systematic errors in the mapping of the Raman scans in Section 5.4.3. Hence, uncertainties for the parameters of the fits are calculated. In the last subsection, the BP characteristics determined with the different models are compared and evaluated (see Section 5.4.4).

5.4.1. Data pre-processing and mapping

Before performing a two dimensional fit on all samples at once, the Raman scans must be mapped to an image of the setup. This is necessary to determine the relative positions of the Raman scans to each other. The image is shown in Figure 5.9a. To ensure correct mapping, the photo is perspective corrected such that the plane of the graphene chip in the photo is parallel to the camera plane. Only then the orientation of the graphene samples can be determined accurately. Therefore, python scripts are written that allow an interactive perspective correction of Figure 5.9a. All data processing steps are performed in python 3.12. The main processing steps are described below. Every paragraph corresponds to a single custom python script.

Image rotation: The image can be rotated with respect to the lower edge of the photo. The user chooses two pixels along the lower edge of the copper holder. The angle between the connecting line of the two pixels and the lower edge of the photo is calculated and corrected. The result is displayed in Figure 5.9b.

Perspective transform: If the photo is taken not perfectly without any perspective angle, objects that are not in parallel to the camera plane appear distorted. For instance, a graphene chip which is quadratic and so the vertical and horizontal edges are parallel, respectively, does not appear as such in the photo. Hence, it must be corrected for. The python library *cv2*[6] provides functions that can change the parallel plane of the photo. Therefore, the four edges of the central graphene chip (sample 4.6) are selected by choosing two pixels at each edge. The intercepts of these four lines are calculated and set as the corners of the graphene chip. With the function *csv.getPrespectiveTransform()* a rotation matrix is calculated. The inputs for this function are the calculated corners and new desired coordinates of the corners of the graphene chip. For the latter the points $[0, 0]$, $[662, 0]$, $[662, 800]$ and $[0, 800]$ in the unit of pixels are chosen. It is very important to have the same width and height ratio in the photo as the measures of the copper holder, which has a width of 47 mm and a height of 56.8 mm. With the resulting

---

[6] `https://docs.opencv.org/4.x/index.html` (visited on 11/20/2025)

matrix the image is corrected with the function *csv.warpPerspective()* and displayed in Figure 5.9c.

Correction of Raman scans: The Raman scans are not perfectly aligned with the graphene sample edges. In principle, it should be position- and rotation-corrected as well. However, the maximum shift in the samples of generation 4 is 200 μm. The rotation has a maximum of 0.2 °. The resolution on the image correction has a much larger uncertainty which is further explained and calculated in Section 5.4.3. Therefore, no specific correction is applied to the Raman scans in this work.

Location of the graphene samples: After the alignment of the graphene sample plane to the camera plane, the distances and the relative rotations between the graphene samples are determined. Therefore, the corners of all samples are selected. Because the corners of sample 4.6 are covered, they are indirectly calculated with the intercepts of the sample edges. The resulting angles and distances are stored in a text file.

Mapping of the Raman scans to the image: The Raman scans of the samples 4.2, 4.3, 4.5 and 4.6 (see Figure 4.14b for orientation) are aligned with the photo. Parts of the graphene samples that were not exposed to the plasma (e.g. the corners of sample 4.6) are filtered. Outliers for which the fit quality in the Raman analysis chain is < 0.999 are filtered as well. Furthermore, data points with the width of the D peak of $\mathrm{FWHM_D} \geq 40\,\mathrm{cm^{-1}}$ are excluded. In Section 3.3.4 it is explained that points above this threshold correspond to a different defect density stage (see Figure 3.6b). The remaining data is shifted and rotated with the values from the previous paragraph. A common color axis is applied to the map, resulting in Figure 5.9d. Sample 4.2 has a cutout which yields from the wire that covered this section. Sample 4.5 is missing a few data points as well. This comes from measurement issues at the CRM. The samples 4.1 and 4.4 are not included in this map because they were damaged in the process of opening the vacuum system.

5.4.2. Fitting BP-models

As a proof-of-principle, different empirically chosen beam profile models are fitted to the $I_\mathrm{D}/I_\mathrm{G}$ Raman scans. A theoretical description of the beam profiles is favorable; however, it goes beyond the scope of this thesis.
Three models are fitted to the combined Raman map in 5.9d. The first two models are based on the model function [110]:

$$I_\mathrm{D}/I_\mathrm{G} = A \cdot e^{-\left\{\frac{1}{\alpha}[q(\mathbf{r})]^{\frac{p}{2}}\right\}} + B\,, \tag{5.1}$$

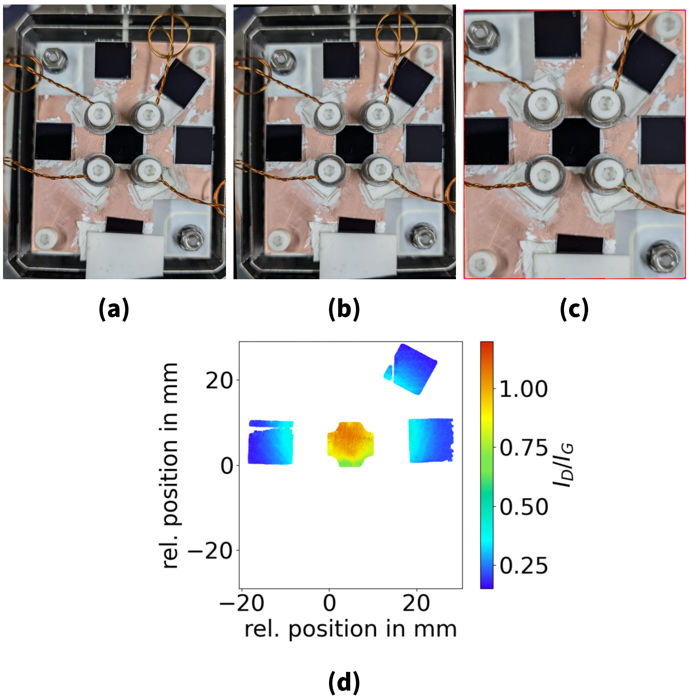

Figure 5.9.: Image processing of the reference photo for graphene generation 4. **(a)** original photo. **(b)** rotated photo such that the lower edge of the copper holder is parallel to the lower edge of the photo. **(c)** Perspective corrected photo. The central graphene chip is chosen as the reference plane. **(d)** Combined Raman scans and mapped to the photo in **(c)**.

with the contour lines $q(\mathbf{r})$ = const.:

$$q(\mathbf{r}) = (\mathbf{r} - \mathbf{r}_0)^T \, \Sigma^{-1} (\mathbf{r} - \mathbf{r}_0) \tag{5.2}$$

with the covariance matrix Σ. The condition for Σ to be positive semi-definite and symmetric yields an eigendecomposition of Σ [110]:

$$\Sigma = R \, D \, R^T \tag{5.3}$$

with the eigenvalues of Σ in a diagonal matrix

$$D = diag(s_x^2, s_y^2) \, , \tag{5.4}$$

and the rotation matrix

$$R = \begin{pmatrix} \cos\phi & -\sin\phi \\ \sin\phi & \cos\phi \end{pmatrix} \, . \tag{5.5}$$

Fixing the parameters $\alpha = \sqrt{2}$ and $p = 2$ in Equation (5.1) results in a Gaussian model function with six free parameters: BP center height A, BP center position $\mathbf{r}_0 = \begin{pmatrix} x_0 \\ y_0 \end{pmatrix}$, the

semi-minor and semi-major axis s_x and s_y, the rotation of the ellipsis ϕ and a background offset B. The parameters are illustrated in Figure 5.10. Fixing $\alpha = 1$ and leaving p as a free parameter results in a generalized normal function with seven free parameters.
The third model function used in this work is a Lorentzian:

$$I_\mathrm{D}/I_\mathrm{G} = \frac{A}{1+q(\mathbf{r})} + B\,, \tag{5.6}$$

with the contour lines from Equation (5.2). The covariance matrix is defined in Equations (5.3),(5.4) and (5.5). Hence, this model has six free parameters that are the same for the Gaussian model.
The ellipsis axes $(s_\mathrm{x}, s_\mathrm{y})$ are defined differently for the generalized normal model and the Lorentzian model. To standardize this, the BP size is introduced via the *full width half maximum* (FWHM). To convert $(s_\mathrm{x,y})$ to $\mathrm{FWHM}_\mathrm{x,y}$ a conversion factor is derived in the following. The first step is to insert $I_\mathrm{D}/I_\mathrm{G} = \frac{A}{2}$ in Equation (5.6):

$$\frac{A}{2} = \frac{A}{1+q} \tag{5.7}$$

$$q = 1 \tag{5.8}$$

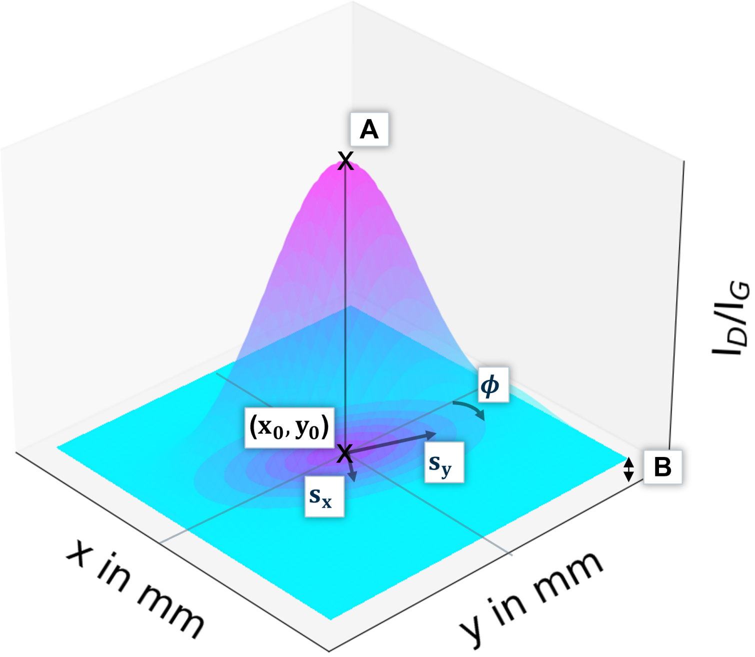

Figure 5.10.: Three-dimensional sketch of a BP with the contours projected on the x-y-plane. The parameters are explained in the main text.

Any point on the contours line is then described via $\mathbf{r} = \mathbf{r}_0 + s\mathbf{u}$ with the distance s from the center to the point on the contours line and the connecting vector $\mathbf{u}$. For Equation (5.8) follows:

$$1 = s^2\, \mathbf{u}^T \Sigma^{-1} \mathbf{u} \tag{5.9}$$

The distance s is $\frac{1}{2}$ FWHM, such that

$$\mathrm{FWHM} = \frac{2}{\sqrt{\mathbf{u}^T \Sigma^{-1} \mathbf{u}}}\ . \tag{5.10}$$

The covariance matrix Σ can be expressed in terms of the variance: $\frac{1}{s_u^2} \equiv \mathbf{u}^T \Sigma^{-1} \mathbf{u}$. The resulting expression for the FWHM in x- and y-direction yields

$$\mathrm{FWHM}_{\text{x,y Lorentz}} = 2 \cdot s_{\text{x,y Lorentz}}\ . \tag{5.11}$$

Analogously derived is the transformation for the generalized normal model in Equation (5.1):

$$\mathrm{FWHM} = 2\,(\alpha \ln 2)^{\frac{1}{p}} \cdot s \tag{5.12}$$

The resulting conversion factors are:

$$\mathrm{FWHM}_{\text{x,y Gauss}} = 2\sqrt{\sqrt{2}\ln 2} \cdot s_{\text{x,y Gauss}} \approx 1.98 \cdot s_{\text{x,y Gauss}}\ , \tag{5.13}$$

$$\mathrm{FWHM}_{\text{x,y gen. normal}} = 2\,(\ln 2)^{\frac{1}{1.765}} \cdot s_{\text{x,y gen. normal}} \approx 1.62 \cdot s_{\text{x,y gen. normal}}\ . \tag{5.14}$$

The factor $p = 1.765$ is the result of the generalized normal fit.
A detailed comparison of BP characteristics is demonstrated in Section 5.4.4.

To fit the model to the data, the function *scipy.optimize.curve_fit*[7] in python is utilized, which calculates a minimum of χ^2 with the least-squares-method. In this section, the fitting results are shown exemplarily only for the Lorentzian model. The plots for the Gaussian model and the generalized normal model are displayed in Section A.2. In Figure 5.11a the I_D/I_G BP resulting from a Lorentzian fit is displayed together with the data. The resulting BP characteristics are a BP center height of $A = 1.08$, a BP center position (which is marked with a cross in Figure 5.11) of $(x_0, y_0) = (4.99\,\text{mm}, 7.47\,\text{mm})$ relative to the bottom left corner of sample 4.6. and the BP size $(s_x, s_y) = (10.98\,\text{mm}, 10.69\,\text{mm})$. The fit quality is represented through the residuals Δ in Figure 5.11c. For pixel (ij) they are defined through the difference of the the measured I_D/I_G and the calculated I_D/I_G:

$$\Delta_{i,j} = (I_\text{D}/I_\text{G})_{ij,\text{model}} - (I_\text{D}/I_\text{G})_{ij,\text{data}}\ . \tag{5.15}$$

---

[7] `https://docs.scipy.org/doc/scipy/reference/generated/scipy.optimize.curve_fit.html` (visited on 11/20/2025).

Outliers with $|\Delta_{ij}| > 0.25$ in the residuals are filtered so that structures in the Δ-bulk become more visible (see Figure 5.11b). The residuals in Figure 5.11c are mostly around zero. However, there are structures with larger residuals up to 0.2, especially for sample 4.6. In the data of 4.6 (Figure 5.11a) structures are visible that do not follow the circular contour-lines of the BP which probably leads to the deviations. Furthermore, the left side of sample 4.6 has a larger Δ. This indicates an asymmetry in the BP. The models utilized in this work do not consider asymmetry.

The goodness of the fit is defined with the χ^2 value:

$$\chi^2 = \sum_{i,j} \left(\frac{\Delta_{i,j}}{\sigma_{ij}} \right)^2 , \tag{5.16}$$

and the reduced χ^2_ν

$$\chi^2_\nu = \frac{\chi^2}{\nu} , \tag{5.17}$$

ν being the degrees of freedom of the model function. σ_{ij} is the uncertainty of the $I_\mathrm{D}/I_\mathrm{G}$ measurement of pixel (ij). The results on the goodness of the fits are displayed in

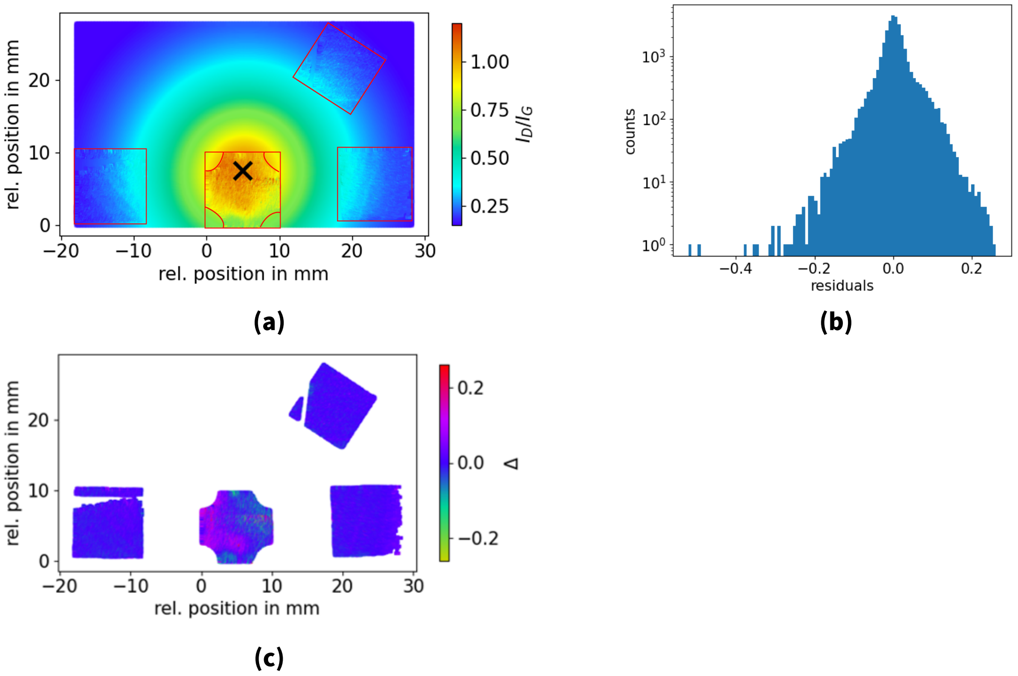

(a)

(b)

(c)

Figure 5.11.: Results of the Lorentzian model fitted to the combined Raman map. **(a)** A contours plot overlapped with the data points that are framed in red. The cross indicates the beam center. **(b)** The histogram of the residuals Δ. Outliers for $|\Delta| > 0.25$ are filtered for **(c)**.

Table 5.2.: Overview of the goodness of the fits for different beam profile models. The goodness of the fit χ^2 is divided by 10^4. The reduced χ^2 is $\frac{\chi^2}{\nu}$ with the degrees of freedom ν.

	Lorentzian	generalized normal	Gaussian
$\frac{\chi^2}{10^4}$	7.3021 ± 0.9340	7.714 ± 0.6950	7.3697 ± 0.6428
$\frac{\chi^2}{\nu}$	2.35 ± 0.3	2.34 ± 0.2	2.37 ± 0.2

Table 5.2. The uncertainty on χ^2 and χ^2/ν is calculated from an uncertainty analysis in Section 5.4.3. The goodness of the fit is very similar for all three models, which enables a comparison between them. The residuals for the Gaussian and generalized normal model are also very similar to the Lorentzian residuals (see Figures A.16c and A.17c). All models have difficulties in representing the left side of sample 4.6. because all models are symmetric.

In Figure A.20 the correlation between the fit parameters is shown. In general, many parameters are correlated. To investigate this, a Monte Carlo (MC) error propagation is performed in Section 5.4.3. A correlation of -0.72 and -0.83 between the background offset B and s_x,s_y, respectively, is relatively high. Furthermore, y_0 is strongly correlated with BP center height A.
An increased correlation is observed for s_x,s_y and ϕ which is reasonable because the size and rotation of the beam profile is strongly dependent on each other, especially when the profile is nearly circular ($s_x \approx s_y$).

5.4.3. Uncertainty analysis

In this Section, the uncertainties in the BP-analysis are calculated and discussed. The CRM is intensity calibrated using the NIST SEM 2242a[8] and the uncertainties given in the calibration data sheet are propagated to the intensity ratios. This results in a statistical error σ_{stat} from data fluctuations and a systematic error σ_{sys} from the absolute intensity calibration of the CRM.

$$\sigma_{\text{tot}} = \sqrt{\sigma_{\text{stat}}^2 + \sigma_{\text{sys}}^2} \tag{5.18}$$

The total uncertainty for every data point σ_{tot} from the Raman scan is propagated via Equation (5.16). The variance of every parameter is calculated through an approximation of the Hessian matrix of the χ^2 function [110]:

$$Var(\theta) = \left(J^T\, W\, J\right)^{-1} \tag{5.19}$$

---

[8] `https://tsapps.nist.gov/srmext/certificates/archives/2242a.pdf` (visited on 11/20/2025).

with the Jacobian matrix J and $W = diag\left(\frac{1}{\sigma_{\text{tot}}^2}\right)$. For the Lorentzian model the parameters are $\theta = [A, x_0, y_0, s_\text{x}, s_\text{y}, \phi, B]$. The fit function *scipy.optimize.curve_fit*[9] calculates Equation (5.19) for every pixel automatically.
Furthermore, an uncertainty on the mapping of the Raman scans to the photo in Figure 5.9c is estimated. Therefore, uncertainties in positioning of the Raman scans to each other have to be considered which are explained in the following:

- In Section 5.4.1, pixels of the edges and corners of the graphene chip are chosen interactively to identify the distances and rotations of the graphene samples to each other.
- The pixel selection depends on the photo quality. Thus, corners and edges are smeared out over multiple pixels. For this, an uncertainty of 15 pixels is chosen, which results in an uncertainty of ±1.065 mm on the x and y positioning. The resulting maximum shift on the rotation is 0.21 °.
- The uncertainty σ_θ is estimated for every parameter θ through Monte Carlo (MC) sampling of positional deviations. Every sample is shifted in x and y and rotated for a random value sampled from a uniform distribution with the limits from above.
- The shifted samples are combined into a common Raman map and the fit is performed including the uncertainty σ_tot on I_D/I_G.
- This procedure is performed 1000 times. Figure 5.12 shows the histograms for every parameter θ of the Lorentzian model.

The results for each parameter are the mean and the standard deviation of the corresponding histogram. The uncertainty on the positioning of graphene samples is ±1.065 mm. This effect is visible in the histogram of the BP position. Especially y_0 does not have a distinct maximum, which results in an uncertainty of 0.48 mm. The ellipsis rotation angle ϕ is very asymmetric with a peak around 1. Also the ratio of s_x and s_y is asymmetric. The correlation plot in Figure A.20 shows an increased correlation between ϕ and s_y of 0.59 but a smaller correlation between ϕ and s_y with 0.24. Furthermore, s_x and s_y are strongly anti-correlated with the background offset B.

To reduce σ_θ the positioning of the graphene samples must be measured with improved accuracy. For example, a photo with a high-resolution camera could be used.

Performing a MC sampling on the Gaussian model as well, a comparison on BP characteristics can be drawn. This is presented in the next section.

---

[9] `https://docs.scipy.org/doc/scipy/reference/generated/scipy.optimize.curve_fit.html` (visited on 11/20/2025).

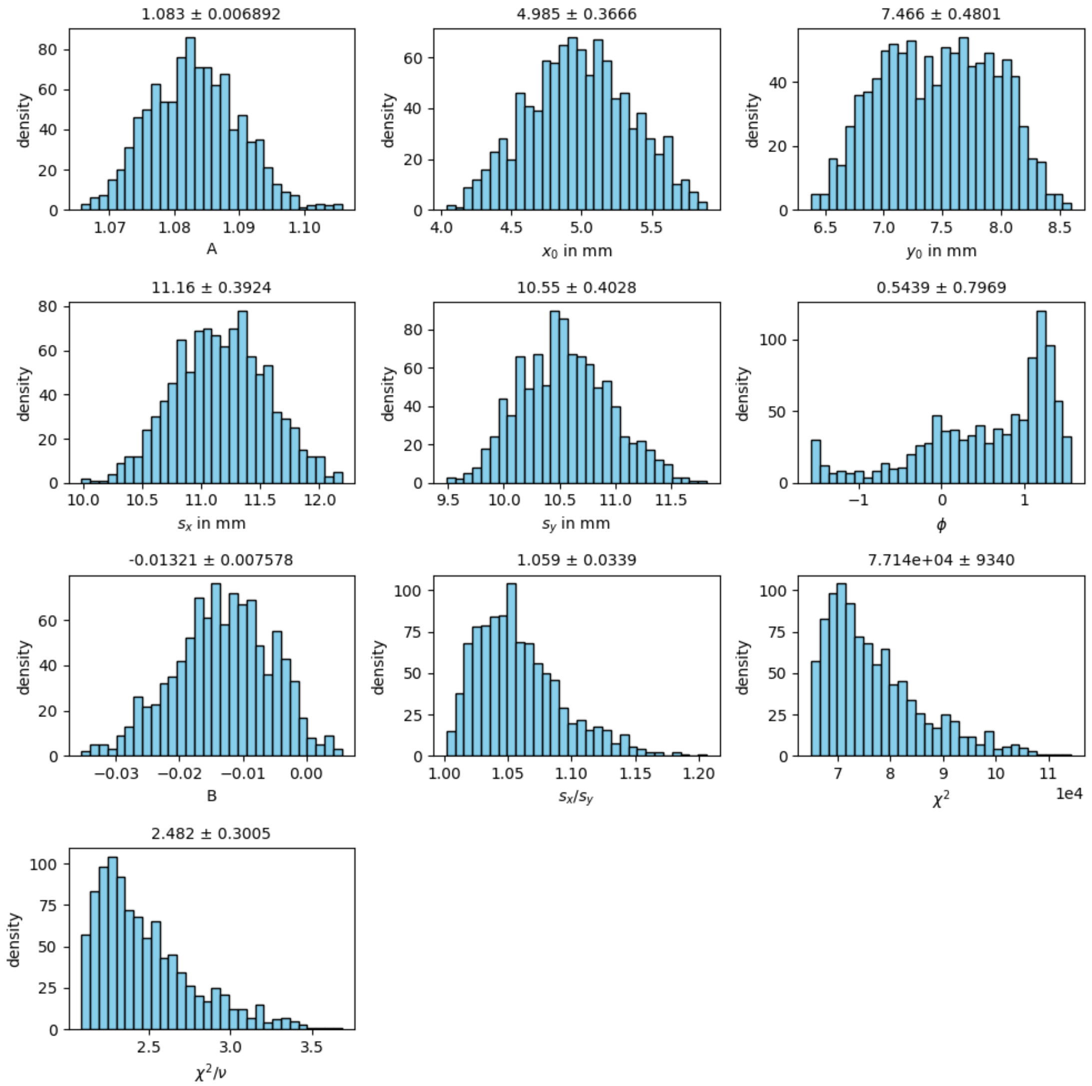

Figure 5.12.: Histograms of MC error propagation of graphene sample positions to the Lorentzian model parameters: BP center height A, BP center position x_0 and y_0, BP size s_x and s_y, rotation of the ellipsis ϕ, and a background offset B. The histograms of χ^2 and χ^2/ν are displayed as well.

5.4.4. Model comparison

The characteristics of the beam emitted from the plasma source are unknown. Therefore, the observed beam profile structure in the $I_\mathrm{D}/I_\mathrm{G}$ Raman scans is modeled independently of the analysis of the plasma source. The BP models (Lorentzian, Gaussian and generalized normal) are chosen empirically. General BP parameters that are valid across all models and the χ^2-values (see Table 5.2) are used to compare the models. The parameters are the BP center height A, the BP center position (x_0, y_0) and the BP size $(\mathrm{FWHM_x}, \mathrm{FWHM_y})$. To calculate the latter, a conversion factor is applied to the parameters $(s_\mathrm{x}, s_\mathrm{y})$ from the models. This is necessary because s_x and s_y are defined differently for each model. The conversion factors and their derivation is given in Section 5.4.2.

The uncertainty σ_θ from the MC analysis from the previous Section is propagated in the same way as Equations (5.11), (5.13) and (5.14).

BP center height:
The resulting A for the models are displayed in Figure 5.13. The values for the different models are not compatible within the 1 σ-uncertainty. The error bar of the generalized normal model is three times larger than for the other models. A correlates strongly with B (see Figure A.22) which is expected because B shifts the BP center height. This correlation is very weak for the other two models (see Figures A.20 and A.21).
The discrepancy for A between the different models is also indicated in the residuals Δ (see Figures 5.11c, A.16c and A.17c). The largest deviation between theory and experiment is observed around the center on sample 4.6. . Therefore, it is possible that all three models are unable to correctly determine the BP center height A.

BP location:
The results on the BP center position (x_0, y_0) are shown in Figure 5.14a. They are compatible for all models. Hence, all three models are equally suited or unsuited to determine the BP location.

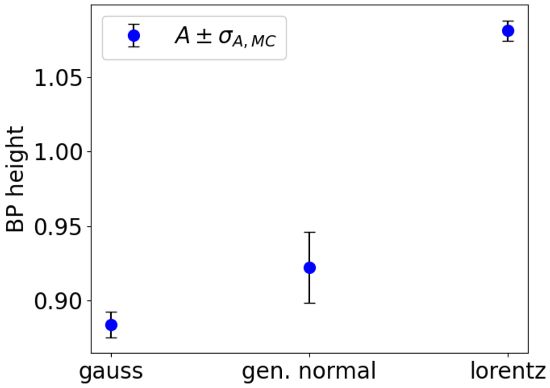

Figure 5.13.: Comparison of the beam profile center height A determined from a Gaussian, a generalized normal, and a Lorentzian model. The results are not compatible within the 1 σ-uncertainty which is denoted as $\sigma_{A,\mathrm{MC}}$ and is estimated from the MC-uncertainty propagation in Section 5.4.3.

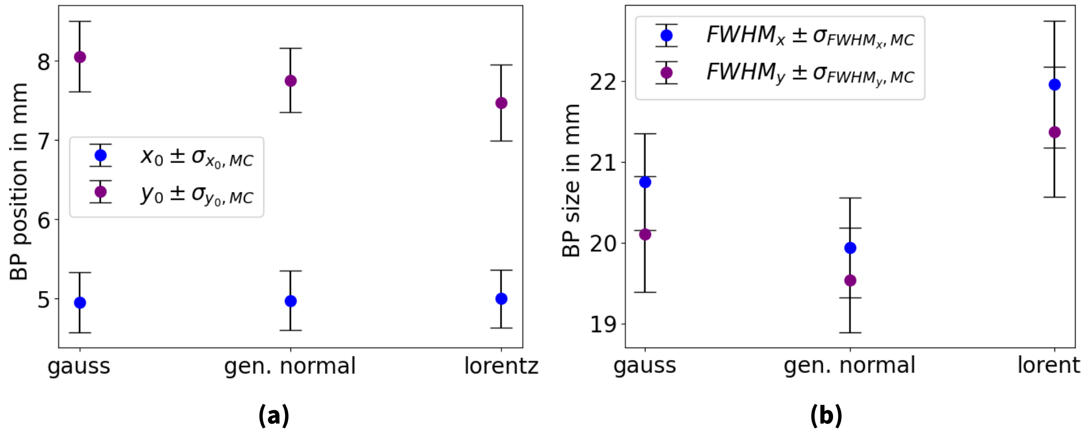

Figure 5.14.: Comparison of beam profile characteristics determined from a Gaussian, a generalized normal, and a Lorentzian model. The uncertainties are estimated from the MC-uncertainty propagation in Section 5.4.3. **(a)** Beam profile position (x_0, y_0). **(b)** Beam profile size defined through the FWHM. A detailed discussion is found in the main text.

BP size:
The results for the BP size ($\mathrm{FWHM_x}, \mathrm{FWHM_y}$) are displayed in Figure 5.14b. The values for the Gaussian model are compatible with the Lorentzian and the generalized normal model. The Lorentzian model is not compatible with the generalized normal model within the 1 σ-uncertainty. However, the values are of the same order of magnitude. The range for the BP size is thus $19 - 23$ mm.

5.5. Conclusion

Samples of a monolayer graphene on SiO_2/Si substrates were used to investigate the beam emitted from the plasma source. Two approaches were utilized to measure structural changes of the graphene caused by exposure to the plasma source:

In-situ sheet resistance: For an in-situ diagnostic tool, a contacting setup was developed to measure the sheet resistance of the graphene sample. The contact quality was tested for temperature changes of up to 300 °C. It was observed, that the contact was lost during an absolute temperature gradient of 4 °C/min. It was demonstrated that the measurement of the two-wire resistances allow the localization of the contact that is lost. Future experiments should perform heating procedures with a temperature gradient < 0.3 °C. A protective layer of gold sputtered onto the corners of the graphene sample is recommended to increase the robustness of the contacting setup.

Ex-situ CRM: The graphene samples were scanned ex-situ in a CRM. A set of loading parameters could be found that ensures an exposure of the graphene samples to the plasma source without removing the graphene layer. Furthermore, it was proven that the plasma source can remove the graphene but heating procedures to not.
The I_D/I_G ratio of the Raman scans was utilized for a determination of beam profile characteristics. A beam profile analysis was performed on a combined Raman map consisting of multiple Raman scans from multiple graphene samples. Three models were fitted to the data and an uncertainty was calculated for the model parameters via an MC error propagation. Beam characteristics were determined and compared for the different models. This beam profile analysis was intended as a proof principle that it is possible to measure a spatially resolved beam profile on graphene samples, that were exposed to the beam, with a CRM, and eventually determine beam profile characteristics from the Raman data. Hence, this method can be used, for example, for non-plasma based dissociators as well.
With the D/D' intensity ratio the defect types could be distinguished. Sample 3.2 could be identified as mainly containing vacancy defects and therefore a defect density of $L_D = 5.5\,\mathrm{nm}$ could be determined. Sample 4.6 was identified as containing a mixture of vacancy defects and sp^3-type defects. For this case, at the time of writing, no established model exists to map this mixture to a defect density.

Combination of in-situ sheet resistance and ex-situ CRM: An in-situ sheet resistance measurement was successfully performed on a graphene sample that was exposed to the plasma source for 24 h. Hydrogenation could not be observed with this sample because heating the sample to 300 °C did not reduce the resistance and the 2D/G intensity ratio of the Raman scans showed that the graphene was removed.
The combination of the sheet resistance and the CRM yielded that the longer the graphene sample is exposed to the plasma source, the more defects are produced. Furthermore, a decrease in sp^3-type defects was observed over time. Therefore the assumption was made, that adsorbed hydrogen atoms are removed during exposure to the plasma source. Hence, a maximum of hydrogen coverage exists. The plasma settings and the exposure time to reach the maximum was not found yet.

6. Characterization of the plasma source with OES

As described in Chapter 5, graphene samples are utilized as a sensor for atomic hydrogen and as a sensor for the beam profile of the beam that is emitted from the plasma source. To improve the interpretation of the observations described in that chapter, knowledge about the gas emitted from the source is desired. Therefore, it is aimed to characterize the plasma itself as it is the first station in the experiment. In contrast to thermal dissociators, the existence of hydrogen atoms is obvious in a plasma, because the radiation from atomic lines lies within the visible wavelength range and can therefore be observed by eye already. The plasma emission is measured and evaluated with OES (see Section 4.2).

In this chapter, a method to characterize a hydrogen plasma with OES is presented (see also Section 2.3.1). The absolute intensity calibration that is required for this method is shown in Section 6.1. Furthermore, studies are performed that test the sensitivity of OES measurements to various changes of the optical system.

In Section 6.2, the stability of the plasma over an operation time of multiple hours is evaluated.

In Section 6.3, the operation of the plasma source in E- and H-mode is demonstrated (see Section 2.2.3).

In Section 6.4, a method is presented and used on measured spectra to evaluate plasma parameters, that are the electron temperature T_e, the electron density n_e and the species densities n_H and n_{H_2}.

6.1. Absolute intensity calibration of the optical system for OES

For this work, an absolute intensity calibration is desired for a dedicated analysis of the plasma parameters. The absolute intensities of Balmer lines and the Fulcher-α-spectrum

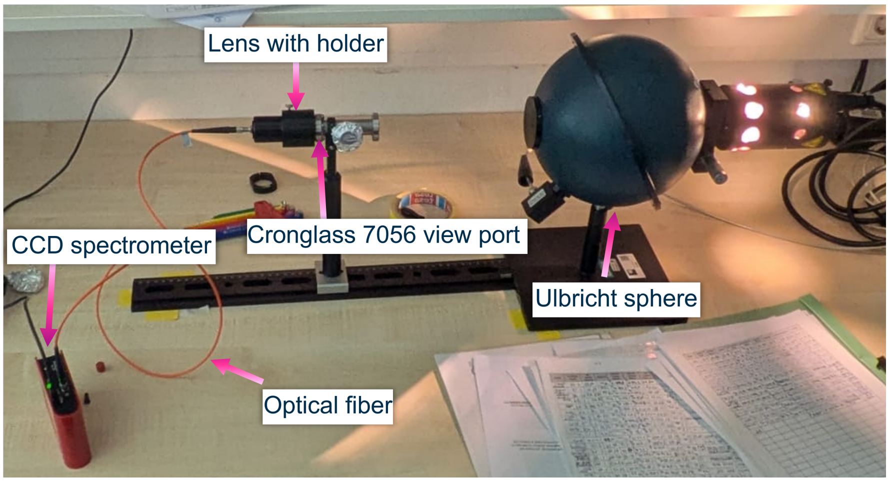

Figure 6.1.: Photo of the absolute intensity calibration setup of the optical system. On the left side are the components of the optical system for OES. The view port is pointed onto an Ulbricht sphere which is utilized for an absolute intensity calibration of the optical system.

are compared for measurements from OES and theoretical calculations from CR-models. (see Section 2.3.4.3). Therefore, the optical system has to be calibrated with respect to the absolute intensity. The calibration setup is shown in Figure 6.1. The optical system is presented in Section 4.2.2. For calibration, an Ulbricht sphere is used which is a homogeneous diffusive light source from which the number of photons per solid angle is known[1].

6.1.1. Determination of the calibration function

The measured intensity $I_{\text{ulbricht,measured}}(\lambda)$ has the units $\frac{\text{cts}\cdot\text{nm}}{\text{s}}$ because the measurement is normalized to s and the CCD chip integrates over a certain wavelength-range. The real intensity $I_{\text{ulbricht,real}}(\lambda)$ of the Ulbricht sphere is expressed in units of $\frac{\text{Photons}}{\text{m}^3\text{s}}$. Therefore, a calibration function $c(\lambda)$ is defined:

$$c(\lambda) = \frac{I_{\text{ulbricht,real}}(\lambda)}{I_{\text{ulbricht,measured}}(\lambda)} \tag{6.1}$$

with the units $\frac{\text{Photons}}{\text{m}^4}$. The calibration function in Equation (6.1) is chosen such that it has to be multiplied with a measured plasma spectrum. The real intensity is modeled with a polynomial of 9^{th} order. The uncertainty on $I_{\text{ulbricht,real}}(\lambda)$ is $< 1\,\%$ and is therefore

---

[1] Many thanks to Dr. Dirk Wünderlich, Dr. Richard Bergmayr and Prof. Dr. Ursel Fantz from IPP-Garching for providing the Ulbricht sphere and helping with the calibration procedure.

neglected because the uncertainty from the optical system, that is determined in the next section, is much larger.

For an absolute intensity calibration, the information of the plasma length l_p is required. The longer the plasma, the smaller the fraction of emitted photons reaching the optical system. To account for this, the measured intensity $I_\mathrm{plasma,measured}(\lambda)$ is multiplied with l_p:

$$I_\mathrm{plasma,absolute}(\lambda) = I_\mathrm{plasma,measured}(\lambda) \cdot c(\lambda) \cdot l_\mathrm{p} \tag{6.2}$$

The plasma length, however, is not known and must therefore be accounted within a sensitivity study. This is further discussed in Section 6.4.5.

6.1.2. Sensitivity of OES measurements to the alignment of the optical system

During the operation of the plasma source it was noticed that the measured intensity can be very dependent on the position of the mount and the lens. To account for this, the components of the optical system are aligned to each other and the position is marked. Since the calibration could only be performed at a late stage during this work, there is no measurement of the plasma with the aligned system. However, the applicability of the calibration function $c(\lambda)$ to measurements with the not-aligned system is tested. In Figure A.23 in Appendix A.3 the relative change in intensity is measured for different rotations and positioning of the optical components against each other. The result of this study shows a maximum change in relative intensity of about 12 %. This value is used as an uncertainty in the following.

6.1.3. Sensitivity of OES measurements to the exposure time

The so-called dark noise is a common background effect for optical spectrometers [111]. Thermal electrons are generated in the silicon structure of the CCD chip. This can also be correlated with the exposure time. Therefore, spectra of the Ulbricht sphere are measured with different exposure times and the effect on the spectra is investigated. In Figure 6.2a spectra for exposure times between 1 ms and 20 ms are compared. One curve on this plot corresponds to an average of a bunch of 10 spectra that were measured in a row. The curves for short exposure times show a higher noise level. This is also visible in the differences Δ in Figure 6.2b. They are defined as:

$$\Delta = I_{20\,\mathrm{ms}} - I_{x\,\mathrm{ms}}\,, \tag{6.3}$$

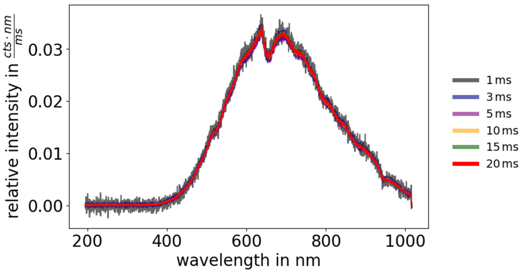

(a)

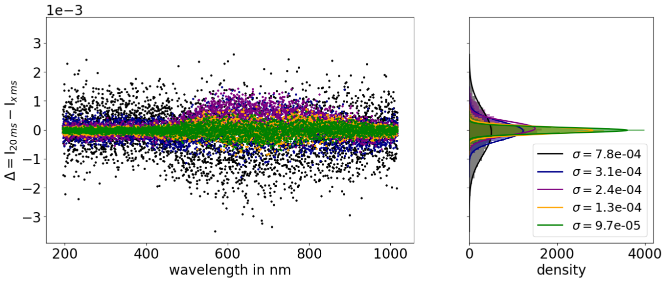

(b)

Figure 6.2.: Variation of intensity for different exposure times in ms. **(a)** Comparison of the spectrum of the Ulbricht sphere. **(b)** Differences between the intensities measured with an exposure time x and 20 ms. The legend shows x in ms.

where $x = [1, 3, 5, 10, 15]$. The differences do not show any significant dependence of the intensity measurement in the investigated range of exposure times.

The dark noise of the CCD spectrometer can dominate for large exposure times, especially if the spectrometer is not cooled [112]. However, the study in Figure 6.2 is performed only for exposure times up to 20 ms. For exposure times greater than this value, the spectrum was over saturated. Thus, the influence of the dark noise is investigated by measuring dark background spectra for exposure times of 50, 500 and 1000 ms. For every exposure time, a bunch of 10 spectra is measured in a row. The bunch is averaged over, and a mean value and a standard deviation are calculated. The result is displayed in Figure A.24. No exposure time dependence is observed.

6.2. Plasma emission stability

In the scope of the characterization of the plasma source, the stability of the plasma is of interest. It is possible that an atomic tritium source will be operated in a continuous mode. Therefore, minimal fluctuations in the plasma parameters will be required.

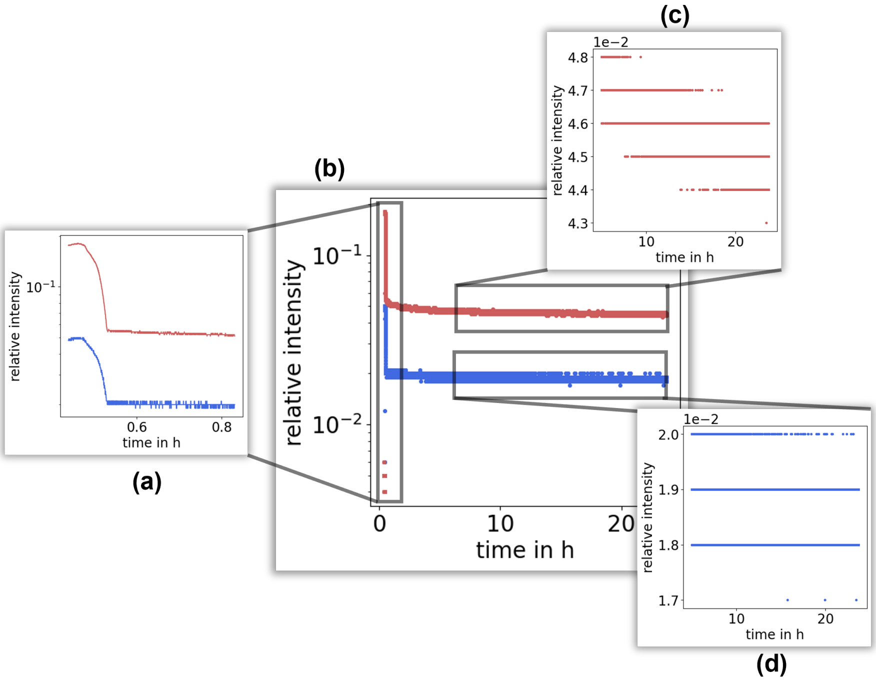

Figure 6.3.: Plasma stability measurement. A hydrogen plasma is operated at a gas flow of 0.5 sccm and a load power of $P_{\mathrm{RF}} = 350\,\mathrm{W}$. The α-line is plotted in *red*, the β-line is plotted in *blue*. The integration limits are 663 – 665.5 nm for the α-line and 485 – 491 nm for the β-line. **(a)** Start phase: The plasma is ignited with a gas flow of 2.5 sccm. **(b)** Full curve profile during the operation of the plasma. **(c)** Monitoring of the α-line for $t \geq 5\,\mathrm{h}$. **(d)** Monitoring of the β-line for $t \geq 5\,\mathrm{h}$.

The stability is investigated by tracking the atomic α- and β-line of a hydrogen plasma, that is operated for one day. The result is shown in Figure 6.3. In inset **(a)** the run-in phase is displayed. The plasma is ignited with a flow of 2.5 sccm After that, the flow is set to 0.5 sccm which is considered as the operating flow. The α- and β-line stabilized after 30 minutes. The fluctuations of the peak intensities after 5 h of operation are $\pm 4\,\%$ for the α-line and $\leq \pm 2\,\%$ for the β-line that is shown in inset **(c)** and **(d)**. A slight drift downwards is visible that is more pronounced for the α-line. Nevertheless, this is a first positive result in regard to developing an atomic tritium source.

Even more important than the stability is the achievable atomic yield. However, the determination of the atomic yield with OES requires an extensive analysis of the peak intensities. A method for the determination of different plasma parameters including the atomic density is presented in Section 6.4. There, the analysis is performed on one single spectrum. The knowledge gained from the stability measurement, could be used to propagate the results for the plasma parameters in time.

6.3. Plasma mode control

In Section 2.2 two operation modes of an ICP are introduced. The plasma can either be driven via capacitive coupling (E-mode) or inductive coupling (H-mode). Usually, the ignition of the plasma is started in the E-mode. To enter the H-mode, the power absorbed by the plasma has to be increased (see Figure 2.8). In terms of operation settings, this means decreasing the gas flow or increasing the drive power P_{RF}. The switch between E- and H-mode is often observed in a hysteresis that arises from different sustaining mechanisms and related collision processes (see References [58] and [63]). It is important to know the plasma settings for E- and H-mode because the intensity differs significantly and therefore also the plasma quantities like electron temperature, electron density and atomic density.

In this section, the transition of the plasma between E- and H-mode is investigated by varying P_{RF}. It is explicitly visible as a jump in the monitoring data of the α- and β-line. Because the intensity is much higher in the H-mode than in the E-mode, the exposure time is adjusted for every transition. An exposure time of 3 ms is set for the measurements in H-mode. An exposure time of 1000 ms is set for the measurements in E-mode. The monitoring data is not displayed here because many data points are over saturated when the plasma is transiting from E- to H-mode with a large exposure time. Thus, spectra are saved manually after every transition. The absolute intensities of the atomic α- β- and γ-lines and the molecular Fulcher-α-band are calculated by applying

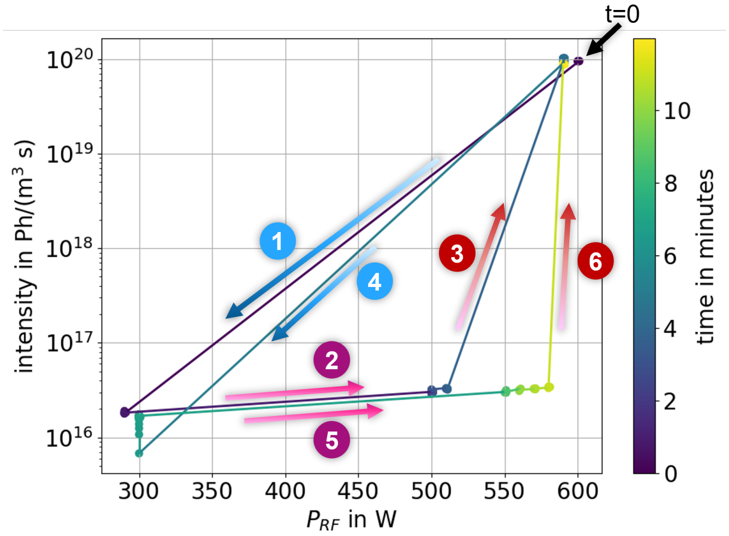

Figure 6.4.: Measurement of the intensity of the α-**line** for different drive powers. For a constant gas flow of 1 sccm the drive power is varied between 270 W and 600 W.

a background subtraction, the calibration function $c(\lambda)$ and the plasma length l_p (see Equation (6.2)). In Section 6.4.1 the determination of the peak intensities is explained in detail. The integration limits for the peak intensities are listed in Table 6.1.

In Figure 6.4 the calculated absolute α-line intensity is displayed (the transition measurement of the β- and γ-line and the Fulcher-α-band is shown in Figure A.25). At time $t = 0$ the plasma is in H-mode. Sudden variations in light intensity correspond to a switch in modes. From this, it is identified that data points with an intensity in the order of $10^{16}\,\mathrm{Ph/(m^3s)}$ correspond to the E-mode. The data points, that are around $10^{20}\,\mathrm{Ph/(m^3s)}$ correspond to the H-mode. Te measurement points are connected to show the observed hysteresis loop. A change of the hysteresis loop over time is observed. This is because the measurement was started a few minutes after the ignition of the plasma, so that the plasma was not yet stabilized and equilibrated with the cavity wall temperature. To measure a rather clear hysteresis loop, at least one hour should be waited between every change of P_{RF}.

In conclusion, it was demonstrated that a hydrogen plasma could be operated in E- and H-mode for a gas flow of 1 sccm. For further investigations of this transition, it is recommended to let the plasma stabilize for $t \geq 1\,\mathrm{h}$.

6.4. Determination of plasma parameters with OES

The optical system used in this work for OES has an absolute intensity calibration (see Section 6.1). Therefore the electron temperature T_{e}, the electron density n_{e}, the atomic density n_{H} and the molecular density $n_{\mathrm{H_2}}$ can be determined (see Section 2.3.4). In this Section, a graphical approach is presented and discussed. It is intended as a demonstration of this method rather than a diagnostics framework with a complete consideration of all physical contributions. Several processes that are not included in this method but could change the resulting plasma parameters are discussed in Section 6.4.5. The analysis presented here is performed with python 3.12.

It is a graphical approach that iteratively determines an allowed phase space for the plasma parameters such that theory and experiment are compatible. The plasma parameters serve as an input for the theoretical calculations, however, for now a global fit was not considered since the phase space has many local minima, leading to unreliable results.

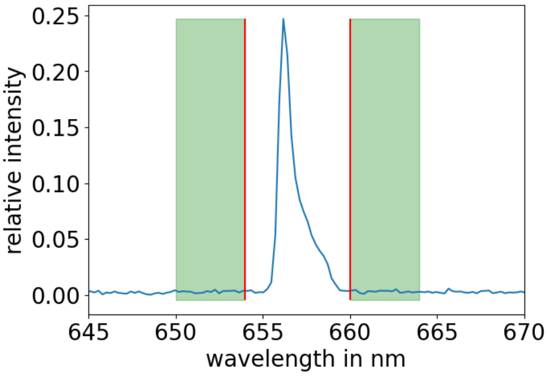

Figure 6.5.: α-line of the hydrogen plasma spectrum. The red lines are the integration limits for the determination of the peak intensity. The green area is the background region.

6.4.1. Pre-processing of the measured spectra

Hydrogen plasma spectra (see Figure A.26a) are measured with the optical system that is shown in Figure 6.1. The data is recorded manually through the export button in the software of the plasma source manufacturer SVTA[2].

Bunches of spectra:
To minimize fluctuations of the spectrometer, the spectra for the analysis are saved in bunches. For the spectrum that is used in this analysis, one bunch consists of 10 spectra. The first step in the analysis script is to average the spectra over the bunch.

Spectra quality investigation:
The bunch-averaged spectrum is manually investigated. In the following, one spectrum is chosen that is shown in Figure A.26. An asymmetry in the measurement is visible, especially for the α-line in Figure A.26b. This is presumably a property of the spectrometer. The spectrum chosen for this analysis is an E-mode spectrum that was operated with a plasma driving power of $P_{\mathrm{RF}} = 350\,\mathrm{W}$. The inlet pressure was $0.27\,\mathrm{mbar}$.

Background subtraction:
For the atomic lines a background subtraction is performed automatically. The background level is determined from the intervals to the left and right of the peak, where no other peak is located. In Figure 6.5 the background is calculated from the green region. The size of the green bands is $r = 4\,\mathrm{nm}$. The background level is determined by averaging the intensities in the green bands. The effect of the background correction on the atomic peak intensities is shown in Figure 6.6 (circles vs. triangles). The effect is most significant for the α-peak.

---

[2] © 2025 SVT Associates, Inc. 7620 Executive Drive, Eden Prairie, Minnesota 55344 USA

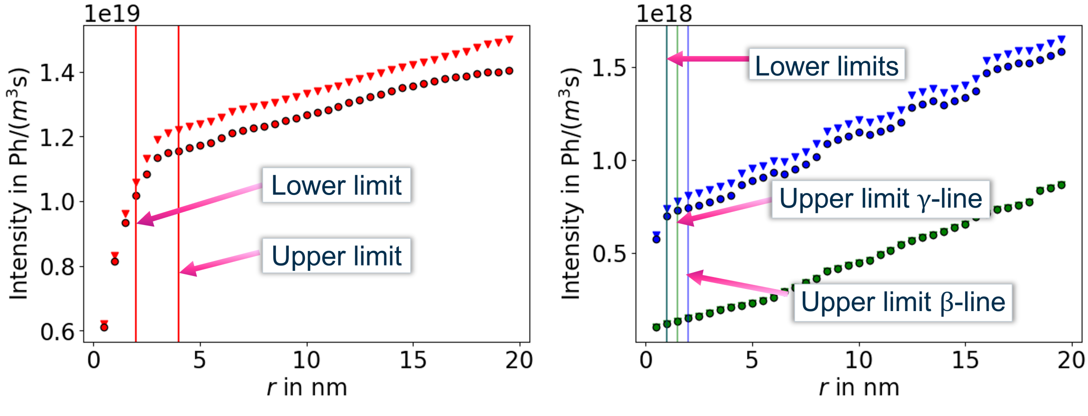

(a) **(b)**

Figure 6.6.: Effect of the peak intensities for different radii r. The α-line intensity in **red**, the β-line intensity in **blue** and the γ-line intensity in **green**.
Triangles: Intensities *without* background subtraction. **Circles:** Intensities *with* background subtraction.

For the Fulcher-band the background subtraction is performed by hand. The peaks within 600 − 640 nm are not so clearly distinguishable from the background as the atomic lines (see Figure A.26e). Here, a background correction of -1.25×10^{-3} is applied.

Absolute intensity calibration of the spectrum:
The spectrum of choice was recorded with an exposure time of the spectrometer of 100 ms. Hence, it is multiplied by 10 to normalize it to 1 s. The spectrum is transformed to a Photons/($\mathrm{m}^3 \cdot \mathrm{s}$) scale by applying the calibration function $c(\lambda)$ and the plasma length l_p from Equation (6.2). The plasma length is estimated to be in the order of magnitude of the length of the plasma cavity $l_p = 10\,\mathrm{cm}$. In this work, the effect of opacity is not considered. A detailed discussion is given in Section 6.4.5.

Integration of peak intensities:
The peaks are numerically integrated with the function *scipy.integrate.simpson* from python. It utilizes the Simpson's rule that is generally more accurate than the trapezoidal rule or Riemann sums because it approximates the curve with parabolas, which better account for the function's concavity [113]. A study on the integration limits is performed. The intensities for the atomic lines are calculated for different integration limits. The integration interval is defined symmetrically around the literature value l of the atomic line[3] $[l - r, l + r]$. The „radius“ r is varied between 0.5 nm and 10 nm. The result is shown in Figure 6.6. Especially for the α-line intensity, the integration limits are sensitive to r. For $r < 4\,\mathrm{nm}$, not the full peak is considered. For $r > 4\,\mathrm{nm}$ the intensity

---

[3] `https://physics.nist.gov/PhysRefData/ASD/lines_form.html` (visited on 11/21/2025).

Table 6.1.: Integration limits used for the determination of peak intensity.

line/band	lower int. limit	upper int. limit
α	654	660
β	485	488
γ	433	435.5
Fulcher-α	600	640

increases constantly because it takes into account other peaks from the hydrogen plasma spectrum. Furthermore, a prominent asymmetry in the α-line (see Figure A.26b) causes the sensitivity on the α-line to the r. Thus, the integration limits should be chosen as close as possible to the peak but not too close such that the hole peak is considered, and an asymmetric choice of the integrations limits is favorable. The integration limits chosen in this work are listed in Table 6.1. The asymmetry of the peaks (see *e.g.* Figure 6.5) is reflected in the integration limits as well. The integration limits for the Fulcher-α-band are motivated in Section 2.3.2.

The output of the analysis in this section is I_{measured}. An error band of 12 %, which is motivated in Section 6.1, is added. This is compared to I_{theory} that is calculated in the next section.

6.4.2. Calculation of theoretical peak intensities

Theoretical peak intensities I_{theory} are calculated through

$$I_{\text{theory}} = n_0\, n_{\text{e}}\, R_{0,p}(T_{\text{e}}, n_{\text{e}}, n_0, T_0) A_{p,k} \ , \tag{6.4}$$

with $n_0 = n_{\text{H,H}_2}$ depending on whether an atomic peak intensity or a molecular spectrum is calculated. The $R_{0,p}$ are the population coefficients that can be calculated with CR-model solvers. In this work, the CR model solver *Yacora on the web* [70] is used which is accessible on the web. It is operated by the IPP at the MPG in Garching, Germany. A detailed explanation for this solver is given in Section 2.3.3. As input parameters, the electron temperature T_{e}, the electron density n_{e}, the particle temperature $T_0 = T_{\text{H,H2}}$ and the particle density n_0 are required. All of them are unknown. Therefore, $R_{0,p}$ is calculated for a set of T_{e}, n_{e} and n_0. The effect of T_0 on the result is supposed to be small because the hydrogen mass is much larger than the electron mass, and therefore the processes are dominated by the electron dynamics [70].

An error band is added to the calculation of I_{theory} in Equation (6.4). It is an acceptance range for the determination of the plasma parameters in Section 6.4.4. The size of the error band depends on the accepted phase space of the plasma parameters. The accepted phase space means the values for T_e, n_e, n_H and n_{H_2} that are allowed such that theory and experiment is in agreement. If the band is too small, the phase space for the plasma parameters is empty. Hence, the error band is gradually increased until a set of plasma parameters is found. In this work, the error band was found to be ±20 %. However, the size of the error band was not explicitly pushed to the minimum as this analysis is just a demonstration of this method to determine plasma parameters.

6.4.3. Comparison of experimental and theoretical intensities

After the determination of the theoretical and experimental peak intensities, they are compared. As an example, the comparison is illustrated in Figure 6.7. The atomic lines are plotted over T_e for fixed n_e and n_H (see Figure 6.9d). Thus, there is a large set of plots for different n_e and n_H. The atomic ratios are plotted over n_e for fixed T_e and n_H. Thus, there is a large set of plots for different T_e and n_H (see Figure 6.7b). For the Fulcher-band a similar set of intensity-T_e-plots is generated (see Figure 6.7c).

6.4.4. Determination of plasma parameters with a graphical approach

The theoretical intensities have intercepts with the experimental values. Because both contain an error band, the intercepts of the error bands are calculated. The values of T_e and n_e for the different intercepts span a phase space. The resulting phase space from the atomic lines is illustrated in Figure 6.8. It is, again, a set of plots for different n_H. Every band represents a set of intercepts for one atomic line. As an example, the plots for $n_H = 10^{18}$, 10^{19} and $10^{20}\,\mathrm{m^{-3}}$ are shown in the Figures 6.8a, 6.8b and 6.8c. The region of interest is where all the bands overlap. Here, the theory is compatible with the experiment.

A similar phase space is produced for the atomic line intensity ratios. The ratios only have one plot because the particle density cancels out (see Equation (2.45)). The region of interest is hatched in white. Furthermore, the phase space for a set of n_{H_2} of the Fulcher-band is shown in Figure 6.9. The acceptance range is narrowed down by cutting the phase-spaces to the region of interest and iteratively comparing them for atomic lines, atomic ratios and the molecular band. The atomic and molecular density can be narrowed down with Equation (2.48). The total particle density inside the plasma

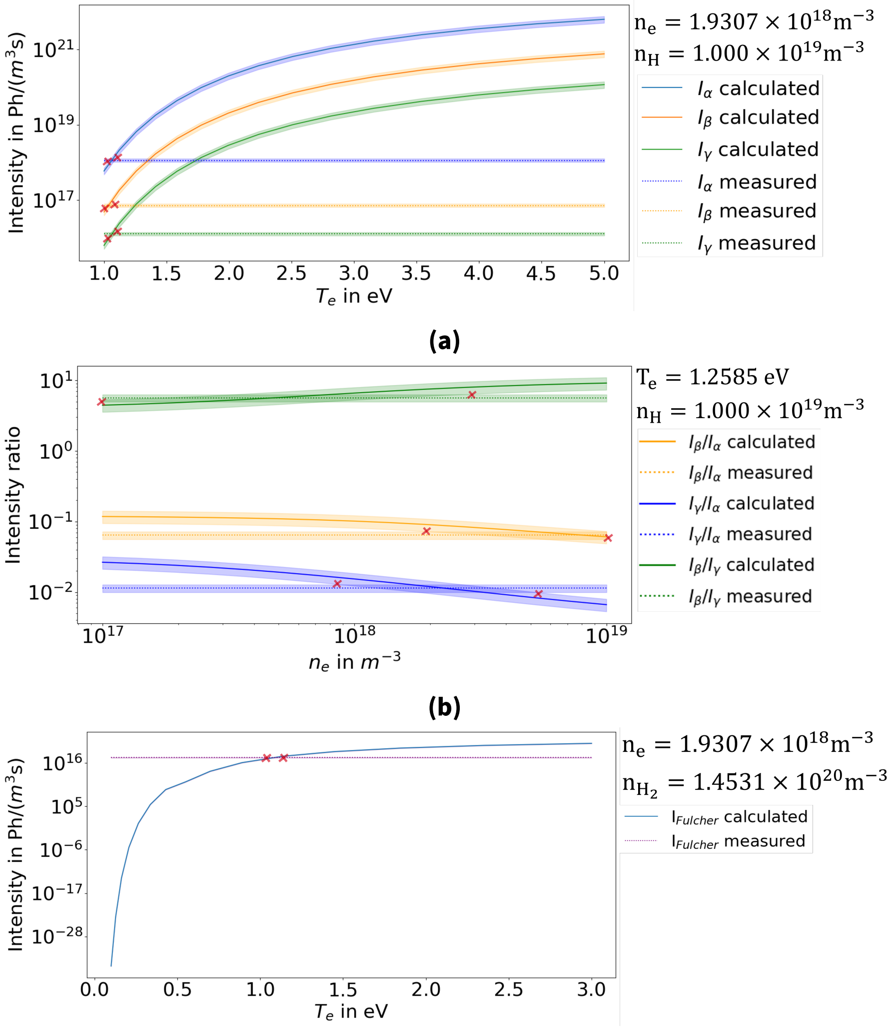

(a)

(b)

(c)

Figure 6.7.: Comparison between theory and experiment. Solid lines are from theoretical calculations. Dotted lines are single values from one measured spectrum. **(a)** Comparison of calculated atomic line intensities with measured absolute line intensities with fixed n_e and n_H. **(b)** Comparison of calculated atomic line intensity ratios with measured line intensity ratios with fixed T_e and n_H. **(c)** Comparison of the calculated Fulcher-band intensity with measured and extrapolated absolute Fulcher-band intensity with fixed n_e and n_H. The red crosses indicate the intercepts of the error bands.

is estimated as $n = 2.38 \times 10^{20}\,m^{-3}$ assuming a temperature of $T_{gas} = 8000\,K$[4] and a measured pressure of $p = 0.27$ mbar. The narrow down procedure works as follows:

---

[4] The choice was made due to the default value T(H) in Yacora on the web. However, it can be assumed that the actual gas temperature is smaller. Nevertheless, this choice is sufficient to demonstrate the method.

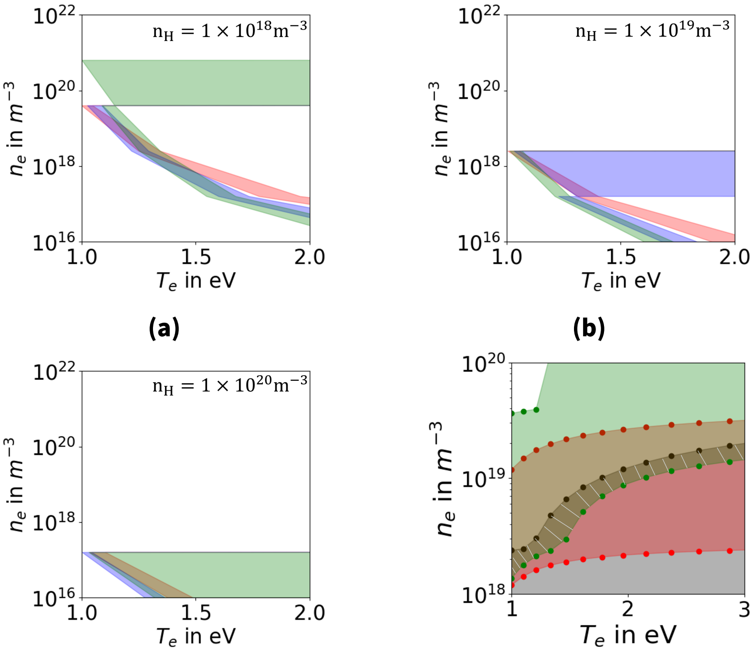

(a) **(b)**

(c) **(d)**

Figure 6.8.: T_e-n_e phase space resulting from the intercepts of calculated and measured intensities (see Figure 6.7). **(a)**-**(c)** Phase space for atomic line intensities. In red: α-line. In blue: β-line. In green: γ-line. Region of interest: The region where all bands overlap. If the python does not find any intercepts, the value is set to $T_e = 10$ eV **(d)** Phase space for atomic line-intensity ratios. In red: I_γ/I_α. In gray: I_β/I_γ. In green: I_β/I_α. White hatched: Region of interest. The region where all bands overlap. If the python script does not find any intercepts, the value is set to $n_e = \pm 10^{22}\,m^{-3}$.

1. Intensities are calculated for a wide range of n_e and T_e. Atomic and molecular density is roughly estimated by calculating the total particle density and choosing a range of $0.1\,\% \cdot n - 100\,\% \cdot n$ for n_H and n_{H_2}, respectively.
2. The n_e and T_e phase space for the absolute atomic intensities is plotted and the region where the bands do not overlap is filtered. For example, in Figure 6.8 **(a)**-**(c)** T_e is restricted to $\approx 1.0 - 1.5$ eV.
3. Further restrictions are made with the phase space of the Fulcher-band. In Figure 6.9 the phase space is plotted for four different n_{H_2} as an example. The regions where the band is not located is cut. In Figure 6.9 T_e is restricted to $\approx 1.0 - 1.5$ eV as well.
4. Furthermore, n_e is restricted by the phase space plot of the atomic line ratios. In Figure 6.8d n_e is restricted to $\approx (1 - 5) \cdot 10^{18}\,m^{-3}$. This refines the mesh on n_H

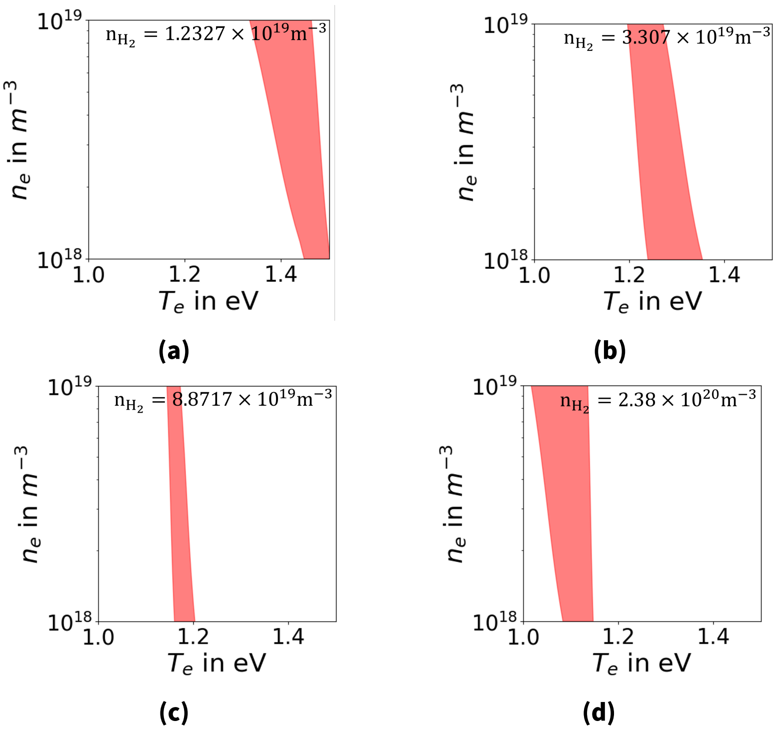

(a) (b) (c) (d)

Figure 6.9.: T_e-n_e phase space resulting from the intercepts of calculated and measured intensities of the Fulcher-band (see Figure 6.7c). The region of interest is marked in red.

and n_{H_2}. For example, $n_H = 10^{20}$ m^{-3} is excluded with the limits on n_e (see Figure 6.8c).

5. The densities n_H and n_{H_2} are also restricted via rearrangement of Equation (2.48).
6. Repeat from step 2 and if the theoretical calculations are not fine enough to further restrict the phase space repeat from step 1 with the refined parameter mesh.

The plasma parameters that result from the narrow-down process are listed in Table 6.2.

6.4.5. Effects that have an influence on the evaluation of plasma parameters

As mentioned before, the values in Table 6.2 are not final values that characterize the plasma source but rather a demonstration of the analysis approach to determine plasma parameters. For a full characterization of the plasma source, a couple of effects have to be considered within sensitivity studies. These effects are discussed in this section.

Table 6.2.: Results for plasma parameters determined with a graphical approach only for demonstration purposes. Only direct excitation is considered, and effects described in Section 6.4.5 are neglected.

parameter	determined range
T_e	$(1.0 - 1.2)$ eV
n_e	$(1.4 - 2.6) \cdot 10^{18}\,\mathrm{m}^{-3}$
n_H	$(0.2 - 2) \cdot 10^{19}\,\mathrm{m}^{-3}$
n_{H_2}	$(2.18 - 2.36) \cdot 10^{20}\,\mathrm{m}^{-3}$

6.4.5.1. Excitation channels

The contribution to the intensity of atomic lines consists of multiple excitation channels (see Figure 2.11). In case of an ionizing plasma [73], the direct excitation and dissociative excitation are dominant. An example by D. Wünderlich and U. Fantz is shown in Figure 6.10. In a plasma with a drive power of $P_{RF} = 70$ kW and a pressure of 0.8 Pa the contribution of the dissociative channel is up to 25 %. In this work, only the direct excitation channel was used. The parameters that are varied are T_e, n_e and n_H. Taking the dissociative excitation channel into account, n_{H_2} would also be a free parameter. This increases the complexity of the graphical analysis approach. Furthermore, it is possible that other excitation channels contribute as well (see Figure 2.11c) if $T_e \sim 1$ eV. Therefore, a purely analytical approach is recommended.

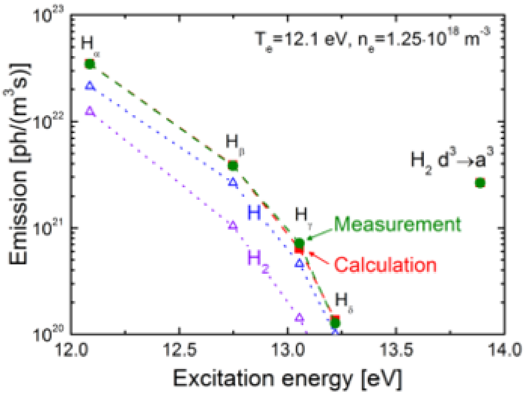

Figure 6.10.: Contributions of different excitation channels to the emission of atomic Balmer lines. Blue: contribution from direct excitation. Purple: Contribution from dissociative excitation. Reprinted from [73].

6.4.5.2. Fulcher extrapolation

The part of the Fulcher spectrum that is observable with the optical system (600 – 640 nm) has to be extrapolated to consider the full spectrum [69]. In this work, a fixed extrapolation factor of 2 is applied to the integrated spectrum. This value was taken after discussions with D. Wünderlich and R. C. Bergmayr that estimated this value from experience in the extrapolation procedure (see *e.g.* References [67] and [69]).

6.4.5.3. Plasma length

The emission intensity measured by the optical system for OES depends on the length of the plasma l_p in the line-of-sight. The longer the plasma, the smaller is the fraction of the light seen by the optical system. The plasma length is a multiplicative factor on the absolute intensity (see Equation 6.2). For a demonstration of the method to determine plasma parameters an „order of magnitude“-estimation of l_p is sufficient. However, the acceptance range of the phase space can be very sensitive to changes in multiplicative factors.

6.4.5.4. Opacity

Not all photons that are produced inside the plasma find their way to the optical spectrometer. This optical thickness of the plasma is called opacity. Some photons are absorbed by the plasma itself. D. Wünderlich et al. observed an overestimation of n_e by almost a factor of 5 and T_e by 20 % when opacity is not considered [114]. Furthermore, an overestimation for the atomic fraction n_H/n_{H_2} of 3.6 was observed. In the scope of an atomic tritium source it is very important to know the atomic fraction precisely. Therefore, the effect of opacity needs to be studied. The consideration of opacity requires the *a priori* calculation of a full set of population escape factors. For this, the plasma geometry and expected emission profiles must be taken into account. The factors are then used as an input for the CR model calculations [114].

6.5. Conclusion

In this section, the plasma source was characterized in terms of plasma emission stability, plasma mode control, and a method to determine the plasma parameters T_e, n_e, n_H and n_{H_2} was presented.

Firstly, an absolute intensity calibration of the optical system was performed with an Ulbricht sphere. Secondly, different sensitivity studies on the spectra were performed: An uncertainty of 12 % on the measurement was evaluated from the dependence of the measurement to the alignment of the components of the optical system. Furthermore, the exposure time dependency from *e.g.* dark noise was investigated. However, no significant dependence was observed.

Plasma stability was investigated by running a hydrogen plasma for 24 h and monitoring the α- and β-line intensities. The results showed a rather stable plasma after a run-in phase of 5 h with a maximum fluctuation of 4 % in the α-line intensity and 2 % in the β-line intensity. The knowledge gained from this measurement, can be used in the future to propagate the results for the plasma parameters in time.

It was demonstrated that the plasma can be operated in a capacitive coupled E-mode or in an inductive coupled H-mode. A hysteresis was observed for the transition between the two modes. However, the hysteresis was changing, most probably because the plasma was not yet thermally stabilized with the cavity walls, this needs further measurements for investigation.

Finally, a method was presented to determine plasma parameters with OES. This method was demonstrated on one spectrum that was measured from a plasma in E-mode. Theoretical calculations were graphically compared to measurements. Iteratively, the acceptance region for the plasma parameters was reduced until a set of electron temperature T_e, electron density n_e, atomic density n_H and molecular density n_{H_2} was found. Since some contributions could not be considered in the scope of this work, the parameters are only for demonstration purposes.

Summary and Outlook

The KATRIN experiment probes the effective anti electron neutrino mass. Recently, the most stringent upper limit of 0.45 eV (90 % C.L.) from direct measurements was reported [3]. For future neutrino mass experiments, a sensitivity on the neutrino mass below inverted mass ordering is aimed for. Therefore, new technologies need to be researched and developed. One limitation of the sensitivity in KATRIN results from the broadening of the $^3\mathrm{HeT}^+$-FSDs that are the product of the molecular tritium decay. Sensitivity studies have shown that significant improvements can be made by transitioning from molecular to atomic tritium. Hence, current efforts aim to develop an atomic tritium source.

As a first step, the KAMATE collaboration aims to identify suitable atomic sources that dissociate molecular tritium. Therefore, three commercially available atomic sources need to be characterized with nonradioactive hydrogen before tritium operation.

The goal of this thesis was the commissioning and characterization of a plasma source in a dedicated vacuum setup with protium. The characterization was chosen to be performed in a twofold manner. The first one is the characterization of the beam emitted from the plasma source. The second one is the characterization of the plasma itself. This is a significant advantage of plasma-based dissociation devices compared to thermal crackers because the plasma can be investigated directly with noninvasive OES.

B/BN deposition on glass
In this work, a study was performed that analyzed glass slides after exposing them to the plasma source. No significant boron or boron nitride deposition could be observed by using microscopy technologies such as DLI, SEM and WLI. An upper limit of 10 nm B/BN layer thickness was found. Therefore, further investigation tools can be placed in front of the plasma source like delicate QMS devices. However, BN flakes were found at the viewport, which is at the gas inlet side of the source. The studies were performed in a horizontal orientation of the source. Thus, observations of B/BN contamination could be different when the source is operated in a vertical orientation, as it would be the case for the Beam for Atomic Tritium Experiment (BeATE) [48] or the MATS setup.

Characterization of the beam emitted from the plasma source
Graphene was utilized as a beam sensor. The structural changes that appear on the

graphene sample during the exposure to the plasma source needed to be monitored. This challenge was met in a qualitative and quantitative way by utilizing a combination of ex-situ Raman spectroscopy and in-situ sheet resistance measurements. First tests were performed that characterized the behavior of the electrical contact during heating procedures of up to 300 °C. The main results for the experiments with graphene were:

- First successful in-situ sheet resistance monitoring of a graphene sample exposed to the plasma source. On the basis of the findings in this work, upgrades to the hardware setup are being made to improve reproducibility of the sheet resistance measurements when heating the samples up to 300 °C. In a joint work with M. Lai and G. Zeller from TLK and with M. Müller and S. Kempf from the Institute of Micro- and Nanoelectronic Systems (IMS), attempts are made to sputter gold onto the corners of the graphene samples to protect them from thermal movement of the contacting washers when large temperature gradients are applied.
- A novel method was demonstrated that utilized the $I_{\mathrm{D}}/I_{\mathrm{G}}$ ratio of the two dimensional Raman scans of the graphene samples. It was demonstrated that a determination of beam profile characteristics like beam profile center position and beam profile size is possible with this method. In the future, graphene samples could be exposed to thermal sources that are currently being characterized within the KAMATE collaboration. Thus, the beams of the sources could be analyzed and compared.
- The combination of the findings with the in-situ sheet resistance measurements and the ex-situ CRM scans yielded a decrease in the amount of sp^3-type (hydrogenation) defects during exposure to the plasma source. Therefore, the assumption was made that the plasma source firstly produces hydrogenation and after a local maximum is reached (which was observed in the sheet resistance during exposure), the hydrogenation is removed. For future work, it could be possible to observe a beam profile in the $I_{\mathrm{D}}/I_{\mathrm{D'}}$ ratio if the graphene sample is loaded so that the local maximum in sheet resistance is not exceeded.

Characterization of the plasma with OES
In low temperature plasmas OES is widely used because it is noninvasive and very powerful if supported by theoretical calculations from CR-models [20]. The main results are:

- The plasma stability was investigated by monitoring the atomic α- and β-lines over a period of 24 hours. The results showed a rather stable plasma after a run-in phase of 5 h with a maximum fluctuation of 4 % in the α-line intensity and 2 % in the β-line intensity.

- Plasma source settings were found that allow E- and H-mode operation. A hysteresis was measured between the two modes. For future studies a stabilization time of a 5 hours is recommended due to thermalization of the plasma with the cavity walls.
- An absolute intensity calibration of the optical system for OES was performed with an Ulbricht sphere at the IPP in Garching with D. Wünderlich, R.C. Bergmayr and U. Fantz. Various sensitivity studies of the optical system were performed that resulted in an systematic uncertainty of 12 % on the measured spectra.
- A graphical approach was demonstrated that determined plasma parameters like electron density, electron temperature, atomic density and molecular density for one hydrogen plasma spectrum in E-mode. In the future, this method could be extended by including further excitation channels in the calculations. Furthermore, sensitivity studies need to be performed concerning the effect of the Fulcher extrapolation, the plasma length and the opacity on the plasma parameters. Implementing these open points as extensively as possible would yield reliable results for quantifying the atomic and molecular density, and therefore, the dissociation fraction.

In summary, the twofold characterization of the plasma source for atomic hydrogen was demonstrated successfully. As a next step, the transition to tritium could be done. Currently, there are no CR models for T and T_2. To determine plasma parameters in a low temperature tritium plasma, an extension of these models to tritium would be required. In this regard, cross section calculations would have to be performed that would serve as an input in the CR models.

Recently, A. Semakin et al. [50] proposed a different approach for an atomic tritium source than the four-staged method followed by KAMATE. They suggested to dissociate T_2 at already cryogenic temperatures of 1 K with an RF discharge. Therefore, the relevance of this thesis increases because cryogenic plasmas can be studied with OES as well.

Bibliography

[1] Y. Fukuda et al. „Evidence for Oscillation of Atmospheric Neutrinos“. In: *Physical Review Letter* 81.8 (Aug. 1998), pp. 1562–1567. DOI: `10.1103/PhysRevLett.81.1562`.

[2] S. Navas et al. „Review of Particle Physics“. In: *Physical Review D* 110.3 (Aug. 2024), p. 030001. DOI: `10.1103/PhysRevD.110.030001`.

[3] M. Aker et al. „Direct neutrino-mass measurement based on 259 days of KATRIN data“. In: *Science* 388.6743 (2025), pp. 180–185. DOI: `10.1126/science.adq9592`.

[4] Max-Planck-Institut für Kernphysik Heidelberg. „1000 days of neutrino mass measurements“. (Oct. 2025). URL: `https://www.mpi-hd.mpg.de/mpi/en/public-relations/news/news-item/1000-days-of-neutrino-mass-measurements` (visited on 11/19/2025).

[5] TRISTAN Group. „Conceptual Design Report: KATRIN with TRISTAN modules“. Tech. rep. KIT, (2021). URL: `https://www.katrin.kit.edu/downloads/TRISTAN__Technical_Design_Report%20(10).pdf`.

[6] S. Mertens, T. Lasserre, S. Groh, G. Drexlin, F. Glück, A. Huber, A.W.P. Poon, M. Steidl, N. Steinbrink, and C. Weinheimer. „Sensitivity of next-generation tritium beta-decay experiments for keV-scale sterile neutrinos“. In: *Journal of Cosmology and Astroparticle Physics* 2015.02 (Feb. 2015), p. 020. DOI: `10.1088/1475-7516/2015/02/020`.

[7] S. Schneidewind, J. Schürmann, A. Lokhov, C. Weinheimer, and A. Saenz. „Improved treatment of the T_2 molecular final-states uncertainties for the KATRIN neutrino-mass measurement“. In: *The European Physical Journal C* 84.5 (May 2024), p. 494. DOI: `10.1140/epjc/s10052-024-12802-w`.

[8] A. Saenz, S. Jonsell, and P. Froelich. „Improved Molecular Final-State Distribution of HeT^+ for the β-Decay Process of T_2“. In: *Phys. Rev. Lett.* 84.2 (Jan. 2000), pp. 242–245. DOI: `10.1103/PhysRevLett.84.242`.

[9] J. A. Formaggio, A. L. C. de Gouvêa, and R. G. H. Robertson. „Direct measurements of neutrino mass“. In: *Physics Reports* 914 (Feb. 2021), pp. 1–54. DOI: `10.1016/j.physrep.2021.02.002`.

[10] A. D. Lambert, B. M. McGregor, R. J. H. Morris, C. P. Parry, D. P. Chu, G. A. Cooke, P. J. Phillips, T. E. Whall, and E. H. C. Parker. „Contamination issues during atomic hydrogen surfactant mediated Si MBE“. In: *Semiconductor Science and Technology* 14.2 (Feb. 1999), pp. L1–L4. DOI: `10.1088/0268-1242/14/2/001`.

[11] K. E. Whitener. „Review Article: Hydrogenated graphene: A user's guide“. In: *Journal of Vacuum Science & Technology A: Vacuum, Surfaces, and Films* 36.5 (Sept. 2018), 05G401. DOI: `10.1116/1.5034433`.

[12] A. C. Ferrari and D. M. Basko. „Raman spectroscopy as a versatile tool for studying the properties of graphene“. In: *Nature Nanotechnology* 8.4 (Apr. 2013), pp. 235–246. DOI: `10.1038/nnano.2013.46`.

[13] T. Fournier, C. Crespos, I. Arshad, M. Dubois, B. Lassagne, M. Monthioux, F. Piazza, and P. Puech. „Quantifying the sp3/sp2 ratio in functionalized graphene“. In: *Carbon* 244 (Sept. 2025), p. 120657. DOI: `0.1016/j.carbon.2025.120657`.

[14] M. M. Lucchese, F. Stavale, E. H. M. Ferreira, C. Vilani, M. V. O. Moutinho, R. B. Capaz, C.A. Achete, and A. Jorio. „Quantifying ion-induced defects and Raman relaxation length in graphene“. In: *Carbon* 48.5 (Apr. 2010), pp. 1592–1597. DOI: `10.1016/j.carbon.2009.12.057`.

[15] A. Eckmann, A. Felten, A. Mishchenko, L. Britnell, R. Krupke, K. S. Novoselov, and C. Casiraghi. „Probing the Nature of Defects in Graphene by Raman Spectroscopy“. In: *Nano Letters* 12.8 (Aug. 2012), pp. 3925–3930. DOI: `10.1021/nl300901a`.

[16] D. Diaz Barrero, G. Zeller, M. Schlösser, B. Bornschein, and H. H. Telle. „Versatile Confocal Raman Imaging Microscope Built from Off-the-Shelf Opto-Mechanical Components“. In: *Sensors* 22.24 (Dec. 2022), p. 10013. DOI: `10.3390/s222410013`.

[17] G. Zeller et al. „Demonstration of tritium adsorption on graphene“. In: *Nanoscale Advances* 6.11 (Mar. 2024), pp. 2838–2849. DOI: `10.1039/D3NA00904A`.

[18] R. Jayasingha, A. Sherehiy, S. Wu, and G. U. Sumanasekera. „In Situ Study of Hydrogenation of Graphene and New Phases of Localization between Metal–Insulator Transitions“. In: *Nano Letters* 13.11 (Sept. 2013), pp. 5098–5105. DOI: `10.1021/nl402272b`.

[19] J. Cha, H. Choi, and J. Hong. „Damage-free hydrogenation of graphene via ion energy control in plasma“. In: *Applied Physics Express* 15.1 (Jan. 2022), p. 015002. DOI: `10.35848/1882-0786/ac4204`.

[20] U. Fantz, H. Falter, P. Franzen, D. Wünderlich, M. Berger, A. Lorenz, W. Kraus, P. McNeely, R. Riedl, and E. Speth. „Spectroscopy—a powerful diagnostic tool in source development“. In: *Nuclear Fusion* 46.6 (June 2006), S297–S306. DOI: `10.1088/0029-5515/46/6/S10`.

[21] L. J. van der Pauw. „A method of measuring specific resistivity and hall effect of discs of arbitrary shape“. In: *Philips Research Reports* 13.1 (Feb. 1958), pp. 174–182. DOI: `10.1142/9789814503464_0017`.

[22] Q. R. Ahmad et al. „Direct Evidence for Neutrino Flavor Transformation from Neutral-Current Interactions in the Sudbury Neutrino Observatory“. In: *Physical Review Letter* 89.1 (June 2002), p. 011301. DOI: `10.1103/PhysRevLett.89.011301`.

[23] K. Zuber. „Neutrino Physics“. 3rd ed. CRC Press, (2020). ISBN: 978-1-315-19561-2. DOI: `10.1201/9781315195612`.

[24] F. An et al. „Neutrino physics with JUNO“. In: *Journal of Physics G: Nuclear and Particle Physics* 43.3 (Feb. 2016), p. 030401. DOI: `10.1088/0954-3899/43/3/030401`.

[25] E. W. Otten and C. Weinheimer. „Neutrino mass limit from tritium β decay“. In: *Reports on Progress in Physics* 71.8 (July 2008), p. 086201. DOI: `10.1088/0034-4885/71/8/086201`.

[26] S. Abe et al. „Search for the Majorana Nature of Neutrinos in the Inverted Mass Ordering Region with KamLAND-Zen“. In: *Physical Review Letter* 130.5 (Jan. 2023), p. 051801. DOI: `10.1103/PhysRevLett.130.051801`.

[27] A.G. Adame et al. „DESI 2024 VI: cosmological constraints from the measurements of baryon acoustic oscillations“. In: *Journal of Cosmology and Astroparticle Physics* 2025.2 (Feb. 2025), p. 021. DOI: `10.1088/1475-7516/2025/02/021`.

[28] E. Fermi. „Versuch einer Theorie der β-Strahlen. I“. German. In: *Z. Phys.* 88.3 (Mar. 1934), pp. 161–177. DOI: `10.1007/BF01351864`.

[29] L. Gastaldo. „Neutrino Mass Measurements Using Cryogenic Detectors“. In: *Journal of Low Temperature Physics* 209.5 (Dec. 2022), pp. 804–814. DOI: `10.1007/s10909-022-02780-2`.

[30] C. Velte et al. „High-resolution and low-background ^{163}Ho spectrum: interpretation of the resonance tails“. In: *The European Physical Journal C* 79.12 (Dec. 2019), p. 1026. DOI: `10.1140/epjc/s10052-019-7513-x`.

[31] F. Adam et al. „Improved limit on the effective electron neutrino mass with the ECHo-1k experiment“. (2025). DOI: `10.48550/arXiv.2509.03423`.

[32] J. Angrik et al. „KATRIN Design Report 2004“. Technical Report FZKA 7090; EXP-01/2005; MS-KP-0501. Karlsruhe, Germany: KATRIN Collaboration, (2005). URL: `https://publikationen.bibliothek.kit.edu/2700601` (visited on 11/20/2025).

[33] M. Aker et al. „The design, construction, and commissioning of the KATRIN experiment“. In: *Journal of Instrumentation* 16.8 (Aug. 2021), T08015. DOI: `10.1088/1748-0221/16/08/T08015`.

[34] M. Aker et al. „Precision measurement of the electron energy-loss function in tritium and deuterium gas for the KATRIN experiment“. In: *The European Physical Journal C* 81.7 (July 2021), p. 579. DOI: `10.1140/epjc/s10052-021-09325-z`.

[35] S. Heyns. PhD thesis in preparation. Karlsruhe Institute of Technology. expected 2027.

[36] M. Schlösser and the KATRIN Collaboration. „Beta decay and neutrino mass: KATRIN and beyond“. In: *Proceedings of Science* NOW2024 (Sept. 2024), p. 049. DOI: `10.22323/1.473.0049`.

[37] F. Toschi, B. Maier, G. Heine, T. Ferber, S. Kempf, M. Klute, and B. von Krosigk. „Optimum filter-based analysis for the characterization of a high-resolution magnetic microcalorimeter“. In: *Physical Review D* 109.4 (Feb. 2024), p. 043035. DOI: `10.1103/PhysRevD.109.043035`.

[38] M. Krantz, F. Toschi, B. Maier, G. Heine, C. Enss, and S. Kempf. „Magnetic microcalorimeter with paramagnetic temperature sensors and integrated dc-SQUID readout for high-resolution x-ray emission spectroscopy“. In: *Applied Physics Letters* 124.3 (Jan. 2024), p. 032601. DOI: `10.1063/5.0180903`.

[39] S. Kempf, A. Fleischmann, L. Gastaldo, and C. Enss. „Physics and Applications of Metallic Magnetic Calorimeters“. In: *Journal of Low Temperature Physics* 193.3 (Nov. 2018), pp. 365–379. DOI: `10.1007/s10909-018-1891-6`.

[40] N. Kovač, F. Adam, S. Kempf, M. Langer, M. Müller, R. Sack, M. Schlösser, M. Steidl, and K. Valerius. „Comparison of the detector response and calibration function of metallic microcalorimeters for X-ray photons and external electrons“. In: *Nuclear Instruments and Methods in Physics Research Section A: Accelerators, Spectrometers, Detectors and Associated Equipment* 1080 (Nov. 2025), p. 170662. DOI: `10.1016/j.nima.2025.170662`.

[41] M. Müller, M. Rodrigues, J. Beyer, M. Loidl, and S. Kempf. „Magnetic Microcalorimeters for Primary Activity Standardization Within the EMPIR Project PrimA-LTD“. In: *Journal of Low Temperature Physics* 214.3 (Feb. 2024), pp. 263–271. DOI: `10.1007/s10909-024-03048-7`.

[42] N. Steinbrink, V. Hannen, E. L. Martin, R G H. Robertson, M. Zacher, and C. Weinheimer. „Neutrino mass sensitivity by MAC-E-Filter based time-of-flight spectroscopy with the example of KATRIN“. In: *New Journal of Physics* 15.11 (Nov. 2013), p. 113020. DOI: `10.1088/1367-2630/15/11/113020`.

[43] B. Monreal and J. A. Formaggio. „Relativistic cyclotron radiation detection of tritium decay electrons as a new technique for measuring the neutrino mass“. In: *Phys. Rev. D* 80.5 (Sept. 2009), p. 051301. DOI: `10.1103/PhysRevD.80.051301`.

[44] A. A. Esfahani et al. „Determining the neutrino mass with cyclotron radiation emission spectroscopy—Project 8“. In: *Journal of Physics G: Nuclear and Particle Physics* 44.5 (Mar. 2017), p. 054004. DOI: `10.1088/1361-6471/aa5b4f`.

[45] A. A. S. Amad et al. „Determining absolute neutrino mass using quantum technologies“. In: *New Journal of Physics* 27.10 (Oct. 2025), p. 105006. DOI: `10.1088/1367-2630/adc624`.

[46] R. D. Williams and S. E. Koonin. „Atomic final-state interactions in tritium decay“. In: *Physical Review C* 27.4 (Apr. 1983), pp. 1815–1817. DOI: `10.1103/PhysRevC.27.1815`.

[47] A. L. Radovinsky, A. Lindman, J. A. Formaggio, and J. V. Minervini. „A Ioffe Trap Magnet for the Project 8 Atom Trapping Demonstrator“. In: *IEEE Transactions on Applied Superconductivity* 30.4 (June 2020), pp. 1–5. DOI: `10.1109/TASC.2020.2985675`.

[48] C. Rodenbeck and L. Thorne. „R&D towards an atomic hydrogen source for future neutrino mass experiments“. In: Zenodo, (June 2024). DOI: `10.5281/zenodo.13385873`.

[49] A. Lindman. „Atomic Tritium Technology: Production, Cooling, and Trapping“. PhD thesis. Johannes Gutenberg-University Mainz, (Mar. 2025). 926 pp. URL: `https://drive.google.com/file/d/1AKRckhDZALAAuhJABqKtipi5BSIMNrve/view` (visited on 11/20/2025).

[50] A. Semakin et al. „Cryogenic source of atomic tritium for precision spectroscopy and neutrino-mass measurements“. In: arXiv, (Nov. 2025). DOI: `10.48550/arXiv.2511.08313`.

[51] E. B. Nelson and J. E. Nafe. „The Hyperfine Structure of Tritium“. In: *Physical Review* 75.8 (Apr. 1949), pp. 1194–1198. DOI: `10.1103/PhysRev.75.1194`.

[52] A. G. Prodell and P. Kusch. „Hyperfine Structure of Tritium in the Ground State“. In: *Physical Review* 106.1 (Apr. 1957), pp. 87–89. DOI: `10.1103/PhysRev.106.87`.

[53] B.S. Mathur, S.B. Crampton, D. Kleppner, and N.F. Ramsey. „Hyperfine separation of tritium“. In: *Physical Review* 158.1 (June 1967), pp. 14–17. DOI: `10.1103/PhysRev.158.14`.

[54] R. G. H. Robertson, T. J. Bowles, J. C. Browne, T. H. Burritt, J. A. Helffrich, D. A. Knapp, M. P. Maley, M. L. Stelts, and J. F. Wilkerson. „The Los Alamos experiment on atomic and molecular tritium“. In: *4th Moriond Workshop: Massive Neutrinos in Particle Astrophysics.* (Jan. 1984), pp. 253–260. URL: `https://inspirehep.net/literature/208109` (visited on 11/20/2025).

[55] J. Slevin and W. Stirling. „Radio frequency atomic hydrogen beam source“. In: *Review of Scientific Instruments* 52.11 (Nov. 1981), pp. 1780–1782. DOI: `10.1063/1.1136497`.

[56] Plasma Science Fusion Center MIT. „What Is Plasma?“ URL: `https://www.psfc.mit.edu/resources/fusion-101/what-is-plasma/` (visited on 09/05/2025).

[57] E. Wagenaars. „Low temperature plasma“. Lecture at the Culham Plasma Physics Summer School. (July 2025). URL: `https://indico.ukaea.uk/event/391/contributions/596/` (visited on 11/20/2025).

[58] M. A. Lieberman and A. J. Lichtenberg. „Principles of Plasma Discharges and Materials Processing“. 1st ed. Wiley, (2005). ISBN: 978-0-471-72001-0 978-0-471-72425-4. DOI: `10.1002/0471724254`.

[59] P. Gibbon. „Introduction to Plasma Physics“. In: *Proceedings of the 2019 CERN–Accelerator–School course on High Gradient Wakefield Accelerators* (July 2020). DOI: `10.48550/arXiv.2007.04783`.

[60] A. Subrahmanyam. „Plasma Overview and the Basics of Cold Plasma: In Material Synthesis“. In: *Cold Plasma in Nano-Matter Synthesis: Basic Principles and Practices*. Cham: Springer Nature Switzerland, (2024), pp. 27–101. ISBN: 978-3-031-64041-4. DOI: `10.1007/978-3-031-64041-4_2`.

[61] D. Sydorenko, I. D. Kaganovich, A. V. Khrabrov, S. A. Ethier, J. Chen, and S. Janhunen. „Simulation of an inductively coupled plasma with a two-dimensional Darwin particle-in-cell code“. In: *Physics of Plasmas* 32.4 (Apr. 2025), p. 043904. DOI: `10.1063/5.0241152`.

[62] A. Al Bastami, A. Jurkov, P. Gould, M. Hising, M. Schmidt, and D. J. Perreault. „Dynamic Matching System for Radio-Frequency Plasma Generation“. In: *IEEE Transactions on Power Electronics* (Mar. 2018), pp. 1940–1951. DOI: `10.1109/TPEL.2017.2734678`.

[63] Y. Mitsui and T. Makabe. „Review and current status: E $\rightleftharpoons$ H mode transition in low-temperature ICP and related electron dynamics“. In: *Plasma Sources Science and Technology* 30.2 (Feb. 2021), p. 023001. DOI: `10.1088/1361-6595/abd380`.

[64] C. M. Ferreira and J. Loureiro. „Characteristics of high-frequency and direct-current argon discharges at low pressures: a comparative analysis“. In: *Journal of Physics D: Applied Physics* 17.6 (June 1984), pp. 1175–1188. DOI: `10.1088/0022-3727/17/6/014`.

[65] U. Fantz. „Atomic and Molecular Emission Spectroscopy in Low Temperature Plasmas Containing Hydrogen and Deuterium“. Tech. rep. IPP-Report 10/21. Max-Planck-Institut für Plasmaphysik, (2002). URL: `https://pure.mpg.de/pubman/faces/ViewItemFullPage.jsp?itemId=item_2138253` (visited on 11/20/2025).

[66] J. Vlcek and V. Pelikan. „Excited level populations of argon atoms in a non-isothermal plasma“. In: *Journal of Physics D: Applied Physics* 19.10 (Oct. 1986), p. 1879. DOI: `10.1088/0022-3727/19/10/012`.

[67] R. C. Bergmayr, D. Wünderlich, and U. Fantz. „Molecular data needs for advanced collisional-radiative modelling for hydrogen plasmas“. In: *The European Physical Journal D* 77.7 (July 2023), p. 136. DOI: `10.1140/epjd/s10053-023-00706-5`.

[68] U. Fantz and D. Wünderlich. „Franck–Condon factors, transition probabilities, and radiative lifetimes for hydrogen molecules and their isotopomeres“. In: *Atomic Data and Nuclear Data Tables* 92.6 (Nov. 2006), pp. 853–973. DOI: `10.1016/j.adt.2006.05.001`.

[69] R. C. Bergmayr, L. H. Scarlett, D. Wünderlich, D. V. Fursa, M. C. Zammit, I. Bray, and U. Fantz. „A fully ro-vibrationally resolved corona model for the molecular hydrogen Fulcher-α system“. In: *Journal of Quantitative Spectroscopy and Radiative Transfer* 338 (June 2025), p. 109414. DOI: `10.1016/j.jqsrt.2025.109414`.

[70] D. Wünderlich, M. Giacomin, R. Ritz, and U. Fantz. „Yacora on the Web: Online collisional radiative models for plasmas containing H, H_2 or He“. In: *Journal of Quantitative Spectroscopy and Radiative Transfer* 240 (Jan. 2020), p. 106695. DOI: `10.1016/j.jqsrt.2019.106695`.

[71] D. Wünderlich, S. Dietrich, and U. Fantz. „Application of a collisional radiative model to atomic hydrogen for diagnostic purposes“. In: *Journal of Quantitative Spectroscopy and Radiative Transfer* 110.1 (Jan. 2009), pp. 62–71. DOI: `10.1016/j.jqsrt.2008.09.015`.

[72] S. D. Cohen, A. C. Hindmarsh, and P. F. Dubois. „CVODE, A Stiff/Nonstiff ODE Solver in C“. In: *Computers in Physics* 10.2 (Mar. 1996), pp. 138–143. DOI: `10.1063/1.4822377`.

[73] D. Wünderlich and U. Fantz. „Evaluation of State-Resolved Reaction Probabilities and Their Application in Population Models for He, H, and H_2“. In: *Atoms* 4.4 (Sept. 2016), p. 26. DOI: `10.3390/atoms4040026`.

[74] K. Sawada and T. Fujimoto. „Effective ionization and dissociation rate coefficients of molecular hydrogen in plasma“. In: *Journal of Applied Physics* 78.5 (Sept. 1995), pp. 2913–2924. DOI: `10.1063/1.360037`.

[75] R. K. Janev, D. Reiter, Samm U., and Forschungszentrum Juelich GmbH. „Collision processes in low-temperature hydrogen plasmas“. Tech. rep. Inst. fuer Plasmaphysik. EURATOM Association, Trilateral Euregio Cluster, (2003). URL: `https://inis.iaea.org/records/2jdhv-j7j44` (visited on 11/20/2025).

[76] W. T. Miles, R. Thompson, and A. E. S. Green. „Electron-Impact Cross Sections and Energy Deposition in Molecular Hydrogen“. In: *Journal of Applied Physics* 43.2 (Feb. 1972), pp. 678–686. DOI: `10.1063/1.1661176`.

[77] L. H. Scarlett, D. V. Fursa, M. C. Zammit, I. Bray, Y. Ralchenko, and K. D. Davie. „Complete collision data set for electrons scattering on molecular hydrogen and its isotopologues: I. Fully vibrationally-resolved electronic excitation of $H_2(X\ {}^1\Sigma_g^+)$“. In: *Atomic Data and Nuclear Data Tables* 137 (July 2021), p. 101361. DOI: `10.1016/j.adt.2020.101361`.

[78] C. V. Raman and K. S. Krishnan. „A New Type of Secondary Radiation“. In: *Nature* 121.3048 (Mar. 1928), pp. 501–502. DOI: `10.1038/121501c0`.

[79] A. Jorio, R. Saito, G. Dresselhaus, and M.S. Dresselhaus. „Raman Spectroscopy in Graphene Related Systems“. 1st ed. John Wiley Sons, Ltd, (2011). ISBN: 9783527632695. DOI: `10.1002/9783527632695`.

[80] P. Y. Yu and M. Cardona. „Fundamentals of Semiconductors: Physics and Materials Properties“. 4th ed. Springer Berlin Heidelberg, (2010). ISBN: 978-3-642-00710-1. DOI: `10.1007/978-3-642-00710-1`.

[81] G. Zeller. „Raman spectroscopy for KATRIN: monitoring of continuous tritium gas flows and tritium-graphene interactions“. PhD thesis. Karlsruher Institut für Technologie (KIT), (Feb. 2024). 170 pp. DOI: `10.5445/IR/1000168486`.

[82] K. S. Novoselov, A. K. Geim, S. V. Morozov, D. Jiang, Y. Zhang, S. V. Dubonos, I. V. Grigorieva, and A. A. Firsov. „Electric Field Effect in Atomically Thin Carbon Films“. In: *Science* 306.5696 (Oct. 2004), pp. 666–669. DOI: `10.1126/science.1102896`.

[83] G. N. Dash, S. R. Pattanaik, and S. Behera. „Graphene for Electron Devices: The Panorama of a Decade“. In: *IEEE Journal of the Electron Devices Society* 2.5 (Sept. 2014), pp. 77–104. DOI: `10.1109/JEDS.2014.2328032`.

[84] H. Aoki and M. S. Dresselhaus, eds. „Physics of Graphene“. 1st ed. Springer Cham, (2014). ISBN: 978-3-319-02633-6. DOI: `10.1007/978-3-319-02633-6`.

[85] C. M. Goringe, D. R. Bowler, and E. Hernández. „Tight-binding modelling of materials“. In: *Reports on Progress in Physics* 60.12 (Dec. 1997), pp. 1447–1512. DOI: `10.1088/0034-4885/60/12/001`.

[86] J. Kong and A. Javey. „Carbon Nanotube Electronics“. 1st ed. Springer New York, (2009). DOI: `10.1007/978-0-387-69285-2`.

[87] R. Gross and A. Marx. „Festkörperphysik“. 1st ed. Oldenbourg Verlag München, (2012). ISBN: 978-3-486-71486-9. DOI: `10.1524/9783486714869`.

[88] C. Neumann and C. Stampfer. „Characterization of Graphene by Confocal Raman Spectroscopy“. In: *Confocal Raman Microscopy*. Ed. by J. Toporski, T. Dieing, and O. Hollricher. Springer International Publishing, (2018), pp. 177–194. ISBN: 978-3-319-75380-5. DOI: `10.1007/978-3-319-75380-5_8`.

[89] P. Venezuela, M. Lazzeri, and F. Mauri. „Theory of double-resonant Raman spectra in graphene: Intensity and line shape of defect-induced and two-phonon bands“. In: *Physical Review B* 84.3 (July 2011), p. 035433. DOI: `10.1103/PhysRevB.84.035433`.

[90] Graphenea Inc. „Monolayer Graphene on 90 nm SiO_2/Si, 2025“. URL: `https://www.graphenea.com/collections/buy-graphene-films/products/monolayer-graphene-on-sio-si-90-nm` (visited on 09/03/2025).

[91] J. Son, S. Lee, S. J. Kim, B. C. Park, H. Lee, S. Kim, J. H. Kim, B. H. Hong, and J. Hong. „Hydrogenated monolayer graphene with reversible and tunable wide band gap and its field-effect transistor“. In: *Nature Communications* 7.1 (Nov. 2016), p. 13261. DOI: `10.1038/ncomms13261`.

[92] L. G. Cançado, A. Jorio, E. H. Martins Ferreira, F. Stavale, C. A. Achete, R. B. Capaz, M. V. O. Moutinho, A. Lombardo, T. S. Kulmala, and A. C. Ferrari. „Quantifying Defects in Graphene via Raman Spectroscopy at Different Excitation Energies“. In: *Nano Letters* 11.8 (Aug. 2011), pp. 3190–3196. DOI: `10.1021/nl201432g`.

[93] J. G. Webster. „Electrical Measurement, Signal Processing, and Displays“. 1st ed. CRC Press LLC, (2004). ISBN: 0-8493-1733-9. DOI: `10.1002/0471724254`.

[94] Keithley Instruments Inc. „Low Level Measurements Handbook: Precision DC Current, Voltage and Resistance Measurements“. 7th ed. (2016). URL: `https://download.tek.com/document/LowLevelHandbook_7Ed.pdf`.

[95] M. Tuszewski. „Planar inductively coupled plasmas operated with low and high radio frequencies“. In: *IEEE Transactions on Plasma Science* 27.1 (Jan. 1999), pp. 68–69. DOI: `10.1109/27.763041`.

[96] M. I. Boulos. „The inductively coupled R.F. (radio frequency) plasma“. In: *Pure and Applied Chemistry* 57.9 (1985), pp. 1321–1352. DOI: `doi:10.1351/pac198557091321`.

[97] SVT Associates Inc. „RF-4.5 Plasma Source“. URL: `https://www.svta.com/uploads/documents/RF_4.5.pdf` (visited on 09/04/2025).

[98] R. D. Penzhorn. „Tritium Manual“. In: *KITopen repository* (May 2025). DOI: `10.5445/IR/1000181603`.

[99] Keyence Deutschland GmbH. „VK-X3000“. URL: `https://www.keyence.de/products/microscope/laser-microscope/vk-x3000/` (visited on 10/08/2025).

[100] E. Hecht. „Optics Global Edition“. 5th ed. Pearson Deutschland, (2016). ISBN: 9781292096933. URL: `https://elibrary.pearson.de/book/99.150005/9781292096964` (visited on 11/20/2025).

[101] J. J. Pouch, S. A. Alterovitz, and K. Miyoshi. „Boron Nitride: Composition, Optical Properties, and Mechanical Behavior“. In: *MRS Online Proceedings Library* 93.2 (Dec. 1987), pp. 323–328. DOI: `10.1557/PROC-93-323`.

[102] N. Morita and A. Yamamoto. „Optical and Electrical Properties of Boron“. In: *Japanese Journal of Applied Physics* 14.6 (June 1975), p. 825. DOI: `10.1143/JJAP.14.825`.

[103] The Engineering ToolBox. „Thermal Conductivity of Metals and Alloys: Data Table Reference Guide“. (2005). URL: `ttps://www.engineeringtoolbox.com/thermal-conductivity-metals-d_858.html` (visited on 11/02/2025).

[104] tectra GmbH. „UHV – Sample Heater Stage“. URL: `https://tectra.de/wp-content/uploads/2017/03/Heater-Stage.pdf` (visited on 10/08/2025).

[105] J. Chen, T. Shi, T. Cai, T. Xu, L. Sun, X. Wu, and D. Yu. „Self healing of defected graphene“. In: *Applied Physics Letters* 102.10 (Mar. 2013), p. 103107. DOI: `10.1063/1.4795292`.

[106] P. Zhang, E. Tevaarwerk, B. Park, D. E. Savage, G. K. Celler, I. Knezevic, P. G. Evans, M. A. Eriksson, and M. G. Lagally. „Electronic transport in nanometre-scale silicon-on-insulator membranes“. In: *Nature* 439.7077 (Feb. 2006), pp. 703–706. DOI: `10.1038/nature04501`.

[107] K. Kitatani, T. Kasuya, T. Nakayama, K. Yamamoto, and M. Wada. „Measurement of velocity distribution functions of neutral particles in ion source plasma“. In: *Review of Scientific Instruments* 73.2 (Feb. 2002), pp. 958–960. DOI: `10.1063/1.1427759`.

[108] H. Shin, S. Kang, J. Koo, H. Lee, J. Kim, and Y. Kwon. „Cohesion energetics of carbon allotropes: Quantum Monte Carlo study“. In: *The Journal of Chemical Physics* 140.11 (Mar. 2014), p. 114702. DOI: `10.1063/1.4867544`.

[109] S. Casolo, O. M. Løvvik, R. Martinazzo, and G. F. Tantardini. „Understanding adsorption of hydrogen atoms on graphene“. In: *The Journal of Chemical Physics* 130.5 (Feb. 2009), p. 054704. ISSN: 0021-9606, 1089-7690. DOI: `10.1063/1.3072333`. URL: `https://pubs.aip.org/jcp/article/130/5/054704/908444/Understanding-adsorption-of-hydrogen-atoms-on` (visited on 10/2025).

[110] K. V. Mardia, J. T. Kent, and J. M. Bibby. „Multivariate Analysis“. In: *Probability and mathematical statistics.* 10th ed. Academic Press Limited, 1979. DOI: `10.1002/zamm.19810610315`.

[111] T. J. Fellers and M. W. Davidson. „Concepts in Digital Imaging Technology CCD Noise Sources and Signal-to-Noise Ratio“. URL: `https://hamamatsu.magnet.fsu.edu/articles/ccdsnr.html` (visited on 11/07/2025).

[112] Thorlabs Inc. „Camera Noise and Temperature Tutorial“. URL: `https://www.thorlabs.com/newgrouppage9.cfm?objectgroup_id=10773&` (visited on 11/07/2025).

[113] Encyclopedia of Mathematics. „Simpson formula“. URL: `http://encyclopediaofmath.org/index.php?title=Simpson_formula&oldid=48712` (visited on 11/06/2025).

[114] D. Wünderlich, S. Briefi, R. Friedl, and U. Fantz. „Emission spectroscopy of negative hydrogen ion sources: From VUV to IR“. In: *Review of Scientific Instruments* 92.12 (Dec. 2021), p. 123510. DOI: `10.1063/5.0075491`.

A. Appendix

A.1. Results of potential boron/boron nitride deposition

A.1.1. Scanning electron microscopy scans

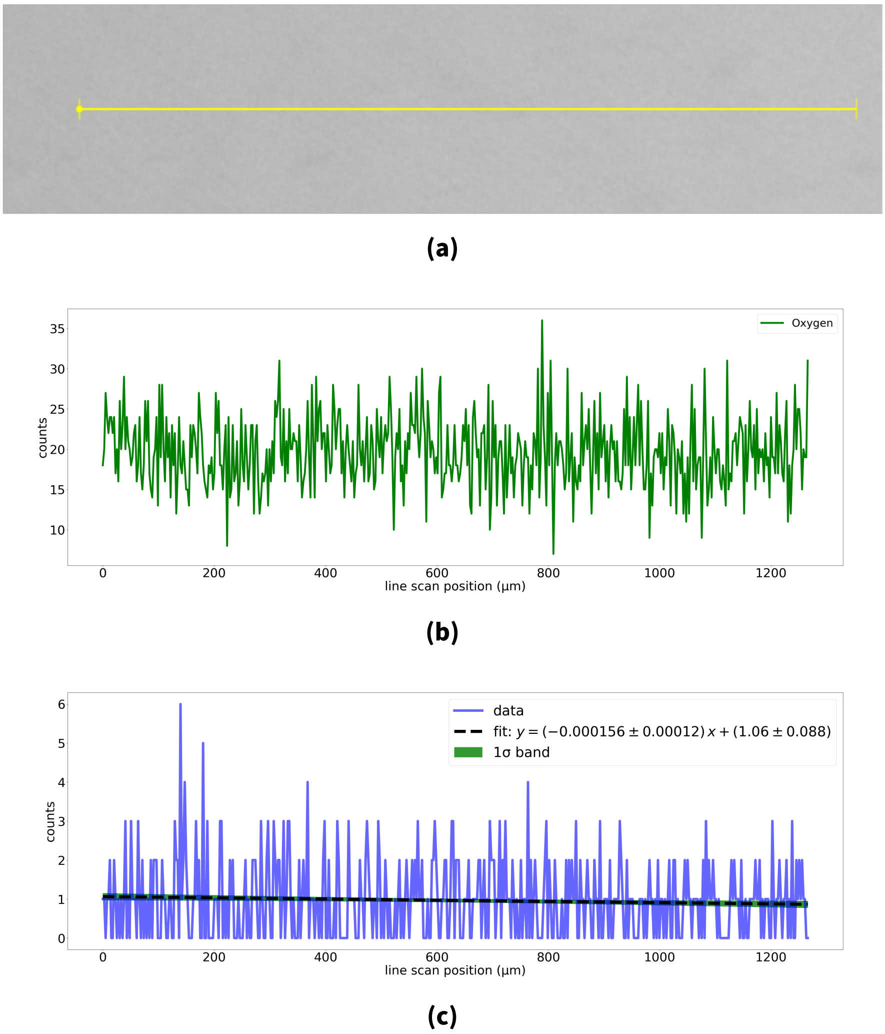

Figure A.1.: Results from the SEM with $E_\mathrm{e} = 1\,\mathrm{keV}$. EDX line scan of the glass slide **before loading** in the center area. **(a)** SEI of the scanned area. **(b)** EDX line scan for oxygen. **(c)** EDX line scan for boron including a linear fit and the $1\,\sigma$ band.

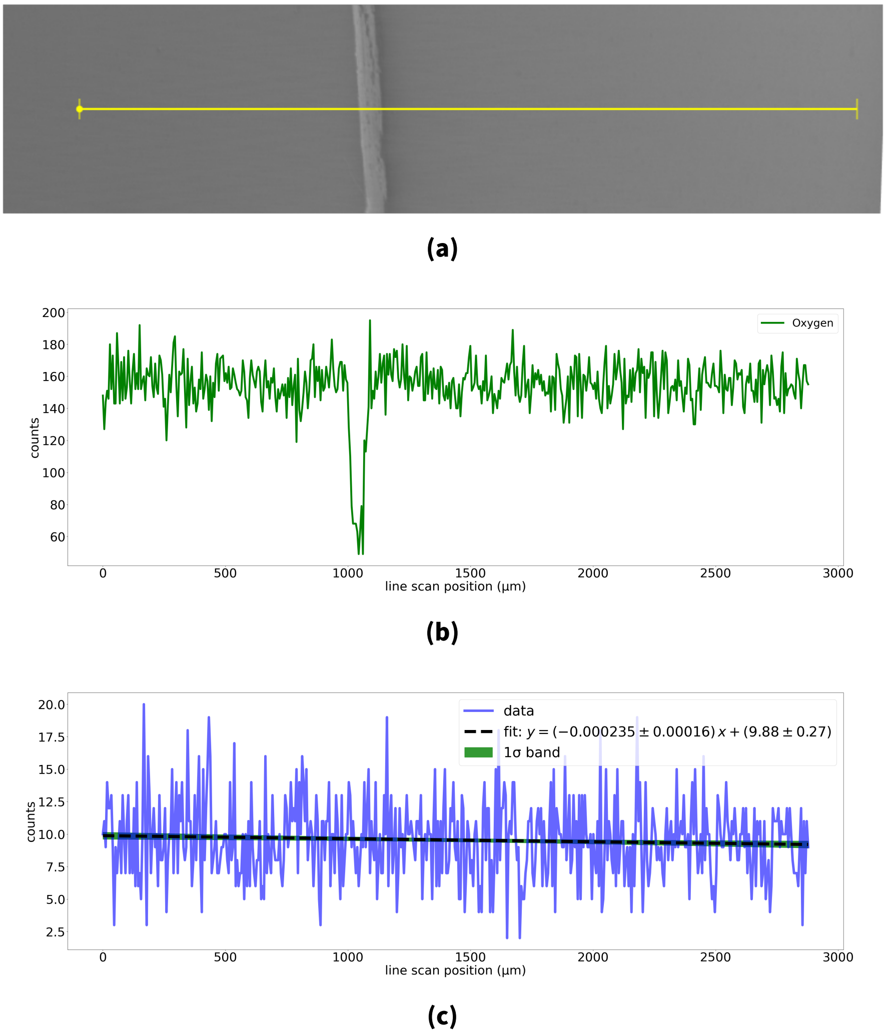

Figure A.2.: Results from the SEM with $E_e = 1\,\text{keV}$. EDX line scan of the glass slide **after loading** in the center with a scratch on it. **(a)** SEI of the scanned area. **(b)** EDX line scan for oxygen. **(c)** EDX line scan for boron including a linear fit and the $1\,\sigma$ band

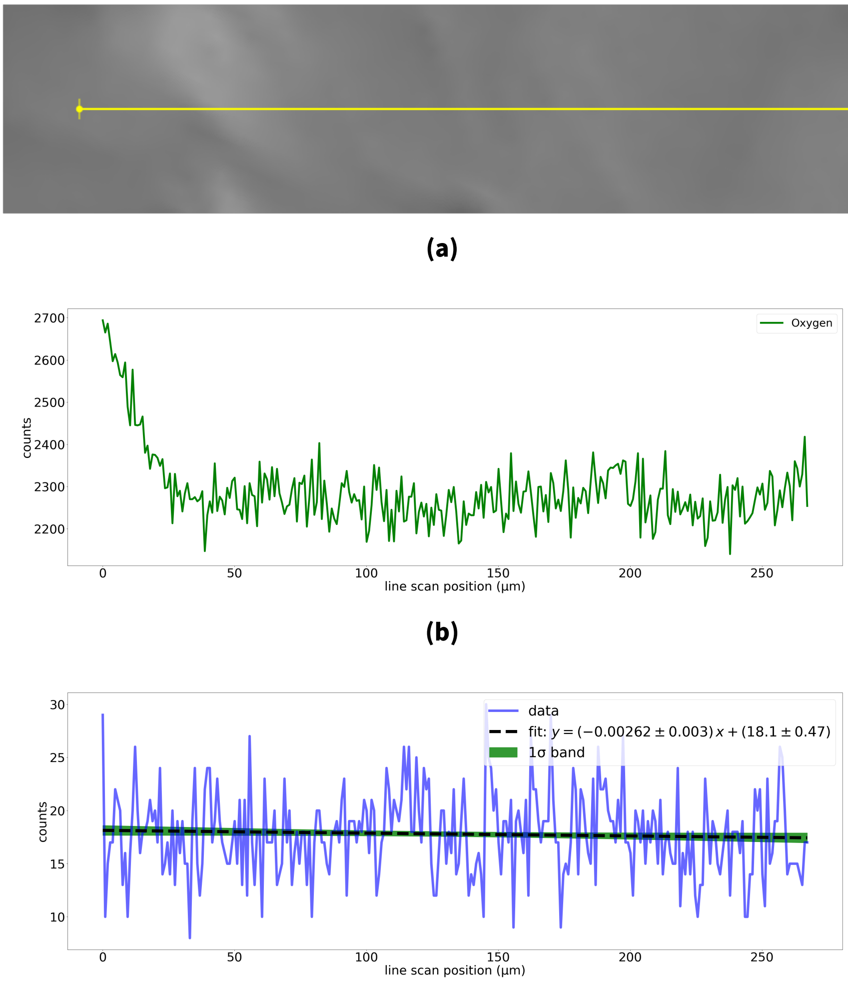

(a)

(b)

(c)

Figure A.3.: Results from the SEM with $E_e = 5\,\text{keV}$. EDX line scan of the glass slide **before loading** in the center area.**(a)** SEI of the scanned area. **(b)** EDX line scan for oxygen. **(c)** EDX line scan for boron including a linear fit and the $1\,\sigma$ band.

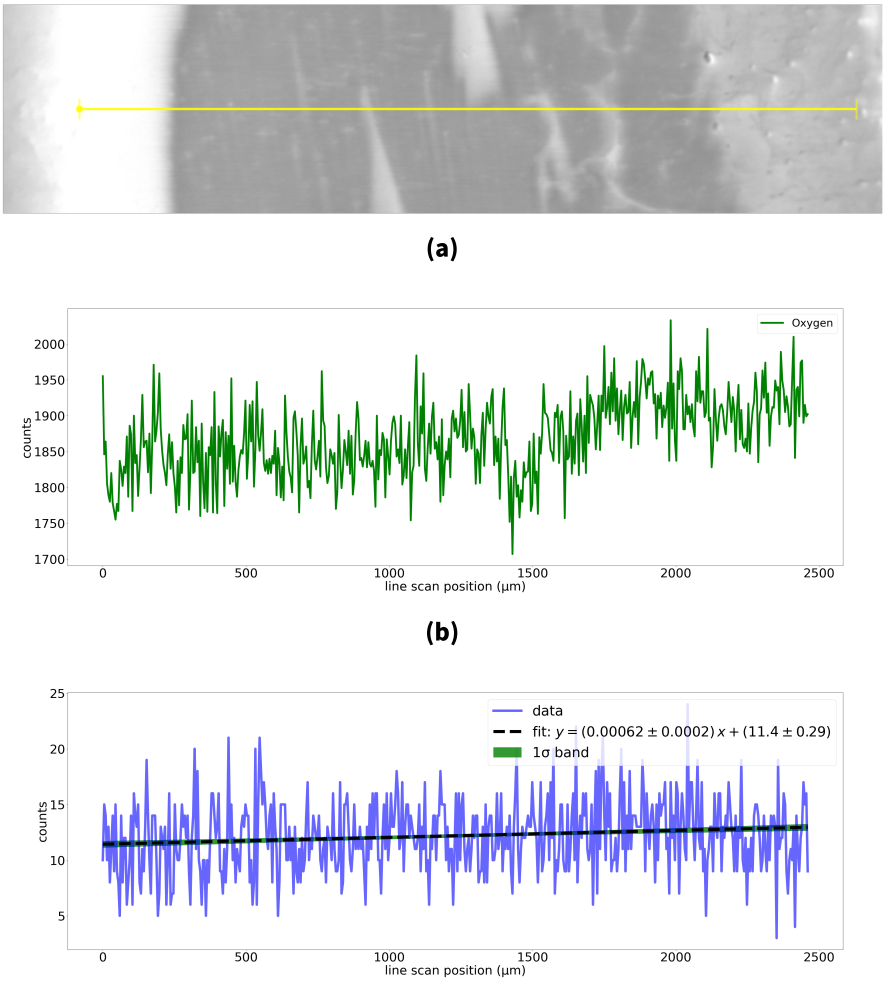

(a)

(b)

(c)

Figure A.4.: Results from the SEM with $E_e = 5\,\mathrm{keV}$. EDX line scan of the glass slide **after loading** in the center with a scratch on it. **(a)** SEI of the scanned area. **(b)** EDX line scan for boron including a linear fit and the 1 σ band.

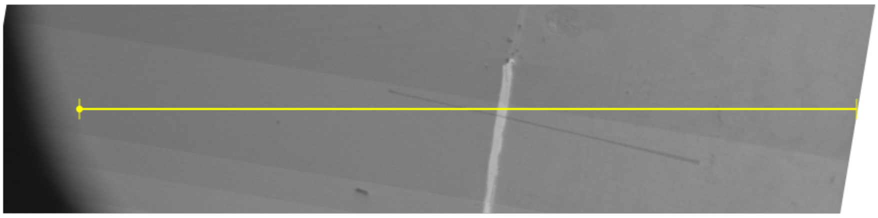

(a)

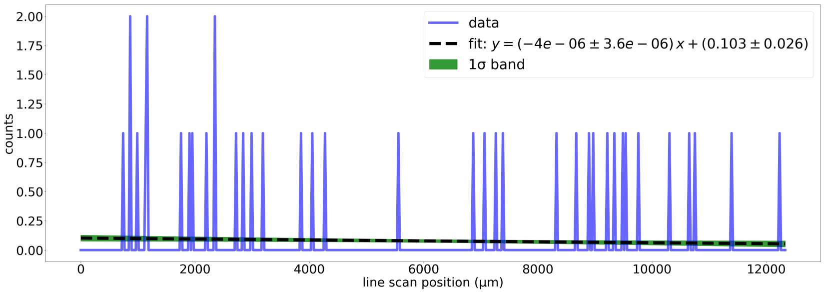

(b)

Figure A.5.: Results from the SEM with $E_e = 300\,\text{eV}$. EDX line scan of the glass slide **after loading** in the center with a scratch on it.**(a)** SEI of the scanned area. **(b)** EDX line scan for boron including a linear fit and the $1\,\sigma$ band.

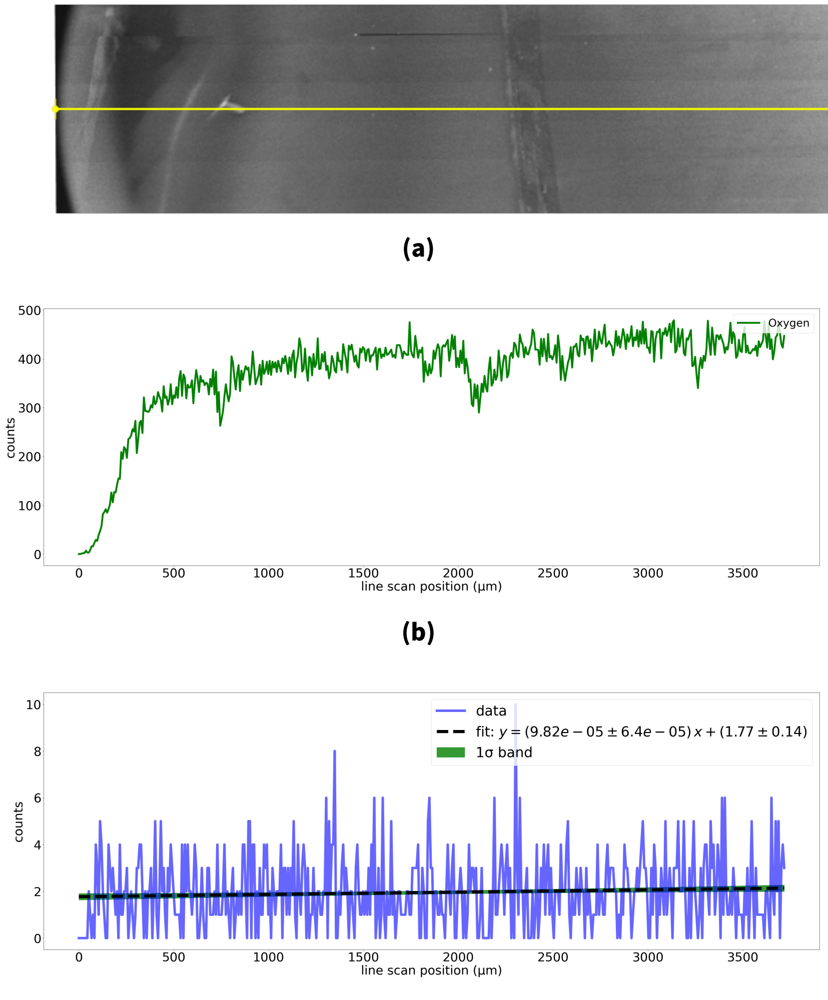

Figure A.6.: Results from the SEM with $E_e = 30\,\mathrm{keV}$. Line scan of the glass slide **after loading** in the center with a scratch on it. **(a)** SEI of the scanned area. **(b)** EDX line scan for oxygen. **(c)** EDX line scan for boron including a linear fit and the $1\,\sigma$ band

A.1.2. White light interferometer scans

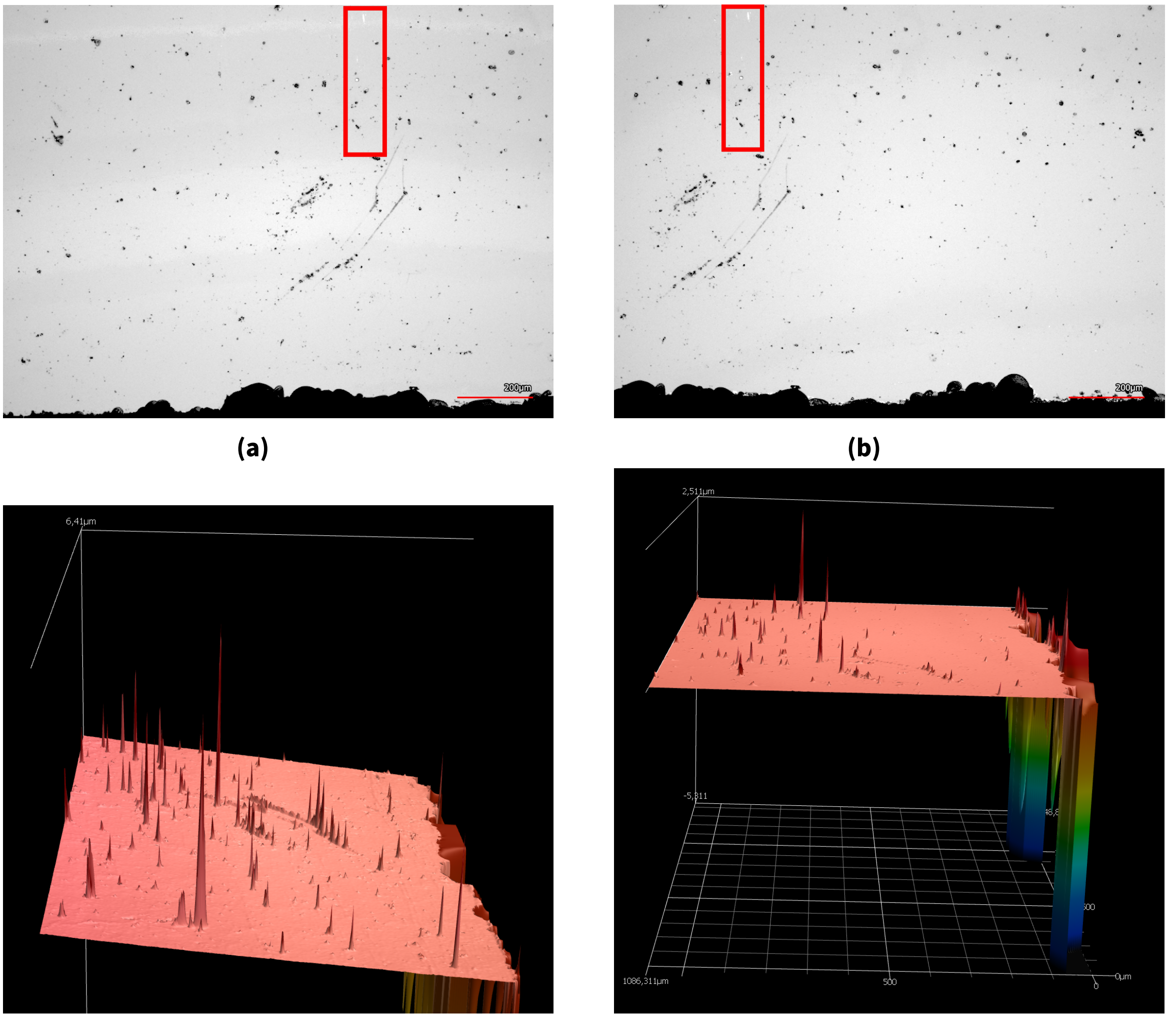

(a)

(b)

(c)

(d)

Figure A.7.: Profile measured with the WLI. 50000% magnification. The right edge of the profile corresponds to the edge of the glass slide. **(a)** optical image of the edge of the glass slide before loading, scanned along z-direction. **(b)** optical image of the edge of the glass slide after loading, scanned along z-direction. Inside the red marked area there is a white mark which is the scratch. On the right side from the scratch the sample was covered with the metal plate. The left side was uncovered. **(c)** Profile scan **before loading** with height scale of 6.4 μm (view is from the x-axis). **(d)** Profile scan **after loading** with height scale of 2.5 μm (view is along the x-axis).

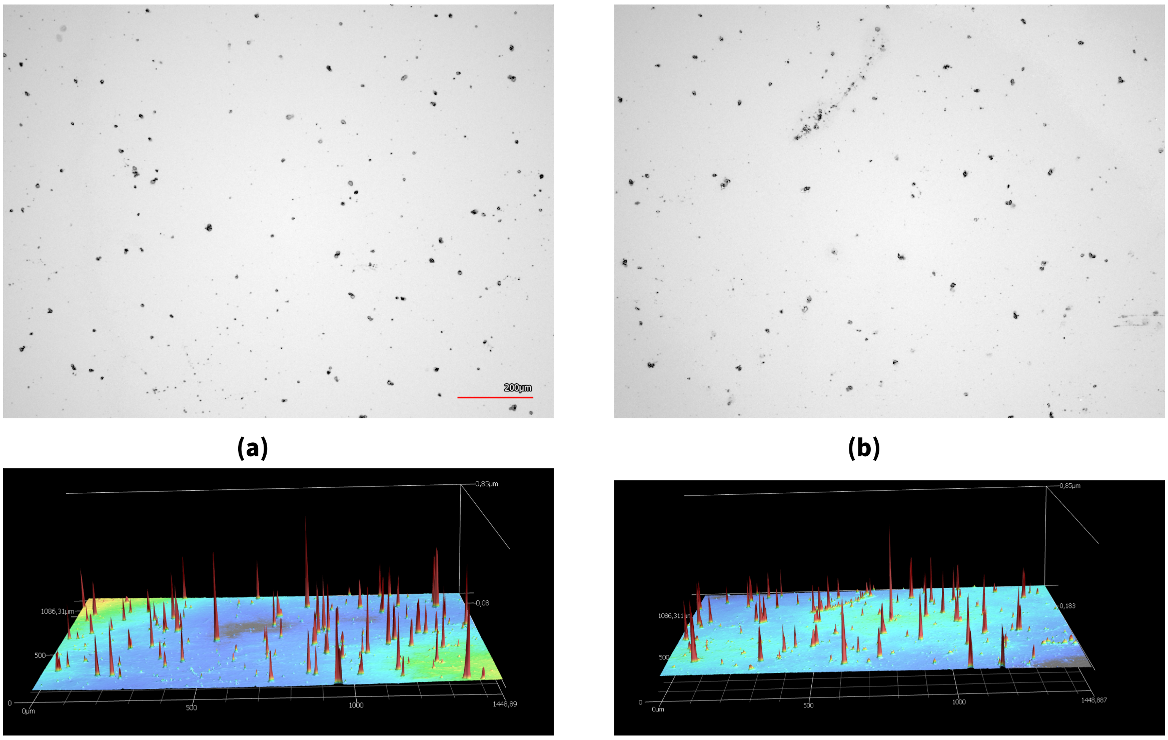

(a) (b)

(c) (d)

Figure A.8.: Profile of the glass slide on the uncovered side measured with the WLI. 50 000 % magnification. Note that the scans before and after loading are not in the same position of the glass slide. **(a)** optical image of the edge of the glass slide before loading along z-direction. **(b)** optical image of the edge of the glass slide after loading along z-direction.**(c)** Profile scan **before loading** with height scale of 0.85 μm (view along the y-axis). **(d)** Profile scan **after loading** with height scale of 0.85 μm (view along the y-axis).

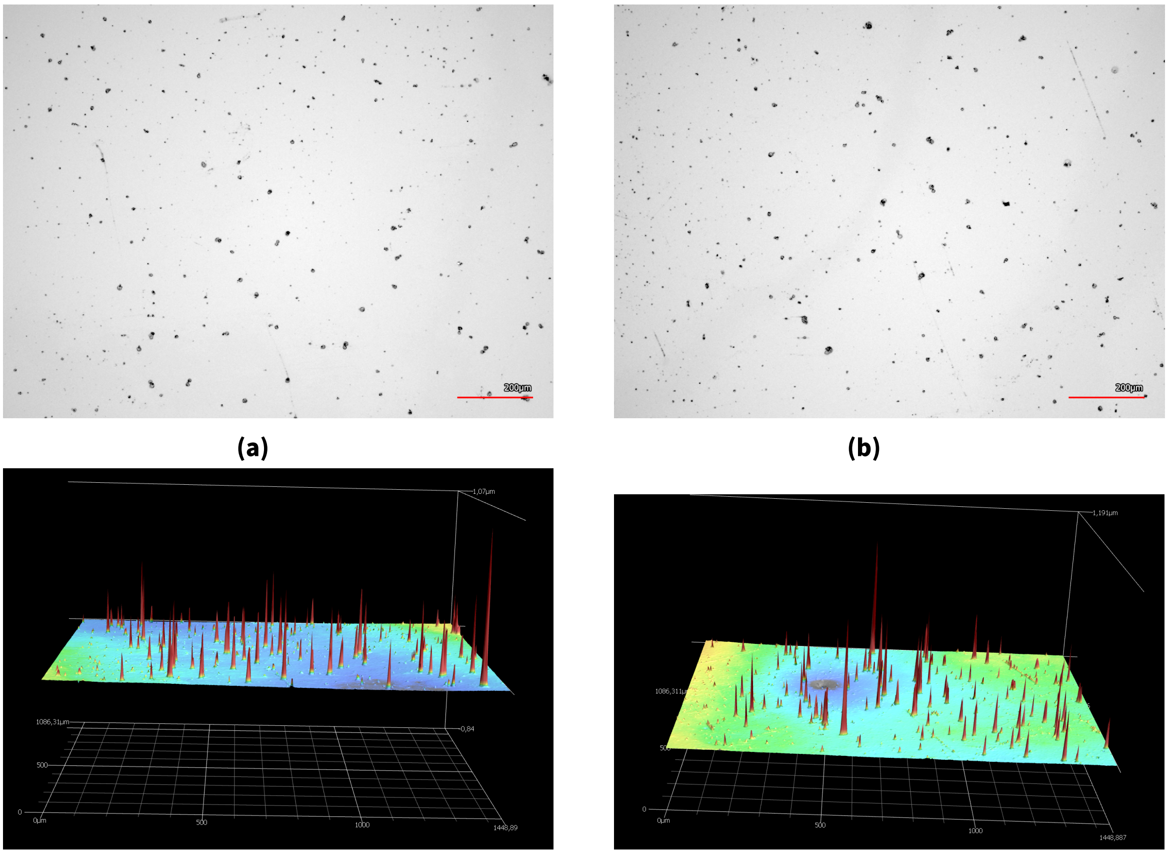

(a) (b)

(c) (d)

Figure A.9.: Profile of the glass slide on the covered side measured with the WLI. 50 000 % magnification. Note that the scans before and after loading are not in the same position of the glass slide. **(a)** optical image of the edge of the glass slide before loading along z-direction. **(b)** optical image of the edge of the glass slide after loading along z-direction.**(c)** Profile scan **before loading** with height scale of 1.07 μm (view along the y-axis). **(d)** Profile scan **after loading** with height scale of 1.191 μm (view along the y-axis).

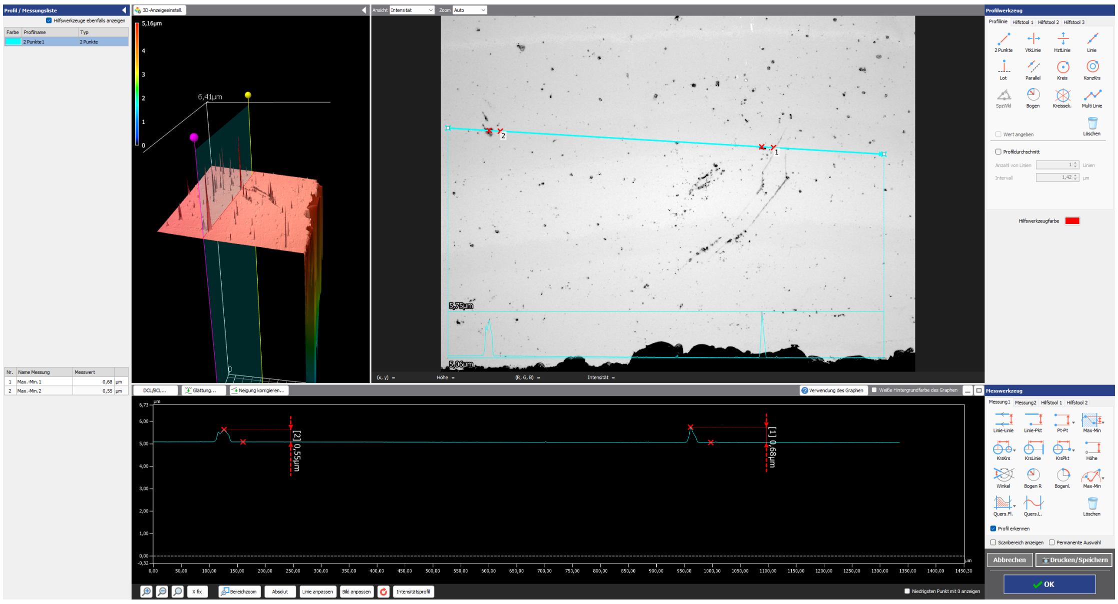

Nr.	Name Messung	Messwert	
1	Max.-Min.1	0,68	µm
2	Max.-Min.2	0,55	µm

Figure A.10.: Determination of max peaks in the profile scan of the unloaded glass slide at the edge.

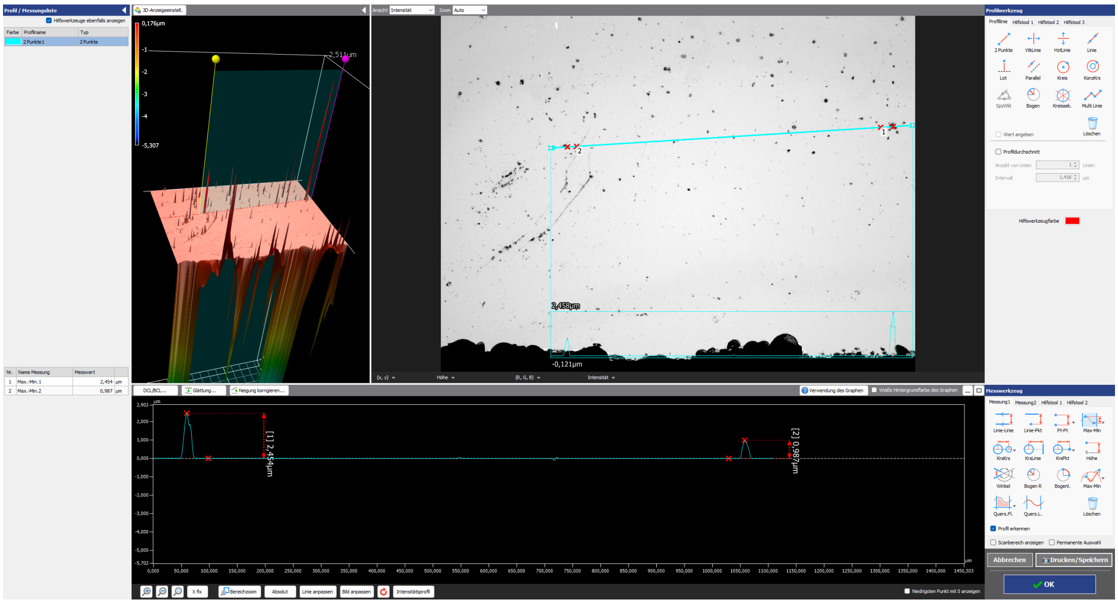

Nr.	Name Messung	Messwert	
1	Max.-Min.1	2,454	µm
2	Max.-Min.2	0,987	µm

Figure A.11.: Determination of max peaks in the profile scan of the loaded glass slide at the edge.

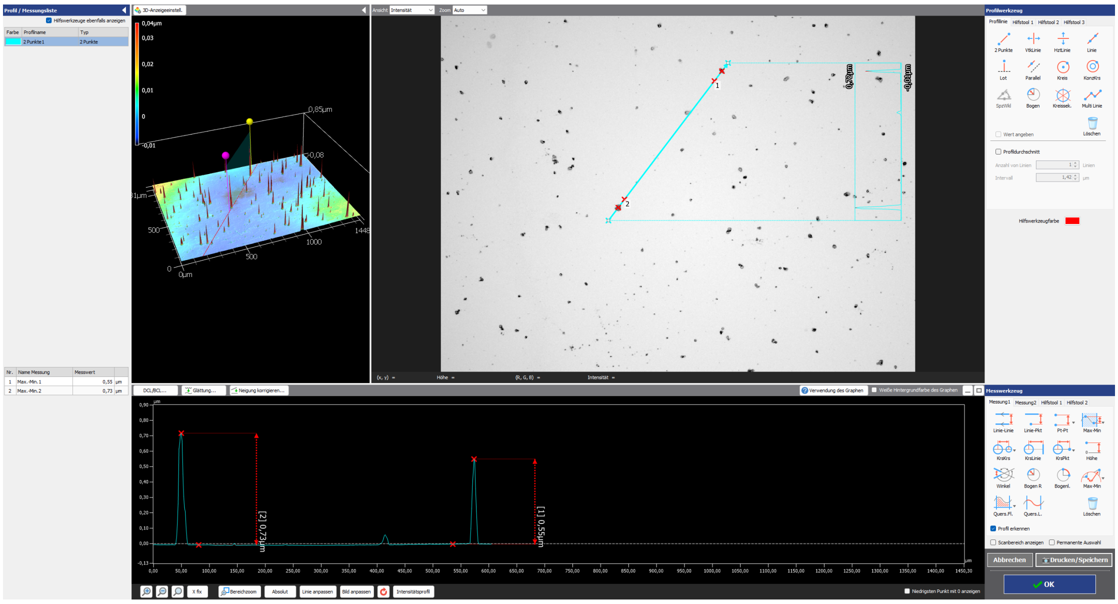

Farbe	Profilname	Typ
🟦	2 Punkte 1	2 Punkte

Nr.	Name Messung	Messwert	
1	Max.-Min.1	0,55	µm
2	Max.-Min.2	0,73	µm

Figure A.12.: Determination of max peaks in the profile scan of the unloaded glass slide on the uncovered side.

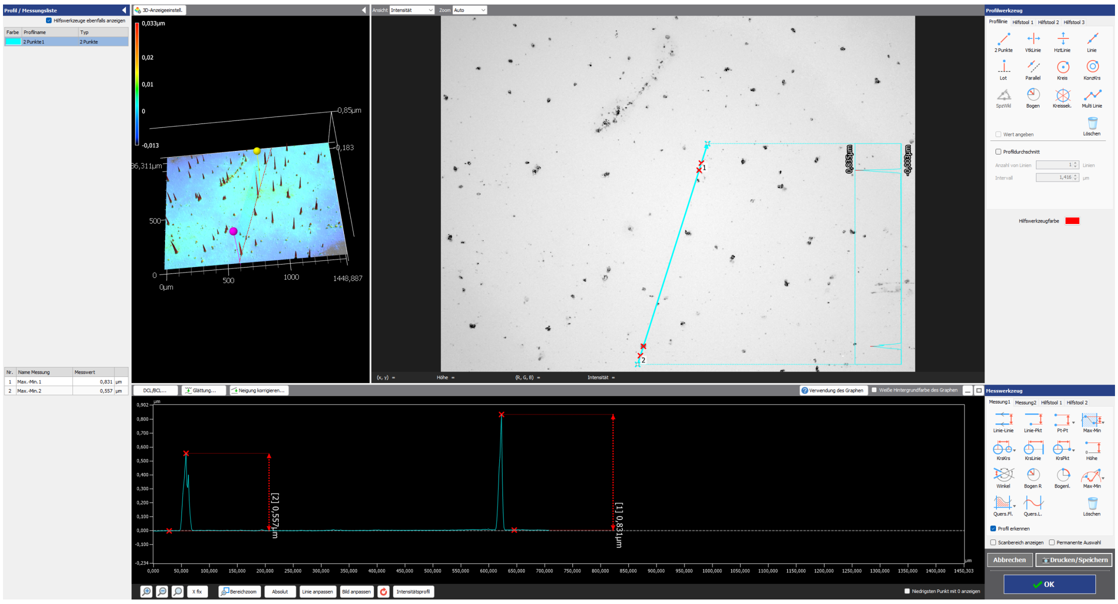

Farbe	Profilname	Typ
🟦	2 Punkte 1	2 Punkte

Nr.	Name Messung	Messwert	
1	Max.-Min.1	0,831	µm
2	Max.-Min.2	0,557	µm

Figure A.13.: Determination of max peaks in the profile scan of the loaded glass slide on the uncovered side.

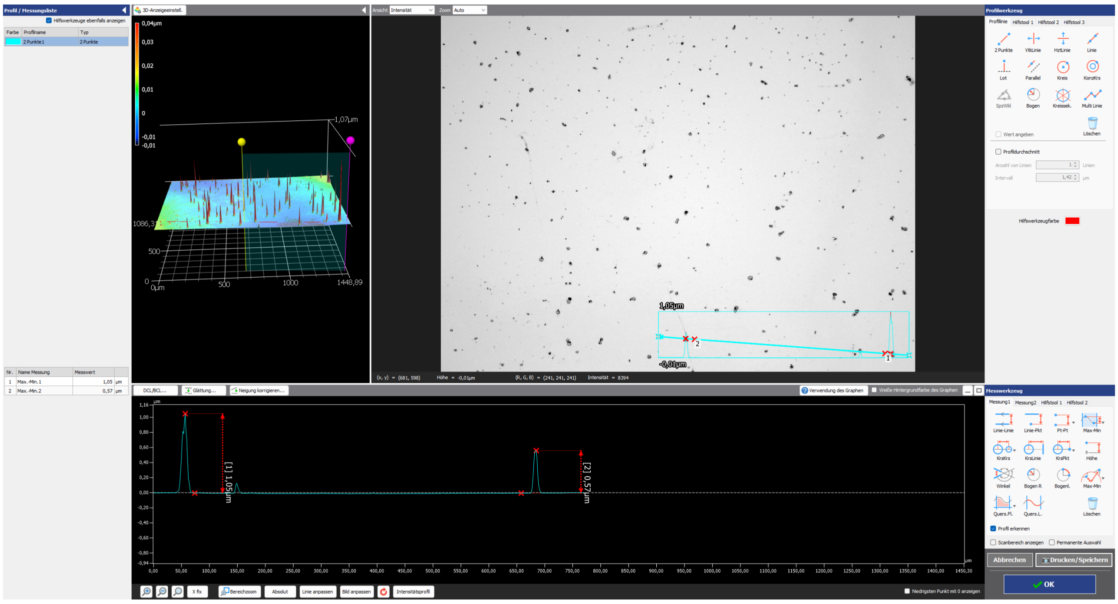

Profil / Messungsliste

☑ Hilfswerkzeuge ebenfalls anzeigen

Farbe	Profilname	Typ
🟦	2 Punkte 1	2 Punkte

Nr.	Name Messung	Messwert	
1	Max.-Min.1	1,05	µm
2	Max.-Min.2	0,57	µm

Figure A.14.: Determination of max peaks in the profile scan of the unloaded glass slide on the covered side.

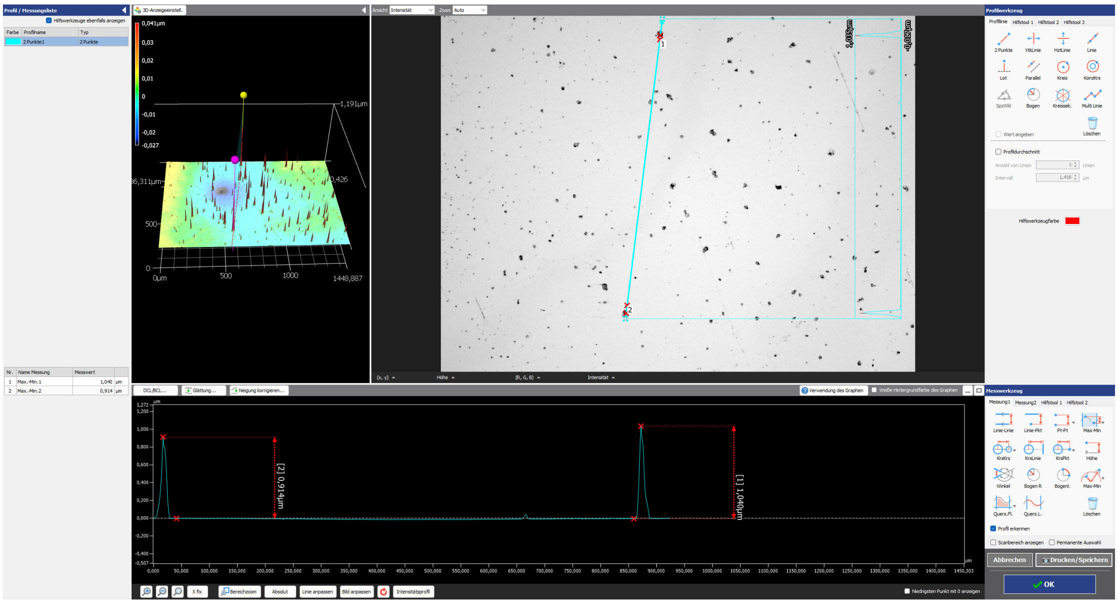

Profil / Messungsliste

☑ Hilfswerkzeuge ebenfalls anzeigen

Farbe	Profilname	Typ
🟦	2 Punkte 1	2 Punkte

Nr.	Name Messung	Messwert	
1	Max.-Min.1	1,040	µm
2	Max.-Min.2	0,914	µm

Figure A.15.: Determination of max peaks in the profile scan of the loaded glass slide on the covered side.

A.2. Results of the beam profile models

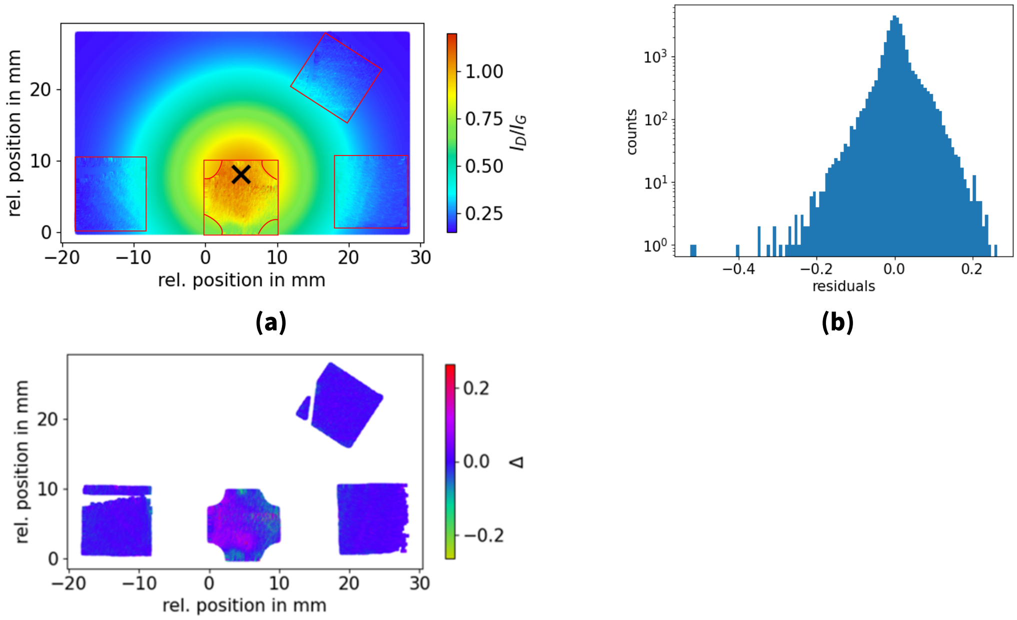

(a) **(b)**

(c)

Figure A.16.: Results of the Gaussian model fitted to the combined Raman map. **(a)** A contours plot overlapped with the data points which framed in red. The cross indicates the beam center. **(b)** The histogram of the residuals Δ. Outliers for $|\Delta| > 0.25$ are filtered for **(c)**

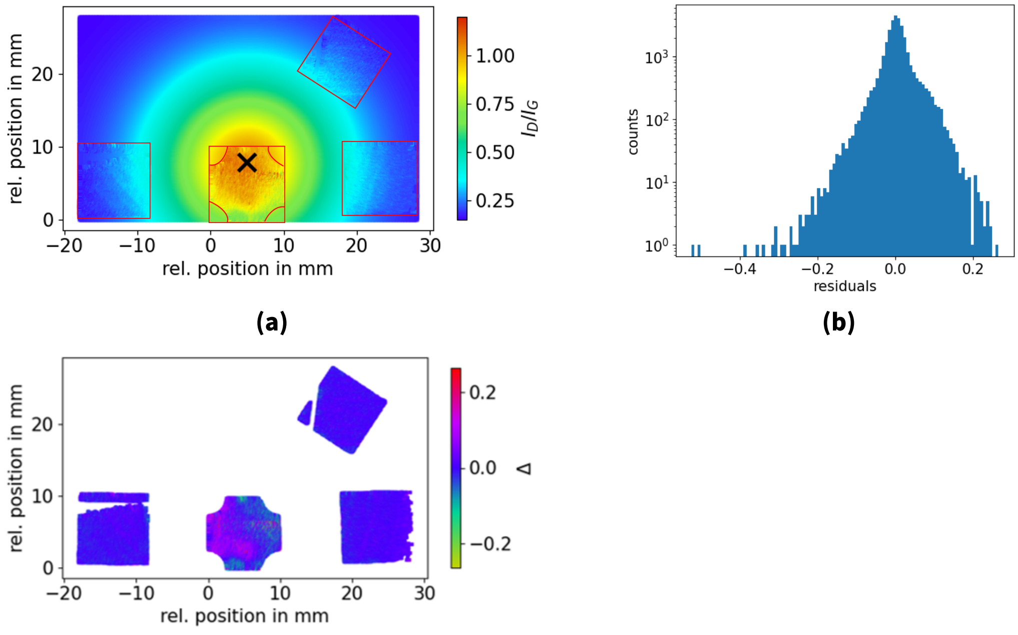

(a) **(b)**

(c)

Figure A.17.: Results of the generalized normal model fitted to the combined Raman map. **(a)** A contours plot overlapped with the data points which framed in red. The cross indicates the beam center. **(b)** The histogram of the residuals Δ. Outliers for $|\Delta| > 0.25$ are filtered for **(c)**

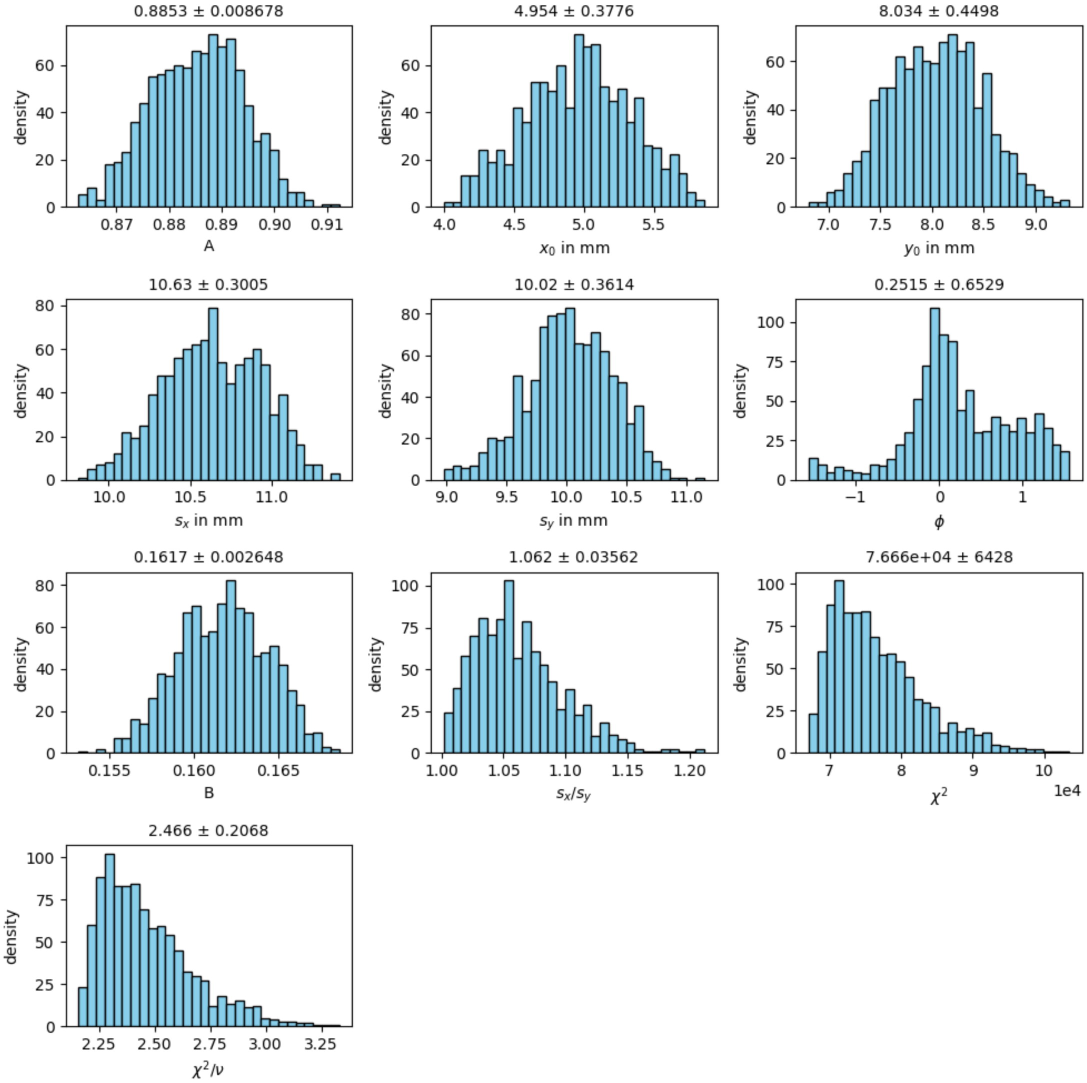

Figure A.18.: Histograms of MC error propagation of graphene sample positions to the Gaussian model parameters: BP center height A, BP center position x_0 and y_0, BP size s_x and s_y, rotation of the ellipsis ϕ, and a background offset B. The histograms of χ^2 and χ^2/ν are displayed as well.

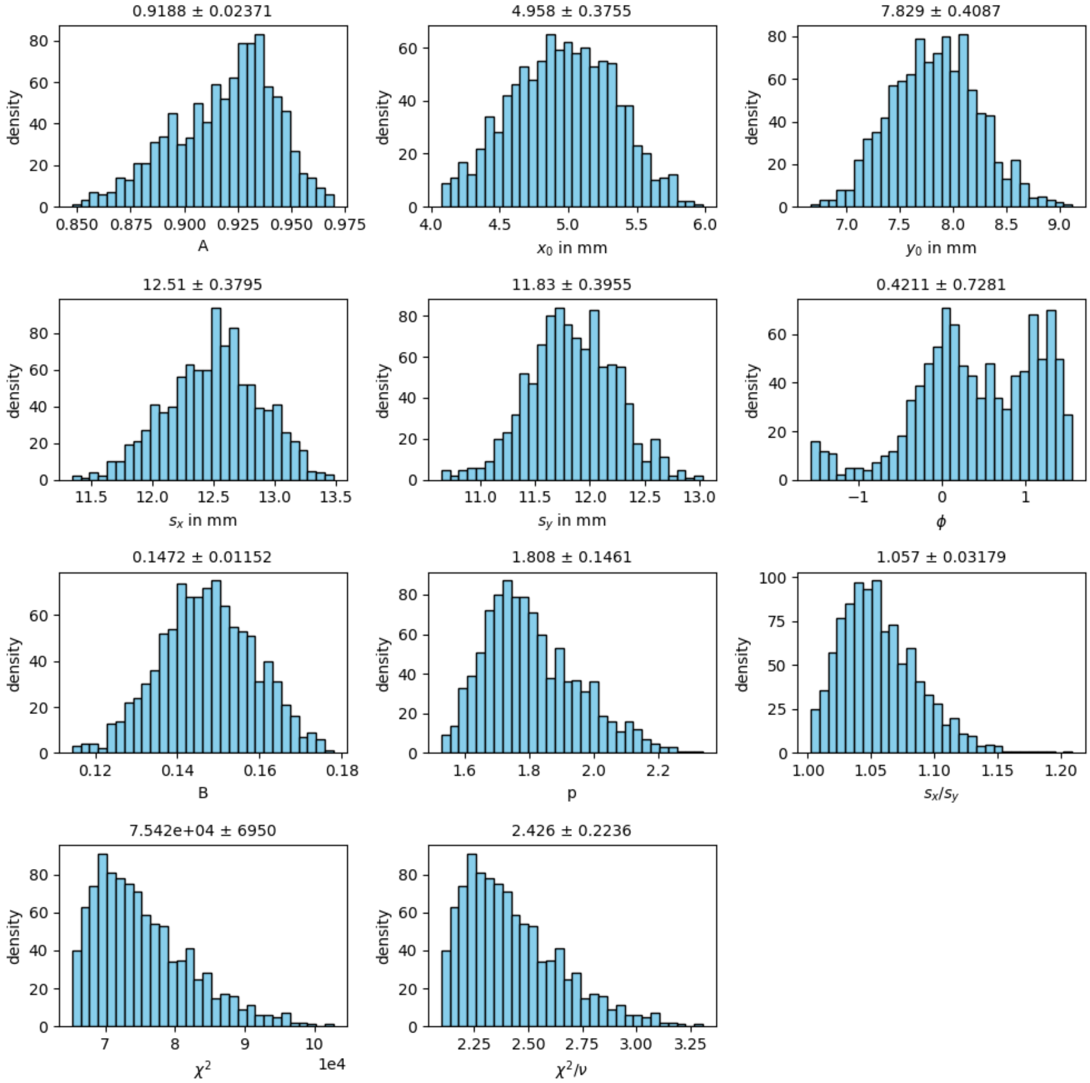

Figure A.19.: Histograms of MC error propagation of graphene sample positions to the generalized normal model parameters: BP center height A, BP center position x_0 and y_0, BP size s_x and s_y, rotation of the ellipsis ϕ, a background offset B and a free exponent p (see Equation (5.1)). The histograms of χ^2 and χ^2/ν are displayed as well.

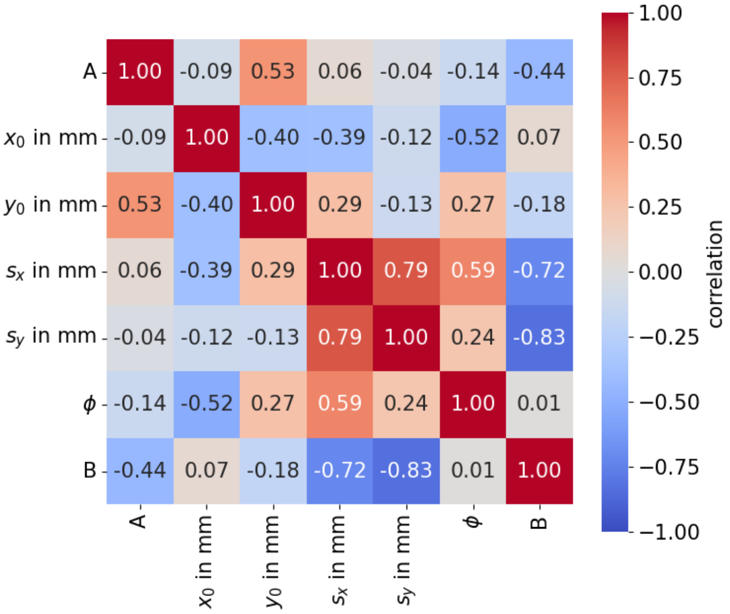

	A	x_0 in mm	y_0 in mm	s_x in mm	s_y in mm	ϕ	B
A	1.00	-0.09	0.53	0.06	-0.04	-0.14	-0.44
x_0 in mm	-0.09	1.00	-0.40	-0.39	-0.12	-0.52	0.07
y_0 in mm	0.53	-0.40	1.00	0.29	-0.13	0.27	-0.18
s_x in mm	0.06	-0.39	0.29	1.00	0.79	0.59	-0.72
s_y in mm	-0.04	-0.12	-0.13	0.79	1.00	0.24	-0.83
ϕ	-0.14	-0.52	0.27	0.59	0.24	1.00	0.01
B	-0.44	0.07	-0.18	-0.72	-0.83	0.01	1.00

Figure A.20.: Correlation of the parameters of the Lorentzian model for the beam profiles. The parameters are: BP center height A, BP center position x_0 and y_0, BP size s_x and s_y, rotation of the ellipsis ϕ, and a background offset B.

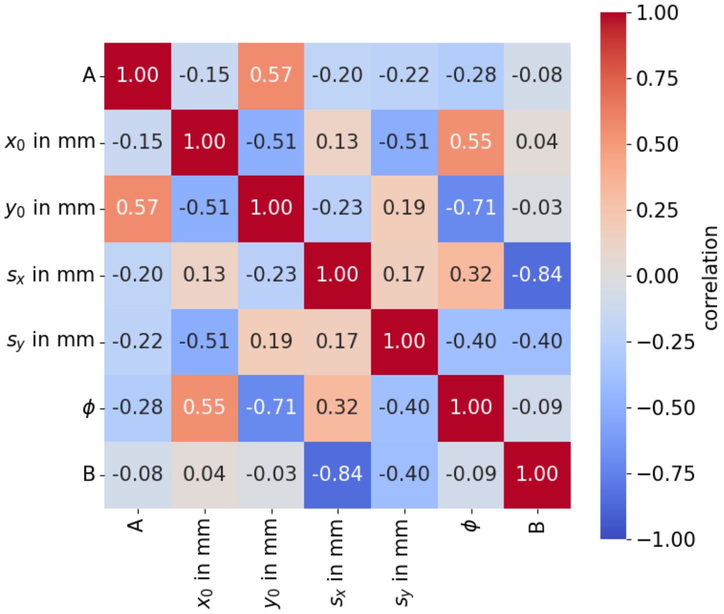

Figure A.21.: Correlation of the parameters of the Gaussian model for the beam profiles. The parameters are: BP center height A, BP center position x_0 and y_0, BP size s_x and s_y, rotation of the ellipsis ϕ, and a background offset B.

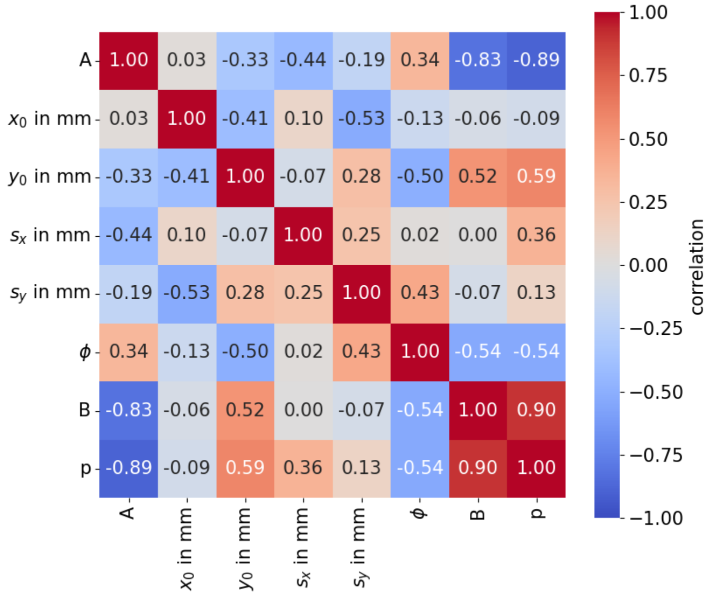

Figure A.22.: Correlation of the parameters of the generalized normal model for the beam profiles. The parameters are: BP center height A, BP center position x_0 and y_0, BP size s_x and s_y, rotation of the ellipsis ϕ, a background offset B and a free exponent p (see Equation (5.1)).

A.3. Calibration tests with the Ulbricht sphere

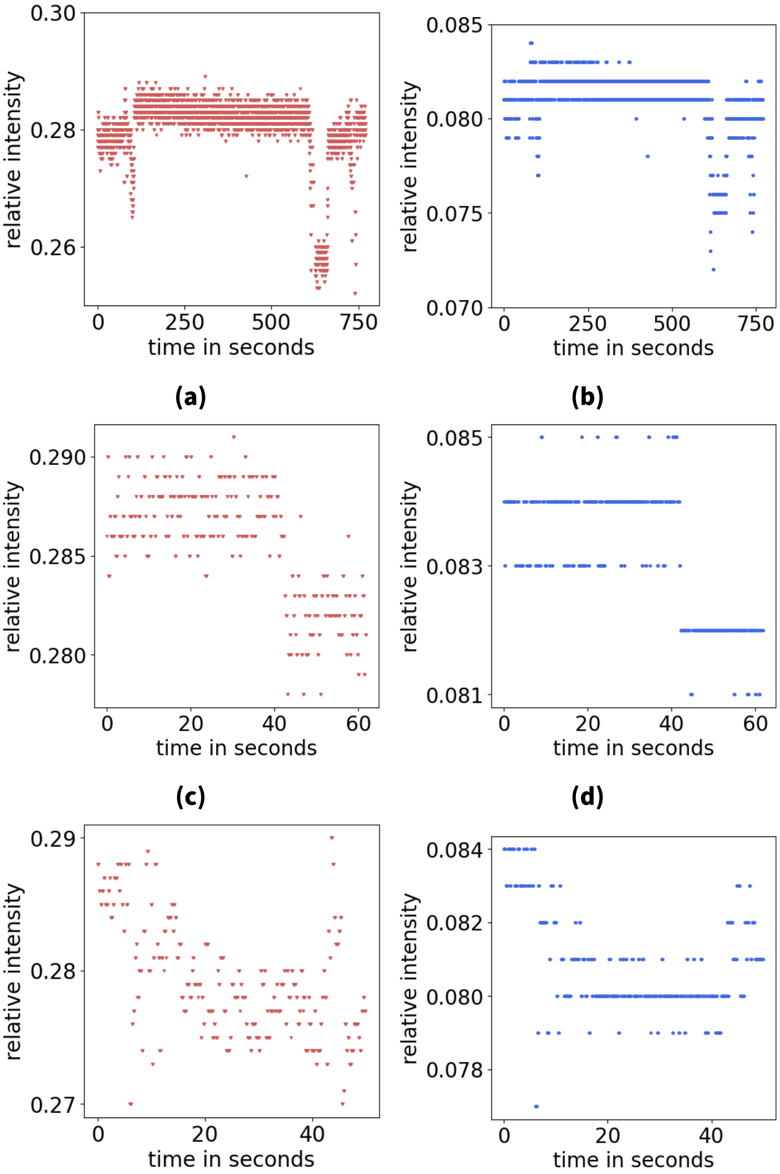

(a) **(b)**

(c) **(d)**

(e) **(f)**

Figure A.23.: Measurement of the intensity of an Ulbricht-sphere with OES. Test of uncertainty of the intensity measurement depending on the orientation of the optical components to each other (see Figure 6.1). The integrations limits are 656.6 – 657 nm for the α-line interval (*red*) and 485 – 488 nm for the β-line interval (*blue*) . **(a)** and **(b)**: During the measurement time, the position of the lens and the mount was varied. The maximum variation in intensity was 12 %. Points with an intensity of 0 are excluded, because here the lens was completely detached from the view port. **(c)** and **(d)**: During the measurement time, the fiber was rotated against the lens position. The maximum variation in intensity was 6 %. **(e)** and **(f)**: During the measurement time, the fiber was rotated against the spectrometer position. The maximum variation in intensity was 6 %.

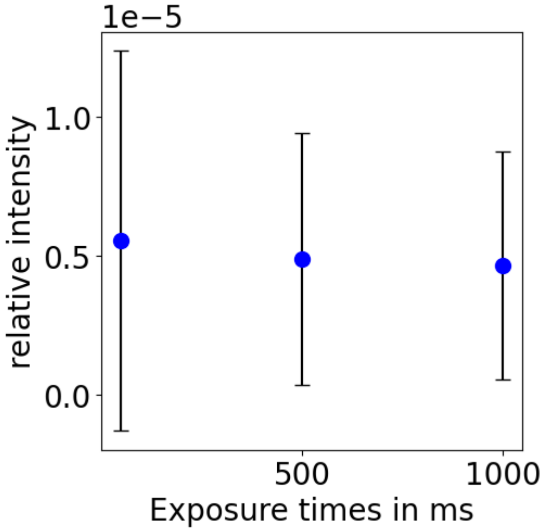

Figure A.24.: Mean values of background spectra measured for exposure times of 50, 500 and 1000 ms. For every exposure time 10 spectra are measured in a row and averaged. The mean and the standard deviation plotted as error bars are calculated from the averaged spectrum.

A.4. E to H mode transitions

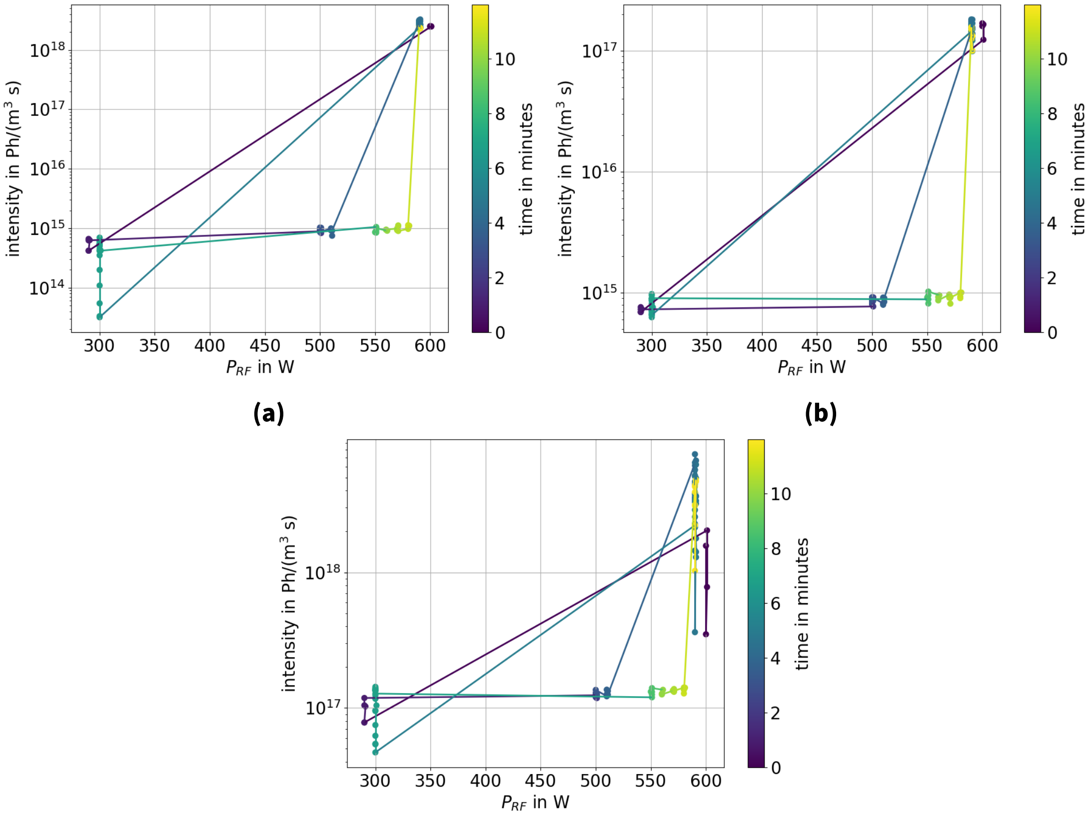

(a)

(b)

(c)

Figure A.25.: Measurement of the absolute intensity for different plasma drive powers of **(a)** the β-line, **(b)** the γ-line and **c** the Fulcher-α-band. The integration limits are listed in Table 6.1.

A.5. Pre-processing of hydrogen spectra

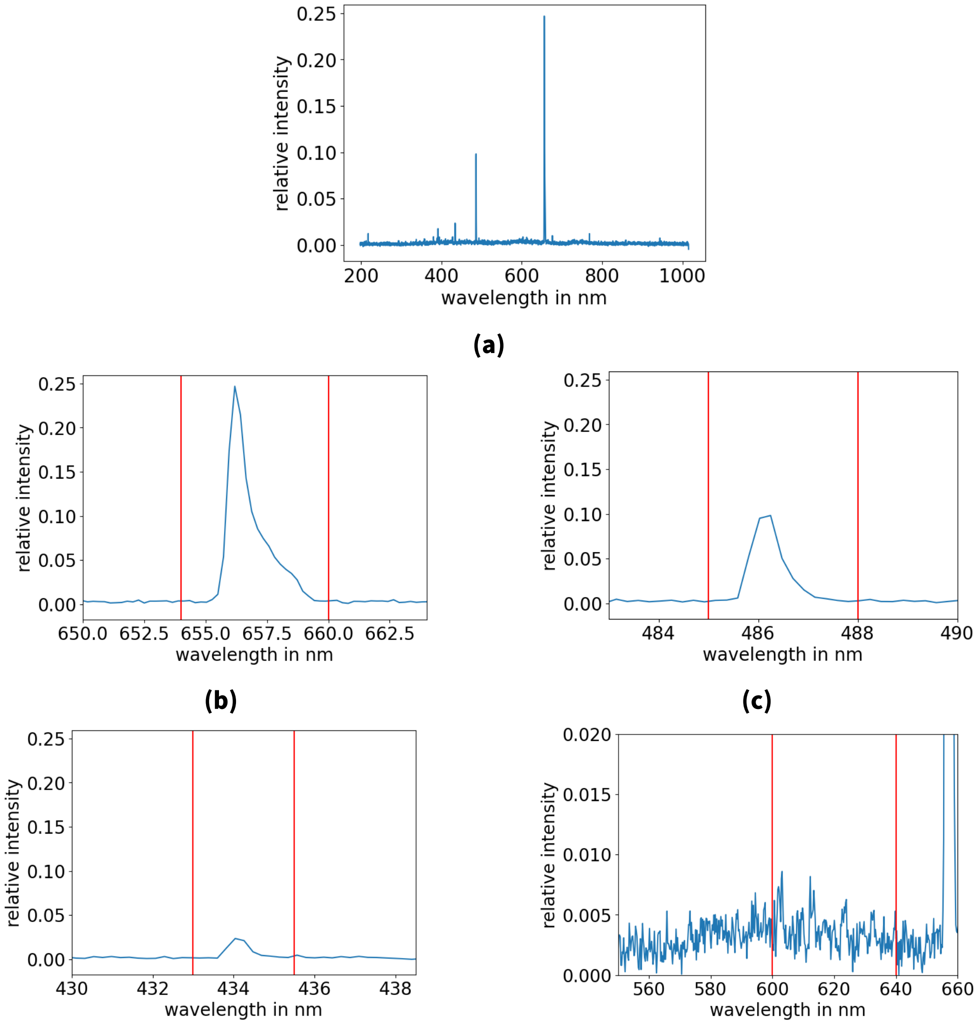

(a)

(b) **(c)**

(d) **(e)**

Figure A.26.: Measurement of a hydrogen plasma spectrum at a gas flow of 1 sccm and a plasma driving power of 350 W. In blue is the data, in red are the integration limits as defined in Table 6.1. Plotted is the **(a)** full hydrogen plasma spectrum, the Balmer **(b)** α-line, **(c)** β-line and **(d)** γ-line and **(e)** the part of the Fulcher-α-band ($600 - 640$ nm). The spectrum was measured with an exposure time of 100 ms.

Acknowledgments

Zuerst möchte ich meinen Dank **Prof. Dr. Kathrin Valerius** und **Prof. Dr. Sebastian Böser** aussprechen, dafür, dass Sie mir diese Arbeit ermöglicht haben. Außerdem hat mich Kathrin auch sonst in allen Angelegenheiten bestmöglich unterstützt. Besonders dankbar bin ich dafür, dass ich die Chance bekommen habe, die Culham Plasma Physics Summer School zu besuchen, was nicht selbstverständlich war.

Dr. Beate Bornschein möchte ich danken, dass ich die Chance bekam meine Masterarbeit am TLK zu schreiben.

Desweiteren bedanke ich mich herzlich bei meinem Gruppenleiter **Dr. Magnus Schlösser**, der mich wöchentlich durch die Masterarbeit begleitet hat. Seine kreative und visionäre Art entfachte auch in mir stets eine Begeisterung für die Wissenschaft, die ich zuvor nicht so von mir kannte.

Ich bedanke mich zutiefst bei meiner Betreuerin **Dr. Caroline Rodenbeck**. Du hast mich ausnahmslos bei allen Ideen und Tätigkeiten unterstützt und hast dir immer die Zeit genommen, mir den Weg zu weisen, wenn ich mal wieder vor einer Wand stand. Ich habe von dir nicht nur das wissenschaftliche Arbeiten, sondern auch viele Softskills gelernt. Besonders bedanken wollte ich mich noch dafür, dass du mit mir sogar nach München zum IPP gefahren bist, um das optische System zu kalibrieren.

Ich bedanke mich zutiefst bei meinem Betreuer **Dr. Genrich Zeller**. Auch du hattest jederzeit ein offenes Ohr für mich und wir hatten viele spannende Diskussionen über die Graphenbeladungen. Du hast mich inspiriert, in das Thema einzutauchen, und ich kann es kaum erwarten, die nächsten Experimente einzuleiten.

Many thanks to **Marcus Lai**, who contributed significantly to the development of the contacting setup for the sheet resistance measurements.

Vielen Dank an **Peter Winney** für die SEM Messungen und **Dr. Adrian Schwenck**, **Michaels Sagawe** und **Judith Schneider** für die WLI Messungen.

Vielen Dank an **Dr. Marco Röllig** und **Leonard Hasselmann** die stets guten Input für meine Arbeit beigetragen haben und immer für ein paar Scherze zu haben waren.

Vielen Dank an **Tobias Weber** für das Design und die Konstruktion des Probenhalters.

Außerdem bedanke ich mich bei **Dr. Stefan Welte**, **Dr. Jürgen Wendel** und **Jörg Neugebauer**, die einen sicheren Betrieb unseres Experiments sicherstellten.

Ich möchte mich bei **Prof. Dr. Ursel Fantz**, **Dr. Dirk Wünderlich** und **Dr. Richard Bergmayr** vom IPP bedanken. Eure Expertise war ein wesentliches Puzzleteil im Bild meiner Masterarbeit. Vielen Dank für die Gastfreundschaft während unseres Besuchs in Garching.

Many thanks to **Brunilda Muçogllava** from JGU Mainz, who was very supportive both scientifically and personally throughout the year.

Many thanks to **Neven Kovač**, who was always interested in my work and who corrected parts of the thesis.

Vielen Dank auch an **Svenja Heyns**, die Teile meiner Arbeit korrigiert hat.

Ich bedanke und entschuldige mich bei allen, die ich hier möglicherweise vergessen habe.

Danke an **Filipe Almeida-Alves**, der mich auch in harten Zeiten stets unterstützt hat.

An dieser Stelle bedanke ich mich bei meiner **Mutter**, meinem **Vater** und meinem **Bruder**, die die wichtigsten Säulen in meinem Dasein sind. Ich bedanke mich vor allem bei **Anna**, die bedingungslos zu mir hält.

Наконец, я хочу поблагодарить мою **бабушку** и **дедушку**. Они являются моим первоначальным источником вдохновения и опорой в жизни.